

THERMAL PHYSICAL PROPERTIES OF NANOCOMPOSITES OF
COMPLEX FLUIDS

by

Parvathalu Kalakonda

A Dissertation

Submitted to the Faculty
of the

WORCESTER POLYTECHNIC INSTITUTE

In partial fulfillment of the requirements for the
Degree of Doctor of Philosophy

in

Physics

by



May 29, 2013

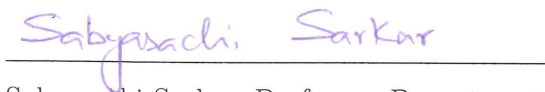
APPROVED:



Germano S. Iannacchione, Professor, Head, Department of Physics, WPI, Advisor



Georgi Georgiev, Professor, Department of Natural Sciences, Assumption College



Sabyasachi Sarkar, Professor, Department of Physics, WPI

Abstract

Composites of nanoparticles with complex fluids represent a unique physical system where thermal physical properties of the components partially or fully mix and new behavior can emerge. Traditional composites are relatively well understood as the superposition, weighted by volume or mass, of the components properties and the interfacial interactions play the role of holding the composite together. As the filler component, nanoparticle, decreases in size, the surface area begins to dominate, leading to unique behavior of the nanocomposites. The richness of the nanocomposites that can be designed by coupling various nanoparticles and complex fluid materials opens a wide field of active research.

This dissertation presents a series of experimental studies on various nanocomposites using modulated differential scanning calorimetry, spectroscopic ellipsometry, dielectric spectroscopy, polarizing microscopy, and conductivity measurements of nanoparticles such as multi-wall carbon nanotubes and quantum dots on the phase transitions of several liquid crystals and polymers. The liquid crystals (LCs) and liquid crystalline polymer (LCP) of interest are: negative dielectric anisotropy alkoxyphenylbenzoate (9004), octylcyanobiphenyl (8CB), decylcyanobiphenyl (10CB), and isotactic polypropylene (iPP) which can form smectic liquid crystal (LC) phase. Studies have been carried out as a function of concentration and temperature spanning through various ordered phases.

The results indicate a mixture of ordering and disordering effects of the nanoparticles on the phases of the complex fluids. In 9004/CNT system, dipole moment of liquid crystal and graphene-like surface can allow a random dispersion of CNT to promote both orientational and positional order. For nCB/CNT, nCB/Quantum dot (QD) systems, nanoparticles induce net disordering effect in LC media. The effect of QDs on LC depends on the anchoring conditions and the QDs size. The results clearly demonstrate that the nematic phase imposes self-assembly on QDs to form one dimensional arrays. This leads to net disordering effect. The thermal/electrical conductivity changes in thin films of iPP/CNT sheared/un-sheared samples and it also varies with temperature for the purpose of inducing anisotropy of those properties in parallel and perpendicular to average orientation. The per-

colation threshold is clearly pronounced in both conductivities due to pressing and shearing treatment of the films. This will further our abilities to nano-engineer material for many important applications.

Table of Contents

List of Figures	vii
List of Tables	xiv
Acknowledgments	xvi
1 Introduction	1
1.1 Nano-Materials	1
1.1.1 Quantum Dots or Nanocrystal	3
1.1.2 Carbon Nanotubes	5
1.1.3 General Properties of CNTs	5
1.1.4 Thermal Properties of CNTs	7
1.1.5 Electrical Properties of CNTs	8
1.1.6 Optical Properties of CNTs	8
1.2 Polymer Nanocomposites	9
1.2.1 General Properties of Polymer Nanocomposites	9
1.2.2 Dispersion of Carbon Nanotubes in Polymers	10
1.2.3 Thermal Properties of Polymer Nanocomposites	10
1.2.4 Electrical Properties of Polymer Nanocomposites	10
1.3 Review of Liquid Crystals	11
1.4 Liquid Crystalline Phases	12
1.4.1 The Isotropic Phase	13
1.4.2 The Nematic Phase	14
1.4.3 The Smectic Phase	15
1.4.4 The Chiral Smectic Phases	18
1.4.5 The Plastic Crystal Phase	19
1.4.6 The Liquid Crystal Polymers	20
1.5 Review of Thermodynamics	20
1.5.1 Thermodynamic State Functions	21
1.5.2 Thermodynamic Response Functions	22

1.6	Phase Transitions	23
1.6.1	Symmetry	24
1.6.2	Order of a Phase Transition	24
1.6.3	Order Parameter	26
1.7	Theoretical Background	26
1.7.1	Landau-de Gennes Theory of Phase transition	26
1.7.2	Isotropic to Nematic (<i>I-N</i>) Phase Transition	28
1.7.3	Nematic to Smectic-A (<i>N-SmA</i>) Phase Transition	30
1.8	Liquid Crystal Nanocomposites	33
1.9	Dissertation Outline	34
2	Experimental Techniques	41
2.1	Modulated Differential Scanning Calorimetry (MDSC)	41
2.2	Dielectric Spectroscopy (DS)	44
2.3	Polarizing Microscopy (PM)	46
2.4	Conductivity Experiments (CE)	47
2.5	Spectroscopic Ellipsometry (SE)	49
2.6	Materials	50
2.6.1	Characteristics of 9004	50
2.6.2	Characteristics of 5CB	51
2.6.3	Characteristics of 8CB	53
2.6.4	Characteristics of 10CB	53
2.6.5	Characteristics of <i>iPP</i>	55
2.6.6	Characteristics of MWCNTs	55
2.6.7	Characteristics of QDs	56
2.7	Sample preparation	58
2.7.1	9004/CNT	58
2.7.2	8CB,10CB/QD	58
2.7.3	<i>iPP</i> /CNT	58
2.8	Methodology	59
2.8.1	MDSC	59
2.8.2	DS	60
2.8.3	PM	61
2.8.4	SE	61
2.8.5	CE	61
3	Calorimetric and Dielectric Study of a Negative Dielectric Anisotropy Alkoxy-phenyl-benzoate Liquid Crystal	66
3.1	Introduction	66
3.2	Results and Discussions	68
3.2.1	Calorimetry	68
3.2.2	Dielectric Measurements	78

4	Calorimetric Study of Nanocomposites of Carbon Nanotubes and a Negative Dielectric Anisotropy Liquid crystal	86
4.1	Introduction	86
4.2	Results and Discussions	88
5	Calorimetric Study of Phase transitions in Nanocomposites of Quantum Dots and a Liquid Crystal	107
5.1	Introduction	107
5.2	Results and Discussions	109
5.2.1	Overview	109
5.2.2	The I-N and N-SmA Phase Transitions	110
5.2.3	The <i>I</i> -SmA Phase Transition in 10CB	114
5.2.4	The Physical Model	119
6	Calorimetric Study of Nanocomposites of Multi-walled Carbon Nanotubes and Isotactic Polypropylene Polymer	126
6.1	Introduction	126
6.2	Results and Discussions	129
6.2.1	Crystallization Behavior of iPP and iPP/CNT Nanocomposites	129
6.2.2	Melting Behavior of iPP and iPP/CNT Nanocomposites . .	130
6.2.3	Effect of Scan Rates on neat iPP and 2 wt% iPP/CNT . . .	136
7	Transport Properties of Melt-Shear Oriented iPP/CNT Thin Films	146
7.1	Introduction	146
7.2	Results and Discussions	148
7.2.1	Electrical Transport Properties	148
7.2.2	Thermal Transport Properties	152
7.2.3	Optical Transport Properties	157
8	Concluding Remarks	162
8.1	Future Directions	164
A	Appendix	166
A.1	Publications	166

List of Figures

1.1	Nanocrystal quantum dots (NCQD) illuminated by UV-light emit light at a wavelength that depends both on the material composition and the size of the NCQDS. Large differences in the fluorescence wavelength result from different band gaps of the materials. Within each color (blue, green, and red) the wavelength is defined by the different sizes of the NCQDs [2].	4
1.2	Chiral vector \vec{C} and chiral angle θ with unit vectors shown in (A). (B) is armchair type $m = n$, (C) is zig-zag $m = 0, n \neq 0$, (D) is chiral type $m \neq n$, (F) shows multi-wall and (E) single-wall carbon nanotubes. \vec{a}_1 and \vec{a}_2 are the unit cell vectors of the two-dimensional hexagonal graphene sheet. The circumference of nanotube is given by the length of chiral vector. The chiral angle θ is defined as the angle between chiral vector \vec{C} and the zigzag axis [10].	6
1.3	Building blocks of LCs [46].	13
1.4	A cartoon of a nematic phase (left) along with a nematic texture (right) observed under polarizing microscope. The scale bar is of 10 μm [46].	14
1.5	Schematic of chiral nematic liquid crystal phase [46].	16
1.6	A cartoon of smectic- <i>A</i> (left) along with smectic- <i>A</i> texture observed under polarizing microscope (right). The scale bar is of 10 μm [46].	17
1.7	A cartoon of smectic- <i>A</i> phase demonstrating molecular arrangement, the director orientation, and density distribution along layer normal z . Variants of Sm <i>A</i> possibly depend on the relation between l and d [46].	18
1.8	A cartoon of smectic- <i>C</i> phase [46].	19
1.9	A cartoon of chiral smectic- <i>C</i> * phase [51].	19
2.1	Modulated Differential Scanning Calorimetry model Q200 from TA Instruments, USA [9].	42

2.2	The specific heat on heating as a function of temperature for 8CB with illustrating the overall background (dashed-dot) and low-temperature wing under the N -SmA peak (dashed) behavior used to determine ΔC_p and δH_{IN}^* (top). Dispersive part of heat capacity on heating with illustrating $\delta H_{IN}''$ and the I - N transition temperature T_{IN}	43
2.3	Design of the dielectric spectrometer [10].	45
2.4	Design of the Polarizing Microscope [15].	47
2.5	Design of the conductivity experiment.	48
2.6	Spectroscopic Ellipsometry model M-2000 from J. A. Wollam Co., Inc., USA, [23].	50
2.7	Molecular structure of the 9OO4 molecule using a ChemBioDraw software.	51
2.8	Structural formulas for liquid crystal referred to in this work.	52
2.9	Molecular structure of the 5CB molecule using a ChemBioDraw software.	52
2.10	3D structure of the 5CB molecule [10] using a MolviZ.Org.	52
2.11	Molecular structure of the 8CB molecule using a ChemBioDraw software.	53
2.12	3D structure of the 8CB molecule [10] using a MolviZ.Org.	53
2.13	Molecular structure of the 10CB molecule using a ChemBioDraw software.	54
2.14	3D structure of the 10CB molecule [10] using a MolviZ.Org.	54
2.15	Molecular structure of the iPP using a ChemBioDraw software.	55
2.16	Structure of the CNT [32].	56
2.17	Quantum dots irradiated with a UV light. Different sized quantum dots emit different color light due to quantum confinement [38].	57
3.1	Overview of the excess reversible (top panel) and non-reversible (bottom panel) specific heat on cooling then heating between ~ 95 and 25 $^{\circ}\text{C}$ by MDSC. This excess specific heat was determined by subtracting a linear background over the entire experimental temperature range from the reversible and non-reversible specific heat. Scans were performed using parameters that most closely approximated static heat capacity results; a base scan rate of ± 0.3 K/min and an induced temperature amplitude of 0.5 K at 120 s heating period. Note that the cooling scan was paused at 47 $^{\circ}\text{C}$ (320.2 K) for ~ 2 hr before continuing.	70

3.2	Detailed view of the excess reversible (top panel) and non-reversible (bottom panel) specific heat about the isotropic to nematic phase transition on cooling then heating about the transition temperature T_{IN} . Quasi-static parameters of Fig. 3.1 were used for these scans. For clarity, every 15 th data point has been plotted. Note the indication of the two-phase ($I+N$) coexistence range by the vertical dashed lines was determined by the non-zero signal in $\Delta C_p''$	71
3.3	The excess reversible specific heat for the nematic to smectic- A phase transition on cooling then heating about the transition temperature T_{NA} using the quasi-static experiment parameters. For clarity, every 15 th data point has been plotted. This excess specific heat was determined by subtraction of the low-temperature specific heat wing of the $I-N$ phase transition. Note that the non-reversible specific heat was essentially zero through this transition, indicating the continuous character of this transition.	72
3.4	The excess reversible specific heat for the smectic- A to smectic- C phase transition on cooling about the transition temperature T_{AC} using the quasi-static experiment parameters. For clarity, every 15 th data point has been plotted. The transition temperature was estimated by the inflection point of δC_p on cooling. This excess specific heat was determined by subtraction of the low-temperature specific heat wing of the N -Sm A phase transition underlying the Sm A -Sm C transition. Note that the non-reversible specific heat was essentially zero through this transition, indicating the continuous character of this transition.	73
3.5	The reversible and non-reversible excess specific heat on cooling over the smectic- C to smectic- B to crystallization transitions as a function of continuous scan rate. For clarity, every 15 th data point has been plotted. Quasi-static modulation parameters were used; 0.5 K temperature amplitude and 120 s heating period, while the cooling rate was varied from the lowest of 0.3 to 0.7 K/min. See legend. Also shown is the 0.3 K/min base rate cooling scan that was paused at 47 °C for 2 hr before proceeding (solid line), the pause point is indicated by the vertical double arrows. The vertical dashed lines approximate the first-order Sm C -Sm B and Sm B - K transitions.	74

3.6	The reversible and non-reversible excess specific heat on heating from the melting to smectic- <i>A</i> transitions as a function of continuous scan rate. For clarity, every 15 th data point has been plotted. Quasi-static modulation parameters were used; 0.5 K temperature amplitude and 120 s heating period, while the cooling rate was varied from the lowest of 0.3 to 0.7 K/min. See legend. The vertical dashed lines approximate the transitions from the crystal to an undetermined smectic phase denoted Sm <i>X</i> and another from Sm <i>X</i> to the Sm <i>A</i> phase. Both observed transitions are first-order.	75
3.7	The real ε' (top panel) and imaginary ε'' (bottom panel) dielectric constant of 9004 in the homogeneous (planar) cell. Data taken on cooling then heating at 100 kHz using ± 0.3 K/min scan rates between 95 and 25 °C. See legend. For clarity, every 10 th data point has been plotted. The vertical dashed lines indicate the <i>I-N</i> , <i>N-SmA</i> , and the Sm <i>C-SmB</i> (cooling only) transitions.	81
4.1	(a) Excess real specific heat ΔC_p associated with the <i>I-N</i> phase transition as function of temperature about T_{IN} on cooling. The definition of the symbols are given in the inset. (b) Excess specific heat ΔC_p associated with the <i>I-N</i> phase transition as function of temperature about T_{IN} on heating.	89
4.2	(a) Excess specific heat δC_p associated with the <i>N-SmA</i> phase transition as function of temperature about T_{NA} on cooling. The definition of the symbols are given in the inset. (b) Excess specific heat δC_p associated with the <i>N-SmA</i> phase transition as function of temperature about T_{NA} on heating.	91
4.3	Excess real specific heat ΔC_p associated with the Sm <i>A-SmC</i> phase transition as function of temperature about T_{AC} on cooling for different CNT content sample. The definition of the symbols are given in the inset.	92
4.4	The inverse electroclinic coefficient e_c^{-1} is shown as a function of temperature for an applied electric field at frequency 25 Hz across the cell containing a 0.05 wt% 9004/CNT sample. The results were fitted a 3-parameter power law and resulted in a susceptibility exponent $\gamma = 0.99 \pm 0.06$. Inset shows an expanded view of the inverse electroclinic coefficient for low temperature range.	93
4.5	(a) Excess real and imaginary specific heat ΔC_p associated with the Sm <i>C-SmB</i> phase transition as function of temperature about T_{CB} on cooling. The definition of the symbols are given in the inset. (b) Imaginary specific heat C_p'' as function of temperature about T_{CB} on cooling.	95

4.6	(a) Excess real and imaginary specific heat ΔC_p associated with the K -Sm X -Sm C phase transition as function of temperature about T_{XA} on heating. The definition of the symbols are given in the inset. (b) Imaginary specific heat C_p'' as function of temperature about T_{XA} on heating.	96
4.7	(a) The phase transition temperature shifts for the I - N (■), N -Sm A (□), Sm A -Sm C (●), and Sm C -Sm B (○) in 9004/CNT samples and the I - N and N -Sm A transition temperature shift for 8CB/CNT [31] (---) as a function of ϕ_w . (b) The phase transition temperature shifts of the Sm B - K (Δ), K -Sm X (□) and Sm X -Sm A (○) for the 9004/CNT samples as a function of ϕ_w	98
4.8	(a) The I - N average fractional effective transition enthalpy for 9004 (○) and 8CB (---) with the function of ϕ_w . (b) The N -Sm A average fractional effective transition enthalpy for 9004 (○) and 8CB (---) with the function of ϕ_w . (c) The effective total transition enthalpy on heating for 9004 (○) and the effective total transition enthalpy on cooling for 9004 (●) with the function of ϕ_w	99
5.1	Excess real specific heat $\Delta C_p'$ associated with the I - N phase transition as function of temperature about T_{IN} on cooling (a) and heating (b). The definition of the symbols are given in the inset.	111
5.2	(a) Excess real specific heat $\delta C_p'$ associated with the N -Sm A phase transition as function of temperature about T_{NA} on cooling. The definition of the symbols are given in the inset.(b) Excess real specific heat $\delta C_p'$ associated with the N -Sm A phase transition as function of temperature about T_{NA} on heating.	112
5.3	The I - N phase transition temperatures T_{IN} (left axis: heating (○) and cooling (●)) and N -Sm A phase transition temperature T_{NA} (right axis: heating (○) and cooling (●)) as a function of ϕ_w . Lines are guides to the eye.	114
5.4	(a) The nematic range on heating (○) and cooling (●) as a function of ϕ_w . (b) The $I+N$ coexistence region on heating (○) and cooling (●) as a function of ϕ_w . Lines are guides to the eye.	115
5.5	(a) The integrated ΔC_p I - N enthalpy δH_{IN}^* (left axis: heating (○) and cooling (●)) and imaginary enthalpy $\delta H_{IN}''$ (right axis: heating (□) and cooling (■)) as the function of ϕ_w . (b) The integrated δC_p N -Sm A enthalpy δH_{NA}^* on heating (○) and cooling (●) as the function of ϕ_w . Lines are guides to the eye.	116
5.6	Excess real and imaginary specific heat $\Delta C_p'$ associated with the I -Sm A phase transition as function of temperature about T_{IA} on heating. The definition of the symbols are given in the inset.	117
5.7	The I -Sm A phase transition temperatures T_{IA} on heating (○) and on cooling (●) as a function of ϕ_w . Lines are guides to the eye.	120

5.8	The QDs configuration in LC media at higher QD concentration in N phase (top panel) and the QDs configuration in LC media at higher QD concentration in SmA phase (bottom panel).	121
6.1	The total specific heat ΔC_p on cooling at -0.5 K/min through crystallization for neat iPP and iPP/CNT nanocomposites. See legend for wt % CNT. Inset shows an expanded view of the low temperature wings revealing a very small ΔC_p feature. See text for discussion.	131
6.2	The crystallization and melting temperatures of the isotropic to mesomorphic α -monoclinic transition for neat iPP and iPP/CNT samples as a function of ϕ_w . Top panel shows the large crystallization ΔC_p position (●) and the small secondary feature (■) on cooling. Bottom panel shows the temperature of two melting features, $T_{M,1}$ (□) and $T_{M,2}$ (○) on heating. Lines are guides to the eye.	132
6.3	The total excess specific heat ΔC_p traces recorded during heating runs at +0.5 K/min through the melting region of the neat iPP and iPP/CNT nanocomposites containing loadings of CNTs listed in the legend. For clarity, the ΔC_p traces are shifted upward successively by 2 J/g K with respect to the neat iPP trace. See legend for sample wt% CNT.	133
6.4	The total effective transition enthalpy of neat iPP and iPP/CNT nanocomposites on cooling (●) and heating (○) as a function of ϕ_w . Lines are guides to the eye.	134
6.5	Melting temperatures $T_{M,1}$ (■) and $T_{M,2}$ (●) plotted against crystallization temperature for iPP filled with various loadings of CNTs. Crystallization and melting temperatures were obtained from non-isothermal MDSC experiments and straight lines from linear regression.	135
6.6	The total excess specific heat ΔC_p on cooling from the isotropic to mesomorphic to α -monoclinic transitions as a function of continuous scan rate (K/min) for neat iPP (top) and 2 wt% of CNTs (bottom). For clarity, every 15 th data point has been plotted. Quasi-static modulation parameters were used; 0.5 K temperature modulation amplitude and 60 s heating period, while the cooling rate was varied from -0.5 to -4 K/min. See legend.	137
6.7	The total excess specific heat ΔC_p on heating from the mesomorphic- α monoclinic to isotropic transitions as a function of continuous scan rate (K/min) for neat iPP (top) and 2 wt% of CNTs (bottom). For clarity, every 15 th data point has been plotted. Quasi-static modulation parameters were used; 0.5 K temperature modulation amplitude and 60 s heating period, while the cooling rate was varied from -0.5 to -4 K/min. See legend.	138

6.8	The crystallization and melting temperatures as a function for neat iPP (cooling (■), heating (□)) and for 2 wt% iPP/CNT sample (cooling (●), heating (○)). Lines are guides to the eye.	139
6.9	The total effective transition enthalpy as function of scan rate for neat iPP (top panel: cooling (■), heating (□)) and for the 2 wt% iPP/CNT sample (bottom panel: cooling (●), heating (○)). Lines are guides to the eye.	140
7.1	Electrical conductivity of non sheared (upper panel) and sheared (lower panel) IPP/CNTs nanocomposite for 40 °C and 20 °C as a function of CNT concentration.	149
7.2	Electrical conductivity of non sheared (upper panel) and sheared (lower panel) IPP/CNTs nanocomposite as a function of CNT temperature.	150
7.3	Anisotropy in electrical conductivity of non sheared and sheared IPP/CNTs nanocomposite as a function of CNT temperature. . . .	151
7.4	Thermal conductivity of non sheared (upper panel) and sheared (lower panel) IPP/CNTs nanocomposite for 40 °C and 20 °C as a function of CNT concentration.	154
7.5	Thermal conductivity of non sheared (upper panel) and sheared (lower panel) IPP/CNTs nanocomposite as a function of CNT temperature.	155
7.6	Anisotropy in thermal conductivity of non sheared and sheared IPP/CNTs nanocomposite as a function of CNT temperature. . . .	156
7.7	Index of refraction (upper panel) and extinction coefficient (lower panel) for pure iPP and 1 wt% CNTs, IPP/CNTs nanocomposite as a function of wavelength.	158
7.8	The refractive index n for iPP nanocomposite with 1 wt% CNT in directions parallel (n_{\parallel}) and perpendicular (n_{\perp}) to the shear direction (top panel) and the percent anisotropy of n (δ, n_s) as a function of wavelength λ (bottom panel).	159

List of Tables

3.1	Summary of the transition temperatures T_C for 9004 based on the quasi-static MDSC results for both cooling and heating scans (superscripts c and h , respectively) in Celsius. First-order transition temperatures are taken as the highest temperature of the two-phase coexistence range (or the lowest temperature of the higher temperature phase) determined from the non-reversible (imaginary) part of the specific heat, $\Delta C_p''$. Continuous-order transition temperatures are taken as the temperature of the peak in the reversible $\Delta C_p'$ for the N -SmA transition or the inflection point of the high temperature side of the $\Delta C_p'$ peak for the SmA-SmC transition. Also shown are the two-phase coexistence range δT_{2p} and the transition temperature hysteresis δT_C . If the transition is monotropic, it is designated <i>mono</i> . Uncertainties stem from determining the onset of non-zero $\Delta C_p''$	77
3.2	Summary of the transition enthalpies for 9004 based on the quasi-static MDSC results for both cooling (c) and heating (h) scans. The transition enthalpy, ΔH , is determined as the root-mean-square of the reversible (real, $\delta H'$) and non-reversible (imaginary, $\delta H''$) enthalpy in Joules per gram. Uncertainties represent integration error, overall uncertainties in determining enthalpy by MDSC is about 10%.	77
4.1	Summary of the calorimetric results for pure and all 9004/CNT samples on cooling and heating. Shown are CNT weight percent ϕ_{CNT} , I - N transition temperature T_{IN} , N -SmA transition temperature T_{NA} , K -SmX transition temperature T_{KX} , SmX-SmA transition temperature T_{XA} , SmA-SmC transition temperature T_{AC} , SmC-SmB transition temperature T_{CB} , SmB- K transition temperature T_{BK} (in Celsius).	97

4.2	Summary of the calorimetric results for pure and all 9004/CNT samples on cooling and heating. Shown are CNT weight percent ϕ_{CNT} , integrated enthalpy change for I - N transition δH_{IN}^* , imaginary enthalpy $\delta H_{IN}''$, integrated enthalpy change for N -SmA transition δH_{NA}^* , integrated enthalpy change for K -SmX transition δH_{KX}^T , integrated enthalpy change for SmX-SmA transition δH_{XA}^T , integrated enthalpy change for SmC- B transition δH_{CB}^T , integrated enthalpy change for SmB- K transition δH_{BK}^T (in J/g).	100
5.1	Summary of the calorimetric results for pure and all 8CB/QD samples on cooling. Shown are quantum dots weight percent ϕ_w , the I - N transition temperature T_{IN} , the N -SmA transition temperature T_{NA} , the nematic range ΔT_N , the coexistence range range ΔT_{I+N} , the integrated enthalpy change δH_{IN}^* , the imaginary enthalpy $\delta H_{IN}''$, and the integrated enthalpy for N -SmA transition δH_{NA}^* . All temperatures are in Kelvin and enthalpies are in Joule per gram.	118
5.2	Summary of the calorimetric results for pure and all 8CB/QD samples on heating. Shown are quantum dots weight percent ϕ_w , the I - N transition temperature T_{IN} , the N -SmA transition temperature T_{NA} , the nematic range ΔT_N , the coexistence range range ΔT_{I+N} , the integrated enthalpy change δH_{IN}^* , the imaginary enthalpy $\delta H_{IN}''$, and the integrated enthalpy for N -SmA transition δH_{NA}^* . All temperatures are in Kelvin and enthalpies are in Joule per gram.	119
6.1	Summary of the transition temperatures T_C and total effective transition enthalpies for iPP and composites based on the quasi-static MDSC results for both cooling and heating scans (superscripts c and h , respectively).	136
6.2	Summary of the transition temperatures T_C , total effective transition enthalpies, peak heights (cooling only) for iPP and 2 wt% of CNT based on the quasi-static MDSC results for both cooling and heating rates (superscripts c and h , respectively). neat iPP (top) and 2 wt% of CNT bottom.	141

Acknowledgments

I would like to offer my deep and sincere gratitude to my supervisor Professor Germano S. Iannacchione, for his excellent guidance, stimulating suggestions, assistance and encouragement throughout this work. His profound knowledge and excellent experimental skill gave me an extraordinary experience. This work would never have been possible without his support and encouragement. I am deeply indebted for putting a lot of effort to teach me about experimental physics, technical writing and presentation techniques. Thank you very much.

I am indebted to the Physics Department for financial support to my graduate studies at WPI. My special thanks goes to the Department Head Prof. Germano Iannacchione for providing me with several opportunities. I would like to thank Prof. P. K. Aravind and Prof. L. Ramdas Ram-Mohan for giving me encouragement and help all the time. I appreciate the department secretaries Jacqueline Malone (Jackie), Margaret Caisse (Peggy) and Michele O'Brien for their help and support all the time. The guidance, help and encouragement of all my professors, colleagues, and friends at WPI are highly acknowledged.

I would like to thank the members of the graduate committee for serving in the committee and for reading my dissertation. I reached here because of help and encouragement of my teachers, colleagues, mentors, and professors of different stages of my life. I would like to express my sincere thanks to all of them.

I sincerely thank to our collaborators Prof. Georgi Georgiev from Assumption College, Prof. Peggy Cebe from Tufts University, Prof. Charles Rosenblatt from Case Western Reserve University, Prof. Izabela Stroe from WPI, Prof. Sabyasachi Sarkar from WPI, and Prof. Rajratan Basu from U.S Naval Academy for providing samples, fruitful discussions, and encouragement.

I would like to thank Prof. Sabyasachi Sarkar from WPI and Prof. Georgi Georgiev from Assumption College for serving my dissertation committee.

I would like to thank my wife Indu and my son Sathvik for their constant and unconditional help and support all the time. We were blessed to have our little baby Likhith during my PhD research period. He is so playful and has added all the joys to our family. Thank you Likhith! Last but not the least, I am so grateful

for the effort, love, support, and encouragement of my parents, my brothers and their families, my sister and her family, and my father-in-law and his family. Your love and support always energize me to move forward!

Dedicated to my Parents, my wife and my sons.

Chapter 1

Introduction

1.1 Nano-Materials

The interest in nanoscale materials stems from the fact that new properties are acquired at this length scale and, equally important, that these properties change with their size or shape. The change in the properties at this length scale is not a result of scaling factors. It results from different causes in different materials. In semiconductors, it results from the further confinement of the electronic motion to a length scale that is comparable to or smaller than the length scale characterizing the electronic motion in bulk semiconducting material (called the electron Bohr radius, which is usually a few nanometers). As noble metals are reduced in size to tens of nanometers, a new very strong absorption is observed resulting from the collective oscillation of the electrons in the conduction band from one surface of the particle to the other. This oscillation has a frequency that absorbs the visible light. This is called a surface plasmon absorption. This strong absorption, giving rise to vivid characteristic color, has been observed and used, but not understood, since the 17th century [1]. The gold particles, giving rise to a brilliant rose color, have been used throughout Europe in stained glass windows of cathedrals and by the Chinese in coloring vases and other ornaments [1]. In transition metal nanoparticles, the decrease in the particle size to the nanometer length scale increases the surface-to-volume ratio. This, together with our ability to make them in different sizes and shapes, makes them potentially useful in the field of catalysis. The past couple of decades have witnessed an exponential growth of activities in

this field worldwide, driven both by the excitement of understanding their science and by the potential hope for applications and economic impacts. The largest activity in this field at this time has been in the synthesis of new nanoparticles of different sizes and new shapes. The unraveling of the physics of these particles and the application of computation methods to understand their behavior is being investigated. Self-assembly of these nanoparticles by different techniques, either from the bottom-up techniques (assembling particles synthesized in solution) or from the top-down techniques (different lithographic methods), is being pursued. Although many future applications will make use of the properties of the individual nanoparticles (sensors, medical diagnostics, homogeneous catalysis, etc.), there are other important applications that would require self-assembled nanoparticles (nanoelectronics, optoelectronics, photonics, heterogeneous catalysis, etc).

Besides giving the materials new properties, creating novel nanostructures requires new understanding of the properties of their surfaces. In most of their potential applications, the quality and the structure of the surface of nanoparticles will undoubtedly play a pivotal role in determining their functions. Being small could make the surface of a nanoparticle unstable due to the high surface energy and the large surface curvature. Thus, the thermal physical properties of materials change as nanoparticles are added. Not only could their surface structure and shape change, but the chemical nature of their surface could be altered, too. In addition, for device applications, these nanoparticles need to be connected to our macroscopic world. The perturbation at interface could have larger effects on the properties of nanoparticles than quantum confinement or other physical forces involved within the nanoparticle space. Thus, it is clear that using these nanoparticles fully and effectively will depend on our understanding of their general properties and also of their surface properties and stability. It is hoped that before we move quickly into producing large-scale dream devices in nanotechnology, the nanoscience is carried out. Not only should we be able to make any nanostructure of any shape and in any assembled form, we should also know a great deal about the properties of the individual nanoparticles as well as their assembled structures.

1.1.1 Quantum Dots or Nanocrystal

The research of microelectronic materials is driven by the need to tailor electronic and optical properties for specific component applications. Progress in epitaxial growth and advances in patterning and other processing techniques have made it possible to fabricate artificial dedicated materials for microelectronics. In these materials, the electronic structure is tailored by changing the local material composition and by confining the electrons in nanometer-size foils or grains [2]. Due to quantization of electron energies, these systems are often called quantum structures. If the electrons are confined by a potential barrier in all three directions, the nanocrystals are called quantum dots (QDs). This review of quantum dots begins with discussion of the physical principles and first experiments and concludes with the first expected commercial applications: single-electron pumps, biomolecule markers, and QD lasers.

In nanocrystals, the crystal size dependency of the energy and the spacing of discrete electron levels are so large that they can be observed experimentally and utilized in technological applications. QDs are often also called mesoscopic atoms or artificial atoms to indicate that the scale of electron states in QDs is larger than the lattice constant of a crystal. However, there is no rigorous lower limit to the size of a QD, and therefore even macromolecules and single impurity atoms in a crystal can be called QDs.

The quantization of electron energies in nanometer-size crystals leads to dramatic changes in transport and optical properties. As an example, Figure 1.1 shows the dependence of the fluorescence wavelength on the dimensions and material composition of the nanocrystals. The large wavelength differences between the blue, green, and red emissions result here from using materials having different band gaps: CdSe (blue), InP (green), and InAs (red). The fine-tuning of the fluorescence emission within each color is controlled by the size of the QDs. This is a scaling effect.

A nanocrystal (NC) is a single crystal having a diameter of a few nanometers. A NCQD is a nanocrystal that has a smaller band gap than the surrounding material. The easiest way to produce NCQDs is to mechanically grind a macroscopic crystal. Currently NCQDs are very attractive for optical applications because their color is directly determined by their dimensions. The size of the NCQDs can be selected

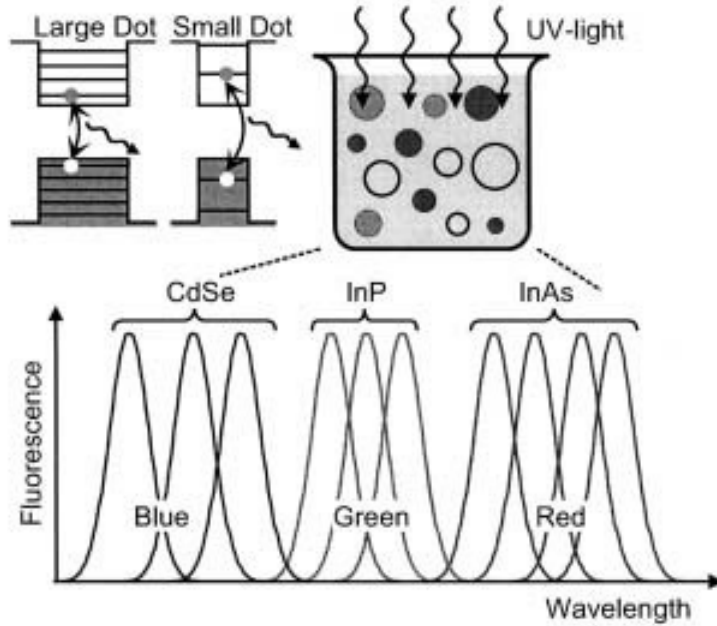


Figure 1.1. Nanocrystal quantum dots (NCQD) illuminated by UV-light emit light at a wavelength that depends both on the material composition and the size of the NCQDs. Large differences in the fluorescence wavelength result from different band gaps of the materials. Within each color (blue, green, and red) the wavelength is defined by the different sizes of the NCQDs [2].

by filtering a larger collection of NCQDs or by tuning the parameters of a chemical fabrication process.

Cadmium selenide (CdS) and zinc selenide (ZnSe) NCQDs are approximately spherical crystalites with either wurtzite or zinc-blend structure. Their diameter ranges usually between 6 and 10 nm. CdSe NCQDs are prepared by standard processing methods. A typical fabrication procedure for CdSe NCQDs is described in [3, 4]. Briefly, $Cd(CH_3)_2$ is added to a stock solution of selenium (Se) powder dissolved in tributylphosphine (TBP). This stock solution is prepared under N_2 in a refrigerator, while tri-*n*-octylphosphine oxide (TOPO) is heated in a reaction flask to 360 °C under argon (Ar) flow. The stock solution is then quickly injected into the hot TOPO, and the reaction flask is cooled when the NCQDs of the desired size is achieved. The final powder is obtained after precipitating the NCQDs with methanol, centrifugation, and drying under nitrogen flow.

1.1.2 Carbon Nanotubes

Carbon is a special element in nature, which chemical versatility makes it the central agent in most applications. Until recently, it had been well known that pure carbon exists in two forms: diamonds and graphite. In 1985, Harold Kroto, Robert Curl, and Richard E. Smally discovered a new form of carbon, fullerenes, which are molecules of pure carbon atoms bonded together forming geometrically regular structures [5]. The best known is the C_{60} , which has precisely the same geometry as the soccer ball, total 60 carbon atoms. Due to the similarity of structure developed by American architect, Buckminster Fuller, this new molecule was named the buckminster fullerene, or bucky-ball. The Carbon Nanotubes (CNTs) were first prepared by M. Endo in 1978, as part of his PhD studies at the University of Orleans in France. He was able to produce very small diameter filaments (about 7 nm) using a vapour-growth technique, but these fibers were not recognized as nanotubes and were not studied systematically. It was only after the discovery of fullerenes, C_{60} in 1985 by Kroto [5], that researchers started to explore carbon structures further. In 1991, when the Japanese electron microscopist Sumio Iijima observed CNTs [6], the field really started to advance. He was studying the material deposited on the cathode during an arc-evaporation synthesis of fullerenes when he observed CNTs. A short time later, Thomas Ebbesen and Pulickel Ajayan, from Iijimas lab, showed how nanotubes could be produced in bulk quantities by varying the arc-evaporation conditions [7]. But the standard arc evaporation method had produced only multiwall nanotubes. After some research, it was found that the addition of metals such as cobalt to the graphite electrodes resulted in extremely fine single-wall nanotubes. The synthesis in 1993 of SWNTs was a major event in the development of CNTs [8, 9]. Although the discovery of CNTs was an accidental event, it opened the way to flourishing research into the properties of CNTs in labs all over the world, with many scientists demonstrating promising physical, chemical, structural, electronic, thermal and optical properties of CNTs.

1.1.3 General Properties of CNTs

Carbon nanotubes are made up of one or more wrapped seamless concentric cylindrical carbon honeycomb lattice or graphene sheet. The theoretically smallest nan-

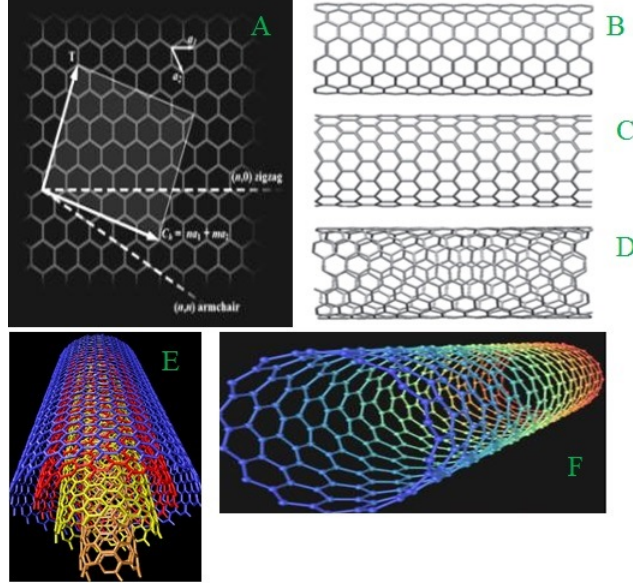


Figure 1.2. Chiral vector \vec{C} and chiral angle θ with unit vectors shown in (A). (B) is armchair type $m = n$, (C) is zig-zag $m = 0, n \neq 0$, (D) is chiral type $m \neq n$, (E) shows multi-wall and (F) single-wall carbon nanotubes. \vec{a}_1 and \vec{a}_2 are the unit cell vectors of the two-dimensional hexagonal graphene sheet. The circumference of nanotube is given by the length of chiral vector. The chiral angle θ is defined as the angle between chiral vector \vec{C} and the zigzag axis [10].

otubes have diameters equal to diameters of C_{60} ($d = 0.7$ nm). The most important structures are single wall (SW) and multiwall carbon nanotubes (MWCNTs). The primary symmetry classification of CNT is divided into two parts, achiral and chiral. An achiral nanotube is defined by a nanotube whose mirror image has an indistinguishable structure to the original one. And, as a consequence, it is superimposable. There are only two cases of achiral nanotubes: armchair and zig-zag nanotubes. Single wall carbon nanotubes are completely described, except for their length, by a single vector \vec{C} pointing from the first atom towards the second one and is defined by the relation Equation 1.1 [10]

$$\vec{C} = n\vec{a}_1 + m\vec{a}_2 \quad (1.1)$$

where n and m are integers. \vec{a}_1 and \vec{a}_2 are the unit cell vectors of the two-dimensional lattice formed by the graphene sheets. The direction of the nanotube axis is perpendicular to this chiral vector. The length of the chiral vector \vec{C} Figure 1.2 is the circumference of the nanotube and is given by the corresponding

relationship:

$$c = \vec{C} = a\sqrt{n^2 + nm + m^2} \quad (1.2)$$

where the value a is the length of the unit cell vector ($a_1 = a_2$). This length a is related to the carbon-carbon bond length. Using the circumferential length c , the diameter of the carbon nanotube is thus given by the relation:

$$D = \frac{c}{n}. \quad (1.3)$$

1.1.4 Thermal Properties of CNTs

The thermal wave propagation differs in carbon nanotubes from metal nanowires. Due to their unique crystalline structure, boundary scattering is nearly absent in CNTs. Thus, CNTs show high thermal and electrical conductivity and this makes CNTs an ideal candidate for promising applications in nanoelectronics. The potential applications and intriguing nanoscale thermal conduction physics has inspired several groups to measure CNTs thermophysical properties. Hone group [11] measured the temperature dependent thermoelectric power (TEP) of crystalline ropes of SWCNTs by simply applying a small temperature difference of maximum ± 0.2 K and measuring the voltage induced in the sample. They observed moderately large hole-like TEP and the TEP approaches zero at high temperature. Thermal conductivities of SWCNTs bundles and mats were measured by Hone group [12, 13]. The measured thermal conductance of millimeter size mat samples made of CNTs shows linear temperature dependence below 25 K and extrapolates to zero at zero temperature. The thermal conductivity at room-temperature is 1750-5800 W/m-K the range for the longitudinal thermal conductivity of a single rope [12]. The measurement results have advanced our understanding of thermal conduction in CNTs. However it is very difficult to extract the thermal conductivity of single wall carbon nanotubes, due to nanotube-nanotube junction and nanotube-interface contact resistances. This is the main reason that theoretical values are always higher, an order of magnitude than the experimental values. Below room temperature, "Umklapp" phonon-phonon scattering became very weak [13, 14] and it does not occur some times. This indicates that the dominant scatter-

ing mechanism is phonon scattering by defects and boundaries of nanotube walls which depends upon the sample geometry, contact surface and interface roughness. There has been some experimental and theoretical work at low temperatures, but no significant information is available at high temperatures for CNTs [13]. The specific heat capacity for single wall carbon nanotube at room temperature is 10 mJ/gK [13]. Our work is based on above room temperature and thermal properties measured for well aligned and random macroscopic composites of MW and SW carbon nanotubes. The results indicate a mixture of ordering and disordering effects of the nanoparticles on the phases of the complex fluids.

1.1.5 Electrical Properties of CNTs

The electron transport in CNT assemblies is different from that in individual nanotubes. It has been reported that single-wall carbon nanotube (SWNT) fibers, either synthesized directly by vertical floating chemical vapor deposition (CVD) methods [15, 16] or extruded from a super-acid suspension, [17] exhibit room-temperature resistivities in the range of 1×10^4 to $7 \times 10^4 \Omega\text{cm}$, which is nearly 100 times higher than the resistivities of single nanotubes. The resistivities of multi-wall carbon nanotube (MWNT) fibers are typically one or two orders of magnitude higher than that of SWNT fibers [18, 19]. Such large differences between single nanotubes and fiber assemblies may arise from a high impurity content (such as amorphous carbon and catalytic particles) in the fibers, which may profoundly affect electron transport by causing significant scattering, and increasing contact resistances between nanotubes. Therefore, two approaches can be used to improve the electrical conductivity of CNT fibers: 1) minimize the contact resistances between nanotubes by improving the alignment of CNTs by increasing the lengths of individual tubes; 2) improve the conductivity of individual CNTs by post-synthesis treatments [20].

1.1.6 Optical Properties of CNTs

The optical properties of carbon nanotubes refer specifically to the absorption and refractive index of carbon nanotubes. Spectroscopic methods offer the possibility of quick and non-destructive characterization of relatively large amounts

of carbon nanotubes. There is a strong demand for such characterization from the industrial point of view: numerous parameters of the nanotube synthesis can be changed, intentionally or unintentionally, to alter the nanotube quality. The refractive index and absorption coefficient of single-shell carbon nanotubes are calculated based on the two-band approximation and Genkin-Mednis approach. The nonlinear refractive index and absorption coefficient reach the order of 10^{-8} and $10^{-4} \text{ cm}^2 \text{ W}^{-1}$ separately, which indicates that carbon nanotubes have improved optical properties [21].

1.2 Polymer Nanocomposites

Polymer nanocomposites have been widely used for various products from automotive parts, electronics to commodities due to their tunable properties suitable for each specific application. Nanotube based polymer composites have a very rich application in the technological field due to their strength, stiffness and heat resistance. These properties depend upon the aspect ratios of fillers and the adhesive strength between filler and polymer matrix. The outstanding thermal and electrical conductivity of the carbon nanotubes make them promising filling material for the fabrication of new advanced composite systems for a broad range of technological applications. Efficient chemical functionalization of CNTs, homogeneous dispersions in solvents and supporting media, and good interconnectivity with polymer matrix still remain very important issues that must be considered in order to achieve heterostructures with enhanced or even new properties. There are numerous methods and approaches for functionalization and further efficient dispersion of the carbon nanotubes in different media [22, 23, 24]. More details on the chemical modification of CNTs, the fabrication of various CNT-based composites, and their possible applications are presented below.

1.2.1 General Properties of Polymer Nanocomposites

Polymers are usually reinforced with fillers such as glass, carbon fibers, carbon nanocomposites etc. to improve their properties (strength, stiffness, thermal conductivity, electrical conductivity etc.). The conventional micro-filler polymer composites often result in phase separation and the degradation in polymer proper-

ties such as decreased ductility, poor moldability and surface smoothen of molded products. Therefore it is expected that the interface deficiency can be reduced and thermal properties can be improved by replacing these microfillers with extremely small nanofillers.

1.2.2 Dispersion of Carbon Nanotubes in Polymers

The dispersion of CNTs in polymer matrix depends on interaction forces. Due to strong van der Waals attraction forces between carbon nanotubes, they lead to aggregate together inside the solution and form ropes, usually with highly entangled network structures. It is very difficult to disperse CNT in the polymers. But, it is possible to mix these two components without severe aggregation of nanotubes. The attractive forces also arise due to an entropic effect inside the polymer matrix [25]. Polymer chains in the region of the colloidal filler suffer an entropic penalty since roughly half of their configurations are precluded. Therefore, there is a depletion of the polymer in this region, resulting in an osmotic pressure forcing the filler particles to come together [22, 23, 24].

1.2.3 Thermal Properties of Polymer Nanocomposites

The thermal properties can be characterized by different quantities such as specific heat, thermal conductivity, thermal stability and so on. Thermal stability of polymer composites is generally estimated from the weight loss measured by thermal gravimetric methods. Recently there are many reports available on the improved thermal stability of nanocomposites [26, 27, 28, 29]. The thermal conductivity values for polymer nanocomposites are in the range of 5-10 W/mK and specific heat capacity observed is in the range of 0.1-10 J/g K [28, 29]. The high thermal conductivity can be achieved by dispersing the nanoparticles. The high aspects ratio, high quality and well dispersed filler materials increase thermal conductivity of their nanocomposites.

1.2.4 Electrical Properties of Polymer Nanocomposites

Polymer nanocomposites exhibit unique electrical properties, which is mainly attributed to their electrical conductivity. The electrical conductivity of the polymer

nanocomposites is strongly affected by the crystallinity of the materials. Nanocomposites with conducting polymers have also been reported including polymers such as polyaniline [30, 31, 32], polypyrrole [33, 34] and polythiophene [33]. The electrical conductivity observed at room temperature for polymer nanocomposites in the range of 10^{-8} to 10^2 S/m [31, 32].

1.3 Review of Liquid Crystals

Liquid crystal (LC) is an anisotropic fluid which exhibits both the properties of crystal and liquid in certain temperature range. As its name suggests it is an intermediate phase of matter in between the liquid and crystal [35, 36]. The molecules in a crystal generally possess both positional and orientational order while the molecules in a liquid do not have any order and can move randomly. The liquid crystal molecules possess orientational and partial translational order in their LC phase. LC can flow as a liquid and at the same time their molecules may be oriented in a certain direction like molecules in a crystal do. LCs possess some crystalline properties such as magnetic, electric and optical anisotropy, periodic arrangement of molecules in one spatial direction as well as some typical properties of a liquid such as fluidity and compressibility. For this reason, the LC phases are called mesophases and the molecules that show mesomorphic phases are called ‘mesogens’. Typically the molecules are rod-like or disk-like. The rod like molecules or rod-like mesogens are elongated (2.5 nm) and have anisotropic geometry which leads to preferential alignment along one spatial direction. Disc-like molecules or discotic mesogens are flat and have more or less disc-shaped central core leading to two dimensional columnar ordering. A large number of well-known compounds show liquid crystalline behavior e.g. DNA, cholesterol esters, lecithin and paraffins.

The credit for the discovery of liquid crystal goes to an Austrian botanical physiologist Friedrich Reinitzer, even though the liquid crystalline behaviour was observed in the past as well [37]. In 1888, Reinitzer observed two melting temperatures of cholesteryl benzoate [38, 39, 40]. At 145.5 °C it melts forming a cloudy liquid, that become clear at 178.5 °C. Reinitzer was puzzled by this peculiar feature shown by the compound and wrote to physicist Otto Lehmann seeking help with polarizing microscopy. After the observation of the sample obtained from Reinitzer,

Lehmann realized that the cloudy liquid observed was a new state of matter and coined the name “liquid crystal”, illustrating that it is something between a liquid and a solid, sharing important properties of both [41]. Today, thousands of other substances are known which have a diversity of phases between the solid and liquids. Interest in LC research increased after World War II. Development of industrial applications and basic studies of structure and phase transition of LCs has promoted dramatic growth in LC research in recent years.

Liquid crystal technology has had a major effect in many areas of science and technology [42, 43]. The most common application of liquid crystal technology is liquid crystal displays (LCDs). From simple wrist watch, computer to an advanced computer screens LCDs have evolved into a versatile interface. LCD uses much less power than that cathode ray tubes use. Progress in understanding LC phases also helps understanding of more complex soft materials such as cell membranes and of natural processes e.g. certain diseases such as sickle-cell anemia [44]. Typically LCs are formed from organic molecules of rigid aromatic core of benzene rings and flexible end group. The molecules of the compounds which form liquid crystalline phase are often found to have the certain structural features:

- (a) Anisotropic shaped molecules such as rod shaped or disc shaped having high aspect ratio which is (length to width ratio) (~ 4 for a typical liquid crystal 5CB)
 - (b) Having a flat segment e.g. a benzene ring.
 - (c) A fairly rigid backbone containing double bonds defines the long axis of the molecule.
 - (d) The existence of easily polarizable and strong dipoles groups in the molecules.
- A broad class of organic molecules with the general pattern as shown in Fig. 1.3 form liquid crystalline phases.

1.4 Liquid Crystalline Phases

Based on the mechanism that drives the liquid crystalline self-assembly, LCs are usually classified into two broad categories: Thermotropic and Lyotropic liquid crystals. Thermotropic LCs are induced by thermal process. They show phase behavior change as a function of temperature. Thermotropic mesogens can be obtained either lowering the temperature of its isotropic phase or raising the tem-

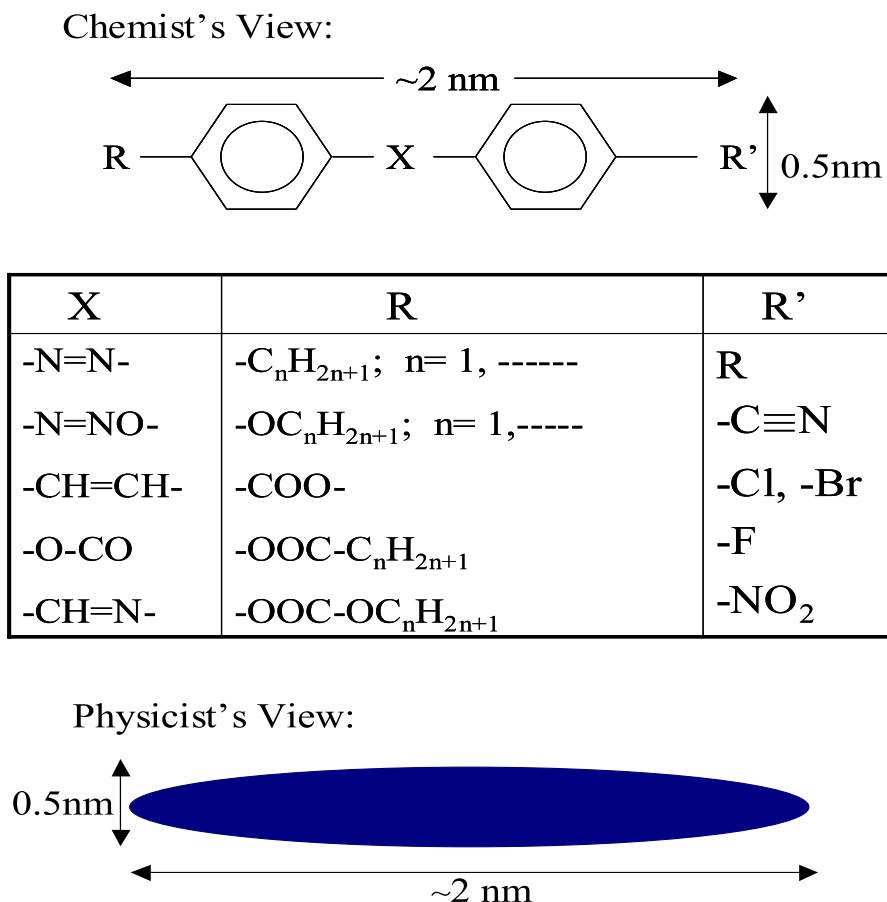


Figure 1.3. Building blocks of LCs [46].

perature of its solid phase. The thermotropic liquid crystals which change their state either from lowering the temperature of a liquid or raising the temperature of a solid. These liquid crystals are called enantiotropic liquid crystals. The liquid crystals which change phase only upon a unidirectional change in temperature is called monotropic liquid crystals. LC display varieties of intermediate thermodynamically stable phases but the most common and important are “Nematic” and “Smectic” phases. This description was provided by Friedel [45]. The brief description of each of these phases are as follows;

1.4.1 The Isotropic Phase

The least ordered phase is most symmetric isotropic (*I*) phase which exhibits isotropic behavior similar to regular liquids such as water. There are, a plethora

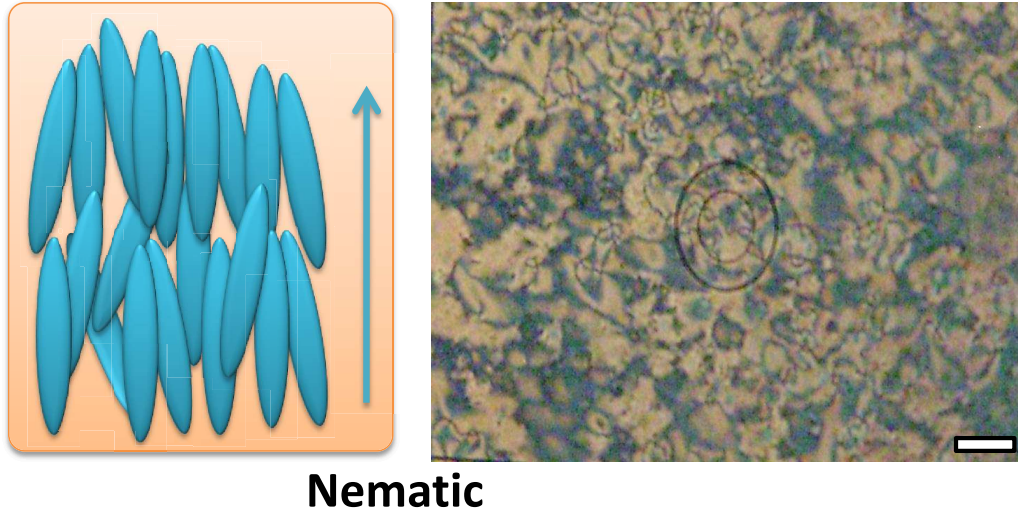


Figure 1.4. A cartoon of a nematic phase (left) along with a nematic texture (right) observed under polarizing microscope. The scale bar is of $10 \mu\text{m}$ [46].

of mesophases of lower symmetry than the I phase before the least symmetric crystalline phase belonging to the 230 space groups which characterize crystals are encountered. This progression may be described in terms of the three types of order described above.

1.4.2 The Nematic Phase

The nematic liquid crystal phase is the simplest liquid crystalline phase. It derives from the Greek word $\nu\eta\mu\alpha$ meaning thread because of the observed thread-like defects in their structures using a polarizing microscope. In nematic phases (Fig. 1.4), the molecules are free to move in all directions i.e. there is no positional order of centers of mass but they tend to orient in a certain direction. The direction of the preferred orientation can be described by a unit vector, \hat{n} , which is called the nematic-director. For an uniaxial nematic, the director \hat{n} is symmetric *i.e.* $\hat{n} = -\hat{n}$. A nematic sample can be considered as a collection of large number of domains each of which has a single director. The directors in different domains may point in different directions. They change smoothly from one domain to another due to the absence of real boundaries between the domains.

The magnitude of local order is described by the orientational order parameter

which is the average of the second Legendre polynomial:

$$S = \langle P_2(\cos\theta) \rangle = (1/2)\langle 3\cos^2\theta - 1 \rangle, \quad (1.4)$$

where θ is the angle between a molecule's long axis and the director \hat{n} . The angled brackets indicate the local average over all the molecules and P_2 is Legendre polynomial function. This quantity measures the average degree of molecular alignment with respect to the director [36]. In an isotropic phase, molecules are randomly oriented in all possible directions where $\langle \cos^2\theta \rangle = 1/3$, so the order parameter is $S = 0$. When the director \hat{n} is parallel to the long molecular axis (if all the molecules are oriented in one direction), $\theta = 0$ for all molecules, then $\langle \cos^2\theta \rangle = 1$ and $S = 1$ and we get perfectly ordered nematic phase.

The information about the order of molecules in a chiral nematic phase, the scalar nematic order parameter S and a macroscopic order parameter are very important parameters to explain chiral nematic phase. This is more general a symmetric and traceless second rank tensor (Q_{ij}) [36] and is established in three dimensions. For uniaxial nematic, it is given by

$$Q_{ij} = \frac{1}{2}S(3\hat{n}_i\hat{n}_j - \delta_{ij}). \quad (1.5)$$

where, $i, j, = x, y, z$ are the axes of the coordinate system and δ_{ij} is the identity tensor.

When a molecule having its mirror image different from itself, called chiral molecule, is introduced in an achiral nematic system then a special type of nematic phase is formed which is known as chiral nematic (N^*) phase or cholesteric phase. In this phase chiral packing produces the helix-like orientation of the director i.e \hat{n} rotates or twists along an orthogonal axis (Fig. 1.5). This phase is characterized by a pitch which is the distance over which the director makes one complete rotation in the helix and typically much larger than the molecular length and is of order of an optical wavelength. The pitch is generally temperature dependent.

1.4.3 The Smectic Phase

As a thermotropic liquid crystal is cooled down from its nematic phase, a one dimensional positional ordering characterized by the formation of planer layers

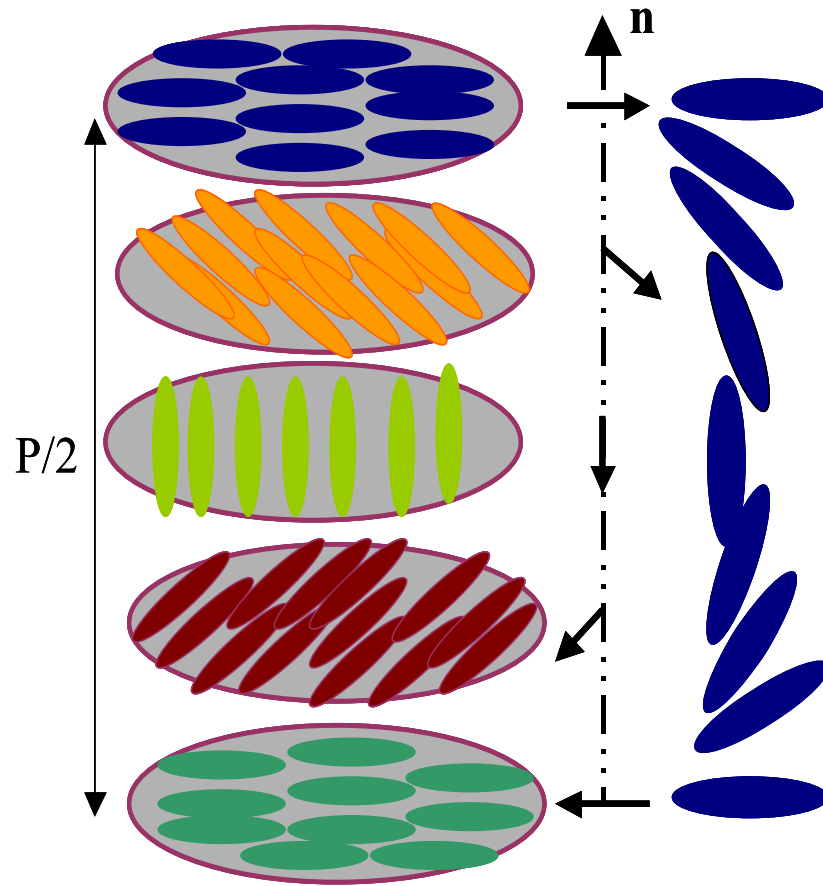


Figure 1.5. Schematic of chiral nematic liquid crystal phase [46].

together with the long-range nematic orientation order develops. The phase thus formed is called smectic phase whose name is derived from the Greek word $\sigma\mu\eta\gamma\mu\alpha$ for soap because of their similar properties. Smectic phases (Fig. 1.6) have a layered structure with the molecules oriented parallel or tilted to the layer normal. In smectic-*A* (Sm*A*), molecules are parallel to layer normal and in smectic-*C* (Sm*C*) phase the molecules are tilted with respect to layer normal. They are characterized by absence of positional order within the layers i.e. molecules have some freedom to move within the layer but they are not free to move between the layers. Smectics can be considered as stacks of two dimensional fluids but they behave as crystals across the layers.

The one dimensional positional ordering in Sm*A* or Sm*C* phases of LCs may be

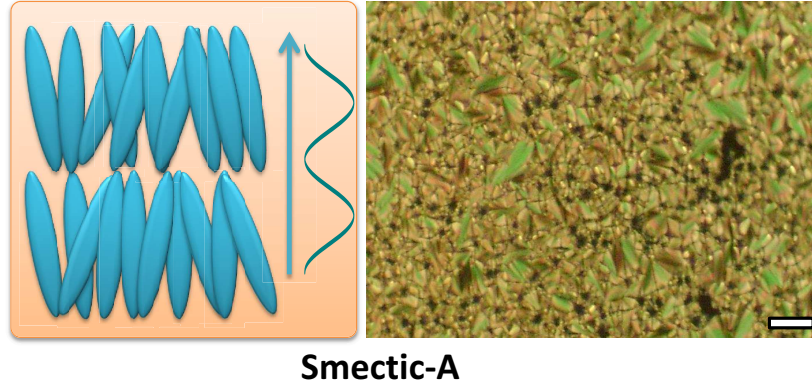


Figure 1.6. A cartoon of smectic-A (left) along with smectic-A texture observed under polarizing microscope (right). The scale bar is of 10 μm [46].

described in terms of a density wave of the center of mass of the molecules [35, 36].

$$\rho(z) = \rho_0 \left[1 + |\psi| \cos \left(\frac{2\pi}{d} z \right) \right] \quad (1.6)$$

where z is the coordinate parallel to the layer normal, ρ_0 is the average density, d is the layer spacing and $|\psi|$ is the amplitude of the density modulation and is a scalar smectic order parameter. When $|\psi| = 0$, the density is uniform and there is no layered structure. Typically the value of $|\psi|$ is much less than one and decreases with increasing temperature. The spatial correlation of molecular positions decay algebraically to zero at long distances in contrary to a 3D solid where it decays to a finite constant. The algebraic decay of the correlation implies that the thermal fluctuations destroy the smectic order over sufficiently large length scale (Landau-Peierls instability) [47, 48]. However, in practice smectic layering is rather easily stabilized by confinement of samples between solid substrate.

In the simplest smectic phase, SmA, the director \hat{n} is perpendicular to the smectic plane (Fig. 1.7). In each layer, the molecular centers of mass are arranged randomly and molecules have liquid-like freedom of translation and of rotation about their long axis [36, 49]. The SmA is optically uniaxial with the optical axis being normal to the layer plane.

In SmC phase (Fig. 1.8), the molecules are arranged in layers as in SmA phase but the director is tilted at an angle θ with respect to smectic layer normal. The SmC is optically biaxial.

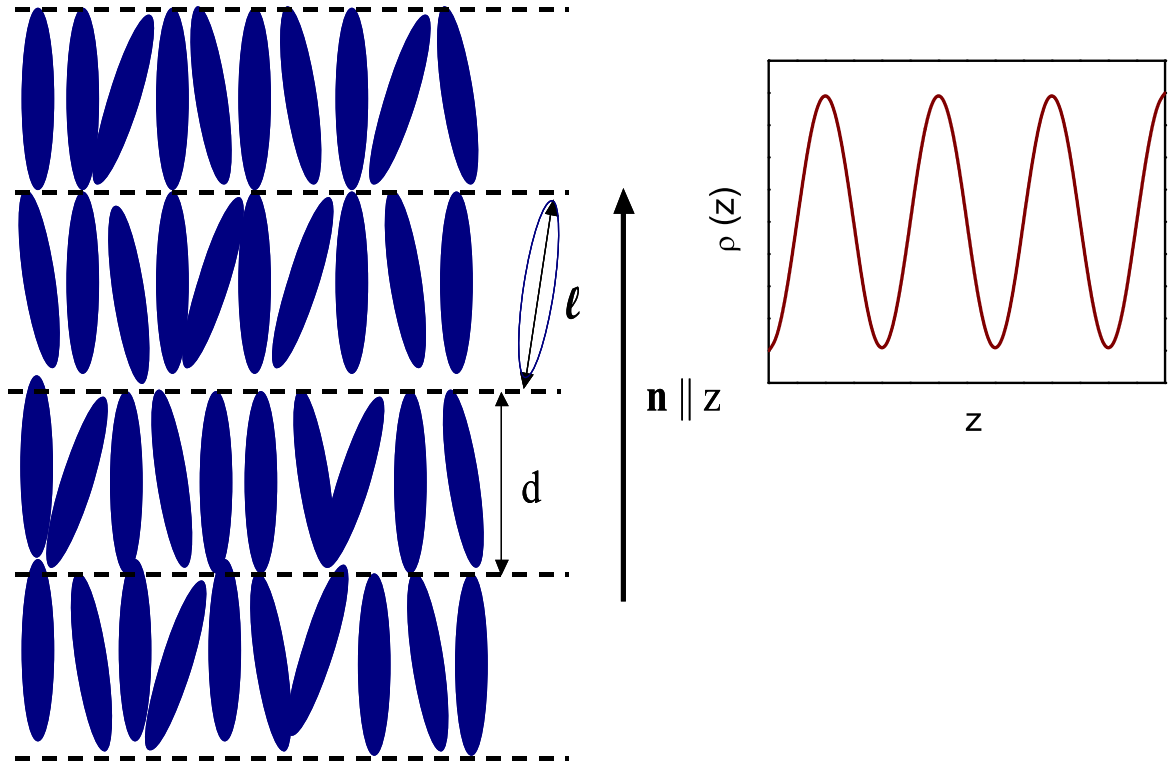


Figure 1.7. A cartoon of smectic- A phase demonstrating molecular arrangement, the director orientation, and density distribution along layer normal z . Variants of $\text{Sm}A$ possibly depend on the relation between l and d [46].

If the chirality is introduced in the $\text{Sm}C$ phase then a chiral smectic- C ($\text{Sm}C^*$) phase is formed. As in the chiral nematic phase, the director in $\text{Sm}C^*$ rotates from layer to layer in a helical fashion.

1.4.4 The Chiral Smectic Phases

Molecules which are not identical to their mirror image are said to be chiral. Molecular chirality has profound influence on the liquid crystal phases with chirality. The temperature dependence of their pitch has been exploited in making thermometers [50]. The schematic diagram of the $\text{Sm}C^*$ is shown in Figure 1.9.

The smectic phases formed by chiral molecules are designated with a $*$ over the letter specifying the analogous non-chiral phase. The chiral smectic- A is abbreviated as $\text{Sm}A^*$. Many of the physical properties of a chiral phase, e.g., the linear electro-optical effect [52] of the $\text{Sm}A^*$ phases, are not present in the $\text{Sm}A$ phase.

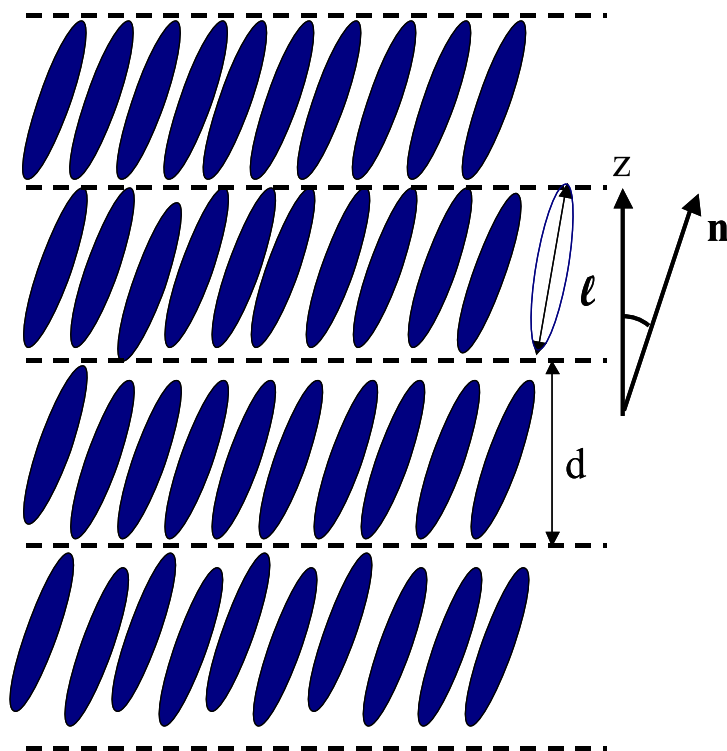


Figure 1.8. A cartoon of smectic- C phase [46].

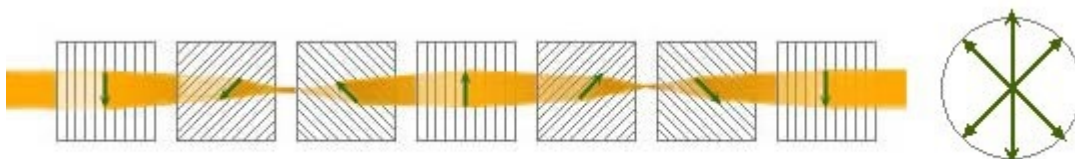


Figure 1.9. A cartoon of chiral smectic- C^* phase [51].

The tilted phase occurs for chiral molecules. The simplest is called the smectic- C , SmC^* , phase. This extra degree of freedom obtained from chirality causes a distortion on the SmC structures, and the direction of tilt precesses around the layer normal as one moves from layer to layer.

1.4.5 The Plastic Crystal Phase

There are several crystalline smectic phases; that is, smectics which are very close to three-dimensional crystals. They differ from true crystal phases in one important aspect. The molecules in them have freedom of rotation about their long axis, i.e.

their thermal motion is not completely frozen out. Such phases in which the position of the molecules is fixed but their motion is not arrested, should more correctly be classified as plastic crystalline phases. The reader who is interested in greater details in this area should read Pershan [53] and references there in. The common feature of these phases is that the average molecular orientation is normal to layers.

1.4.6 The Liquid Crystal Polymers

Liquid crystal polymers (LCPs) obtained by heating a polymer above its glass or melting transition and they are present in melting or liquid or solid form [54]. The chemical structure of these LCPs consist of linearly substituted aromatic rings linked amide groups. The most of LCPs produced in the 1980s, displayed order in the melt phase and processing of LCPs from liquid crystal phases or mesophases gives rise to fibers having good mechanical properties. LCPs have a high mechanical strength at high temperatures and extreme chemical resistance. They have more stress cracking in the presence of most chemicals at wide temperatures, including aromatic, strong acids, bases and ketone's. LCPs have many applications in electrical, mechanical parts and food containers [55].

1.5 Review of Thermodynamics

The materials presented in this dissertation involve the characterization of thermal parameters like heat capacity, latent heat, enthalpy, entropy, free energy etc. In this section a brief review of thermodynamic parameters and basic thermodynamic relations are presented. The word 'thermodynamics' comes from Greek origin meaning heat (therme) and energy or power (dynamics). Thermodynamics is that branch of physics which deals with the transformation of heat into mechanical work. Thermodynamics is used in many discipline such as physics, engineering, biochemistry etc. to understand physical processes and has innumerable applications. In thermodynamics, we consider macroscopic systems and never are interested in the atomic constitution of the matter.

1.5.1 Thermodynamic State Functions

1. Internal or Intrinsic energy: The internal energy [56] of a thermodynamic system is the energy possessed by the system by the virtue of its molecular constitution and the positions of the molecules and is defined by the equation,

$$dU = dQ - dW \quad (1.7)$$

where dW is the external work done and may be replaced by PdV and dQ may be replaced by TdS by second law of thermodynamics. Therefore,

$$dU = TdS - PdV \quad (1.8)$$

When a system passes from one state to another, the change in internal energy is independent of the route followed between the two states.

2. Helmholtz free energy: Helmholtz Free energy [56] is defined as

$$F = U - TS \quad (1.9)$$

A small change in the Helmholtz free energy is related to change in heat and work via first law of thermodynamics:

$$dF = dU - d(TS) = dQ - dW - SdT - TdS = dQ - TdS - SdT - dW \quad (1.10)$$

In reversible processes [56]:

$$dF = -SdT - dW \quad (1.11)$$

At constant temperature,

$$dF = -dW \quad (1.12)$$

The Helmholtz free energy measures the amount of work a system can do in an isothermal reversible process. If the process is not reversible, $dQ - TdS \neq 0$ and $dQ < TdS$. Therefore, $dF < -dW$. F is at constant, T is a minimum as a function of all parameters which are not fixed by external constraints.

3. Enthalpy: Enthalpy [56] is defined as

$$H = U + PV \quad (1.13)$$

Enthalpy measures the amount of work a system can do in an adiabatic, isobaric process. This is the amount of non-mechanical work, since the pressure has to be kept constant.

4. Gibb's free energy: Gibb's free energy [56] is defined as,

$$G = U - TS + PV \quad (1.14)$$

The Gibbs free energy measures the amount of work a system can do at constant temperature and pressure. The Gibbs potential measures the amount of non-mechanical work a system can do on the outside world at constant pressure and temperature.

1.5.2 Thermodynamic Response Functions

Thermodynamic response functions are derivatives of one thermodynamic parameter with respect to another under specific conditions on the remaining variables.

1. Heat Capacity: Heat capacity [56] is one of the most important response functions to measure. Measurement of heat capacity is the heart of our research in AC-calorimetry. It tells us how much heat the system will absorb, if we increase its temperature. These measurements can be done either at fixed pressure or volume. The specific heat at constant pressure is given by

$$C_p = \left(\frac{dH}{dT} \right)_p = T \left(\frac{\partial S}{\partial T} \right)_p = -T \left(\frac{\partial^2 G}{\partial T^2} \right) \quad (1.15)$$

In general, the heat capacities (C) is complex parameter and it contains both real and imaginary parts. However, for most materials the characteristic relaxation times of the energy fluctuations are too short to be sensed by traditional calorimetric techniques. Nevertheless, a complex heat capacity (C^*) may be defined containing a real (C') and imaginary (C'') component indicating the storage (capacitance) and loss (dispersion) of the energy in

the sample analogous to complex permittivity.

$$C^* = C' - iC'' \quad (1.16)$$

2. Thermal Expansivity: Another important response function is thermal expansivity [56] α (or coefficient of thermal expansion) which is defined as

$$\alpha = \frac{1}{V} \left(\frac{\partial V}{\partial T} \right)_p \quad (1.17)$$

It is the tendency of matter to change in volume in response to a change in temperature. When a substance is heated, the particles begin moving more and thus usually maintain a greater average separation. Materials which contract with increasing temperature are unusual. This effect is limited in size, and only occurs within limited temperature ranges. The degree of expansion divided by the change in temperature is called the material's coefficient of thermal expansion and generally varies with temperature.

3. Isothermal Compressibility: The isothermal compressibility [56] κ is defined as

$$\kappa = -\frac{1}{V} \left(\frac{\partial V}{\partial P} \right)_T \quad (1.18)$$

Isothermal compressibility is the fractional change in volume of a system as the pressure changes at constant temperature. The inverse of the isothermal compressibility is called the bulk modulus. All substances have compressibility. If a substance does not undergo, for example, chemical or structural changes in the process of compression, the original volume is restored when the external pressure returns to its initial value.

1.6 Phase Transitions

A sudden, dramatic change in a system's properties may occur by altering the thermodynamic variables such as temperature, pressure etc. We refer to this situation as a phase transition. Phase transitions present a challenge to statistical mechanics. By definition, at the transition point the system is expected to exhibit

singular behavior [56]. Line of discontinuous transitions terminates at a critical point, and the isotherms exhibit singular behavior in the vicinity of this point. The singular behaviors occur for specific values of intensive variables such as the temperature or the magnetic field.

1.6.1 Symmetry

Symmetry is inevitably accompanied by continuous (the modes which do not cost any energy to excite). A phase transition has driven by many parameters such as temperature, pressure, chemical composition, magnetic and electric field. If the driving parameter is temperature, the high-temperature phase is more disordered and has a higher symmetry than the low-temperature phase. When symmetry is broken, one needs to introduce one or more extra variables to describe the state of the system. For example, in the ferromagnetic phase, one must provide the net magnetization, whose direction was spontaneously chosen when the system cooled below the Curie point. Such variables are examples of order parameters. An order parameter is a measure of the degree of order in a system, it ranges between zero for total disorder and the saturation value for complete order [56]. For example, an order parameter can indicate the degree of order in a liquid crystal. However, note that order parameters can also be defined for non-symmetry-breaking transitions.

1.6.2 Order of a Phase Transition

Order of a phase transition is an important tool to classify the nature of the non-analytic behavior at the phase transition. Traditionally, phase transitions were characterized, by Paul Ehrenfest, on the basis of the nature of kink (discontinuity) in Gibbs free energy. If n^{th} derivative of G with respect to temperature T , keeping other intensive variables constant, is discontinuous then the transition was said to be n^{th} order [56]. Since $(\partial G/\partial T)_p = -S$, we see that the discontinuity in $(\partial G/\partial T)$ is the change in entropy between the two phases. Thus in a first order phase transition, the entropy changes discontinuously, while at second order and higher order transitions the entropy varies continuously. And since the latent heat is given by $T\Delta S$, it follows that latent heat involved with a first order phase transition, but not with higher orders. When two phases co-exist, then they will

each have the same Gibbs free energy G [56]. Nowadays Ehrenfest classification is no longer used. According to modern classification, there are two types of transitions one being a first-order and the other second-order or continuous phase transition. First-order phase transition involves latent heat and discontinuity in thermodynamical parameters. In second-order phase transition no discontinuity occurs; all the quantities vary continuously [56]. A first-order phase transition from phase a to phase b can be formulated as [56]

$$\begin{aligned}
 G_a - G_b &= 0 \\
 - \left[\frac{\partial G_b}{\partial T} \right]_P + \left[\frac{\partial G_a}{\partial T} \right]_P &= S_b - S_a = \Delta S = L/T \\
 \left[\frac{\partial G_b}{\partial P} \right]_T - \left[\frac{\partial G_a}{\partial P} \right]_T &= V_b - V_a = \Delta V
 \end{aligned} \tag{1.19}$$

where ΔS and ΔV are changes in entropy and volume respectively at the transition. For a first-order transition, changes in enthalpy ΔH or (ΔS) and in volume ΔV are observed.

For a second-order phase transition both ΔH and ΔV are zero but second derivative of the Gibbs function with respect to temperature and pressure leads to change in heat capacity, expansivity and compressibility [56].

$$\begin{aligned}
 G_a(T, P) &= G_b(T, P) \\
 - \left[\frac{\partial G_b}{\partial T} \right]_P + \left[\frac{\partial G_a}{\partial T} \right]_P &= S_b - S_a = \Delta S = 0 \\
 \left[\frac{\partial G_b}{\partial P} \right]_T - \left[\frac{\partial G_a}{\partial P} \right]_T &= V_b - V_a = \Delta V = 0 \\
 \left[\frac{\partial^2 G_b}{\partial T^2} \right]_P + \left[\frac{\partial^2 G_a}{\partial T^2} \right]_P &= \frac{1}{T} [C_{p_a} - C_{p_b}] = \frac{\Delta C_p}{T} \\
 \left[\frac{\partial^2 G_b}{\partial P^2} \right]_T - \left[\frac{\partial^2 G_a}{\partial P^2} \right]_T &= V [K_a - K_b] = V \Delta K \\
 \left[\frac{\partial^2 G_b}{\partial P \partial T} \right] - \left[\frac{\partial^2 G_a}{\partial T \partial P} \right] &= V [\alpha_a - \alpha_b] = V \Delta \alpha.
 \end{aligned} \tag{1.20}$$

1.6.3 Order Parameter

A phase transition occurs when a new state of symmetry develops from either ordered (low temperature) or disordered (high temperature) phase. The ordered phase has a lower symmetry due to the breaking of symmetry during the transition of disordered to ordered phase. The ordered state can be characterized by introducing a parameter that describes the character and strength of the broken symmetry which is called order parameter. The order parameter provides the extent to which the configuration of molecules in the less symmetric (more ordered) phase differs from that in the more symmetric (less ordered) phase. In general, an order parameter describing a phase transition must satisfy the following requirements:

1. $\phi = 0$, in the more symmetric (less ordered) phase, and
2. $\phi \neq 0$, in the less symmetric (more ordered) phase.

The choice of an order parameter depends upon the system involved but not in the unique way given by the above conditions. In the case of ferromagnetic transitions, the magnetization which is a vector with three components is an order parameter. In the case of liquid-vapor transition, the order parameter is the difference in density between liquid and vapor phases [56].

1.7 Theoretical Background

1.7.1 Landau-de Gennes Theory of Phase transition

The theory for the liquid crystal phases at and in the vicinity of their transitions has been developing in several directions. One of the most applied approaches is the Landau-de Gennes (LD) theory which is concerned with a phenomenological description of phase transition. The powers of the LD theory are in its simplicity and ability to capture the most important elements of phase transition [56]. It has been applied to many other phase transitions involve symmetry breaking [56]. Generally more symmetric (disordered) phase is a high-temperature phase and lower symmetric (ordered) phase is a low-temperature phase. This symmetry breaking can be represented by the order parameters. The original Landau theory is based

on the fact that the thermodynamic quantities of the lower symmetric phase and it can be obtained by expanding the thermodynamic potential in powers of the order parameters. It is spatial variation in the neighborhood of the order-disorder transition point and that sufficiently close to the transition, only the leading terms of the series are important. So the expansion becomes a single low-power polynomial. The thermodynamic behavior of the order parameters in the more ordered phase is then determined by minimizing the thermodynamic potential [56]. Let us consider a macroscopic system which equilibrium state is characterized by a spatially invariant, dimensionless, scalar order parameter ϕ . The general form of the Landau free energy is postulated to be [56]:

$$F(P, T, \phi) = F(P, T, 0) + r\phi + \frac{1}{2}A\phi^2 + \frac{1}{3}B\phi^3 + \frac{1}{4}C\phi^4 + \dots \quad (1.21)$$

where $F(p, T, 0)$ is free energy for a given pressure and temperature of the state with $\phi = 0$. The coefficients r , A , B , C are phenomenological constants and function of temperature and pressure. The equilibrium states can be obtained by minimizing F with respect to ϕ for fixed P and T . *i.e.*:

$$\frac{dF}{d\phi} = 0, \quad \frac{d^2F}{d\phi^2} > 0. \quad (1.22)$$

At the transition temperature these stability conditions are:

$$\frac{dF}{d\phi} = r = 0, \quad \frac{d^2F}{d\phi^2} = A = 0. \quad (1.23)$$

because of the coexistence of both regions. The condition, $r = 0$, is derived from the fact that high temperature phase with $\phi = 0$ must give rise to an extreme value of $F(P, T, \phi)$. The second condition, $A = a(T - T_c)$ with $a = (dA/dT)_{T_c} > 0$, follows from the behavior of F at $\phi = 0$, for T above and below the transition temperature T_c . The Landau theory postulates that the phase transition can be described by the expression:

$$F(P, T, \phi) = F(P, T, 0) + \frac{1}{2}a(T - T_c)\phi^2 - \frac{1}{3}B\phi^3 + \frac{1}{4}C\phi^4 + \dots \quad (1.24)$$

The Eq. (1.24) has the following solutions near the phase transition:

$$\phi = 0; \quad \phi = \frac{B \pm [B^2 - 4aC(T - T_c)]^{1/2}}{2C} \quad (1.25)$$

The coefficients B and C may be treated as temperature independent coefficients. The discontinuity of ϕ at the transition requires $B = 0$ for low temperature ϕ reads [56]

$$\phi = \frac{a[(T - T_c)]^{1/2}}{C}; \quad C > 0 \quad (1.26)$$

For a phase which remains invariant by replacing ϕ with $-\phi$, only even powers of ϕ survive. Thus in case of a second order phase transition:

$$F(P, T, \phi) = F(P, T, 0) + \frac{1}{2}A\phi^2 + \frac{1}{4}C\phi^4 + \dots \quad (1.27)$$

For spatially non-uniform system where the order parameter varies in space ($\phi = \phi(r)$), we need to add a term of the form $\gamma[\nabla\phi(r)]^2$ in the free energy expansion. The equation then reads,

$$F(P, T, \phi) = F(P, T, 0) + \frac{1}{2}A\phi^2 - \frac{1}{3}B\phi^3 + \frac{1}{4}C\phi^4 + \dots + \frac{1}{2}\gamma[\nabla\phi(r)]^2 \quad (1.28)$$

Even though the Landau theory is mainly for second order phase transitions, it can be extended to first order phase transitions. For first order transitions, $B = 0$, $C < 0$ and the third order term $B\phi^3$ must be present in the free energy expansion. The problem with this theory is that the coefficients appearing in the expansion are phenomenological and their dependence on the molecular properties are not defined. In addition, this theory does not contain any information about the molecular interactions. Despite these difficulties, Landau's theory has been successfully applied to a variety of phenomena.

1.7.2 Isotropic to Nematic (*I-N*) Phase Transition

The nematic state is described by the symmetric traceless tensor order parameter Q . For the description of isotropic to nematic (*I-N*) phase transition, the free energy density (energy per unit volume) f near the transition is expanded up to fourth or sixth order in Q [56] and all the terms must be invariant combinations

of the order parameter under all rotations [56]. For a uniaxial nematic, in general, the free energy density is given by [56],

$$f = f_0 + \frac{1}{2}A\left(\frac{2}{3}\text{Tr}(Q^2)\right) - \frac{1}{3}B\left(\frac{4}{3}\text{Tr}(Q^3)\right) + \frac{1}{4}C\left(\frac{4}{3}\text{Tr}(Q^4)\right) + \dots \quad (1.29)$$

$$+ D[\nabla Q]^2 + E(\hat{n} \cdot \nabla Q)^2 + f_{FE} + f_{SE} + f_{EM} + \mathcal{O}(Q^5)$$

where A, B, C, D, and E are phenomenological parameters. The terms f_{FE} , f_{SE} , and f_{EM} , add the contribution of free energy due to the elastic energy, surface elastic free energy, and electromagnetic interaction respectively. The terms containing a gradient, account for the spatial variation of the order parameter. The presence of cubic term, ensures the first order nature of the I - N phase transition. Since the I - N transition takes place near $A = 0$ it is assumed that the parameter A is only temperature dependent term and the others can be regarded as temperature independent. We can write:

$$A = a(T - T^*) \quad (1.30)$$

where a is a positive phenomenological constant and T^* is the limit of metastability of the isotropic phase. In the simplest model and in terms of scalar nematic order parameter S , the free energy density for the I - N phase transition can be written as [56]:

$$f = f_0 + \frac{1}{2}AS^2 - \frac{1}{3}BS^3 + \frac{1}{4}CS^4 + \dots \quad (1.31)$$

In the isotropic phase $S = 0$ and in the nematic phase $S \neq 0$. The constant $B > 0$ for uniaxial phase with positive anisotropy. The thermodynamic quantities, such as transition temperature T_{IN} , the value of order parameter, entropy and latent heat can be calculated by requiring that f be an extreme with respect to S in equilibrium and that the free energies of the ordered and disordered phases (nematic and isotropic) be equal at the transition. The later condition implies that the nematic and the isotropic phases can coexist at the transition temperature. If other variables such as pressure, density are included in our expression, the two phase would exist along a range of temperatures rather than at a single point. The equations determining thermodynamic parameters are [56]:

$$f = \left[\frac{1}{2}a(T_{IN} - T^*) - \frac{1}{3}BS + \frac{1}{4}CS^2\right]S^2 = 0 \quad (1.32)$$

$$\frac{\partial f}{\partial S} = [a(T_{IN} - T^*) - BS + CS^2]S = 0 \quad (1.33)$$

Solving these equations, we can get two possible solutions:

$$S_{IN} = 0; \quad T_{IN} = T^* \quad (1.34)$$

$$S_{IN} = \frac{2B}{3C}; \quad T_{IN} = T^* + \frac{2B^2}{9aC} \quad (1.35)$$

When $T^* < T < T_{IN}$, the minimum corresponds to a nematic phase. There exist local minima corresponding to a possible supercooled isotropic state. The transition entropy density at T_{IN} is given by [56]:

$$\Delta s = -\frac{\partial(f - f_0)}{\partial T}\bigg|_{T=T_{IN}} = -\frac{1}{2}aS^2 = -\frac{2aB^2}{9C^2} \quad (1.36)$$

The other contributions than are included in the model always ensure the positive value of the entropy. Since the I - N is a first-order transition, there is presence of latent heat (discontinuity of enthalpy) associated with the transition. The latent heat per unit volume is given by [56]:

$$\Delta H = T_{IN}\Delta s = \frac{2aB^2T_{IN}}{9C^2}. \quad (1.37)$$

The heat capacity C_p in the nematic phase diverges close to T_{IN} as [56]:

$$C_p \sim |t|^{-0.5} \quad (1.38)$$

where $t = (T^{**} - T)/T_{IN}$, and T^{**} is the superheating temperature of the nematic phase. In the isotropic phase, $C = C_0$ is constant and at T^{**} it shows a jump.

1.7.3 Nematic to Smectic-A (N - SmA) Phase Transition

The nematic to smectic- A (N - SmA) transition in an uniaxial nematic liquid crystal involves the rearrangement of the molecules in the layered structure. Molecular centers in SmA are, on average, arranged in equidistant plane. Within the planes, the molecules can move randomly perpendicular to the smectic layers. In the thermodynamic limit, there exist no true long-range translational order in SmA phase and the N - SmA phase transition theory is a theory of one dimensional melt-

ing. At N -SmA phase transition, the continuous translational symmetry of the nematic phase is spontaneously broken by the appearance of one dimensional density wave in the SmA phase. Mcmillan [57] and de Gennes [36] theories suggested that the N -SmA transition could be first-order or second-order changing the order at tricritical point (TCP). However HPL theory [58, 59] argued that the N -SmA transition can never be second order ruling out the possibility of TCP. Now, it is believed that the N -SmA phase transition is continuous in the absence of special circumstances [36].

The Landau-de Gennes theory for the N -SmA phase transition can be developed by the order parameter for the SmA phase. The order parameter is $|\psi|$ and is defined as the amplitude of a one dimensional density wave where wave vector q_0 is parallel to the nematic director (the z-axis), $\rho(\vec{r}) = Re[\rho_0 + \exp(i\vec{q}_0 \cdot \vec{r})\psi(\vec{r})]$, $q_0 = 2\pi/d$ is the wave vector corresponding to the layer spacing d . The complex field $\psi(\vec{r}) = \psi_0 \exp(i\vec{q}_0 \cdot \vec{r})$ has its spatial variation on the scale larger than d . Since the difference between $-|\psi|$ and $|\psi|$ only an amount to the choice of origin. The expansion of $|\psi|$ is only contains even-power terms. The free energy density near the N -SmA transition is given by [56]:

$$f_{SmA} = \frac{1}{2}\alpha|\psi|^2 + \frac{1}{4}\beta|\psi|^4 + \dots \quad (1.39)$$

where $\alpha = \alpha_0(T - T_0)$, α_0 , and β are constants. At temperature $T_{NA} = T_0$ and below T_0 , α vanishes and above this temperature it is positive. The coefficient β is always positive. On these consideration alone one could have second-order (continuous) N -SmA phase transition but there are number of complications that needs to be considered. First, the coupling between smectic order parameter ψ and scalar nematic order parameter S . To account for this coupling, a term of the form $f_1 = -C\psi^2\delta S$ should be added in the free energy density expression. Here, C is a positive constant and $\delta S = S - S_0$ is an increase in the nematic order that comes from the fact that the value of S does not coincide with S_0 obtained in the absence of smectic order. Second, the nematic free energy density which is minimum for $\delta S = 0$ must be added to the free energy expression (1.39). The

nematic free energy density is given by [56]:

$$f_N = f_N(s_0) + \frac{1}{2\chi}\delta S^2, \quad (1.40)$$

where $\chi(T)$ is a response function (susceptibility), which is large but finite near the I - N transition T_{IN} and small for $T < T_{IN}$, because of the nearly saturation of S_0 . The total free energy density is [56]:

$$f_S = f_N(s_0) + f_1 + f_{SmA} = f_N(s_0) + \frac{1}{2}\alpha|\psi|^2 + \frac{1}{4}\beta|\psi|^4 - C\psi^2\delta S + \frac{1}{2\chi}\delta S^2 + \dots \quad (1.41)$$

Minimizing f_S with respect to δS , we get $\delta S = C\psi^2\chi$. Therefore:

$$f_S = f_N(s_0) + \frac{1}{2}\alpha|\psi|^2 + \frac{1}{4}\beta'|\psi|^4 + \dots \quad (1.42)$$

with $\beta' = \beta - 2C^2\chi$. Depending on the values of C and χ and the resulting sign of β' three different cases can be obtained:

(i) If $T_0 \sim T_{IN}$, $\chi(T_0)$ is large and β' is negative. In this case the transition is of first-order and takes place at $T_{NA} > T_0$. One must add a positive sixth order term in the free energy to ensure the stability.

(ii) If $T_0 \ll T_{IN}$, $\chi(T_0)$ is large and β' is positive. In this case the transition is of second-order and takes place at $T_{NA} = T_0$.

(iii) When $\beta' = 0$, $\chi(T_{NA}) = 2\beta/C^2$ and one has a crossover from a continuous (second-order) to first-order transition and corresponds to a tricritical point (TCP).

We also need to consider the following effects:

(i) The director fluctuation in nematic phase [60, 61] which gives rise to a coupling term of the form $f_{\hat{n}} = -C_{\hat{n}}|\psi|^2$ and should be added to the free energy relation.

(ii) Layer fluctuation in the smectic phases.

(iii) The coupling between the nematic order parameter tensor Q_{ij} with the smectic order parameter (may be in the form of $f_2 \sim D\psi^2\delta Q$).

In summary, one should include all possible effect in free energy.

1.8 Liquid Crystal Nanocomposites

As a way of exploring the fundamental nature of the LC interactions responsible for mesogenic order, critical behavior, and the tuning of viscoelastic properties, attention has been drawn to the study of miscible mixtures of liquid crystals [62, 63, 64, 65, 66]. X-ray diffraction experiments performed on the smectic-*A* and smectic-*C* phases of thermotropic liquid crystals mixed with an organic solvent have shown that the smectic layer spacing increases with solvent content [66]. This research also demonstrated the formation of an organic lyotropic lamellar liquid crystal phase in which the solvent molecules largely intercalate between the smectic layers of the LC.

When CNTs and QDs are dispersed in a liquid crystal, they can modify the physical properties of the liquid crystal. In a well-dispersed CNT and QD in a LC host, there is surface anchoring of the LCs on the CNT surfaces, presumably through the $\pi - \pi$ stacking of the hexagonal structure of both the biphenyl and graphene, that is strengthened by a binding energy originating from charge transfer between the LCs and CNT [67]. In recent years, the dispersion of carbon nanotubes and QD in liquid crystal media has attracted intense interest. Research has been focused on dispersion and alignment of CNTs and QDs in liquid crystals [68, 69, 70, 71, 72, 73, 74], and studies of LC/CNT, LC/QD nanocomposite system for improving electro-optical switching properties [75, 76, 77, 78, 79]. Some research efforts have also been made to study the phase behavior and phase transitions of LC/CNT mixtures [80, 81, 82]. LC/CNT binary systems were investigated using optical microscopy and DSC, finding an enhancement of the isotropic to nematic (*I-N*) phase transition temperature revealing a “chimney” type phase diagram in LC/CNT mixtures over a narrow range of $\sim 0.1-0.2$ wt % of CNT [80]. An *I-N* phase transition was observed in a LC/CNT suspension due to the joule heating produced by a dc-electric field that rotates the CNTs out of sample plane short-circuiting the electrodes and producing a current flow through the CNT [82]. Recently, the research has been focused on understanding of the self assembly, structures of various shapes of nanoparticles and shape tuning in nematic liquid crystals [83, 84, 85]. All the observations showed that the *I-SmA* transition is more first-order than the very weak *I-N* transition indicating that the orientational order of SmA phase is higher than that in the nematic phase. The significant effort was

applied to the study of the I - SmA transition behavior, many problems related to fundamentals of the different phase transitions are yet to be solved.

1.9 Dissertation Outline

This dissertation presents the experimental results on the effect of nanoparticles on the liquid crystalline polymer and liquid crystal phase transitions using modulated differential scanning calorimetry, dielectric spectroscopy, and polarizing microscopy. It also provides transport properties of polymer nanocomposites. We mainly emphasize on the phase transition behavior of liquid crystals and transport properties of polymer nanocomposites.

Chapter 1 describes with introduction and overview of the nano materials and complex fluids. Chapter 2 deals with the brief review of experimental techniques, modulated differential scanning calorimetry (MDSC), polarizing microscopy (PS), and dielectric spectroscopy (DS). Chapter 3 presents the result of dynamics behavior of pure 9004 liquid crystal phase transitions with MDSC and DS. Chapter 4 provides the effect of carbon nanotubes on the phase transitions of 9004/CNT system. Chapter 5 presents the effect of QDs on the phase transitions in 8CB, 10CB system. Chapter 6 provides the effect of carbon nanotubes on the crystallization and melting behavior of iPP polymer. Chapter 7 provides the studies on the transport properties of polymer nanocomposites (iPP/CNT). Chapter 8 presents the conclusion of our work and the future directions.

Bibliography

- [1] C. Burda, X. Chen, R. Narayanan and M. El-Sayed, *Chem. Rev.*, **105**, 1025 (2005).
- [2] M. A. Kastner, *Physics Today*, **46**, 2431 (1993).
- [3] C. B. Murray, D. J. Morris, and M. G. Bawendi, *J. Am. Chem. Soc.*, **115**, 8706 (1993).
- [4] X. Peng, M. C. Schlamp, A. V. Kadavanich, and A. P. Alivisatos, *J. Am. Chem. Soc.*, **119**, 7019 (1997).
- [5] H. W. Kroto, J. R. Heath, S. C. OBrain, R. F. Curl, and R. E. Smalley, *Nature*, **318**, 162 (1985).
- [6] S. Ijima, *Nature*, **354**, 56 (1991).
- [7] T.W. Ebbesen and P.M. Ajayan, *Nature*, **358**, 220 (1992).
- [8] S. Ijima and T. Ichihashi, *Nature*, **363**, 603 (1993).
- [9] D. S. Bethune, C. H. Klang, M. S. de Vries, G. Gorman, R. Savoy, J. Vazquez, and R. Beyers, *Nature*, **363**, 605 (1993).
- [10] N. R Pradhan, *Thermal Conductivity of Nanowires, Nanotubes and Polymer-Nanotubes Composites*, Ph. D. Dissertation, WPI (2010).
- [11] J. Hone, I. Ellwood, M. Munro, Ari Mizel, Marvin L. Cohen, A. Zettl, Andrew G. Rinzler, and R. E. Smalley, *Phys. Rev. Lett.*, **80**, 1042 (1998).

- [12] J. Hone, M. Whitney, C. Piskoti, and A. Zettl, *Phys. Rev. B.*, **59**, R2514 (1999).
- [13] J. Hone, M. C. Llaguno, N. M. Nemes, A. T. Johnson, J. E. Fischer, D. A. Walters, M. J. Casavant, J. Schmidt, and R. E. Smalley, *Appl. Phys. Lett.*, **77**, 666 (2000).
- [14] S. Berber, Y. K. Kwon, and D. Tomanek, *Phys. Rev. Lett.*, **84**, 4613 (2000).
- [15] H. W. Zhu, L. Xu, D. Wu, B. Q. Wei, R. Vajtai, P. M. Ajayan, *Science*, **296**, 884 (2002).
- [16] Y. Li, I. A. Kinloch, A. H. Windle, *Science*, **304**, 276 (2004).
- [17] W. Zhou, J. Vavro, C. Guthy, K. I. Winey, J. E. Fisher, R. E. Smalley, *J. Appl. Phys.*, **95**, 649 (2004).
- [18] L. Zhu, J. Xu, Y. Xiu, W. H. Hess, C. P. Wong, *Carbon*, **44**, 253 (2006).
- [19] M. Zhang, K. R. Atkinson, R. H. Baughman, *Science*, **306**, 1358 (2004).
- [20] K. Iakoubovskii et al, *Appl. Phys. Lett.*, **89** (17), 173108 (2006)
- [21] N. Xiong and Gui-guang, *WUJNS*, **03A**, 1007 (2003).
- [22] A. Hirsch and O. Vostrowsky, *Funct. Mol. Nanostr.*, **245**, 193 (2005).
- [23] S. Banerjee, M. G.C. Kahn, and S. S. Wong, *Chemistry-A*, **52**, 1899 (2003).
- [24] K. Balasubramanian and M. Burghard, *Small*, **1**(2), 180 (2005).
- [25] C. Bechinger, D. Rudhardt, P. Leiderer, R. Roth, and S. Dietrich, *Phys. Rev. Lett.*, **83**, 3960 (1999).
- [26] J. W. Gilman, *Appl. Clay Sci.*, **15**, 31 (1999).
- [27] J. Zhu, A. B. Morgan, F. J. Lamelas, and C. A. Wilkie, *Chem. Mater.*, **13**, 3774 (2001).
- [28] M. Zanetti, G. Cammino, G. Thomann, and R. Mulhaupt, *Polymer*, **42**, 4501 (2001).

- [29] S. T. Lim, Y. H. Hyun, H. J. Choi, and M. S. Jhon, *Chem. Mater.*, **14**, 1839 (2002).
- [30] V. Mehrotra and E. P. Giannelis, *Sol Stat Comm.*, **77**, 155 (1991).
- [31] Q. H. Zeng, D. Z. Wang, A. B. Yu, and G. Q. Lu, Perth, *Australia Con.*, 9-12 July (2000).
- [32] Q. H. Zeng, D. Z. Wang, A. B. Yu, and G. Q. Lu, *Nanotechnology*, **13**, 549 (2002).
- [33] C. O. Oriakhi and M. M. Lerner, *Mater Res. Bull.*, **30**, 723 (1995).
- [34] V. Mehrotra and E. P. Giannelis, *Sol. State Ionics*, **51**, 115 (1992).
- [35] S. Chandrashekar, *Liquid Crystals*, England: Cambridge University Press (1992).
- [36] P. G. de Gennes and J. Prost, *The Physics of Liquid Crystals*, Clarendon, Oxford, England: Oxford University Press (1993).
- [37] P. Palffy-Muhoray, *Physisc Today*, **60**, 54 (2007).
- [38] H. Kelker, *Mol. Liq. Cryst.*, **21**, 1 (1973).
- [39] P. J. Collings, *Liquid Crystals: Natures Delicate Phase of Matter*, USA: Princeton University Press, 2nd edition (2002).
- [40] T. J. Sluckin, D. Dunmer, and H. Stegemeyer, *Crystal That Flow*, Taylor & Francis (2004).
- [41] O. Lehmann, *Z. Physika. J. Am. Chem. Soc.*, **4**, 462 (1889).
- [42] B. Bahadur, eds. *Liquid Crystals-Applications and Uses*, Singapore: 1-3 World Scientific (1990).
- [43] D. Demus, J. Goodby, G. Gray, H. Spiess, and V. V. eds., *Hand Book of Liquid Crystals*, Canada: 1 Wiley-VCH, Weinheim (1998).
- [44] T. E. Wellems, K. Hayton, R. M. Fairhurst, *J. Clin. Invest.*, **119**, 2496 (2009).

- [45] G. Friedel, *Ann. de Phys.*, **18**, 273 (1922).
- [46] K. Sigdel, *Phase Transition Studies of Liquid Crystal Colloids with Solvents and Nano-solids*, Ph. D. Dissertation, WPI (2011).
- [47] C. Bahr, *Int. J. Mod Phys : Condensed Matter Physics, Statistical Mechanics, Applied Physics*, **8**, 3051 (1994).
- [48] W. de Jue, B. I. Ostrovskii, and A. Shakginov, *Rev. Mod. Phys.*, **75**, 181 (2003).
- [49] S. Singh, *Physics Reports*, **324**, 107 (2000).
- [50] I. Dierking, *Textures of Liquid Crystals*, Weinheim: Wiley-VCH (2003).
- [51] Rosenblatt, *liq-xtal.case.edu*, Case Western Reserve University (2010).
- [52] *Internation Tables for X-ray Crystallography, 2nd Edn.*, Kluwer Academic Publisher, Netherlands (1999).
- [53] P. S. Pershan, *Structure of Liquid Crystal Phases*, World Scientific, New Jersey (1988).
- [54] Callister, *Materials Science and Engineering - An Introduction*, 557 (2007).
- [55] FCI, *Metral Signal Header 1 Mod, 4 Row Press-Fit*, **1**, (2000).
- [56] H. B. Callen, *Thermodynamics*, New York: J. Wiley and Sons, 376 (1960).
- [57] W. L. McMillan, *Phys. Rev. A*, **4**, 1238 (1971).
- [58] B. Halperin, T. C. Lubensky, and S. K. Ma, *Phys. Rev. Lett.*, **32**, 292 (1974).
- [59] M. A. Anisimov, P. E. Cladis, E. E. Gorodetskii, D. A. Huse, V. E. Podneks, V. G. Taratuta, W. van Saarloos, and V. P. Voronov, *Phys. Rev. A*, **41**, 674 (1990).
- [60] B. R. Patton and B. S. Andereck, *Phys. Rev. Lett.*, **69**, 1556 (1992).
- [61] B. S. Andereck and B. R. Patton, *Phys. Rev. E*, **49**, 1393 (1994).

- [62] K. Denolf, G. Cordoyiannis, C. Glorix, and J. Thoen, *Phys. Rev. E*, **76**, 051702 (2007).
- [63] K. Denolf, B. V. Roie, C. Glorix, and J. Thoen, *Phys. Rev. Lett.*, **97**, 107801 (2006).
- [64] P. K. Mukherjee, *J. Chem. Phys.*, **116**, 9531 (2002).
- [65] S. DasGupta and S. K. Roy, *Phys. Lett. A*, **288**, 323 (2001).
- [66] T. P. Rieker, *Liq. Cryst.*, **19**, 497 (1995).
- [67] K. A. Park, S. M. Lee, S. H. Lee, and Y. H. Lee, *J. Phys. Chem. C*, **111**, 1620 (2007).
- [68] M. D. Lynch and D. L. Patrick, *Nano Letters*, **2**, 1197 (2002).
- [69] I. Dierking, G. Scalia, P. Morales, and D. LeClere, *Adv. Mater.*, **16**, 865 (2004).
- [70] I. Dierking, G. Scalia, and P. Morales, *J. Appl. Phys.*, **97**, 044309 (2005).
- [71] J. P. F. Lagerwall, G. Scalia, M. Haluska, U. Dettlaff-Weglikowska, F. Gieselmann, and S. Roth, *Phys. Stat. Sol.*, **243**, 3046 (2006).
- [72] S. Kumar and H. K. Bisoyi, *Angew. Chem.*, **119**, 1523 (2007).
- [73] V. Popa-Nita and S. Kralj, *J. Mem. Phys.*, **132**, 024902 (2010).
- [74] G. Scalia, *Chem. Phys. Chem.*, **11**, 333 (2010).
- [75] P. V. Kamat, K. G. Thomas, S. Barazzouk, G. Girishkumar, K. Vinodgopal, and D. Meisel, *J. Am. Chem. Soc.*, **126**, 10757 (2004).
- [76] H. Y. Chen and W. Lee, *Opt. Rev.*, **12**, 223 (2005).
- [77] I. S. Baik, S. Y. Jeon, S. H. Lee, K. A. Park, S. H. Jeong, K. H. An, and Y. H. Lee, *Appl. Phys. Lett.*, **87**, 263110 (2005).
- [78] H. Y. Chen, W. Lee, and N. A. Clark, *Appl. Phys. Lett.*, **90**, 033510 (2007).
- [79] M. Rahman and W. Lee, *J. Phys. D: Appl. Phys.*, **42**, 063001 (2009).

- [80] H. Duran, B. Gazdecki, A. Yamashita, and T. Kyu, *Liq. Cryst.*, **30**, 815 (2005).
- [81] J. P. F. Lagerwall, R. Dabrowski, and G. Scalia, *J. Non-Cryst. Sol.*, **353**, 4411 (2007).
- [82] H. J. Shah, A. K. Fontecchio, D. Mattia, and Y. Gogotsi, *J. Appl. Phys.*, **103**, 064314 (2008).
- [83] B. Senyuk, J. S. Evans, P. J. Ackerman, T. Lee, P. Manna, L. Vigderman, E. R. Zubarev, J. van de Lagemaat, and I. I. Smalyukh, *Nano Lett.*, **12**, 955 (2012).
- [84] J. Dontabhaktuni, M. Ravnik, and S. Zumer, *Soft Matt.*, **8**, 657 (2012).
- [85] J. Jeong and M. W. Kim, *Phys. Rev. Lett.*, **108**, 207802 (2012).

Experimental Techniques

2.1 Modulated Differential Scanning Calorimetry (MDSC)

Modulated (temperature) differential scanning calorimetry (MTDSC/MDSC) allows for the simultaneous measurement of both the heat flow and heat capacity. In DSC, the sample and the reference samples are maintained at the same temperature by supplying different quantities of the heat to them. In AC-calorimetry, the basic principle is that a periodic heat input is supplied to the sample. MDSC is essentially the combination of traditional AC-calorimetry with DSC shown in the Fig. 2.1. This method allows for measuring the total heat flow (enthalpy) as well as its non-reversible (kinetic or imaginary component) and the reversible (real component) heat capacities. A detailed description of the MDSC method can be found elsewhere [1, 2, 3, 4, 5, 6, 7].

MDSC experiments were performed using a Model Q200 from TA Instruments, USA. Prior to all measurements, temperature calibration was done with a sapphire disc, under the same experimental conditions used for all samples. The analysis method used to extract the complex specific heat is based on linear response theory [1, 8]. In general, a temperature oscillation is described as $T(t) = T_0 + \dot{T}_0 t + A_T \sin(\omega t)$ where T_0 is the initial temperature at time $t = 0$, T is the absolute temperature at time t , \dot{T}_0 is the baseline temperature scan rate, A_T is the temperature amplitude, and ω ($\omega = 2\pi f$) is the angular frequency of the tem-



Figure 2.1. Modulated Differential Scanning Calorimetry model Q200 from TA Instruments, USA [9].

perature modulation. The temperature rate is also time dependent and is given by $\dot{T}(t) = dT/dt = \dot{T}_0 + A_q \cos(\omega t)$ where A_q is the amplitude of the temperature modulation rate ($A_q = \omega A_T$). Since the applied temperature rate consists of two components, \dot{T}_0 the underlying rate and $A_q \cos(\omega t)$ the periodic rate, the measured heat flow (HF) can also be separated into two components in response to these rates. The periodic component can be described by $HF_q = A_{HF} \cos(\omega t - \varphi)$, where A_{HF} is the amplitude of the heat flow and φ is the phase angle between heat flow and temperature rate. The absolute value of the complex specific heat is written as $C_p^* = A_{HF}/mA_q$ where m is the mass of the sample. The phase angle φ requires a small correction (calibration) to account for finite thermal conductivities of the sample and cell [7]. The real (reversible) C_p' and imaginary (non-reversible) C_p'' parts of the specific heat are then given by [1]:

$$C_p' = C_p^* \cos(\varphi) \quad (2.1)$$

$$C_p'' = C_p^* \sin(\varphi) \quad (2.2)$$

which allows for a consistent definition of the complex specific heat. Typically, under equilibrium conditions, $C_p'' = 0$ after φ correction (or have a weak linear temperature dependence remaining). The appearance of a peak-like non-zero C_p'' feature commensurate with a peak in the real part of the specific heat indicates that this feature is a first-order transition and involves a latent heat, the total heat

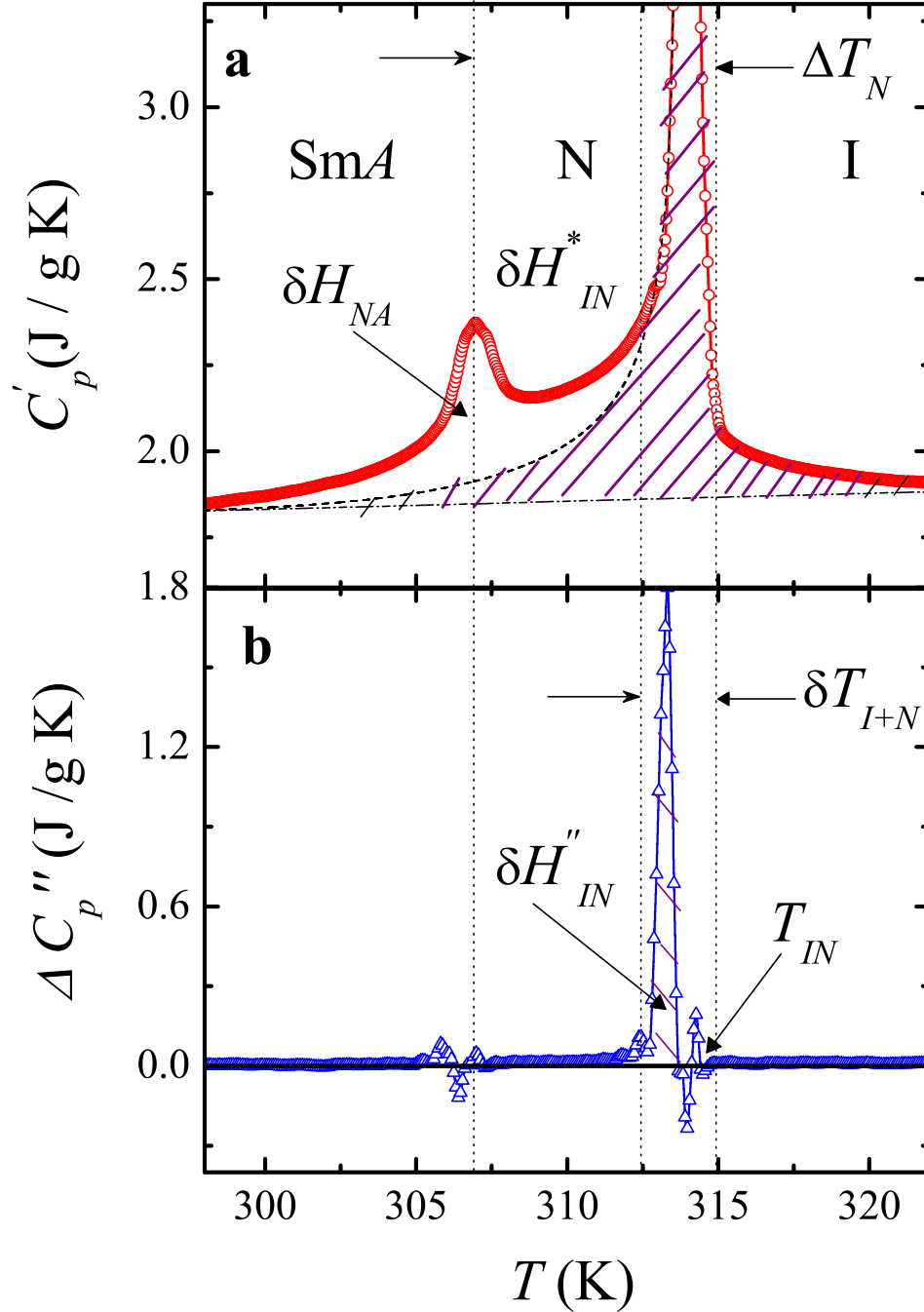


Figure 2.2. The specific heat on heating as a function of temperature for 8CB with illustrating the overall background (dashed-dot) and low-temperature wing under the N -SmA peak (dashed) behavior used to determine ΔC_p and δH_{IN}^* (top). Dispersive part of heat capacity on heating with illustrating $\delta H''_{IN}$ and the I - N transition temperature T_{IN} .

capacity is given by $C_p = \sqrt{C_p'^2 + C_p''^2}$.

The excess specific heats were determined in order to isolate the contribution from the various transitions. A linear baseline was used over the entire temperature scan range in order to determine $\Delta C_p = C_p - C_{baseline}$ for both the real and imaginary components, though C_p'' always exhibited a very shallow linear baseline that was very close to zero, indicating near-equilibrium conditions for the experimental parameters used in this work. For specific heat features that are close in temperature, the wing of one peak (usually the higher temperature peak) is subtracted from the lower specific heat peak in order to isolate the excess specific heat of the lower temperature transition, denoted as $\delta C_p = \Delta C_p - C_{wing}$, where C_{wing} is a mimic function (polynomial) of the underlying wing. This calculation was only applied to the real component of the specific heat.

The particular transition enthalpy component is simply the integration of the excess specific heat component over a consistent temperature range, e.g $\Delta H' = \int \Delta C_p' dT$ for the real and $\Delta H'' = \int \Delta C_p'' dT$ for the imaginary enthalpy. The total magnitude of the transition enthalpy is defined as $\Delta H = \sqrt{(\Delta H')^2 + (\Delta H'')^2}$. Finally, for first-order transitions, the transition temperature is determined as the highest temperature of the two-phase coexistence region indicated by the onset of non-zero values of $\Delta C_p''$. For continuous transitions, the transition temperature is taken as the $\Delta C_p'$ peak temperature. The nematic range is defined as $\Delta T_N = T_{IN} - T_{NA}$ and the ΔT_{I+N} , is determined taking the difference of high-temperature and low-temperature limits of C_p'' peak (Fig. 2.2).

2.2 Dielectric Spectroscopy (DS)

Materials which are electrical insulators but can be polarized and can store electrical energy are called dielectrics. An electric field causes the charges of a dielectric material to displace slightly from their equilibrium positions. The polarization after the application of an electric field takes a finite time to reach its maximum value. The phenomenon is generally described by a general term "dielectric relaxation". The term 'dielectric' is connected to the materials with a high polarizability and is expressed by a number and called a dielectric constant. It can be shown that under an alternating electric field the real and imaginary components of the dielectric

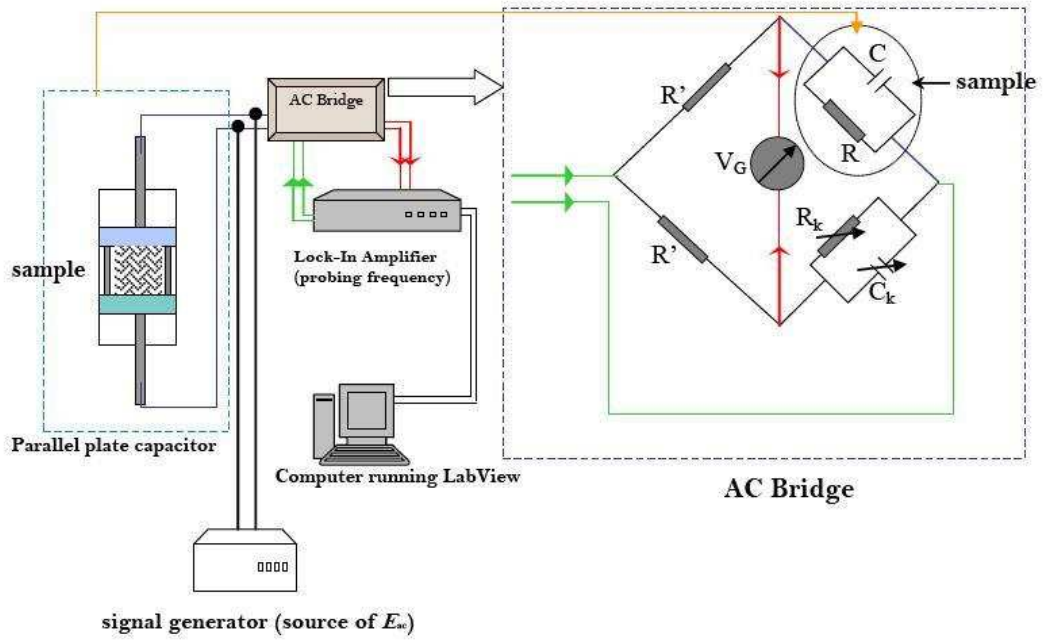


Figure 2.3. Design of the dielectric spectrometer [10].

constant are given by [11]:

$$\varepsilon' = \varepsilon_{\infty} + \frac{\Delta\varepsilon}{1 + (\omega\tau)^2} \quad (2.3)$$

and

$$\varepsilon'' = \frac{\Delta\varepsilon}{1 + (\omega\tau)^2}(\omega\tau) \quad (2.4)$$

where ω is sweeping frequency, τ is the relaxation time, and $\Delta\varepsilon = \varepsilon_0 - \varepsilon_{\infty}$ is the dielectric relaxation strength for a single relaxation process. Here, ε_0 , and ε_{∞} are dielectric constants at infinite frequency (dynamic dielectric constant) and zero frequency (static dielectric constant) respectively. The complex dielectric constant of a material can be expressed as [11]:

$$\varepsilon^*(\omega) = \varepsilon'(\omega) - i\varepsilon''(\omega) \quad (2.5)$$

The real part represents the storage of the electric field energy and the imaginary part corresponds to the dispersion (dissipation) of energy through a relaxation process.

The dielectric constant ϵ^* can be measured by performing the capacitance measurement as the dielectric constant of a sample is the ratio of sample filled capacitance and empty cell capacitance. Our experimental set-up is based on the ac-capacitance bridge technique [11, 12, 13]. The experiment is started by balancing the ac-bridge at some frequency. A frequency (or voltage or temperature) scan is then performed. The off-balance in-phase and out-of-phase signals are acquired by digital lock-in amplifier [14]. The off-balance signal is converted to the equivalent change in capacitance by a simple multiplicative conversion factor and converted into the dielectric constant dividing it by the empty cell capacitance. The absolute real and imaginary parts of the complex dielectric constant are determined by adding or subtracting (depending on whether the frequency is increasing or decreasing from the reference frequency) the off-balance signal to that directly measured at the reference frequency. The spectrometer set-up is as shown in Fig. 2.3 [10].

2.3 Polarizing Microscopy (PM)

The polarizing microscopy was originally developed for investigating structures of rocks and minerals. But this technique has become a popular tool for different field of science such as biology, medicine, polymer chemistry, physics, etc.

The polarized light microscope is used to study the materials that are visible due to their optical anisotropic property. These materials have two different refractive indices for different colors of light which is called birefringence. The microscope must be equipped with a polarizer and an analyzer. The polarizer is positioned in the light pathway before the sample to be studied and the analyzer is placed in the pathway between the objective of the microscope and the sample. Liquid crystal textures were observed under the crossed-polarizers condition where the polarizer and analyzer are perpendicular to each other. In the absence of a sample, a dark field of view is observed because of the action of crossed polarizer analyzer arrangement. When a sample, such as liquid crystal is inserted in between the crossed-polarizers, textures or patterns are observed due to the interaction of light with the sample. The simple experimental arrangement is shown Fig. 2.4 [15]. Because liquid crystals exhibit optical anisotropy (birefringence), polarizing

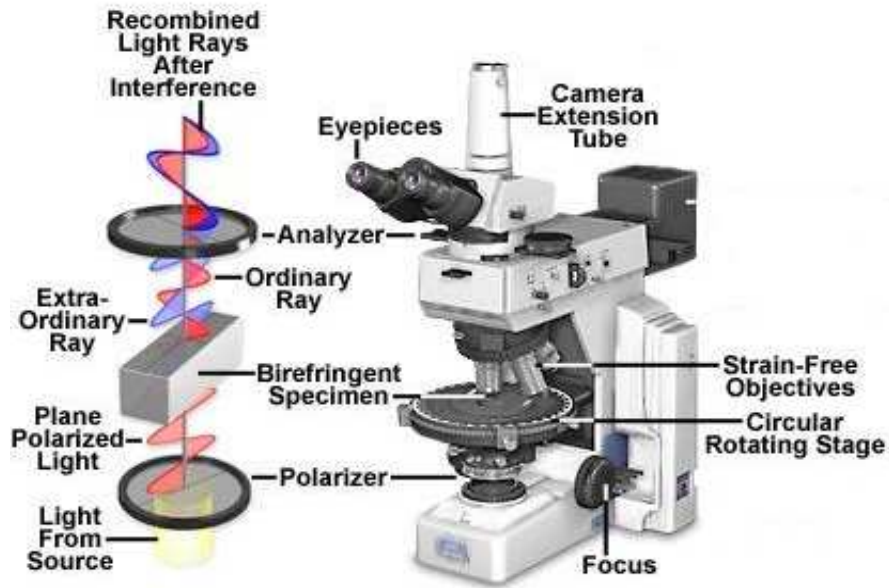


Figure 2.4. Design of the Polarizing Microscope [15].

microscopes are popular to study them. Optical patterns within a liquid crystal sample can be observed by using a polarizing microscope. The phases and defects can be investigated by observing these optical patterns.

Textures for different liquid crystals of nanomaterial composites were observed as a function of temperature. The temperature control of the system was achieved using a hot stage.

2.4 Conductivity Experiments (CE)

The samples cell were sandwiched between two metal plates. Two electrical leads were connected to both metal plates. The electrical conductivity was measured using a Pico-ammeter with varying voltage across the samples, which is the direction perpendicular to the rotation of the glass plates in the Linkham CSS 450 shearing stage. The electrical conductivity of the sheared sample gives the perpendicular component and of an un-shear samples give average of conductivity. Voltages from 0 to 100 V were applied across the samples for electrical conductivity and the current was recorded with Pico-ammeter. All measurements were done

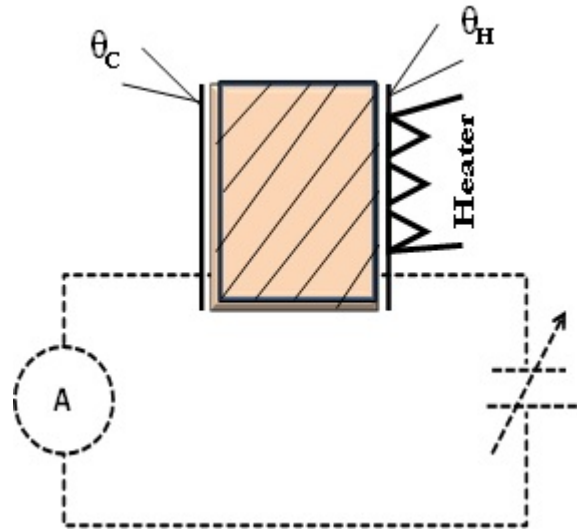


Figure 2.5. Design of the conductivity experiment.

from temperature of 0 to 50 °C. The experimental set up shown in Fig. 2.5 lead in this equation $V = IR$, where V = power supply, I =Current and R = electrical resistance. The resistance of samples were recorded and measured electrical conductivity of iPP/CNT samples. Thermal resistance is given by $R = d/\sigma A$, where σ is electrical conductivity, d is thickness and A is the cross-sectional area of the sample ($A = wL$, where w is the width and L is the length of the sample).

The same set up was used to measure the thermal conductivity measurements. The two thermo couple wires were connected to either side of sandwich cell with heater attached one side to apply power supply. The thermal conductivity was measured using varying power and recorded temperature difference for both sides of plates, $\Delta T = RP$, where $\Delta T = T_h - T_c$, R = thermal resistance, and P = power. Voltages from 0 to 6 V were applied to heater to record ΔT . All measurements were done from temperature of -50 to 50 °C. The thermal resistance of samples were recorded and measured thermal conductivity of iPP/CNT samples, $R = d/\kappa A$, where κ is thermal conductivity, d is thickness and A is the cross-sectional area of the sample, ($A = wL$, where w is the width and L is the length of the sample). The the power dissipated through the wires and only 4% of power was going through the samples. The set of Mylar, Kapton and iPP samples were used to calibrate power in thermal conductivity measurements and corrected entire data.

The both conductivities were measured for sheared and un-sheared (average)

samples for a wide temperature range -50 to 50 °C.

2.5 Spectroscopic Ellipsometry (SE)

Ellipsometry is used in the past for an optical technique for the investigation of the dielectric properties (complex refractive index or dielectric function) of thin films. Recently, the techniques are applied to characterize roughness, thickness (depth), crystallinity, doping concentration, and other material properties associated with a change in the optical response of an incident radiation that is made to interact with the material being investigated.

Typically, reflective ellipsometry measures changes in the polarization state of light reflected at an oblique angle to a surface and the Maxwells equations describe these interactions [16, 17, 18, 19, 20]. The polarization change is quantified by the amplitude ratio, ψ , and the phase difference, Δ . The signal depends on the thickness as well as the materials properties and hence ellipsometry is a universal tool for contact free determination of thickness and optical constants of films of all kinds. Polarization state changes are expressed as a ratio of the complex reflection coefficients, R_p (electric field parallel to plane of incidence) and R_s (electric field perpendicular to plane of incidence). Both R_p and R_s depend on material optical properties expressed by [17, 18]:

$$\rho = \frac{R_p}{R_s} = \tan(\psi)\exp^{i\Delta} \quad (2.6)$$

Ellipsometry parameters are typically expressed as $\psi(\lambda)$ and $\Delta(\lambda)$, where λ is wavelength. Data thus obtained are compared to an optical model describing the system. The model includes a set of parameters which values are determined by non-linear regression optimization. The goodness of fit is expressed by mean-square-error (MSE), defined as:

$$MSE = \sqrt{\frac{1}{2N - M} \sum_{i=1}^N \left[\left(\frac{\psi_i^{Mod} - \psi_i^{Exp}}{\sigma_{\psi,i}^{Exp}} \right)^2 + \left(\frac{\Delta_i^{Mod} - \Delta_i^{Exp}}{\sigma_{\Delta,i}^{Exp}} \right)^2 \right]} \quad (2.7)$$

Here, MSE is experimental standard deviations, N is the number of data points and M is the number of fit parameters. The MSE is minimized with respect to

parameter values. Dielectric functions represent material response to electromagnetic radiation over a range of frequencies, and are related to refractive index (n) and extinction coefficient (k) by [21]:

$$\varepsilon_1 = n^2 - k^2 \quad (2.8)$$

$$\varepsilon_2 = nk \quad (2.9)$$

Extinction coefficient k , is related to absorption coefficient α , by [21]

$$\alpha = \frac{4\pi k}{\lambda} \quad (2.10)$$

It is thus possible to determine dielectric functions from optical constants and vice versa and the ellipsometry set-up [22] shown in Figure 2.6.

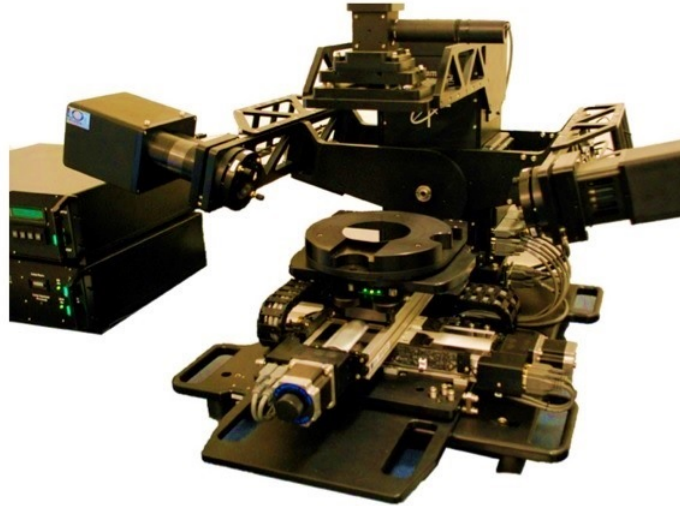


Figure 2.6. Spectroscopic Ellipsometry model M-2000 from J. A. Wollam Co., Inc., USA, [23].

2.6 Materials

2.6.1 Characteristics of 9004

The liquid crystal 9004 is a phenyl benzoate containing an oxoester linking group with two alkoxy end groups (Figure 2.7). The molecular mass for 9004 is $M =$

424.657 g/mol with an extended molecular structure approximately 4 nm long and 0.8 nm wide. The 9OO4 was kindly provided by Prof. Charles Rosenblatt and used after degassing for 2 hours at 320 K temperature. This LC has a structure and molecular weight similar to the relatively well-studied liquid crystals pentylphenylthiol alkoxybenzoate ($\bar{8}S5$) and butoxybenzylidene octylaniline (4O.8). For $\bar{8}S5$, the phase sequence (in degrees Celsius) is K - 57.9 - SmC - 56.1 - SmA - 63.6 - N - 86.2 - I while 4O.8 has the phase sequence of K - 38.4 - CrB - 49.2 - SmA - 63.8 - N - 79 - I where CrB is a plastic crystal B phase and the SmC phase for $\bar{8}S5$ is monotropic to the crystal phase (K). These types of liquid crystal molecules have a negative dielectric anisotropy, the dielectric constant perpendicular to the long molecular axis ε_{\perp} is larger than the parallel component ε_{\parallel} . From molecular modeling [24], this anisotropy emerges from the linking group of the two phenyl rings and the presence of alkyl (or alkoxy) end groups. However, molecular modeling suggests that the effective dipole moment for $\bar{8}S5$ and 4O.8, though perpendicular to molecular long axis, lies nearly in the plane of the phenyl rings. For 9OO4, modeling suggests that due to the carbon - oxygen double bond in the oxoester linking group, its effective dipole moment is pointing nearly perpendicular to the plane of the phenyl rings. Note that the estimated dipole moment magnitude is smallest for $\bar{8}S5$ while approximately the same for 4O.8 and 9OO4.

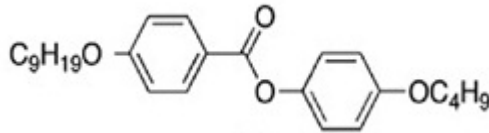


Figure 2.7. Molecular structure of the 9OO4 molecule using a ChemBioDraw software.

2.6.2 Characteristics of 5CB

5CB is the abbreviated name of the LC pentylcyanobiphenyl or 4-cyano-4'-pentylbiphenyl. 5CB has a typical rod-like molecule, with a rigid biphenyl core, to which are attached an aliphatic tail and a polar cyano head group. Its molecular weight is $M = 249.36$ g/mol and density is 1.008 g/mL at 25 °C. The transition enthalpy of *I-N* transition is 3.5 J/g [10]. Liquid crystal 5CB was purchased from Frinton laboratory [26] and used after degassing them in their isotropic phase for about

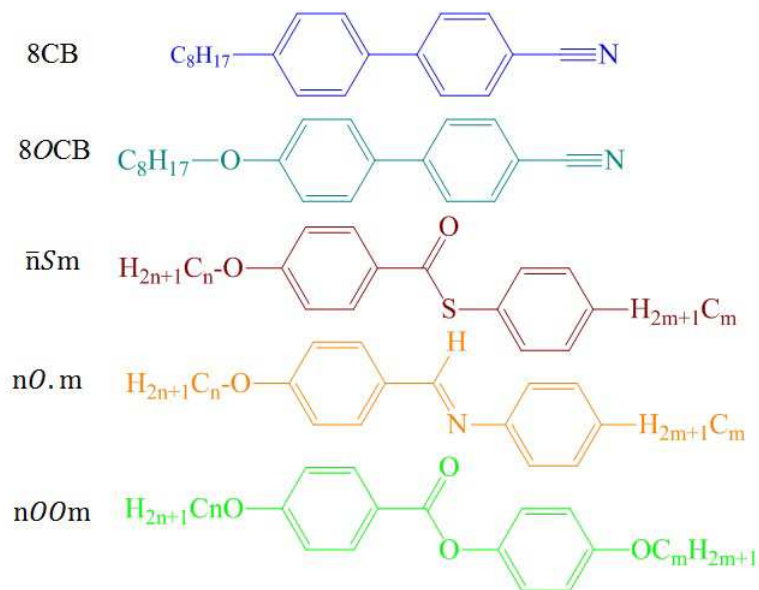


Figure 2.8. Structural formulas for liquid crystal referred to in this work.

2 hours. It was used without further purification. The molecular structures are shown in Fig. 2.9 and 2.10.

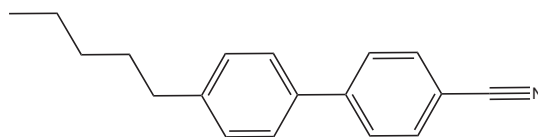


Figure 2.9. Molecular structure of the 5CB molecule using a ChemBioDraw software.

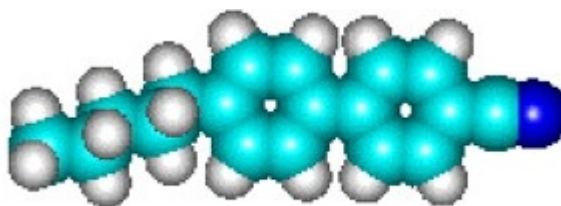
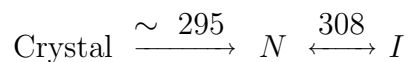


Figure 2.10. 3D structure of the 5CB molecule [10] using a Molviz.Org.

Pure 5CB undergoes a weakly first-order isotropic to nematic phase transition, at $T_{IN}^o = 308$ K. The phase sequence (in Kelvin) for 5CB is



2.6.3 Characteristics of 8CB

8CB is the abbreviated name of the *LC* octylcyanobiphenyl or 4-cyano-4'-octylbiphenyl. It is one of the most well known and probably the most studied *LC*s. 8CB has a typical rod-like molecule, with a rigid biphenyl core, to which are attached an aliphatic tail and a polar cyano head group. Its molecular weight is $M = 291.44$ g/mol and density is 1.03 g/mL at 25 °C. The transition enthalpy of the *I-N* transition is 5.58 J/g and *N-SmA* transition enthalpy is 0.8 J/g [25]. Liquid crystal 8CB was purchased from Frinton laboratoty [26] and used after degassing them in their isotropic phase for about 2 hours. It was used without further purification. The molecular structures are shown in Fig. 2.11 and 2.12.

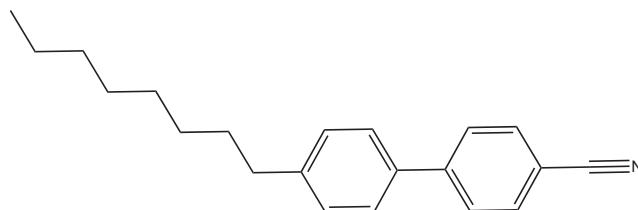


Figure 2.11. Molecular structure of the 8CB molecule using a ChemBioDraw software.

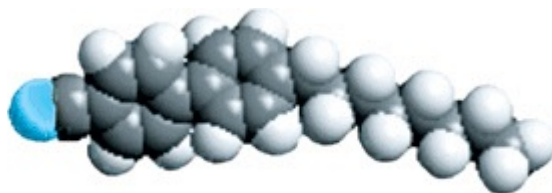
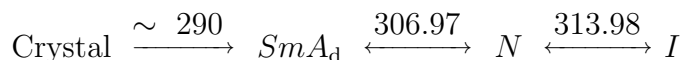


Figure 2.12. 3D structure of the 8CB molecule [10] using a MolviZ.Org.

Pure 8CB undergoes a weakly first-order isotropic to nematic transition, at $T_{IN}^o = 313.98$ K, and a continuous nematic to smectic-*A* transition, at $T_{NA}^o = 306.97$ K. Below 290 K 8CB crystallizes via a first order transition. The phase sequence (in kelvin) [28, 27] for 8CB is:



2.6.4 Characteristics of 10CB

10CB is the abbreviated name of the *LC* decylcyanobiphenyl or 4-cyano-4'-decylbiphenyl. 10CB has a typical rod-like molecule, with a rigid biphenyl core, to which are at-

tached an aliphatic tail and a polar cyano head group. Its molecular weight is $M = 319.49$ g/mol and density is 1.02 m/mL at 25 °C. Molecules are 2.45 nm long and 0.5 nm wide [29]. Liquid crystal 10CB was purchased from Frinton laboratoty [26] and used after degassing them in their isotropic phase for about 2 hours. It was used without further purification. The molecular structures are shown in Fig. 2.13 and 2.14.

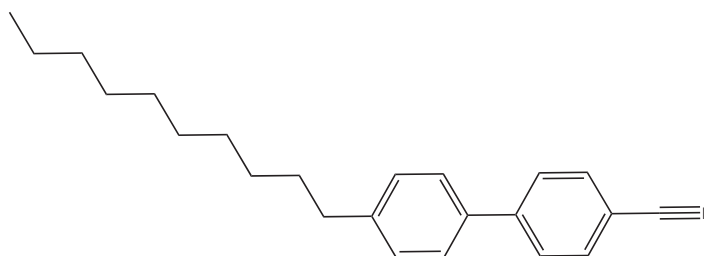


Figure 2.13. Molecular structure of the 10CB molecule using a ChemBioDraw software.

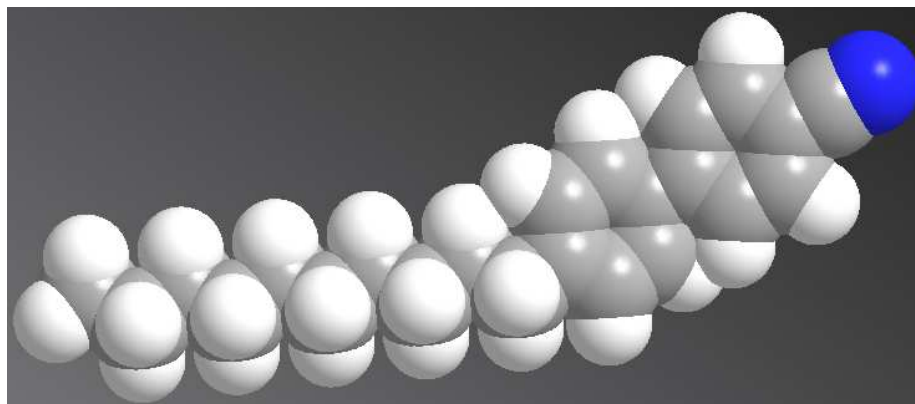
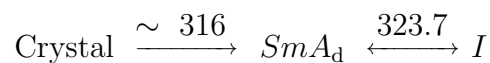


Figure 2.14. 3D structure of the 10CB molecule [10] using a MolviZ.Org.

Pure 10CB undergoes direct isotropic to smectic-*A* transition, at $T_{IA}^o = 323.69$ K. This transition is a first-order. This has a strongly first-order smectic-*A* to crystal transition at ~ 316 K [30, 31]. The transition enthalpy of *I*-Sm*A* transition is 5.14 J/g [29] and the phase sequence (in kelvin) for 10CB is



2.6.5 Characteristics of *iPP*

Isotactic polymers have their functional groups on the same side of the molecular backbone and the molecular structure of *iPP* is shown Fig 2.15. The isotactic type of polypropylene has generated extensive interest and usage in industry. It is because *iPP* has a high tendency to crystallize and depending on thermal and mechanical conditions different crystal phases can be formed. The crystal modifications of *iPP* include monoclinic (α), hexagonal (β), and triclinic (γ). Isotactic polypropylene (*iPP*) was obtained from Scientific Polymer Products, Inc. as Catalog #130 in powder form. The most frequent modifications are the monoclinic and hexagonal ones which are depicted. The crystal unit of the α phase has the following dimensions: $\alpha = 9.9$ nm, $a = 0.665$ nm, $b = 2.078$ nm, and $c = 0.650$ nm (Lotz, 1986). And the β modification is characterized by: $a = b = 1.103$ nm, and $c = 0.649$ nm.

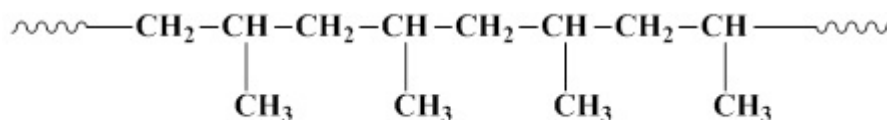


Figure 2.15. Molecular structure of the *iPP* using a ChemBioDraw software.

2.6.6 Characteristics of MWCNTs

Carbon nanotube (CNT) is an allotrope of carbon and is a member of the fullerene structural family. CNTs consist of tubular structures whose walls are made up of carbon atoms regularly arranged into a honey-comb lattice or graphene sheet (Fig 2.16). They have diameters on the order of nanometers and lengths ranging from micrometers to millimeters even centimeters possessing an extremely high aspect ratio (diameter to length ratio). CNTs are therefore single-molecule ‘string-like’ particles. CNTs can be metallic or semiconducting depending upon the chirality (the way how the graphene sheet is rolled up). Carbon nanotubes with diameter 0.14 ± 0.30 μm and lengths 7 ± 2 μm for 9004 project was kindly provided by Prof. Charles Rosenblatt and *iPP*/CNT samples were provided by Prof. Georgi Georgiev.

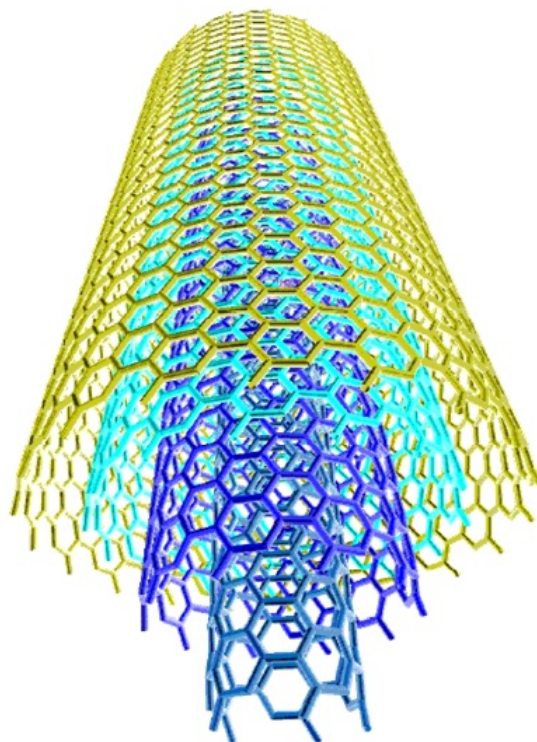


Figure 2.16. Structure of the *CNT* [32].

If a CNT has only one wrapped concentric cylinder, it is called single-walled CNT. If two concentric tubes are present, it is a double-walled and if it consists of multiple concentric tubes, it is a multi-wall CNT (Fig. 2.16). Due to the combination of peculiar geometry and graphitic nature of the walls, CNTs have exceptional mechanical, electrical and thermal properties [33]. The outstanding properties, the small scale and shape of CNTs create a unique combination appealing for many diverse applications as a single molecule or as sets. The addition of CNTs improve the thermal physical properties of the complex fluids.

2.6.7 Characteristics of QDs

A quantum dot is a portion of matter (e.g., semiconductor) whose excitons are confined in all three spatial dimensions. Consequently, such materials have electronic properties intermediate between those of bulk semiconductors and those of discrete molecules [34, 35]. They were discovered at the beginning of the 1980s by [36] in a glass matrix and by Louis E. Brus in colloidal solutions. The term

“quantum dot” was coined by Mark Reed [37]. CdS quantum dots (QDs) (UV absorption peak: 361 nm) and diameter of 2.3 nm in toluene solvent dispersed was purchased from NN-Labs. The oleic acid used as ligand (capped) for CdS quantum dots with total diameter of 6 nm and used after careful degassing for about 2 hours at a temperature of 320 K.

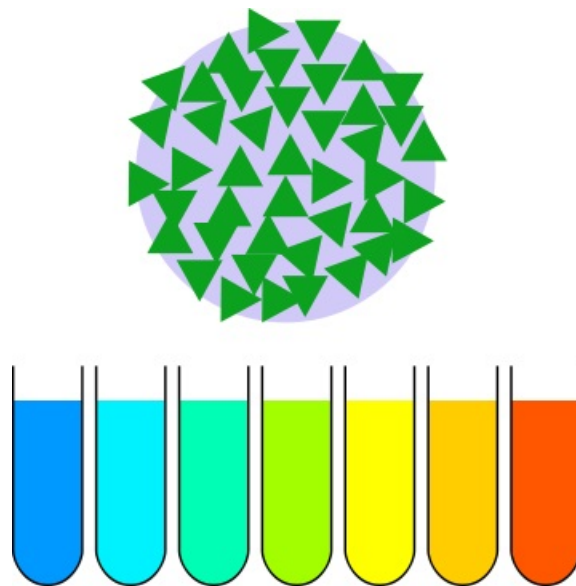


Figure 2.17. Quantum dots irradiated with a UV light. Different sized quantum dots emit different color light due to quantum confinement [38].

Cadmium Sulfide (CdS) nanocrystals are single crystal semiconductor nanoparticles, also known as quantum dots. The uniqueness of these quantum dots comes from their size dependent optical/electronic properties and flexible processability. The size of these quantum dots ranges from 2 to 7 nm with their optical properties spanning the UV to blue spectral window. Typical CdS quantum dots are inorganic semiconductors with an outer surface coating of organic ligands. These ligands allow for the stability, solubility, and processability of these nanocrystals in solution. Unlike organic dyes, quantum dots have a broad absorption with finite emission positions. This allows the quantum dots to be excited over a broad range while emitting at a finite position, yielding true color emission. The emission potential of the quantum dots is dependent upon the quality and size distribution of the nanocrystals in solution.

2.7 Sample preparation

2.7.1 9OO4/CNT

To reduce aggregation, a small amount of CNTs were dispersed first in acetone and shaken using a mixer for 30 min, followed by sonication for 3 hours. The 9OO4 was added to the acetone+CNT mixture to achieve the desired final weight percent ϕ_w of CNTs. The mixture was then sonicated for 3 hours to facilitate dispersion. Finally, the acetone was evaporated slowly, then degassed under a modest vacuum in the isotropic phase of 9OO4 at ~ 364 K (or 90 °C) for about 2 hours. Microbalance massing of the mixture was done to ensure complete removal of acetone before being sealed in the experimental cells. This process was repeated to prepare 0 (pure 9OO4), 0.008, 0.010, 0.025, and 0.200 wt% CNT calorimetry samples

2.7.2 8CB,10CB/QD

To reduce aggregation, a small amount of QDs with toluene were mixed in a vial. The 8CB/10CB was added to the toluene+QD mixture to achieve the desired final weight percent ϕ_w of QDs. The mixture was then shaken using a mixer for 30 min, followed by sonication for 3 hours to facilitate dispersion. Finally, the toluene was evaporated slowly, then degassed under a modest vacuum in the isotropic phase of 8CB at ~ 364 K for about 2 hours. Microbalance massing of the mixture was done to ensure complete removal of toluene before being sealed in the experimental cells. This process was repeated to prepare 0 (pure 8CB), 0.3, 0.4, 0.5, 0.8, 1, 2 and 3 wt% QD samples.

2.7.3 iPP/CNT

Nanocomposites were prepared by sonicating CNTs in xylene at 323 K in a flask for 30 min. The iPP polymer was added to the xylene containing the CNTs to form the different weight percent concentrations of CNT in the nanocomposites for the study. The solution was then heated and stirred by placing the flask in an oil bath on a hot plate. Once the iPP was completely dissolved, the solution was mixed slowly into a non-solvent (a polar compound such as alcohol) with about a

5X volume dilution. The resulting precipitate was dried and then pressed into a film using a compression molding hot press at a temperature of 473 K and pressure of 20-40 MPa. The samples were then crystallized at 403 K for 30 minutes and cooled to room temperature for handling.

The iPP/CNT thin films were heated in a Linkam CSS 450 shearing stage. The samples were held at 200 °C for five minutes to melt any previous crystals. Then they were sheared at 1 Hz with a 50 μm gap while cooled to 145 °C for the smectic phase to form. The samples were then crystallized at 135 °C for 30 minutes and cooled to room temperature. This process was repeated to prepare sheared and non-sheared 0 (neat iPP), 0.01, 0.1, 1, 2, and 5 wt% CNT samples.

Crystallization and melting properties of the polymer and nano composites were investigated using a Model Q200 from TA Instruments, USA under nitrogen flow. Small pieces (8-10 mg) cut from unsheared films were encapsulated in aluminum pans, and underwent subsequent cooling and heating scans between 300 K to 470 K at ± 0.5 K/min with a modulation time period of 60 sec and a modulation amplitude 0.5 K.

2.8 Methodology

2.8.1 MDSC

This section describes the experimental procedure and provides the parameters used such as frequency, thermal scan rate etc. in the experiments. For 9004, the first cooling scan followed by a heating scan was performed with a thermal scan from 0.3 to 0.7 K/min . The sample was kept in isotropic phase for about 20 min in between the cooling scan and the following heating scan. Another set of heating and cooling was done at a frequency of 0.0083 Hz and with amplitude 0.5 K. All the samples experienced the same thermal history. The second set of data is presented here. For 9004, 9004/CNT and 8CB, 10CB/QD, the first cooling scan followed by a heating scan was performed with a thermal scan of 0.5 K/min . The sample was kept in isotropic phase for about 30 min in between the cooling scan and the following heating scan. Another set of heating and cooling was done at a frequency of 0.0083 Hz and with amplitude 0.5 K. All the samples experienced the same thermal history. For iPP/CNT, the first cooling scan followed

by a heating scan was performed with a thermal scan from 0.3 to 4 K/min . The sample was kept in isotropic phase for about 20 min in between the cooling scan and the following heating scan. Another set of heating and cooling was done at a frequency of 0.0083 Hz and with amplitude 0.5 K. All the samples experienced the same thermal history. For iPP/CNT, the first heating scan followed by cooling scan was performed with thermal scan rates from 0.3 to 4 K/min. All the samples experienced the same thermal history and The second set of data is presented here.

2.8.2 DS

Dielectric measurements were performed on a homebuild dielectric spectrometer using a General Radio 1615-A AC-capacitance bridge, a Stanford Research SR830 DSP lock-in-amplifier, a Lakeshore 310 temperature control with a Mettler hot-stage, and an Instec liquid crystal cell primarily used for electro-optical (switching) experiments as the capacitive sample cell. The instrument has a temperature stability of better than ± 0.01 K, a wide scan rate capability, and a frequency range of about 10 Hz to 105 kHz. The procedure requires the empty cell's capacitance C_{empty} to be measured prior to filling with sample. The dielectric constant is then determined by the ratio of $\varepsilon = C_{filled}/C_{empty}$, where the real part is the in-phase and imaginary part is the out-of-phase parts of the LIA signal.

Measurements were performed on a sample of 9OO4 taken from the same batch as the sample used for the calorimetry measurements. Two Instec electro-optical cells, one with homeotropic (perpendicular) and the other homogeneous (anti-parallel rubbed, planar) surface alignment each having a 10×10 mm area and $20 \mu\text{m}$ gap, were filled in the isotropic phase of 9OO4 then thermally cycled between the isotropic and nematic phases a few times to ensure complete filling and alignment. Uniform alignment was observed by polarizing optical microscopy. Temperature scan dielectric measurements used 1 V as the excitation voltage amplitude at 100 kHz with a scan rate of 0.3 K/min, first cooling then heating, and were repeated twice. Switching experiments were performed in the Crystal, SmC, and N phases using 100 kHz voltages that ranged from 0.5 to 36 V (electric fields of 0.05 to $1.75 \text{ V}/\mu\text{m}$) for both cells. Again, the switching experiments were repeated twice. For both the temperature scan and voltage scan experiments, the results were reproducible to well within 1 %.

2.8.3 PM

Same samples used in calorimetry were used to observe the texture in the polarizing microscope (crossed-polarizer). For the LC/QD studies microscope slides with a concave cavity were used. After putting a drop of sample it was covered by a cover slip. The cover-slip was glued over the slide using super-glue. In the case of LC/QDs sample, a drop of samples was put on the plane surface of the microscope slide and was covered by a cover-slip. Thus made slides were observed under the crossed-polarizer and analyzer arrangements.

2.8.4 SE

Films were handled carefully and kept in dust free environments. They were mounted on flat surfaces using adhesive tape in order to collect specular reflections. Visible-UV and near IR light in the range of 250 to 1000 nm was used to analyze the sample at angles of incidence ranging from 50 to 70 degrees. Measurements were made on a M2000X system from the J.A.Woollam Co. The samples were taken as square shape for sheared and non-sheared of iPP/CNT and all measurements were performed at room temperature and on surfaces without any further treatment. After the data were collected, an optical model was constructed in the Complete EASE environment. Polymer films were modeled as a bulk layer and optical constants were extracted by allowing a b-spline function to capture changes in the ellipsometric parameters. This optical model optimized the refractive index and extinction coefficient values for the material using multiple sample measurements. Surface roughness of each individual sample was also allowed to vary independent of the other samples. After a good fit was achieved for a number of samples, the b-spline optical constants were recorded. For the pure iPP layer, the b-spline approximation was then modeled as a Cauchy dispersion layer.

2.8.5 CE

iPP/CNT sheared and non-sheared films were handled carefully and kept in dust free environments. The thin-film samples were sandwiched between two metal plates. Two electrical leads were connected to both metal plates. The conductivity was measured using a Pico-ammeter with varying voltage across the samples, which

is the direction perpendicular to the rotation of the glass plates in the Linkham CSS 450 shearing stage. The conductivity of the sheared sample gives the perpendicular component and of an un-shear samples give average of conductivity. Voltages from 0 to 100 V were applied across the samples and the current was recorded with a Keithly Pico-ammeter. All measurements were done from temperature of -50 to 50 °C. The film dimensions were: for length, between 7 and 8 mm and for width, between 6 and 7 mm for sheared and non-sheared samples. The thickness of the films was determined by a micrometer and varied from 50 to 90 μm for the iPP/CNT. The heater used for thermal conductivity measurements with resistance is 120 Ω and the power varied from 0 to 6 V. Two K-type thermocouples wires were used to record temperature on both sides of sandwich set up. The calibrated DC power source and Pico-ammeter were used in electrical conductivity measurements to record electrical resistance for iPP/CNT samples. The Tenny oven used to control wide range of temperature for both transport measurements.

Bibliography

- [1] J. E. K. Schawe, *Thermochim. Acta.*, **260**, 1 (1995).
- [2] N. J. Coleman and D. Q. M. Craig, *Int. J. Pharmaceut.*, **135**, 13 (1996).
- [3] J. M. Hutchinson and S. Montserrat, *J. Therm. Anal.*, **47**, 103 (1996).
- [4] A. Hensel, J. Dobbertin, A. Boller, and J. E. K. Schawe, *J. Therm. Anal.*, **46**, 935 (1996).
- [5] B. Wunderlich, *J. Therm. Anal.*, **48**, 207 (1997).
- [6] S. R. Aubuchon and P. S. Gill, *J. Therm. Anal.*, **49**, 1039 (1997).
- [7] S. Weyer, A. Hensel, and C. Schick, *Thermochim. Acta.*, **304/305**, 267 (1997).
- [8] J. E. K. Schawe, *Thermochim. Acta.*, **271**, 127 (1996).
- [9] TA Instruments, New Castle DE, USA.
- [10] R. Basu, Dielectric Studies of nanostructures and Directed Self-assembled Nanomaterials in nematic Liquid Crystals, Ph. D. Dissertation, WPI (2010).
- [11] M. C. Foote and A. C. Anderson, *Rev. of Sci. Instrum.*, **58**, 130 (1987).
- [12] S. Pilla, J. A. Hamida, and N. S. Sullivan, *Rev. of Sci. Instrum.*, **70**, 4055 (1999).
- [13] S. C. Bera and S. Chattopadhyay, *Measurement*, **33**, 3 (2003).
- [14] Standford Research Systems, <http://www.thinksrs.com>.

- [15] Nikon MicroscopyU, <http://www.microscopyu.com>.
- [16] H. G. Tompkins and W. A. McGahan, *Spectroscopic Ellipsometry and Reflectometry: A User's Guide; 1st ed.*, (Wiley-Interscience, New York) (1999).
- [17] R. M. A. Azzam and N. M. Bashara, *Ellipsometry and Polarized Light*, (Elsevier B.V.: Amsterdam, The Netherlands) (1977).
- [18] H. Fujiwara, *Spectroscopic Ellipsometry: Principles and Applications*, (John Wiley and Sons Ltd., Chichester, West Sussex, UK) (2007).
- [19] B. Johs, J. A. Woollam, C. M. Herzinger, J. N. Hilfiker, R. A. Synowicki and C. L. Bungay, *Opt. Metrology*, **CR72**, 29 (1999)
- [20] J. A. Woollam, B. Johs, C. M. Herzinger, J. N. Hilfiker, R. A. Synowicki and C. L. Bungay, *Opt. Metrology*, **CR72**, 3 (1999)
- [21] A. Rseiler, H. G. Tompkins and E. A. Irene, *Handbook of Ellipsometry, Eds.*, (William Andrew: Norwich, NY) (2005).
- [22] <http://nanomelbourne.com/assets/ellipsometer.png>.
- [23] J A Wollam Inc, Lincoln, NE, USA.
- [24] Molecular modeling was done using Avogadro: an open-source molecular builder and visualization tool., Version 1.XX. <http://avogadro.openmolecules.net>.
- [25] B. Zhou, G. S. Iannacchione, C. W. Garland, and T. Bellini, *Phys. Rev. E*, **55**, 2962 (1997).
- [26] Frinton Laboratory, <http://www.frinton.com>.
- [27] J. Thoen, *Int. J. Mod. Phys. B*, **9**, 2157 (1995).
- [28] G. S. Iannacchione, C. W. Garland, J. T. Mang, and T. P. Rieker, *Phys. Rev. E*, **58**, 5966 (1998).
- [29] A. Leadbetter, J. Frost, J. Gaughan, G. Gray, and A. Mosley, *J. Physique*, **40**, 375 (1979).

- [30] J. Leys, G. Sinha, C. Glorieux, and J. Thoen, *Phys. Rev. E*, **71**, 051709 (2005).
- [31] F. V. Chavez, R. Acosta, and D. Pusiol, *Chem. Phys. Lett.*, **392**, 408 (2004).
- [32] <http://upload.wikimedia.org> and <http://students.chem.tue.nl>.
- [33] R. Saito, M. S. Dresselhaus, and G. Dresselhaus, *Physical Properties of Carbon Nanotubes*, Imperial College Press, London (1998).
- [34] L.E. Brus, *J. Chem. Phys.*, **79** (2007).
- [35] D.J. Norris, *Measurement and Assignment of the Size-Dependent Optical Spectrum in Cadmium Selenide (CdSe) Quantum Dots*, Ph D Dissertation, MIT (2009).
- [36] A. I. Ekimov and A. A. *JETP Lett.*, **34**, 345 (1981).
- [37] M. A. Reed, J. N. Randall, R. J. Aggarwal, R. J. Matyi, T. M. Moore, A. E. Wetsel, *Phys. Rev. Lett.*, **60**, 535 (1988).
- [38] Terahertz Spectroscopy of CdSe Quantum Dots (www.docstoc.com).

Calorimetric and Dielectric Study of a Negative Dielectric Anisotropy Alkoxy-phenyl-benzoate Liquid Crystal

3.1 Introduction

The study of liquid crystals affords a unique opportunity to connect microscopic character of the molecule to the macroscopic phase ordering of the ensemble [1, 2, 3, 4]. The single feature of molecular anisotropy leads to two thermodynamically stable phases between the isotropic and a full three-dimensionally ordered solid phases. These two are the nematic (N) phase that exhibits only orientational order due to alignment of LC molecules and the smectic- A (SmA) phase where the molecules are arranged in liquid-like layers and so exhibit partial translational order characterized by a $1-d$ density wave. However, liquid crystal ordering is much richer (chirality, layer spacing versus molecule length, molecule tilt with respect to the layer normal, in-plane ordering, etc.) and it is of great interest to understand the connection between a microscopic characteristic of the molecule and the resulting macroscopic phase. In addition, the higher order, lower symmetry, mesophases that emerge are not only interesting in their own right, they also provide a rich range of physical model system to explore open questions of self-assembly, interactions

with external fields and surfaces as well as multi-component colloidal mixtures [3].

Because the focus is on the connection between the molecule and the phase ordering of the ensemble, there are two general experimental approaches. The first approach is to determine in greater detail the molecular structure and dynamics via spectroscopy and the other are the various thermo-physical property measurements of the resulting ordered phases. Typically, the latter type of experiments are more straight-forward while the former require careful attention to sample preparation and purity. Since most liquid crystals are relatively simple, low molecular weight, organic molecules, molecular modeling using well-established force-fields is easily accessible and can be used to augment thermo-physical experiments and provide guidance to microscopic experiments. Of the various thermo-physical experiments possible in studying phases and phase transitions, calorimetry and dielectric measurements are particularly useful. Here, two experimental techniques were employed, modulated differential scanning calorimetry (MDSC) and dielectric spectroscopy. For MDSC, the sample specific heat is decomposed into reversing (real) and non-reversing (imaginary) components and allows for a consistent definition of dynamic thermal analysis in analogy to dynamic mechanical or dielectric spectroscopies [5, 6, 7, 8, 9, 10] where the complex dynamics is related to either entropy (constant volume) or enthalpy (constant pressure) fluctuations [10]. This complex calorimetric technique dovetails closely with dielectric spectroscopy, which probes at a given frequency the dielectric constant of various modes and so provides a bridge between microscopic and macroscopic measurements.

In this work, we study the phase behavior by molecular modeling, calorimetry, and dielectric spectroscopy of a negative dielectric anisotropy alkoxyphenylbenzoate liquid crystal that is denoted 9OO4. This liquid crystal has molecular structure closely similar to two other liquid crystal homologous series pentylphenylthiol alkoxybenzoate ($\bar{n}S5$) and alkoxybenzylidene alkylaniline (nO.m). However, 9OO4 has a different linking group between the two aromatic rings and alkoxy groups on both ends, comparatively. The experiments on 9OO4 here reveal some unique features compared to the two well-studied members of these related series, $\bar{8}S5$ and 4O.8. One striking difference given the similar structure is that 9OO4 exhibits two monotropic smectic phases, a tilted smectic- C (SmC) and an in-plane hexatic ordered smectic- B (SmB) between its SmA and crystal phases while $\bar{8}S5$ only has

a monotropic SmC phase and 4O.8 has a plastic crystal-*B* (Cr*B*) phase between their monomeric Sm*A_m* and crystal. The conversion into the Sm*B* phase is very slow, exhibiting strong variations and multiple steps even for very slow scan rates. Also, the *N*-Sm*A* transition in 9OO4 has an unusually small enthalpy of 0.3 J/g compared to that in $\bar{8}$ S5 and 4O.8 of about 2 J/g. The dielectric constant of the Sm*A* phase has a hysteresis begin larger on cooling than heating under identical conditions and so depends on whether the Sm*A* formed from the *N* or crystal phase. Intriguingly, on heating 9OO4 exhibits a stable specific heat and dielectric feature that indicates an intermediate smectic-like phase between the crystal and smectic-*A* phase. Modeling indicates that the primary difference between $\bar{8}$ S5 and 4O.8 with 9OO4 is that the effective dipole moment of all three, though perpendicular to the long molecular axis, is oriented essentially parallel to the plane of the two-phenyl rings of $\bar{8}$ S5 and 4O.8 while in 9OO4 it is oriented nearly perpendicular. Not only does the different linking groups in these types of LCs have different structure and flexibility but changes the orientation of the effective dipole moment. This feature may explain the unusual phase ordering.

3.2 Results and Discussions

3.2.1 Calorimetry

The overview of the excess reversible ($\Delta C'_p$) and non-reversible ($\Delta C''_p$) specific heat taken first on cooling then on heating using the quasi-static parameters mentioned in Sec. 3.2.1 is shown in Fig. 3.1. It should be noted that the cooling scan was paused at 47 °C for \sim 2 hr in order to allow for the Sm*B* phase to fully form before the cooling scan proceeded. On cooling, 9OO4 exhibits the phase sequence *I* -*N* - Sm*A* - Sm*C* - Sm*B* - Crystal (*K*) while on heating, melting occurs nearly 25 K higher that is followed by a specific heat peak almost 2 K higher before entering the Sm*A* phase. Further heating yields the *N* and *I* phases. Based on the $\Delta C''_p$ behavior, the *I*-*N* is weakly first-order, the *N*-Sm*A* is continuous, the Sm*A*-Sm*C* is continuous, the Sm*C*-Sm*B* is first-order, and the Sm*B*-*K* strongly first-order. The strongly first-order melting followed by a second, first-order, C_p feature indicates the presence of an intermediate phase (labeled Sm*X*) between *K* and Sm*A* on heating. For first-order transitions, we take the transition temperatures (T_{IN} ,

T_{CB} , T_{BK} , T_{KX} , and T_{XA} as the highest temperature of the two-phase coexistence indicated by the onset of non-zero values of $\Delta C_p''$. For continuous transitions, we take the temperature of the $\Delta C_p'$ peak as T_{NA} and the inflection point of the $\Delta C_p'$ step on the high temperature side as T_{AC} . These transition temperatures on cooling and heating as well as the two-phase coexistence range (the range of non-zero $\Delta C_p''$) and the transition temperature hysteresis (difference of T_C on heating and cooling) are summarized in Table 4.1.

For the I - N phase transition, the real and imaginary excess specific heat signatures are typical for this weakly first-order transition. See Figure 5.1. The transition hysteresis is $\delta T_{hyst} = T_{IN}^h - T_{IN}^c = +0.01$ K where the non-zero non-reversible part of the specific heat does not show a simple peak, as is typical for a pure AC-calorimetric method [11]. The character of the non-zero $\Delta C_p''$ region is that of an oscillation rather than a peak as shown in Fig. 5.1, indicating that the phase shift angle has aliased within the $I+N$ coexistence range, which can happen in the Fourier Transform analysis method of MDSC. On cooling, the effective enthalpy components for the I - N phase transition are $\delta H'_{IN} = 3.91 \pm 0.08$ J/g and $\delta H''_{IN} = 0.98 \pm 0.08$ J/g yielding a total I - N transition enthalpy of $\Delta H_{IN} = 4.9 \pm 0.1$ J/g. For the I - N transition on heating, these values are $\delta H'_{IN} = 4.90 \pm 0.08$ J/g and $\delta H''_{IN} = 0.95 \pm 0.08$ J/g yielding a total I - N transition enthalpy of $\Delta H_{IN} = 5.9 \pm 0.1$ J/g. There is an observed difference of about 1 ± 0.2 J/g in total enthalpy for the I - N transition. Total enthalpy values are summarized in Table 4.2. These results are all consistent with the I - N phase transition being a weakly first-order phase transition typical of liquid crystals.

The N - SmA phase transition does not exhibit any feature in the imaginary specific heat indicating the lack of a latent heat. The excess real part of the specific heat is isolated by using a simple polynomial to model the low-temperature wing of the I - N transition that underlies the N - SmA . The resulting $\delta C_p'$ on cooling then heating as a function of temperature about T_{NA} is shown in Fig. 5.2. There is a small hysteresis in T_{NA} between heating and cooling of about $\delta T_{hyst} \approx +0.15$ K, much larger than that observed for the I - N transition. While the $\delta C_p'$ wings overlap very well, the peak is larger on heating than on cooling. This is reflected by a larger real enthalpy (equal to the total enthalpy since $\delta H''_{NA} = 0$) on heating than cooling ($\delta H'_{NA} = 3.32$ J/g versus 3.02 J/g, respectively) well outside the estimated

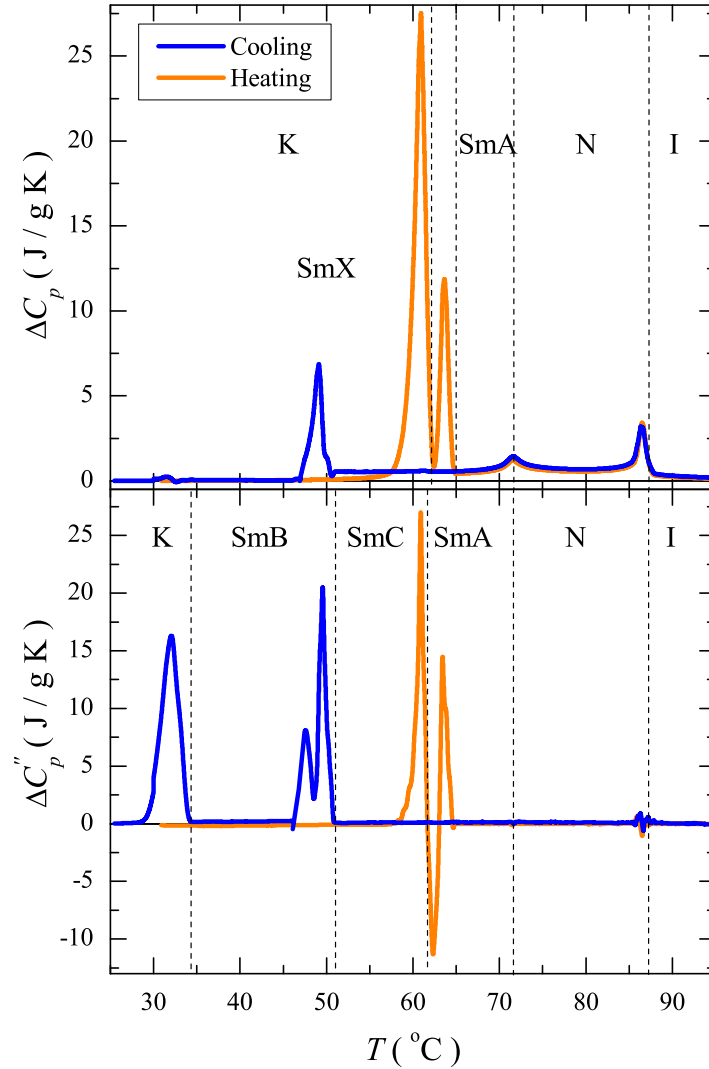


Figure 3.1. Overview of the excess reversible (top panel) and non-reversible (bottom panel) specific heat on cooling then heating between ~ 95 and 25 $^{\circ}\text{C}$ by MDSC. This excess specific heat was determined by subtracting a linear background over the entire experimental temperature range from the reversible and non-reversible specific heat. Scans were performed using parameters that most closely approximated static heat capacity results; a base scan rate of ± 0.3 K/min and an induced temperature amplitude of 0.5 K at 120 s heating period. Note that the cooling scan was paused at 47 $^{\circ}\text{C}$ (320.2 K) for ~ 2 hr before continuing.

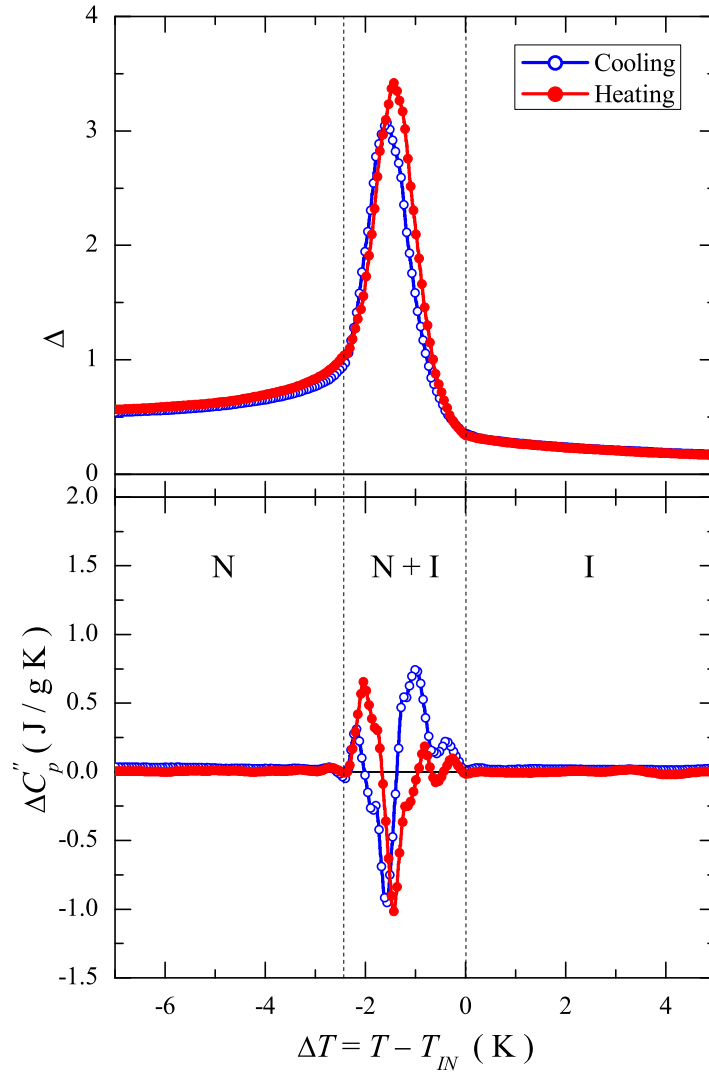


Figure 3.2. Detailed view of the excess reversible (top panel) and non-reversible (bottom panel) specific heat about the isotropic to nematic phase transition on cooling then heating about the transition temperature T_{IN} . Quasi-static parameters of Fig. 3.1 were used for these scans. For clarity, every 15th data point has been plotted. Note the indication of the two-phase ($I+N$) coexistence range by the vertical dashed lines was determined by the non-zero signal in $\Delta C_p''$.

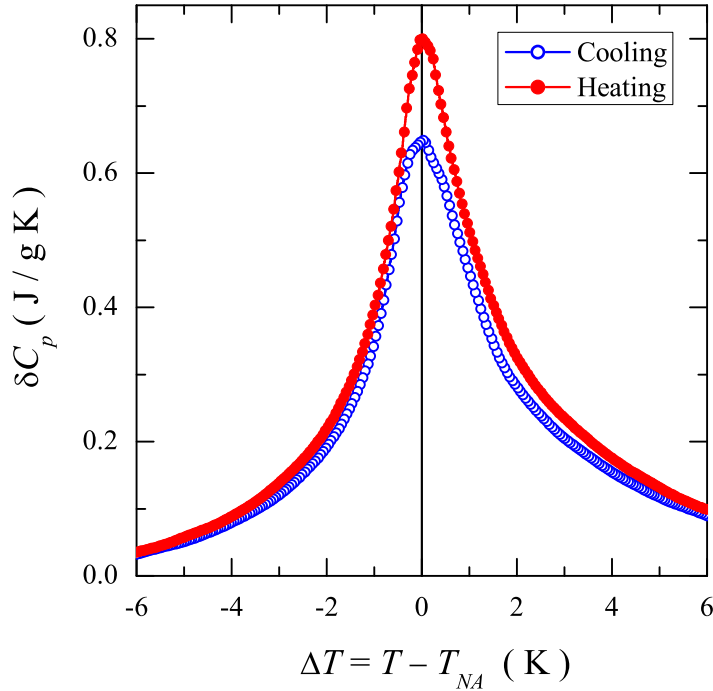


Figure 3.3. The excess reversible specific heat for the nematic to smectic-*A* phase transition on cooling then heating about the transition temperature T_{NA} using the quasi-static experiment parameters. For clarity, every 15th data point has been plotted. This excess specific heat was determined by subtraction of the low-temperature specific heat wing of the *I-N* phase transition. Note that the non-reversible specific heat was essentially zero through this transition, indicating the continuous character of this transition.

uncertainties of ~ 0.1 J/g. Despite the hysteresis behavior, reproducible after multiple cooling and heating cycles, the *N-SmA* transition for 9004 is continuous.

The excess specific heat of the *SmA-SmC* phase transition δC_{AC} was isolated by subtracting the low temperature wing of the *N-SmA* C_p peak and is shown in Fig. 4.3. The δC_{AC} peak is monotropic and exhibits no imaginary C_p feature. Given the shape and continuous nature of the transition, it is classified as a Landau (mean-field) second-order transition [3]. The *SmA-SmC* phase transition temperature T_{AC} is taken as the inflection point on the high-temperature side of the δC_{AC} peak yielding $T_{AC} = 61.50$ °C. The effective transition enthalpy $\delta H'_{AC} = 0.32 \pm 0.08$ J/g, determined by integrating δC_{AC} from about 2 K above T_{AC} down to temperature of the *SmC-SmB* transition, is typical for this transition.

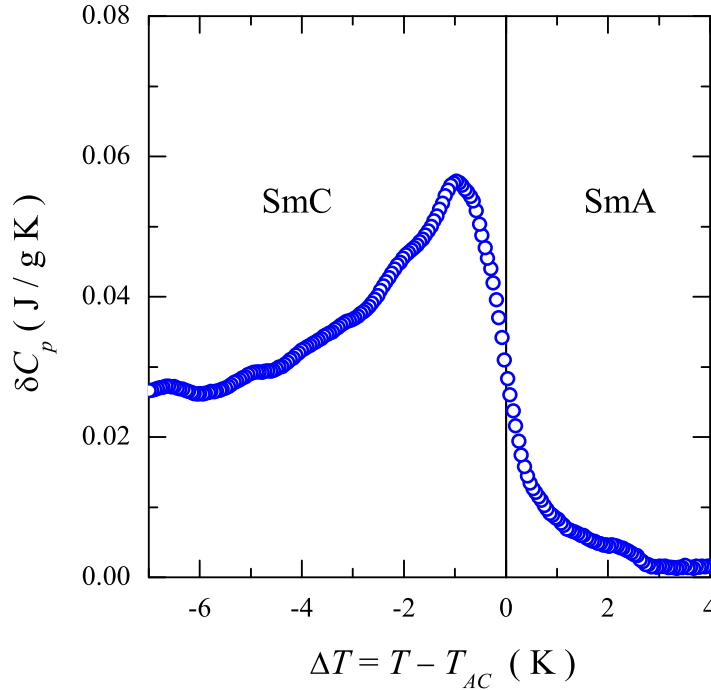


Figure 3.4. The excess reversible specific heat for the smectic-*A* to smectic-*C* phase transition on cooling about the transition temperature T_{AC} using the quasi-static experiment parameters. For clarity, every 15th data point has been plotted. The transition temperature was estimated by the inflection point of δC_p on cooling. This excess specific heat was determined by subtraction of the low-temperature specific heat wing of the *N*-Sm*A* phase transition underlying the Sm*A*-Sm*C* transition. Note that the non-reversible specific heat was essentially zero through this transition, indicating the continuous character of this transition.

The excess specific heat ΔC_p of the Sm*B* temperature range on cooling is shown in Fig. 3.5 as a function of baseline scan rate from 0.3 to 0.7 K/min with the modulation parameters were kept fixed. Clear observations of scan rate dependence is seen in both the real and imaginary parts of the specific heat. The Sm*C*-Sm*B* transition is marked by a strongly first-order specific heat signature at $T_{CB} = 49.38$ °C with the imaginary C_p peak being much larger than the real C_p peak and both peaks generally decreases in amplitude with increasing scan rate. Specifically, as the scan rate increase from 0.3 to 0.7 K/min the enthalpy components of the Sm*C*-Sm*B* transition decreases; the total enthalpy decreases smoothly from ≈ 46 to 35 J/g, respectively. Surprisingly, given the very low scan

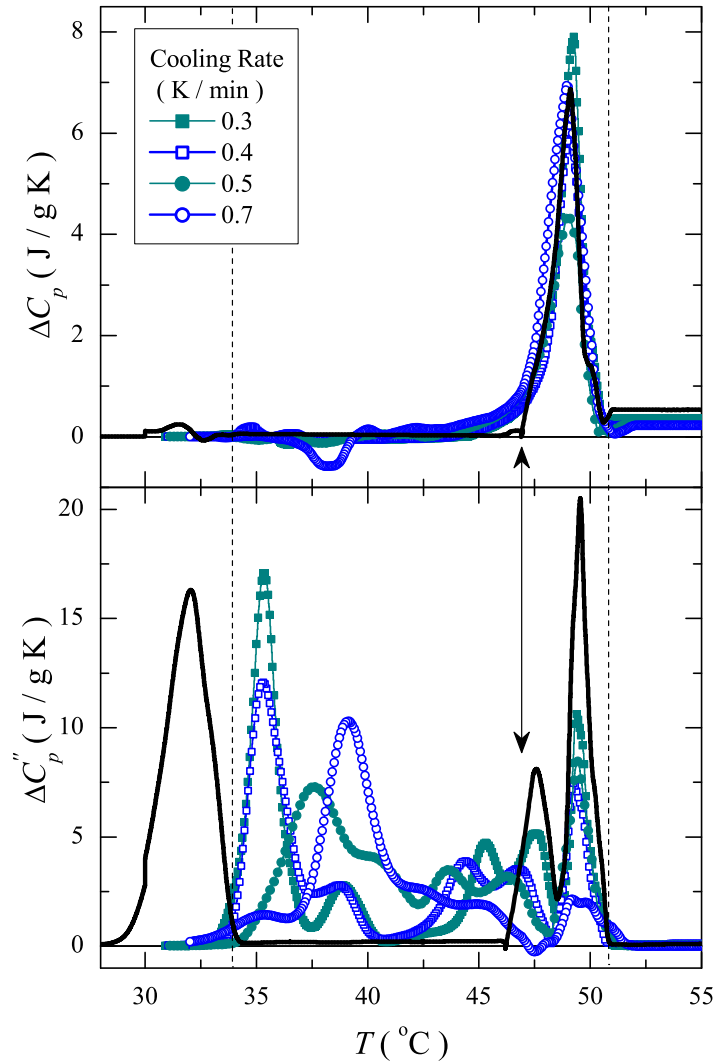


Figure 3.5. The reversible and non-reversible excess specific heat on cooling over the smectic- C to smectic- B to crystallization transitions as a function of continuous scan rate. For clarity, every 15th data point has been plotted. Quasi-static modulation parameters were used; 0.5 K temperature amplitude and 120 s heating period, while the cooling rate was varied from the lowest of 0.3 to 0.7 K/min. See legend. Also shown is the 0.3 K/min base rate cooling scan that was paused at 47 °C for 2 hr before proceeding (solid line), the pause point is indicated by the vertical double arrows. The vertical dashed lines approximate the first-order SmC-SmB and SmB-K transitions.

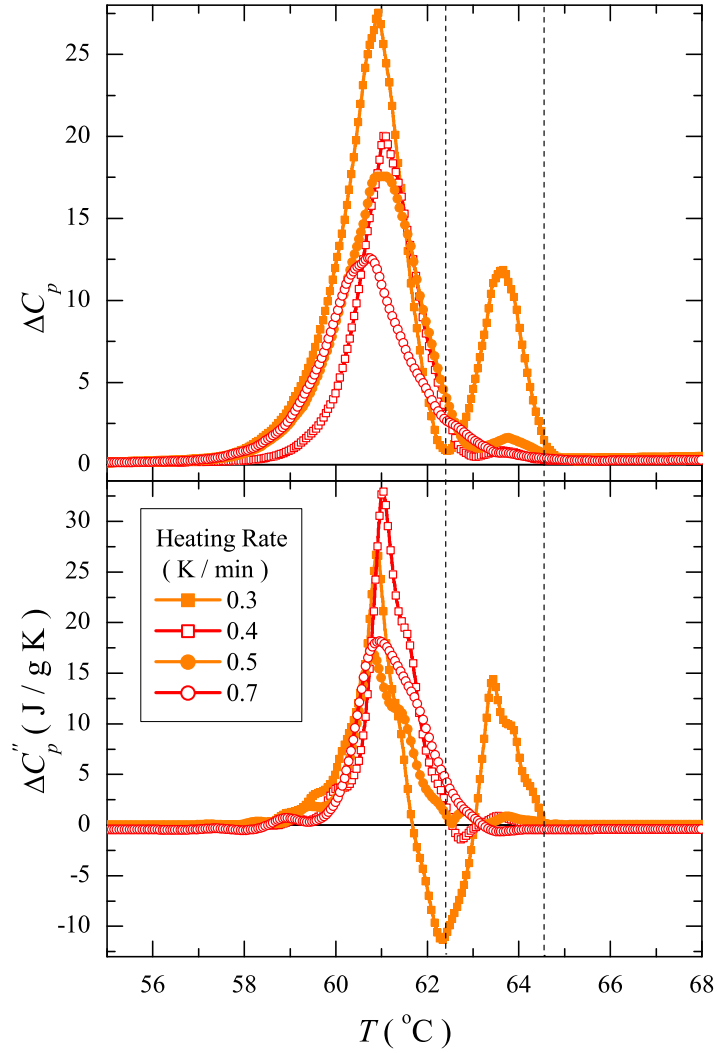


Figure 3.6. The reversible and non-reversible excess specific heat on heating from the melting to smectic-*A* transitions as a function of continuous scan rate. For clarity, every 15th data point has been plotted. Quasi-static modulation parameters were used; 0.5 K temperature amplitude and 120 s heating period, while the cooling rate was varied from the lowest of 0.3 to 0.7 K/min. See legend. The vertical dashed lines approximate the transitions from the crystal to an undetermined smectic phase denoted Sm*X* and another from Sm*X* to the Sm*A* phase. Both observed transitions are first-order.

rates employed, as the temperature continuously cools, several $\Delta C_p''$ signatures are observed that are highly baseline scan rate dependent, in general smearing out over the entire SmB temperature range as the scan rate increases. As the scan rate increases, the real component $\Delta C_p'$ increasingly exhibits small undulations that also increase in amplitude. See Fig. 3.5. The SmB phase on cooling ends with a very strongly first-order C_p signature of crystallization at $T_{BK} \sim 35$ °C having a very small real component and a very large imaginary component. In general, the integrated enthalpy over this entire temperature range is only weakly scan rate dependent indicating that these multiple complex features are due to very slow conversion from the SmC to the SmB phase. To test this, a cooling scan using the quasi-equilibrium parameters was performed where the scan was stopped just below T_{CB} at 47 °C for 2 hr then resumed. This scan, shown as the solid line in Fig. 3.5 where the scan pause is indicated by the vertical double arrow, still found a small $\Delta C_p''$ below the large one associated with the SmC-SmB transition but prior to the pause. However, no other feature is observed in either the real or imaginary components until crystallization is reached at a lower temperature of $T_{BK} = 31.5$ °C. This is consistent since a not fully formed SmB phase would provide many nucleation sites for crystallization to occur and so be at a higher temperature when the scan was continuous.

Upon heating under continuous quasi-equilibrium conditions, the crystal phase super heats until a strongly first-order specific heat feature is observed that ends at ≈ 61 °C. Upon further heating, a second first-order feature is seen nearby that ends when the SmA phase appears at ≈ 64 °C. See Figure 3.6. Because of the slow SmB phase conversion observed on cooling, a similar scan rate study was done over the same range of rates on heating and these are also shown in Fig. 3.6. Here, the melting C_p peak generally decreases in amplitude and smears in temperature with an effective total enthalpy of $\delta H_{KX} = 72$ J/g and an effective total enthalpy of the second feature of $\delta H_{XA} = 32$ J/g. Interestingly, the second feature *decreases* in size rapidly with increasing scan rate, suggesting that this feature is not due residual crystals melting. Because of the magnitude of the enthalpy involved it is possible that this feature is a transition into an intermediate smectic phase before

Table 3.1. Summary of the transition temperatures T_C for 9004 based on the quasi-static MDSC results for both cooling and heating scans (superscripts c and h , respectively) in Celsius. First-order transition temperatures are taken as the highest temperature of the two-phase coexistence range (or the lowest temperature of the higher temperature phase) determined from the non-reversible (imaginary) part of the specific heat, $\Delta C_p''$. Continuous-order transition temperatures are taken as the temperature of the peak in the reversible $\Delta C_p'$ for the N -SmA transition or the inflection point of the high temperature side of the $\Delta C_p'$ peak for the SmA-SmC transition. Also shown are the two-phase coexistence range δT_{2p} and the transition temperature hysteresis δT_C . If the transition is monotropic, it is designated *mono*. Uncertainties stem from determining the onset of non-zero $\Delta C_p''$.

Transition	T_C^c	T_C^h	δT_{2p}	δT_C
$I-N$	86.23 ± 0.06	86.19 ± 0.04	2.5	0.01
N -SmA	71.49 ± 0.09	71.68 ± 0.05	0	0.15
SmA-SmC	61.50 ± 0.08	–	0	<i>mono</i>
SmC-SmB	49.38 ± 0.04	–	4.6	<i>mono</i>
SmB-K	35.30 ± 0.02	–	5.8	<i>mono</i>
K -SmX	–	60.92 ± 0.09	3.9	<i>mono</i>
SmX-SmA	–	63.64 ± 0.08	2.1	<i>mono</i>

Table 3.2. Summary of the transition enthalpies for 9004 based on the quasi-static MDSC results for both cooling (c) and heating (h) scans. The transition enthalpy, ΔH , is determined as the root-mean-square of the reversible (real, $\delta H'$) and non-reversible (imaginary, $\delta H''$) enthalpy in Joules per gram. Uncertainties represent integration error, overall uncertainties in determining enthalpy by MDSC is about 10%.

Transition	T_C^c	T_C^h	δT_{2p}	δT_C
$I-N$	86.23 ± 0.06	86.19 ± 0.04	2.5	0.01
N -SmA	71.49 ± 0.09	71.68 ± 0.05	0	0.15
SmA-SmC	61.50 ± 0.08	–	0	<i>mono</i>
SmC-SmB	49.38 ± 0.04	–	4.6	<i>mono</i>
SmB-K	35.30 ± 0.02	–	5.8	<i>mono</i>
K -SmX	–	60.92 ± 0.09	3.9	<i>mono</i>
SmX-SmA	–	63.64 ± 0.08	2.1	<i>mono</i>

heating into the SmA phase. We denote this phase as SmX and are unclear as to whether this phase is SmB or SmC like since the melting occurs very near T_{AC} on cooling. The remaining transitions from SmA- N and N - I exhibit specific heat features consistent with that seen on cooling and those typical in the literature. Note that a summary of the transition temperatures are given in Table 4.1 and total

transition enthalpy on heating, cooling, and their average are given in Table 4.2. Also given is the total enthalpy of all phase transitions from the crystal to isotropic phases, which is on average 103 J/g. This total shows a difference of about 21 J/g between heating and cooling that is within $\sim 10\%$ of each other, which is about the uncertainty of the absolute enthalpy for this technique.

3.2.2 Dielectric Measurements

In order to illuminate the transition features as well as explore the slow phase conversions observed, dielectric measurements were performed at a frequency of 100 kHz on the two capacitive cells each having the same active area and gap but differ in alignment for both temperature and voltage switching scans. All dielectric measurements were carried out over the same temperature range and using the same baseline scan rate of ± 0.3 K/min as was used in the MDSC measurements. Thus, the dielectric and calorimetry measurements experienced the same thermal conditions. As mentioned earlier, multiple scanning cycles were done and found very good reproducibility.

Cooling then heating scans for the real ϵ' and imaginary ϵ'' components of the dielectric constant for the homogeneous (planar) aligned cell are shown in Fig. 3.7. This cell alignment has the long axis of the LC molecule parallel to the surface and its dipole moment parallel to the applied electric field. On cooling, a very small feature is observed in ϵ' and ϵ'' through the *I-N* and *N-SmA* transition with ϵ' increasing with decreasing temperature, both with 0.2 K of the specific features for these transitions. However, ϵ'' decreases with decreasing temperature until the *N-SmA* transition where it sharply changes slope and begins to increase with decreasing temperature. Upon further continuous cooling, the real component ϵ' sharply changes slope and begins to smoothly decrease with decreasing temperature with no discernable feature seen in ϵ'' at the *SmA-SmC* transition. Approximately mid-range of the *SmC* phase while ϵ' continues to decrease smoothly, ϵ'' exhibits a broad peak at ~ 56 °C then decreases continuously with decreasing temperature until the *SmC-SmB* transition. At the *SmC-SmB* transition, both ϵ' and ϵ'' exhibit a sharp decrease within 0.1 K of T_{CB} observed by calorimetry. Cooling through the *SmB* phase continuously, a single step-like feature is seen in ϵ' commensurate with a small peak in ϵ'' . The onset of crystallization is marked

by a sudden temperature independence of ϵ' and no signature in ϵ'' . This onset matches well this the temperature for crystallization seen in the calorimetry under continuous cooling. See Figure 3.7 and Figure 3.1.

On heating, ϵ'' smoothly increases with increasing temperature while ϵ' is essentially constant until about 40 °C where it begins to very slightly decrease. When melting is reached, there is a very sharp increase in both components of ϵ followed immediately by a decrease in value until another sharp increase in both is observed ~ 2 K higher. As seen in Fig. 3.7, the jump in ϵ' does not reach the value on cooling while ϵ'' is much larger than that seen on cooling in the SmA phase. The heating only matches the cooling values above the N -SmA transition; in the nematic and isotropic phases. Again, all dielectric features observed correlate very closely to those observed by calorimetry.

Voltage scans between 0.5 and 36 V across the 20 μm gap found no switching change in either ϵ' or ϵ'' for the homogeneous (planar) aligned cell in either the crystal, SmC, or N phases. This is consistent with the negative dielectric anisotropy of 9OO4 and indicating that the results described above and shown in Fig. 3.7 should be independent of applied electric field. However, voltage scans for the homeotropic (perpendicular) aligned cell found a strong switching behavior where ϵ' begins to increase at ≈ 4 V, shown an inflection at ≈ 9 V, nearly saturating at 36 V in the nematic phase (77 °C) yielding a $\Delta\epsilon' = 0.16$. Over this voltage range ϵ'' decreases slightly from 0.315 to 0.305. No switching behavior is observed for the homeotropic cell in the SmC or crystal phases of 9OO4, as expected for these higher-order phases.

The temperature scans for the homeotropic cell were conducted at 0.5 V and 35 V on cooling then heating using ± 0.3 K/min for consistency. The cooling at 0.5 V reproduces the magnitude and temperature dependence of the homogeneous cell shown in Fig. 3.7 in the isotropic phase. However, upon entering the nematic phase, ϵ' begins to decrease strongly from about 4 near the I - N to ≈ 3 just above the SmB-SmC transition with small features indicating the N -SmA and the SmA-SmC transitions. Once in the SmB phase at ≈ 48 °C, the low voltage scan shows a sharp step down for ϵ' to 2.6 then constant for 3 K when it steps up broadly over nearly 2 K back to ~ 2.9 at ≈ 43 °C. On further cooling, ϵ' remains nearly constant until ≈ 35 °C where it begins to smoothly decrease to

2.5 at ≈ 30 °C completing the entry into the crystal phase. Cooling scans in the switched state using 35 V nearly reproduce exactly ϵ' for the homogeneous cell, indicating a uniform and complete switch of the cell, except for the temperature range just in the Sm*B* phase. For the switched cell, beginning at ~ 48 °C, ϵ' remains at ~ 3.1 with only a very small feature marking the 5 K range where the unswitched cell saw a step-down - step-up behavior. The onset process for crystallization begins at ≈ 37 °C and is completed at the same temperature of 30 °C. In contrast, the homogeneous cell data reveals a an initial step once the Sm*B* phase is entered the is intermediate between the Sm*C* value and the plateau value prior to crystallization. On heating, the low and high voltage scans (unswitched and switched) reproduce each other and the homogeneous cell ϵ' up to the *N*-Sm*A* transition. The switched homeotropic cell follows closely the homogeneous cell while the unswitched homeotropic cell reproduces its cooling scan. It should be noted that the dispersion ϵ'' for the homeotropic cell has the same temperature dependence in shape but larger in magnitude by a factor of 10, indicating that the frustration for the molecular surface alignment and the direction of the dipole moment for 9OO4 in a homeotropic cell leads to much larger dispersion losses.

All these voltage and temperature scan results indicate that 9OO4 has a strongly temperature dependent negative dielectric anisotropy below the *I*-*N* transition similar to that of 4O.8 and $\bar{8}$ S5. Also, there is a 5 K temperature range just below the Sm*B*-Sm*C* transition where the ordering is difficult to establish, presumably because of the frustration between the steric interactions of the molecule and the perpendicular dipole moment.

The phase ordering of 9OO4 presented in this work has four notable features compared to the two similar LCs $\bar{8}$ S5 and 4O.8. Firstly, 9OO4 exhibits two monotropic smectic phases, the Sm*C* and Sm*B* phases while $\bar{8}$ S5 only has a monotropic Sm*C* phase. Secondly, the *N*-Sm*A* transition in 9OO4 has an unusually small enthalpy of 0.3 J/g compared to that in $\bar{8}$ S5 and 4O.8 of about 2 J/g. Thirdly, the conversion into the Sm*B* phase is very slow, exhibiting strong variations and multiple steps even for very slow scan rates. Finally, on heating 9OO4 exhibits a stable specific heat and dielectric feature that indicates an intermediate smectic-like phase between the crystal and smectic-*A* phase.

These results can be understood in terms of a combination of molecular packing

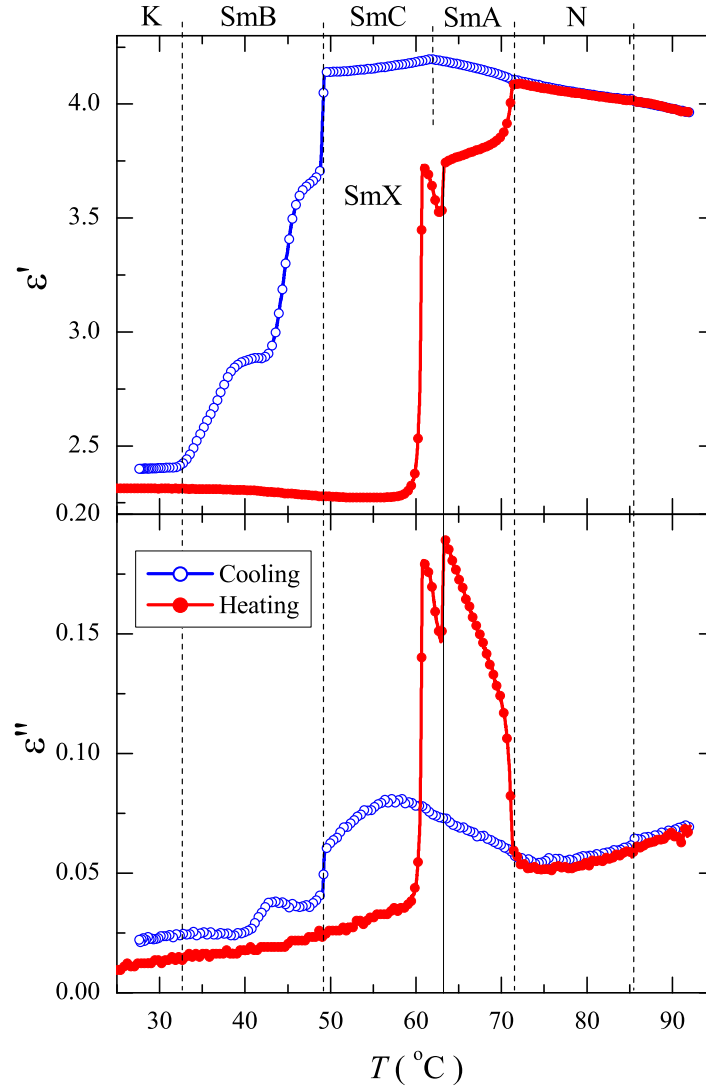


Figure 3.7. The real ϵ' (top panel) and imaginary ϵ'' (bottom panel) dielectric constant of 9OO4 in the homogeneous (planar) cell. Data taken on cooling then heating at 100 kHz using ± 0.3 K/min scan rates between 95 and 25 °C. See legend. For clarity, every 10th data point has been plotted. The vertical dashed lines indicate the I - N , N - SmA , and the SmC - SmB (cooling only) transitions.

and the influence of the unusual effective dipole moment of 9OO4. An analysis of the (volume) thermal expansion coefficient α_V and the x-ray scattering measured smectic layer-spacing for the $\bar{n}S5$ series was analyzed in terms of two linear thermal expansion coefficient components parallel α_{\parallel} and perpendicular α_{\perp} to the smectic-

A layer normal and found that $\alpha_{||} < 0$ and diverges toward negative infinity upon approaching *N-SmA* from below [12]. From a similar Pippard analysis, 4O.8 was found to have $\alpha_{||} = 0$ as well as many members of the nO.m series. The difference between $\bar{8}S5$ and 4O.8 behavior was determined to be due to the flexible -C(O)-S- linking group for $\bar{8}S5$ compared to the rigid -C(H)=N- linking group for 4O.8 between their aromatic rings [12]. Both of these LCs have a slightly bent core with their two phenyl rings twisted with respect to each other. This structure is also expected for 9OO4 and supported by molecular modeling [13]. From Fig. 10 of Ref. [12], the $\bar{n}S5$ and 4O.m series follow the same trend on a $\log(\delta H_{NA})$ versus McMillan ratio $R_M \equiv T_{NA}/T_{IN}$ while the nCB and nOCB liquid crystal series follow a parallel trend but nearly an order of magnitude smaller enthalpy. The *N-SmA* enthalpy for 9OO4 have $R_M = 0.959$ is nearly along the trend for the polar nCB and nOCB series rather than that for the series of similar structure. Unfortunately, the quality of the MDSC data does not allow for detailed power-law analysis to extract the *N-SmA* or the *SmC-SmA* critical behavior, but the enthalpy of the *N-SmA* suggests a behavior similar to the nCB/nOCB series and the shape of the *SmC-SmA* closely resembles that expected [14]. Overall, the comparisons and observations suggests that the -C(=O)-O- linking group for 9OO4 is as flexible as that for the $\bar{8}S5$ linking group but with a differently oriented in-plane dipole moment that would lead to *SmB*-like ordering. The possibility of the in-plane dipole moments pairing, forming perhaps a cybotactic group, would indicate that the smectic-*A* phase for 9OO4 is a partial bi-layer (*SmA_d*) rather than the monomeric smectic-*A* (*SmA_m*) of either $\bar{8}S5$ or 4O.8. This may also lead to the unusually slow *SmB* phase conversion and appearance of an intermediate smectic phase on heating.

The observations presented in this work for the liquid crystal 9OO4 have revealed an interplay between the LC ordering due to molecular shape (steric) and a perpendicularly aligned dipole moment. These interactions emerge directly from the particular molecular structure of 9OO4 and can be placed now in context with other LCs of similar structure. In this work, the specific heat, dielectric constant, and molecular modeling suggest that the combination of bent/twisted core structure, the core flexibility, and orientation of the effective dipole moment lead to the onset of a monotropic *SmB* phase that converts very slowly from a *SmC* phase, an

N-SmA transition similar to a very different LC structure, and the appearance of an intermediate smectic-like phase between melting and the Sm*A*. Detailed dielectric measurements exploring the anisotropy as a function of frequency through the various transitions would be very helpful as well as x-ray scattering to determine the smectic-*A* layer spacing behavior. Higher resolution calorimetry would confirm the expected critical behavior of the continuous transitions.

Bibliography

- [1] J. W. Goodby, Waugh, S. M. Stein, and E. Chin, *Nature*, **337**, 449 (1989).
- [2] S. Chandrashekar, *Liquid Crystals* (Cambridge University Press, England, 1992).
- [3] D. Demus, J. W. Goodby, G. Gray, H. Spiess, and V. Vill, eds., *Handbook of Liquid Crystals* (Wiley-VCH, Canada) (1998).
- [4] P. G. de Gennes and J. Prost, *The Physics of Liquid Crystals*, (Oxford University Press, Clarendon, Oxford, England) (1993).
- [5] T. Christensen, *J. Phys. Colloques*, **46**, 635 (1985).
- [6] N. O. Birge, *Phys. Rev. B*, **34**, 1631 (1986).
- [7] P. K. Dixon, *Phys. Rev. B*, **42**, 8179 (1990).
- [8] N. O. Birge and S. R. Nagel, *Phys. Rev. Lett.*, **54**, 2674 (1985).
- [9] N. O. Birge, P. K. Dixon, and N. Menon, *Thermochim. Acta.*, **304/305**, 51 (1997).
- [10] J. E. K. Schawe, *Thermochim. Acta.*, **271**, 127 (1996).
- [11] D. Finotello and S. Qian and G. S. Iannacchione, *Thermochim. Acta.*, **304**, 52 (1997).
- [12] E. Anesta and G. S. Iannacchione and C. W. Garland, *Phys. Rev. E.*, **70**, 4 (2004).

- [13] Molecular modeling was done using Avogadro: an open-source molecular builder and visualization tool., Version 1.XX. <http://avogadro.openmolecules.net>.
- [14] S. Weyer, A. Hensel, and C. Schick, *Thermochim. Acta.*, **304/305**, 267 (1997).

Calorimetric Study of Nanocomposites of Carbon Nanotubes and a Negative Dielectric Anisotropy Liquid crystal

4.1 Introduction

Composites of nano-particles with fluids or complex fluids represent a unique physical system where properties of the components only partially mix and new behavior can emerge. Traditional composites are relatively well understood as the superposition, weighted by volume or mass, of the component's properties and the interfacial interactions that play a role in holding the composite together. As the filler shrink in size, the surface area begins to dominate, leading to unique behavior of the nanocomposites. Carbon nanotubes (CNT) and liquid crystals (LC) are good examples of such components.

Since their discovery in 1991 [1], carbon nanotubes have emerged as a new class of nanosized particles for incorporation into various liquid crystal systems, attracting considerable interest from both basic science research and industry. As a result of the exceptional intrinsic properties of carbon nanotubes, novel materials can be envisioned that exhibit property enhancements, even at CNT concentrations much lower than in conventional composite technology [2]. In the

field of thermoplastic nanocomposites, reported property enhancements include improved mechanical performance [3, 4], high thermal and electrical conductivity [5, 6, 7], increased crystallization rate [8, 9, 10], and altered rheological behavior [11, 12]. In addition to CNT's thermal, mechanical, and magnetic properties [13, 14, 15, 16, 17, 18, 19, 20, 21, 22], their unique electrical character makes them potentially useful materials for use in nanoelectronic devices [23, 24, 25, 26].

Liquid crystals [27, 28, 29] are anisotropic fluids that exhibit numerous thermodynamically stable phases between an isotropic liquid and a full, three-dimensionally ordered solid. In the nematic (N) phase, LCs show orientational order. In the smectic- A (Sm A) phase, the rod-like molecules are arranged in layers with their long axes on average, normal to the layer planes, and they show both orientational and partial translational order characterized by a quasi-1-d density wave. The smectic phases incorporate structures with diverse symmetry groups [30], such as that of smectic- C (Sm C), which has the layer tilting away from the director. The smectic- B (Sm B) phase the molecules show short-range hexagonal ordering within the layers but not from layer to layer and it shows a short or long-range translational order. Higher-order, lower-symmetry, liquid crystalline materials have been studied because of their industrial applications as well as important physical models of self-assembly [29, 30].

When CNTs are dispersed in a liquid crystal, they can modify the physical properties and hence the phase behavior of the nanocomposite. Due to the specific surface anchoring between nanoparticle and LC, the nanoparticles can act either as nucleation sites for a given type of order or as disordering sites that stabilize the isotropic phase [31, 32]. However, if the local ordering effect of CNT surfaces are randomly arranged, this can lead to a random-field effect [33] and an overall disordering of the composites. Investigations have been made on liquid crystal nanocomposites using optical microscopy and differential scanning calorimetry (DSC), finding an enhancement of the isotropic to nematic phase transition temperature and revealing a “*chimney – type*” phase diagram over a narrow range of CNT weight percent between 0.001 - 0.002 wt% [34]. However, other studies have found disordering effects of CNT on LC phase transitions [31]. Other work has shown improved electro-optical switching properties of nanocomposites in thermotropic or lyotropic liquid crystals and CNTs [35, 36, 37, 38, 39, 40]. In liquid

crystals, the effect of carbon nanotubes on the phase ordering of LC/CNT composites depends on the surface coupling of the molecule and graphene surface as well as the distribution of those surfaces. In fact, it is also observed that aligned CNTs can cause an increase of the orientational order in the LC [41]. Such composites have been proposed as memory devices by exploiting their nanoelectromechanical properties [42]. Recently, investigations on LC/CNT composites have shown that the CNTs can induce chirality in the bulk LC [43, 44, 45]. Most of these studies were focused on nematic ordering and the isotropic (I) to nematic (N) phase transition behavior in LC/CNT composites.

In this work, we study the phase transition behavior of the liquid crystal alkoxyphenylbenzoate (9OO4) doped with multiwall carbon nanotubes as a function of CNT weight percent. The incorporation of CNTs in 9OO4 reveals that all mesophase transition temperatures and the crystallization transition temperatures shift upward. This results suggest that the interactions between molecular structure, dipole moment of liquid crystal, and graphene-like surface can allow the random dispersion of CNTs to promote both orientational and positional order. We interpret this effect in terms of pinning the director at the CNT surface with bulk-like scalar order parallel to the CNT long axis over distances that span multiple nematic domains while allowing the LC molecule to slide along the surface, accommodating various positional order.

4.2 Results and Discussions

For the pure 9OO4, calorimetry shows that the I - N phase transition occurs at $T_{IN} = 86.23$ °C, the N - SmA phase transition at $T_{NA} = 71.49$ °C, the SmA - SmC phase transition at $T_{AC} = 61.5$ °C, the SmC - SmB phase transition at $T_{CB} = 49.38$ °C, and SmB - K phase transition at $T_{BK} = 35.3$ °C in good agreement with literature values [46]. All the phase transitions are characterized by a distinct C_p peaks at a nearly equilibrium scan rate of ± 0.3 K/min (Figures 2 to 6). The strongly first-order melting followed by a second first-order C_p feature indicates the presence of an intermediate phase (labeled SmX) between K and SmA on heating. The transition temperatures and enthalpies of pure 9OO4 on cooling and heating are presented in Tables 4.1 and 4.2

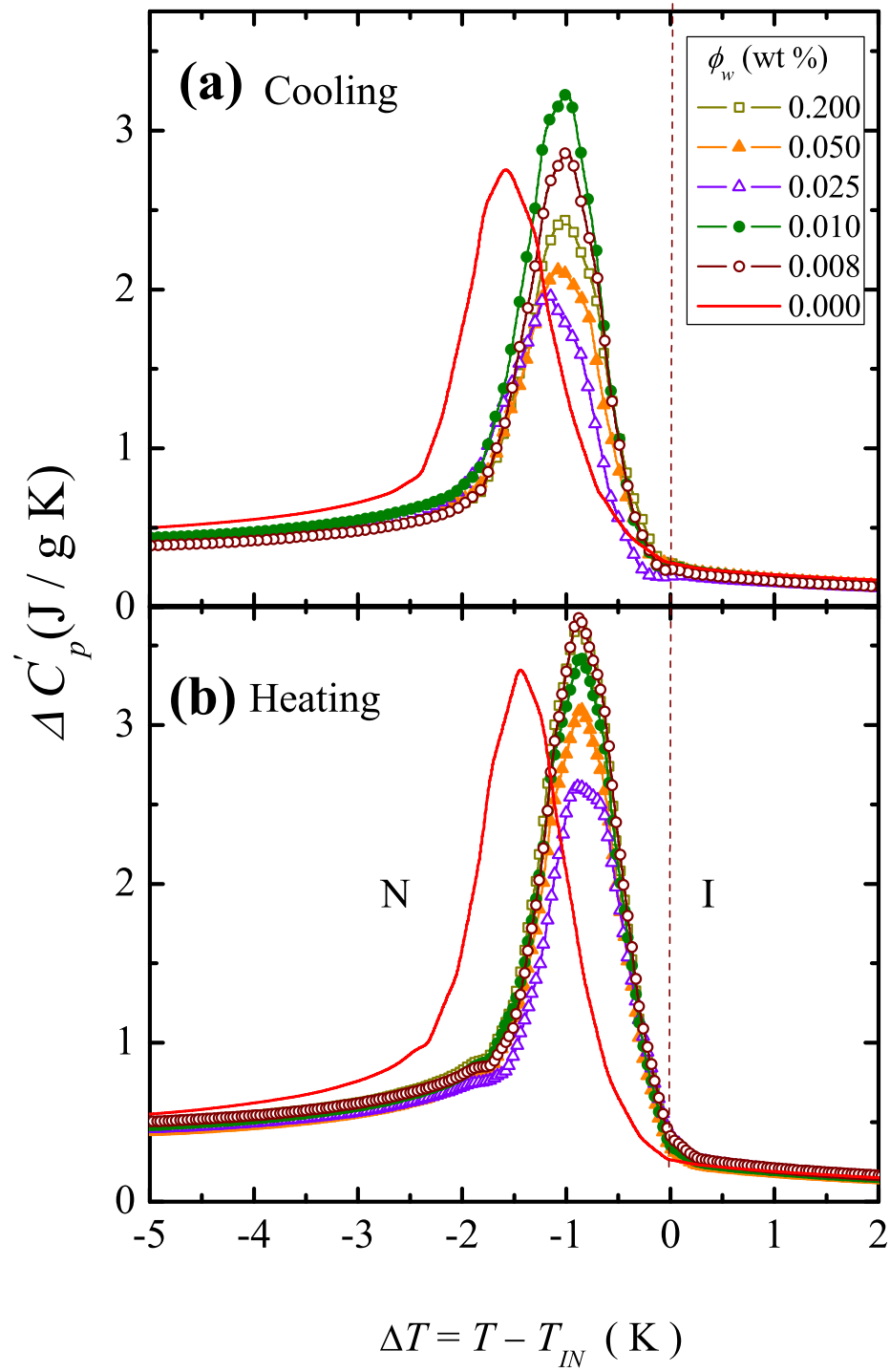


Figure 4.1. (a) Excess real specific heat ΔC_p associated with the I - N phase transition as function of temperature about T_{IN} on cooling. The definition of the symbols are given in the inset. (b) Excess specific heat ΔC_p associated with the I - N phase transition as function of temperature about T_{IN} on heating.

For the I - N phase transition, the excess real specific heat signatures as a function of temperature about T_{IN} for pure 9OO4 and 9OO4/CNT composite samples are shown in Figure 5.1. The $\Delta C'_p$ of 9OO4/CNT for the I - N transition phase is steeper and narrower than in the pure 9OO4, with the peak maximum nearer the high-temperature side of the coexistence region. The $\Delta C'_p$ and C''_p behavior are consistent on heating and cooling as well as being reproducible after multiple thermal cycles. The $\Delta C'_p$ wings above and below the I - N transition match each other and that in pure 9OO4 on heating and cooling. The $\Delta C'_p$ peak height for cooling and heating scans within the two-phase $I+N$ coexistence region is about the same as that in pure 9OO4 up to $\phi_w \simeq 0.010$, decreasing markedly for the 0.025 sample, then rising with increasing ϕ_w up to the highest CNT content sample of 0.20 wt% studied.

For the N -SmA phase transition, the excess specific heat $\delta C'_p$ on cooling and heating as a function of temperature about T_{NA} are shown in Figure 5.2 for pure 9OO4 and 9OO4/CNT composite samples. For all samples, the N -SmA phase transition does not exhibit any feature in the imaginary specific heat, indicating an apparent absence of latent heat and the continuous nature of this transition. The $\delta C'_p$ of the N -SmA transition for the 9OO4/CNT samples over lay each other for all ϕ_w and for pure 9OO4 on the SmA side while are systematically below pure 9OO4 on the nematic side of the transition. Given no strong change in the $\delta C'_p$ behavior as a function of ϕ_w , no power-law fits were attempted.

For the SmA-SmC phase transition, the excess specific $\delta C'_p$ as the function of temperature for pure 9OO4 and 9OO4/CNT composite samples are shown in Figure 4.3. The observed shape and continuous nature of the $\delta C'_p$ peak for pure 9OO4 is consistent with a Landau (mean-field) second-order transition [30] with no observed signature in C''_p . The $\delta C'_p(AC)$ for the 9OO4/CNT samples, heights are the same as pure 9OO4 up to 0.025 wt% and then decrease for the 0.05 and 0.20 wt% samples. The step in $\delta C'_p(AC)$ on the SmC-side for below T_{AC} is 0.025 J/gK for pure 9OO4 and all 9OO4/CNT samples, independent of ϕ_w .

The tilt susceptibility at the SmA-SmC transition was examined by measuring the electroclinic effect [47] in the LC/CNT mixtures. In the past, it has been shown that there is a nonzero enantiomeric excess for these CNTs, as well as a net chirality for CNTs from four other manufacturers [41]. When dissolved in a liquid crystal,

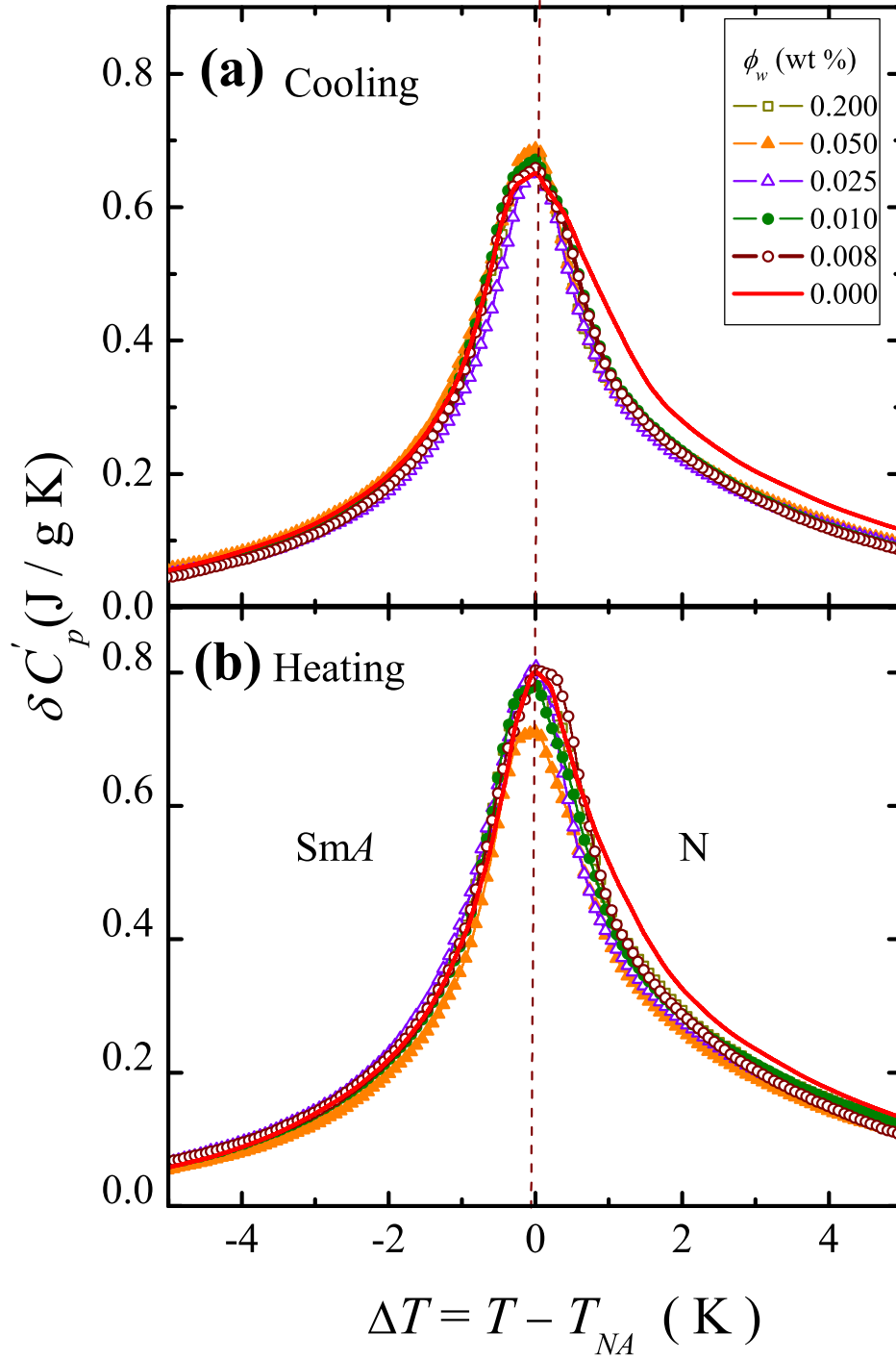


Figure 4.2. (a) Excess specific heat δC_p associated with the N -SmA phase transition as function of temperature about T_{NA} on cooling. The definition of the symbols are given in the inset. (b) Excess specific heat δC_p associated with the N -SmA phase transition as function of temperature about T_{NA} on heating.

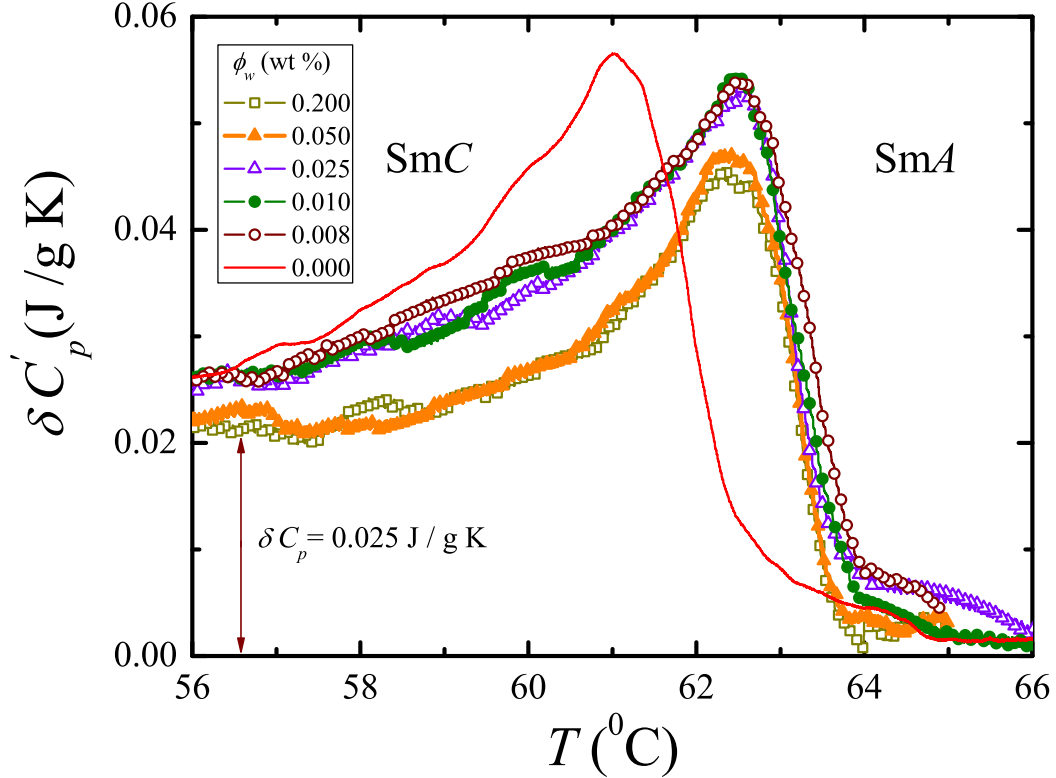


Figure 4.3. Excess real specific heat ΔC_p associated with the SmA-SmC phase transition as function of temperature about T_{AC} on cooling for different CNT content sample. The definition of the symbols are given in the inset.

the CNT imparts a net chiral environment to the liquid crystal in the vicinity of the CNT surface. On application of an electric field, a surface electroclinic effect obtains, which requires the presence of a chiral symmetry environment and in which the director rotates by an angle $\theta \propto E$. Because of the sufficiently high concentration of CNTs, the polarized light “sees” an average rotation of the liquid crystal director for the entire sample.

The inverse electroclinic coefficient e_c^{-1} is shown as a function of temperature for the 0.05 wt% 9004/CNT sample in Figure 4.4 approaching the SmC phase from the SmA. A three parameter amplitude, T_{AC} , and susceptibility exponent γ power-law fit of e_c^{-1} versus temperature resulted in $\gamma = 0.99 \pm 0.06$. Despite the localization of the chirality induced in the liquid crystal to within a few nanometers of the CNT surface [48], the susceptibility exponent clearly is mean-field-like and apparently unaffected by the presence of the nanotubes. This result suggests that

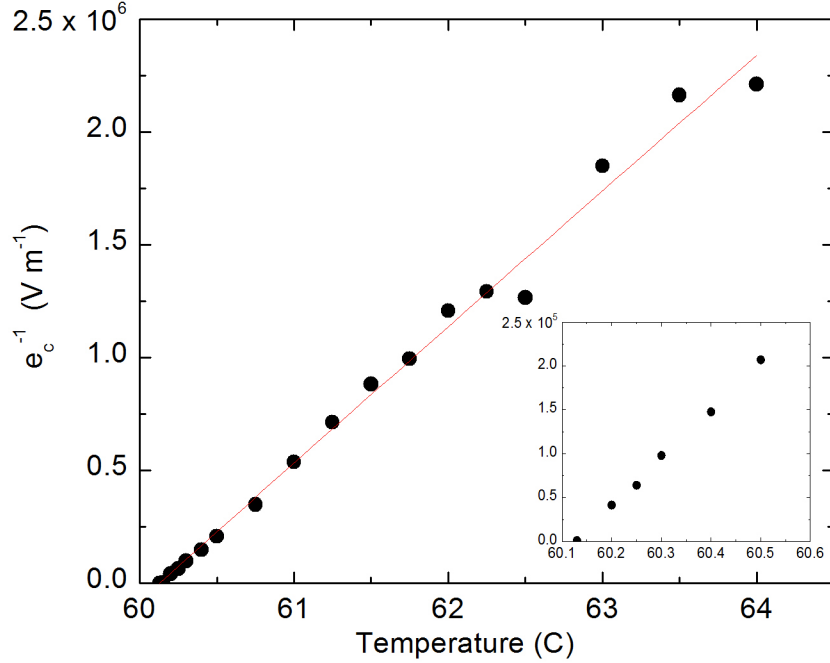


Figure 4.4. The inverse electroclinic coefficient e_c^{-1} is shown as a function of temperature for an applied electric field at frequency 25 Hz across the cell containing a 0.05 wt% 9004/CNT sample. The results were fitted a 3-parameter power law and resulted in a susceptibility exponent $\gamma = 0.99 \pm 0.06$. Inset shows an expanded view of the inverse electroclinic coefficient for low temperature range.

the director rotation extends a length scale ξ , comparable to the SmC correlation length, into the bulk liquid crystal from the narrow chiral region immediately surrounding the CNTs, which is the region that responds directly to the applied field. As an aside, we note that although T_{AC} was obtained for this concentration of nanotubes, it is not possible to compare it with the transition temperature in the absence of nanotubes, for which chirality would be absent and no electroclinic effect would be present.

For the SmC-SmB-K phase transition sequence on cooling, the $\Delta C'_p$ and C''_p signatures for pure 9004 and 9004/CNT composite samples over a range from +4 to -10 K about T_{CB} are shown in Figure 4.5. All peak signatures remain sharp while the peak height of the SmC-SmB phase transition decreases with increasing ϕ_w . The SmC-SmB transition is marked by a strongly first-order specific heat

signature at $T_{CB} = 49.38$ °C, with the imaginary part being much larger than the real part. The total transition enthalpy ΔH_{CB} decreases slightly while ΔH_{BK} increases slightly with increasing ϕ_w . Similarly, the imaginary part is much larger than the nearly non-existent $\Delta C'_p$ for the SmB-K transition. This is consistent with both the SmC-SmB and SmB-K phase transitions being strongly first-order, as expected. Note that the C''_p behavior observed in the SmB phase are due to a very slow phase conversion to the SmB from the SmC.

For all samples, upon heating under continuous quasi-equilibrium conditions, the crystal phase superheats slightly until a strongly first-order specific heat feature is observed. Upon further heating, a second first-order feature is seen before the SmA phase appears. See Figure 4.6 for pure 9OO4 and 9OO4/CNT composite samples over a range from -10 to +4 K about T_{XA} . The K-SmX ΔC_p peak is narrower for composite samples, except for the $\phi_w = 0.025$ wt% sample, as compared to the pure 9OO4. The melting $\Delta C'_p$ peak generally decreases in amplitude with an increase in the C''_p peak. The total transition enthalpy of $\Delta H_{KX} \simeq 72$ J/g for pure 9OO4 decreases slightly for the 9OO4/CNT samples with increasing ϕ_w . The $\Delta H_{XA} \simeq 32$ J/g and strongly decreases with ϕ_w . Interestingly, the second feature specific heat peak height decreases with increasing ϕ_w and suggests that this feature is not due to residual crystal melting. Because of the magnitude of the enthalpy involved, it is possible that this feature is a transition into an intermediate smectic phase before heating into the SmA phase. We denote this phase as SmX and are unclear from polarizing microscopy image as to whether this phase is SmB or SmC-like since the melting occurs very near T_{AC} on cooling.

While the calorimetric and electroclinic behavior of the phases and phase transitions for the 9OO4/CNT samples are clearly retaining the character found in pure 9OO4, the phase boundaries have more shrinking changes due to the CNT. The transition temperature changes from pure 9OO4 for all 9OO4/CNT samples are shown in Figure 5.7. On cooling, the I - N transition temperature in the 9OO4/CNT samples shift upward by nearly a constant +1.13 K compared to that in pure 9OO4 while the two-phase $I+N$ coexistence width shrink from ~ 2.5 K in pure 9OO4 to a constant ~ 1.5 K in 9OO4/CNT over this range of ϕ_w . For the N-SmA transition temperature in 9OO4/CNT shifts upward by +1.31 K compared to pure 9OO4, shrinking the nematic temperature range $\Delta T_{nem} = T_{IN} - T_{NA}$ by

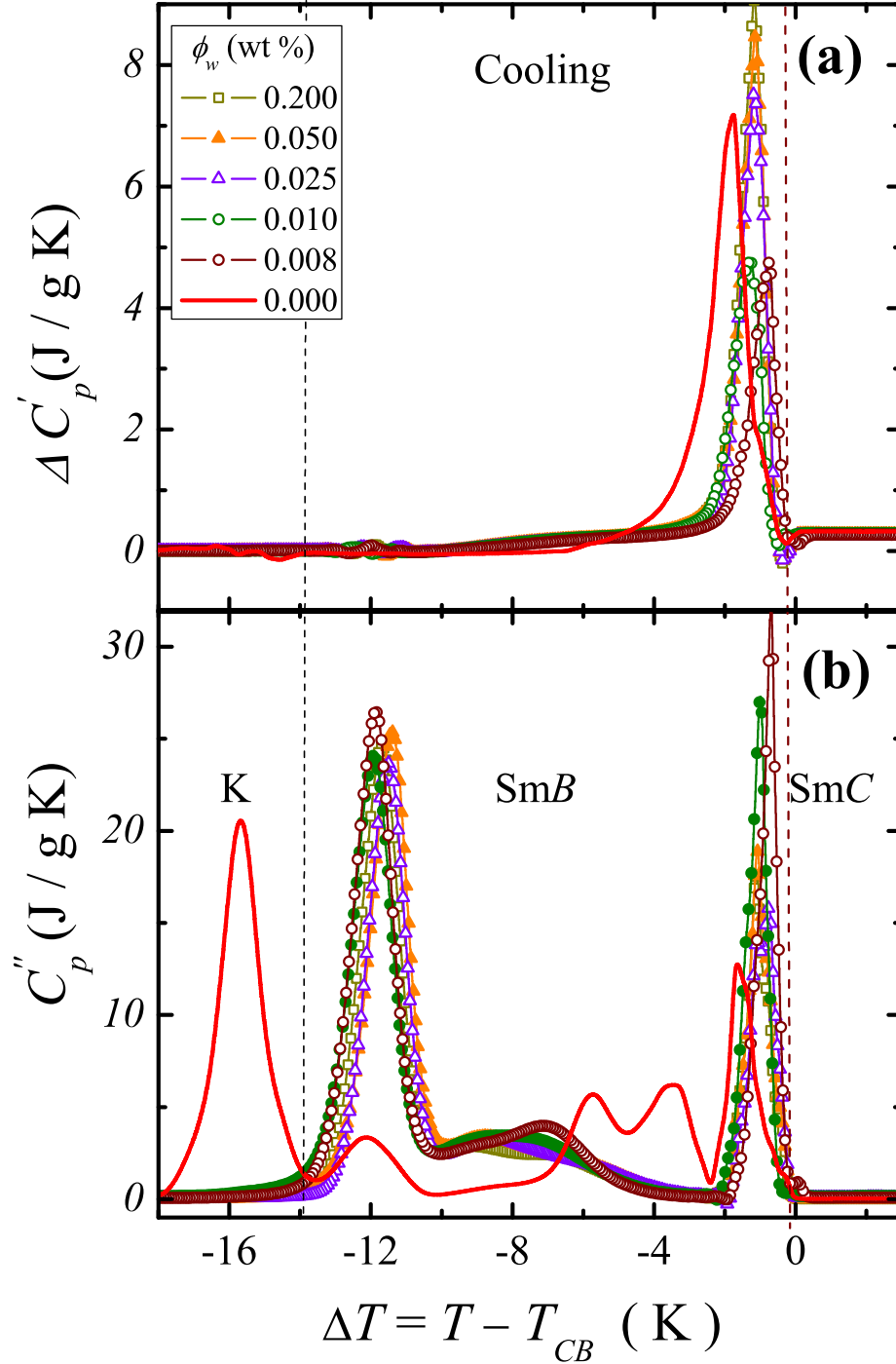


Figure 4.5. (a) Excess real and imaginary specific heat ΔC_p associated with the SmC-SmB phase transition as function of temperature about T_{CB} on cooling. The definition of the symbols are given in the inset. (b) Imaginary specific heat C''_p as function of temperature about T_{CB} on cooling.

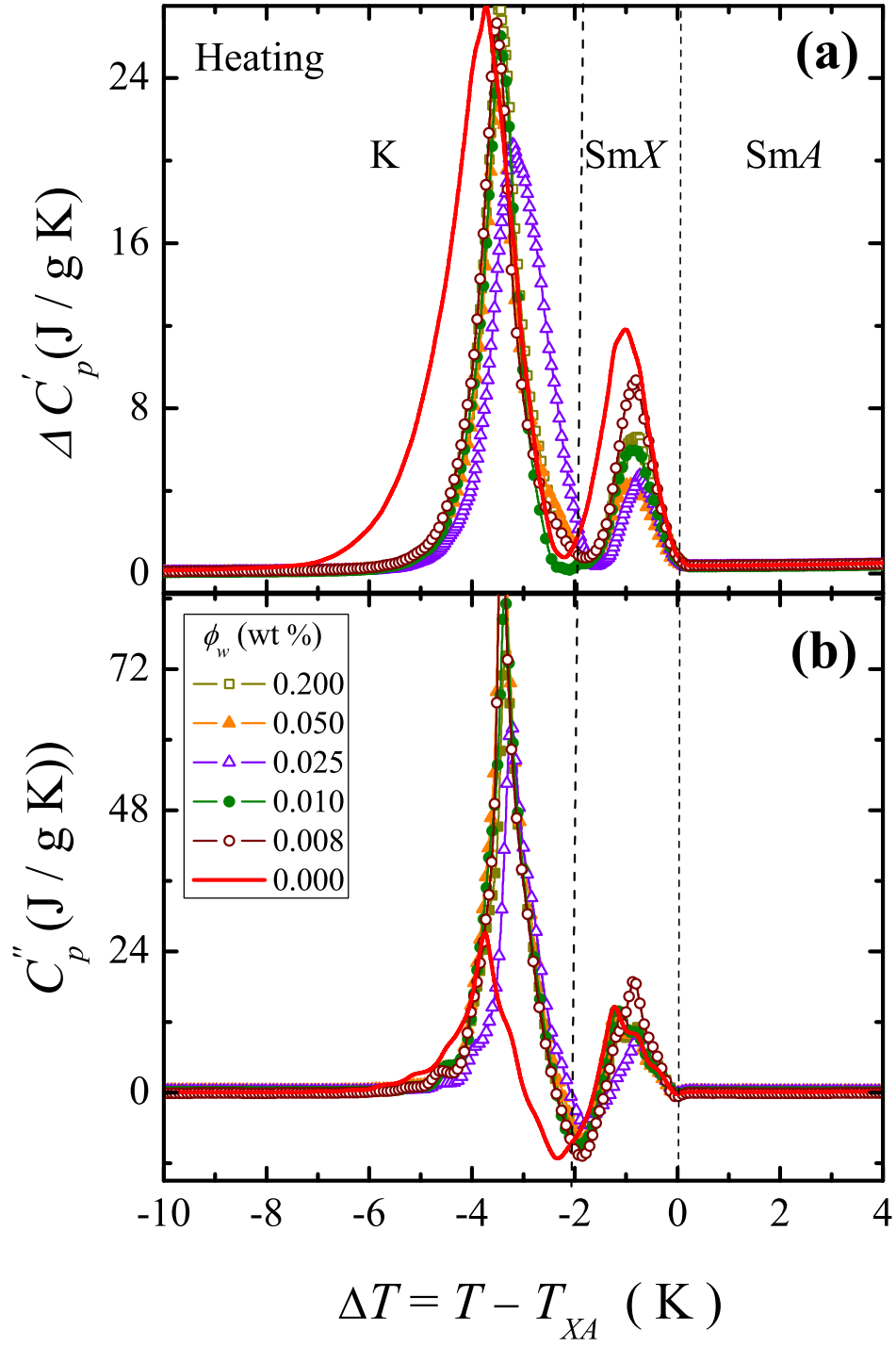


Figure 4.6. (a) Excess real and imaginary specific heat ΔC_p associated with the K - SmX - SmC phase transition as function of temperature about T_{XA} on heating. The definition of the symbols are given in the inset. (b) Imaginary specific heat C''_p as function of temperature about T_{XA} on heating.

Table 4.1. Summary of the calorimetric results for pure and all 9004/CNT samples on cooling and heating. Shown are CNT weight percent ϕ_{CNT} , I - N transition temperature T_{IN} , N - SmA transition temperature T_{NA} , K - SmX transition temperature T_{KX} , SmX - SmA transition temperature T_{XA} , SmA - SmC transition temperature T_{AC} , SmC - SmB transition temperature T_{CB} , SmB - K transition temperature T_{BK} (in Celsius).

ϕ_{CNT}	T_{IN}	T_{NA}	T_{AC}	T_{CB}	T_{BK}
0.000	86.24 ± 0.20	71.27 ± 0.12	61.50 ± 0.00	49.38 ± 0.02	35.00 ± 0.02
0.008	87.31 ± 0.22	72.68 ± 0.13	62.56 ± 0.02	50.33 ± 0.03	39.16 ± 0.03
0.010	87.37 ± 0.18	72.69 ± 0.11	62.50 ± 0.02	50.26 ± 0.02	39.34 ± 0.02
0.025	87.37 ± 0.21	72.2 ± 0.14	62.50 ± 0.01	50.26 ± 0.03	39.34 ± 0.04
0.050	86.93 ± 0.22	72.5 ± 0.12	62.28 ± 0.02	50.17 ± 0.04	39.85 ± 0.02
0.200	86.93 ± 0.23	72.5 ± 0.15	62.36 ± 0.02	50.13 ± 0.04	39.56 ± 0.01
ϕ_{CNT}	T_{KX}	T_{XA}	T_{NA}	T_{IN}	
0.000	60.96 ± 0.13	63.55 ± 0.01	71.46 ± 0.12	86.48 ± 0.22	
0.008	61.36 ± 0.12	64.06 ± 0.02	72.62 ± 0.13	87.31 ± 0.21	
0.010	61.45 ± 0.14	64.06 ± 0.02	72.85 ± 0.11	87.63 ± 0.19	
0.025	61.45 ± 0.14	64.34 ± 0.03	72.65 ± 0.14	87.09 ± 0.23	
0.050	61.42 ± 0.12	64.06 ± 0.03	72.53 ± 0.12	87.39 ± 0.25	
0.200	61.37 ± 0.13	64.06 ± 0.01	72.57 ± 0.15	87.32 ± 0.22	

~ 0.3 K for all ϕ_w . The SmA - SmC transition temperature in 9004/CNT shifts upward by about +1 K, widening the SmA range by +0.4 K for all ϕ_w . The SmC - SmB transition temperature shifts upward by +0.7 K, widening the SmC range slightly for all ϕ_w studied. Finally on cooling, the SmB - K crystallization shifted upward by the largest, +4 K for all ϕ_w , narrowing the SmB range by 3 K. On heating, the K - SmX melting superheats an additional +0.4 K, similarly for the SmX - SmA boundary compared to pure 9004 for all ϕ_w samples. The T_{NA} on heating is +1.2 K and the T_{IN} is +0.8 K higher than in pure 9004, narrowing the nematic range ΔT_{nem} by 0.4 K, similar to that seen on cooling.

It is useful to compare these results with another high-resolution phase transition study on 8CB/CNT nanocomposites, which also used near equilibrium calorimetric conditions and identical mixing method of CNTs from the same source [31]. The 8CB is a typical rod-like molecule, with biphenyl core, to which are attached an aliphatic tail and a polar cyano head group, whereas 9004 has a benzoate group linking the two phenyl rings and having alkoxy end tails. See Figure 2.7.

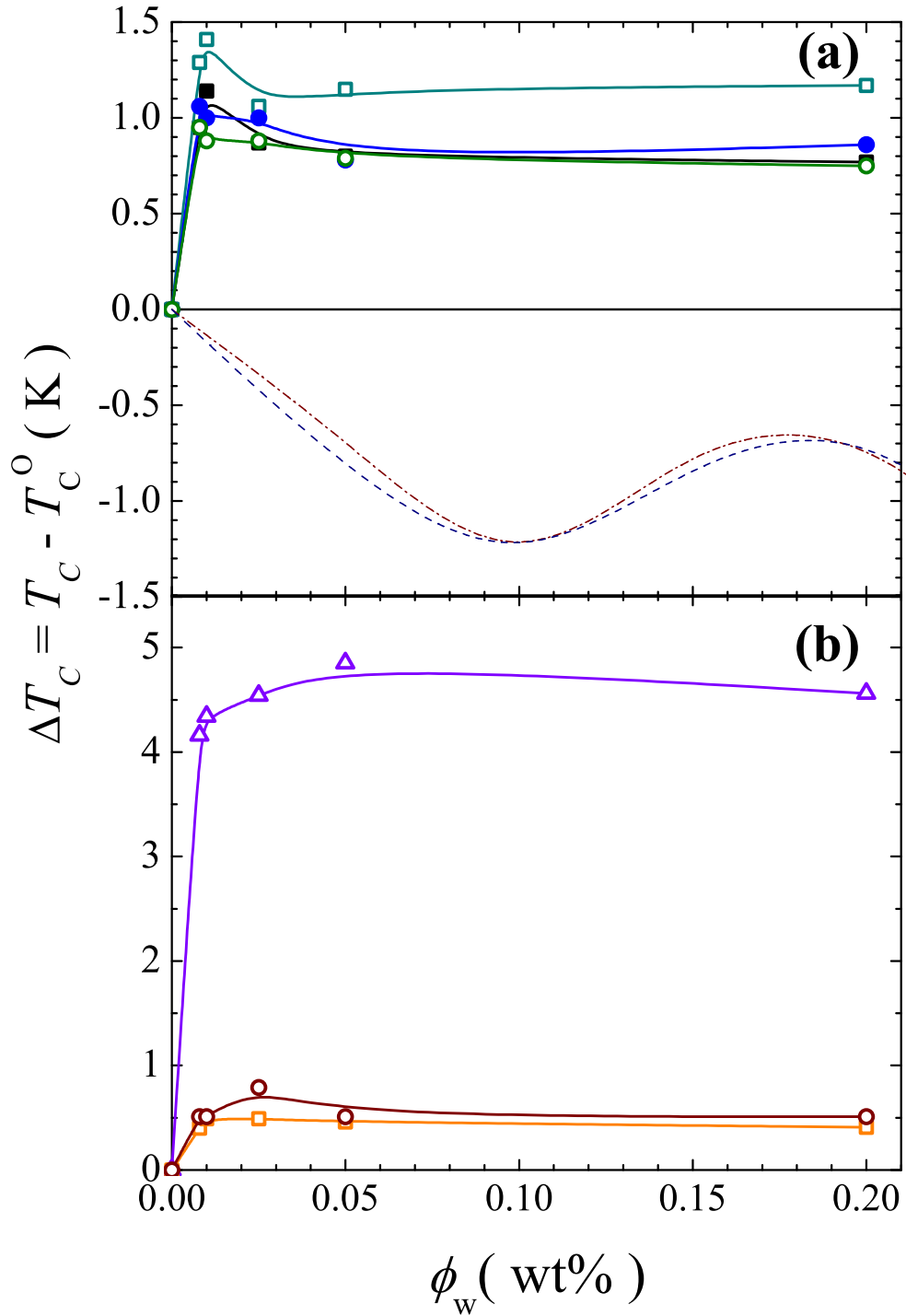


Figure 4.7. (a) The phase transition temperature shifts for the $I-N$ (■), $N-SmA$ (□), $SmA-SmC$ (●), and $SmC-SmB$ (○) in 90O4/CNT samples and the $I-N$ and $N-SmA$ transition temperature shift for 8CB/CNT [31] (---) as a function of ϕ_w . (b) The phase transition temperature shifts of the $SmB-K$ (Δ), $K-SmX$ (□) and $SmX-SmA$ (○) for the 90O4/CNT samples as a function of ϕ_w .

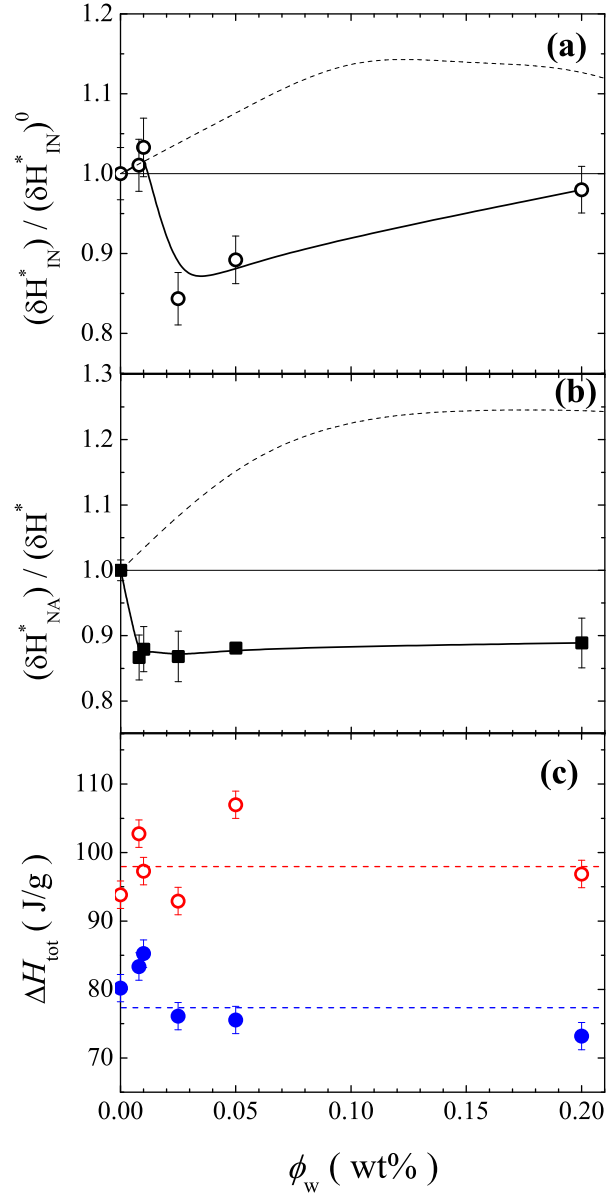


Figure 4.8. (a) The $I-N$ average fractional effective transition enthalpy for 90O4 (\circ) and 8CB (---) with the function of ϕ_w . (b) The $N-SmA$ average fractional effective transition enthalpy for 90O4 (\circ) and 8CB (---) with the function of ϕ_w . (c) The effective total transition enthalpy on heating for 90O4 (\circ) and the effective total transition enthalpy on cooling for 90O4 (\bullet) with the function of ϕ_w .

Table 4.2. Summary of the calorimetric results for pure and all 9004/CNT samples on cooling and heating. Shown are CNT weight percent ϕ_{CNT} , integrated enthalpy change for I - N transition δH_{IN}^* , imaginary enthalpy $\delta H_{IN}''$, integrated enthalpy change for N -SmA transition δH_{NA}^* , integrated enthalpy change for K -SmX transition δH_{KX}^T , integrated enthalpy change for SmX-SmA transition δH_{XA}^T , integrated enthalpy change for SmC- B transition δH_{CB}^T , integrated enthalpy change for SmB- K transition δH_{BK}^T (in J/g).

ϕ_{CNT}	δH_{IN}^*	$\delta H_{IN}''$	δH_{NA}^*	δH_{CB}^T	δH_{BK}^T	ΔH_T
0.000	3.9 ± 0.4	0.95 ± 0.03	3.10 ± 0.05	35.88 ± 0.06	33.28 ± 0.05	80.2 ± 0.55
0.008	3.8 ± 0.2	0.99 ± 0.04	2.59 ± 0.06	38.92 ± 0.05	40.98 ± 0.07	84.09 ± 0.42
0.010	4.3 ± 0.4	0.96 ± 0.02	2.63 ± 0.07	39.73 ± 0.04	39.15 ± 0.05	84.38 ± 0.62
0.025	3.2 ± 0.3	0.69 ± 0.03	2.55 ± 0.08	29.14 ± 0.08	33.60 ± 0.08	70.11 ± 0.55
0.050	3.4 ± 0.2	1.01 ± 0.04	2.75 ± 0.09	31.20 ± 0.06	39.22 ± 0.08	72.40 ± 0.38
0.200	3.6 ± 0.3	1.03 ± 0.03	2.68 ± 0.08	27.37 ± 0.09	39.56 ± 0.11	69.98 ± 0.45
ϕ_{CNT}	δH_{KX}^T	δH_{XA}^T	δH_{NA}^*	δH_{IN}^*	$\delta H_{IN}''$	ΔH_T
0.000	72.00 ± 0.16	32.00 ± 0.06	3.02 ± 0.06	4.9 ± 0.3	0.98 ± 0.02	83.47 ± 0.32
0.008	69.16 ± 0.15	17.12 ± 0.04	2.87 ± 0.08	5.1 ± 0.2	0.90 ± 0.04	84.52 ± 0.40
0.010	67.44 ± 0.12	13.59 ± 0.03	2.91 ± 0.08	4.8 ± 0.4	0.99 ± 0.02	84.93 ± 0.54
0.025	67.76 ± 0.06	10.47 ± 0.04	2.92 ± 0.07	4.2 ± 0.3	1.04 ± 0.02	75.03 ± 0.48
0.050	61.93 ± 0.08	10.26 ± 0.02	2.80 ± 0.06	4.4 ± 0.2	0.90 ± 0.03	85.32 ± 0.62
0.200	62.00 ± 0.08	12.70 ± 0.06	2.92 ± 0.09	5.0 ± 0.3	0.93 ± 0.03	86.53 ± 0.64

The transition temperatures and enthalpies of the isotropic to nematic and nematic to smectic- A phase transitions in 9004/CNT and 8CB/CNT systems [31] are shown in Figure 5.7 and Figure 5.5. In the 8CB/CNT system, both transition temperatures shift downward by ~ 1.5 K and has significant and non-linear ϕ_w dependence, while ΔT_{nem} remains constant as seen by the dashed and dash-dotted lines in panel (a) of Figure 5.7. Clearly, the same surface and distribution of CNTs for 8CB produce disordering effects on orientational order shifting both the I-N and N-SmA transitions.

The transition enthalpies of the I - N and N -SmA phase transitions in the 8CB/CNT system increases over a broad range of ϕ_w and then remain constant for higher ϕ_w . The total transition enthalpy of 8CB/CNT system has been interpreted as the sum of the pure transition contribution and a random-field induced distortion energy. Apparently, given the near constant decrease of the enthalpy of the 9004/CNT, the ordering is bulk-like with a reduction perhaps due to suppression of long-wavelength director fluctuations. If the enthalpy suppression of the I - N

and N -SmA in 9OO4/CNT were due to surface pinning, it should scale with CNT surface area, approximately linear in ϕ_w for these low concentrations, which is not observed. This suggests a different surface interaction for the 9OO4 than 8CB molecule with the CNT. The electroclinic effect result suggests that the director rotation θ extends a length scale ξ , comparable to the SmC correlation length, into the bulk liquid crystal forming a chiral region immediately surrounding the CNTs. This chiral region responds to the applied field, resulting in a tilt over the entire SmC correlation region. On cooling, the 9OO4/CNT SmB-K phase transition temperature increases 4 K and K-SmX phase transition temperature increases 0.5 K on heating for all ϕ_w while the total transition enthalpy remains constant on heating and cooling. See Figure 5.7 and Figure 5.5. It is important to note that all experimental results presented here are reproducible over repeated scans.

From the calorimetric observations presented here, the effect of CNTs on the phase transitions of 9OO4 apparently enhances orientational order and is compatible with various positional order of all the higher order phases (broken symmetries) up to and including the crystal phase. This is despite the globally random dispersion of CNTs in these nanocomposites and in contrast to the disordering effects observed in the 8CB/CNT system [31]. Clearly, at such low concentrations with random CNT distribution, the specific CNT- LC boundary condition must play an important role along with the ultra-high aspect ratio (string-like structure) of the CNT nanoparticles.

To account for the opposing the behavior of the I - N transition between 9OO4/CNT and 8CB/CNT given the similar chemical nature of both liquid crystals and common graphene surface, the CNT may promote nematic order in both liquid crystals but with different correlation lengths of the local anchoring field. For 8CB/CNT system, the nucleated local director for 8CB varies in orientation along the long-axis of the CNT creating a surface para-nematic layer while further away from the CNT surface, \hat{n} becomes aligned parallel to the CNT strands [31]. This would mean that the local anchoring field direction varies along the CNT strands over a distance comparable to or shorter than the \hat{n} correlation length leading to quenched random-field disordering effects [33]. For 9OO4/CNT system, the surface anchoring orientation correlation length must be larger than the \hat{n} correlation length of

the LC, likely parallel to the CNT long-axis with essentially no distortion (elastic strain) of \hat{n} further away from the strand surface. This would yield a quenched locally-non-random field that spans more than one nematic domain while still possessing a global (macroscopic) random distribution. This is consistent with the observed ECE in 9OO4/CNT and not in 8CB/CNT [43, 45], which would also account for the suppression of smectic order in the 8CB/CNT system as the pinned surface para-nematic layer would further disorder any positional ordering. In 9OO4/CNT, the local field spans multiple nematic domains and would actually suppress director fluctuations and so promote smectic ordering.

However, the observed enhancement of the higher order smectic phases as well as the crystal phase implies that the uniform surface orientational anchoring is not accompanied by positional pinning along the CNT for the 9OO4 molecule. This degree of freedom of the LC molecule to essentially slide along the surface and each other parallel to the CNT long-axis is needed to accommodate all the higher positional ordering (broken symmetries) in pure 9OO4 yielding the observed bulk-like behavior and phase boundary enhancement in this work. The origin of these two different behavior between 9OO4 and 8CB with CNT is not immediately known but may be due to either the negative dielectric anisotropy of 9OO4 as opposed to that in 8CB or the different commensurate surface packing of the phenyl rings onto the graphene surface by these two LCs

Bibliography

- [1] S. Iijima, *Nature.*, **354**, 56 (1991).
- [2] E. T. Thostenson, Z. F. Ren, and T. W. Chou, *Compos. Sci. Technol.*, **61**, 1899 (2001).
- [3] J. N. Coleman, U. Khan, and Y. K. Gunko, *Adv. Matter*, **18**, 689 (2006).
- [4] J. N. Coleman, U. Khan, W. J. Blau, and Y. K. Gunko, *Carbon*, **44**, 1624 (2006).
- [5] F. H. Gojny, M. H. G. Wichmann, B. Fiedler, I. A. Kinloch, W. Bauhofer, A. H. Windle, and K. Schulte, *Polymer*, **47**, 2036 (2006).
- [6] Z. Qunaies, C. Park, K. E. Wise, E. J. Siochi, and J. S. Harrison, *Compos. Sci. Technol.*, **63**, 1637 (2003).
- [7] R. Haggemueller, C. Guthy, J. R. Lukes, J. E. Fischer, and K. I. Winey, *Macromolecules*, **40**, 2417 (2007).
- [8] A. R. Bhattacharyya, T. V. Sreekumar, T. Liu, S. Kumar, L. M. Ericson, R. H. Hauge, and R. E. Smalley, *Polymer*, **44**, 2373 (2003).
- [9] E. Assouline, A. Lustiger, A. H. Barber, C. A. Cooper, E. Klein, E. Wachtel, and H. D. Wagner, *J. Polym. Sci., Part B: Polym. Phys.*, **41**, 520 (2003).
- [10] J. K. W. Sandler, S. Pegel, M. Cadek, F. H. Gojny, M. V. Es, J. Lohmar, W. J. Blau, K. Schulte, A. H. Windle, and M. S. P. Shaner, *Polymer*, **45**, 2001 (2004).

- [11] P. Potechke, T. D. Fornes, and D. R. Paul, *Polymer*, **43**, 3247 (2002).
- [12] S. B. Kharchenko, J. F. Douglas, J. Obrzut, E. A. Grulke, and K. B. Migler, *Nat. Matter*, **3**, 564 (2004).
- [13] P. Poncharal, Z. L. Wang, D. Ugarate, and W. A. de Heer, *Science*, **283**, 1513 (1999).
- [14] L. Wang and Z. M. Dang, *Appl. Phys. Lett.*, **87**, 042903 (2005).
- [15] Y. Xu, Y. Zhang, and E. Suhir, *J. Appl. Phys.*, **100**, 074302 (2006).
- [16] G. L. Zhao, D. Bagayoko, , and L. Yang, *J. Appl. Phys.*, **99**, 114311 (2006).
- [17] S. Sinha, S. Barjami, G. Iannacchione, A. Schwab, and G. Muench, *J. Nanopart. Res.*, **7**, 651 (2005).
- [18] O. Stephan, D. Taverna, M. Kociak, K. Suenaga, L. Henrard, and C. Colliex, *Phys. Rev. B.*, **66**, 155422 (2002).
- [19] A. Madarhri, G. Pecastings, F. Carmona, and M. E. Achour, *J. Microwave Optoelect.*, **6**, 36 (2007).
- [20] Y. Sato, M. Terauchi, Y. Saito, and R. Saito, *J. Electron Microsc.*, **55**, 137 (2006).
- [21] P. Ptschke, S. M. Dudkin, and I. Alig, *Appl. Phys. Lett.*, **89**, 5023 (2003).
- [22] K. Ahmad, W. Pan, and S. L. Shi, *Polymer*, **55**, 133122 (2006).
- [23] R. H. Baughman, A. A. Zakhidov, and W. A. de Heer, *Science*, **297**, 787 (2002).
- [24] P. G. Collins and P. Avouris, *Sci. Am.*, **283**, 38 (2000).
- [25] A. Javey, Q. Wang, A. Urai, Y. Li, and H. Dai, *Nano Lett.*, **2**, 929 (2002).
- [26] R. Martel, T. Schmidt, H. R. Shea, T. Hertel, and P. Avouris, *Appl. Phys. Lett.*, **73**, 2447 (1998).
- [27] J. W. Goodby, Waugh, S. M. Stein, and E. Chin, *Nature*, **337**, 449 (1989).

- [28] S. Chandrashekar, *Liquid Crystals* (Cambridge University Press, England) (1992).
- [29] D. Demus, J. W. Goodby, G. Gray, H. Spiess, and V. Vill, eds., *Handbook of Liquid Crystals* (Wiley-VCH, Canada) (1998).
- [30] P. G. de Gennes and J. Prost, *The Physics of Liquid Crystals* (Oxford University Press, Clarendon, Oxford, England) (1993).
- [31] K. P. Sigdel and G. S. Iannacchione, *Euro. Phys. J.E.*, **34**, 11034 (2011).
- [32] G. S. Iannacchione, S. Park, C. W. Garland, R. J. Birgeneau, and R. L. Leheny, *Phys. Rev. E*, **67**, 011709 (2003).
- [33] G. S. Iannacchione, *Fluid Phase Equilibria.*, **222/223**, 177 (2004).
- [34] H. Duran, B. Gazdecki, A. Yamashita, and T. Kyu, *Liq. Cryst.*, **32**, 815 (2005).
- [35] A. M. Somoza, C. Sagui, and C. Roland, *Phys. Rev. B.*, **63**, 081403(R) (2001).
- [36] W. Song, I. A. Kinloch, and A. H. Windle, *Science*, **303**, 1363 (2003).
- [37] W. Song and A. H. Windle, *Macromolecules*, **38**, 6181 (2005).
- [38] S. Zhang and S. Kumar, *Small*, **4**, 1270 (2008).
- [39] H. Y. Chen, W. Lee, and N. A. Clark, *App. Phys. Lett.*, **90**, 033510 (2007).
- [40] H. Y. Chen and W. Lee, *Opt. Rev.*, **12**, 223 (2005).
- [41] R. Basu and G. Iannacchione, *Phys. Rev. E.*, **81**, 051705 (2010).
- [42] R. Basu and G. Iannacchione, *J. Appl. Phys.*, **106**, 124312 (2009).
- [43] R. Basu, J. S. Pendery, . R. G. Petschek, R. P. Lemieux, and C. Rosenblatt, *Phys. Rev. Lett.*, **104**, 237804 (2011).
- [44] R. Basu, C. Rosenblatt, and R. P. Lemieux, *Liq Cryst.*, **39**, 199 (2012).
- [45] R. Basu, C. L. Chen, and C. Rosenblatt, *J. Appl. Phys.*, **109**, 083518 (2011).

- [46] P. Kalakonda and G. Iannacchione, *Liq. Cryst.*, submitted (2013).
- [47] S. Garoff and R. B. Meyer, *Phys. Rev. Lett.*, **38**, 848 (1977).
- [48] R. Berardi, H. G. Kuball, R. Memmer, and C. Zannon, *J. Chem. Soc., Faraday Trans.*, **94**, 1229 (1998).

Calorimetric Study of Phase transitions in Nanocomposites of Quantum Dots and a Liquid Crystal

5.1 Introduction

Composites of nano-particles with complex fluids represent a unique physical system where properties of the components only partially mix and new behavior can emerge. Traditional composites are relatively well understood as the superposition, weighted by volume or mass, of the component's properties and the interfacial interactions that play a role in holding the composite together. As the quantum dots added enough to the complex fluids, the surface area begins to dominate, leading to unique behavior of the nanocomposites. The richness of the nanocomposites that can be designed by coupling various colloids and liquid crystalline materials opens wide field of research. Quantum dots (QDs) and liquid crystals (LC) are good examples of such components.

Controlled self-assembly of semiconductor quantum dots (QDs) holds great promise for numerous applications, such as next generation photonic devices, QD displays, biomedical imaging [1, 2, 3, 4, 5, 6, 7, 8, 9]. Recently, it has been demonstrated that nanomaterials such as nanotubes or nanorods can be organized by nematic liquid crystals LCs [10, 11]. In this case, the anisotropic order of the LC imparts order onto the nanosize guest particles, along the nematic director average

orientational direction of the LC molecules, for example, due to the reduction in excluded volume [12]. Because the director can be aligned by external electric fields, the nanoscale assemblies of the QDs in the LC can be manipulated. Recent research shows that smectic LC environment allows QDs to achieve high spatial ordering into quasi-one-dimensional arrays along the director [13]. Understanding the interaction of nanoparticles with LC and the principles governing their assembly through LC mediated.

Liquid crystals LCs [14, 15] are anisotropic fluids that have numerous thermodynamically stable phases exhibiting molecular order in between an isotropic liquid and a three dimensionally ordered solid. It has been shown that to minimize elastic distortions in the LC, micrometer size spherical particles tends to be distributed into cylindrically symmetric chain or strands along the global nematic director, which is essential a minimization of excluded volume [12]. However, it is not clear how this analysis would change or remain valid as the spherical particles diameter is reduced to nanometer scales, such as QDs. The direct first-order transition from the isotropic (*I*) to the smectic-*A* (*SmA*) phase has attracted attention in experimental [16, 17, 18, 19, 20, 21, 22, 23, 24] and theoretical research [25, 26, 27, 28] as a prototypical symmetry breaking phase transition. High-resolution synchrotron X-ray diffraction study of the *I-SmA* phase transition in 10CB-aerosil showed that the transition remains first order for all gel densities with systematic evolution of correlation length [21]. The study of phase transition behavior of 10CB in the presence of silica aerogels showed that the direct *I-SmA* transition occurs through the nucleation of smectic domains [20]. The effect of pressure on the *I-SmA* phase transition was examined and pointed out that the effect is to increase the transition temperature and to decrease the discontinuity of the transition [27]. The macroscopic dynamic behavior was studied in vicinity of the *I-SmA* transition and the dynamic equations were presented on the *I* and *SmA* side of the phase transition incorporating the effect of an external electric field [28]. The existence of surface induced order was shown in the isotropic phase of 12CB, which has the direct *I-SmA* transition, confined to anapore membranes through specific heat and x-ray scattering studies [16]. Recently, the research has been focused on understanding of the self assembly, structures of various shapes of nanoparticles and shape tuning in nematic liquid crystals [29, 30, 31]. All the observations showed that the *I-SmA*

transition is more first-order than the very weak I - N transition indicating that the orientational order of SmA phase is higher than that in the nematic phase. Even though significant effort was applied for the study of the I -SmA transition behavior, many problems related to fundamentals of the transition are yet to be solved.

In this work, we study the phase transition behavior of the liquid crystal 4-cyano-4-octylbiphenyl, 8CB, doped with cadmium sulfate quantum dots as a function of QDs concentration. The incorporation of QDs in 8CB reveals that mesophase transition temperatures shift downward. This results suggest that the interactions between molecular structure, dipole moment of liquid crystal, and quantum dots can allow random dispersion of QDs to both surface and disorder effects despite being randomly dispersed and without any external field.

5.2 Results and Discussions

5.2.1 Overview

For the pure 8CB used in this study, the I - N phase transition occurs at $T_{IN} = 313.91$ K while the N -SmA transition occurs at $T_{NA} = 307$ K, agreeing well with the values reported in the literature [32]. The I - N effective transition enthalpy $\delta H_{IN}^* = 6.05 \pm 0.15$ J/g, the N -SmA effective transition enthalpy $\delta H_{NA}^* = 0.68 \pm 0.03$ J/g and the I - N dispersive enthalpy $\delta H_{IN}'' = 1.33 \pm 0.05$ J/g in pure 8CB are within uncertainties 8 % of the literature value [33]. These results are used for comparison to the composite results.

The resulting real part of specific heat C'_p data for 8CB/QD samples studied on heating and cooling as a function of temperature are shown Figure 2.2 (a). The C'_p wings are similar for all 8CB/QD composite samples and pure 8CB below and above the transition revealing that the bulk-like order fluctuations are in isotropic, nematic and smectic- A phases. The imaginary specific heat $\Delta C''_p$ as a function of temperature is shown in Figure 2.2 (b). The imaginary specific heat $\Delta C''_p$ exhibits a sharp peak associated with the I - N phase transition and negligible small peak corresponding to the N -SmA phase transition. This is consistent with I - N phase transition being weakly first-order and N -SmA being continuous or second order phase transition for all ϕ_w . The linear background correction C''_p is about

zero. A summary of transition temperatures, the nematic temperature ranges, and enthalpies for all samples on cooling and heating are given in Tables 5.1 and 5.2.

5.2.2 The I-N and N-SmA Phase Transitions

For the I - N phase transition, an expanded view of the I - N excess specific heat $\Delta C'_p$ on cooling and heating as a function temperature about T_{IN} are shown in Figure 5.1. The $\Delta C'_p$ peak height for cooling and heating scans within the two-phase $I+N$ coexistence region is rising up to $\phi_w \simeq 0.3$, then decreasing with increasing ϕ_w up to the highest QD content sample of 3 wt% studied. The $\Delta C'_p$ peaks for I - N transition in 8CB/QD samples (higher QD content) are slightly broader than that in pure 8CB. The $\Delta C'_p$ and $\Delta C''_p$ behavior are consistent on heating and cooling as well as being reproducible after multiple thermal cycles. The $\Delta C'_p$ wings above and below the I - N transition match each other and that in pure 8CB on heating and cooling. The I - N $\Delta C'_p$ peaks are within the coexistence region on cooling and heating. But, there is a hysteresis of the $\Delta C'_p$ in the two-phase $I+N$ region between heating and cooling with the heating $\Delta C'_p$ peaks are slightly higher in temperature for above $\phi_w \simeq 0.65$ wt% samples. The consistency of $\Delta C'_p$ data on heating and cooling shows that the sample does not phase separate on the macroscopic level and the sample is in equilibrium. However, the microscopic (nanoscopic) phase separation and diffusion of QD in LC media may still form different configuration in N and SmA phases for higher QD concentration.

For the N -SmA phase transition, the excess specific heat $\delta C'_p$ on cooling and heating as a function of temperature about T_{NA} are shown in Figure 5.2 for pure 8CB and 8CB/QD composite samples. For all samples, the N -SmA phase transition does not exhibit any feature in the imaginary specific heat, indicating an apparent absence of latent heat and the continuous nature of this transition. The excess specific heat $\delta C'_p$ of N -SmA phase transition shows a lower wing on the SmA-side for 8CB/QD composite samples compared to the pure 8CB. The $\delta C'_p$ of the N -SmA transition for the 8CB/QD samples overlap each other for all ϕ_w and for pure 8CB on the SmA side while are systematically above pure 8CB on the nematic side of the transition. Given no strong change in the $\delta C'_p$ behavior as a function of ϕ_w , no power law fits were attempted.

The I - N phase transition temperature T_{IN} is defined as the temperature of

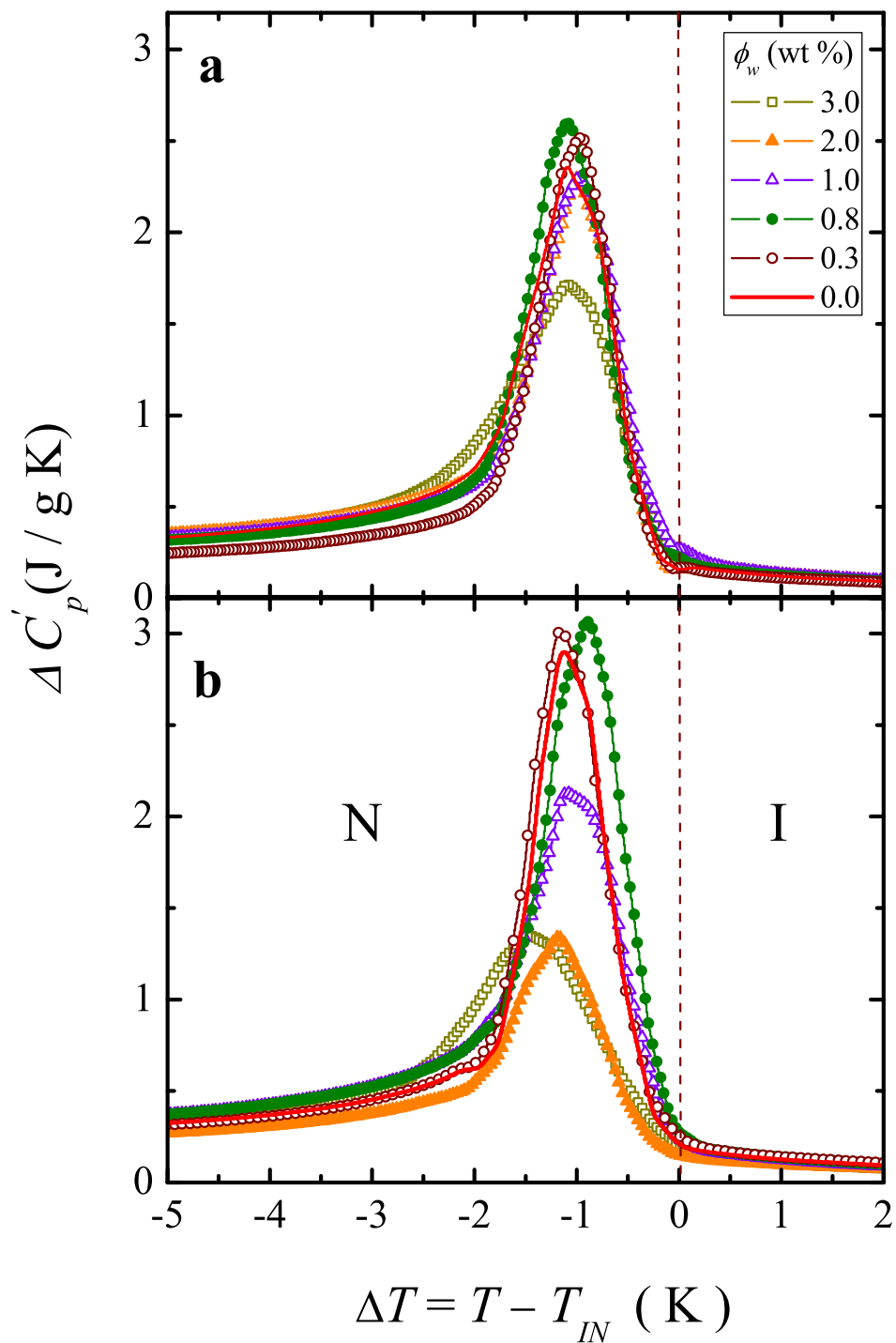


Figure 5.1. Excess real specific heat $\Delta C'_p$ associated with the I - N phase transition as function of temperature about T_{IN} on cooling (a) and heating (b). The definition of the symbols are given in the inset.

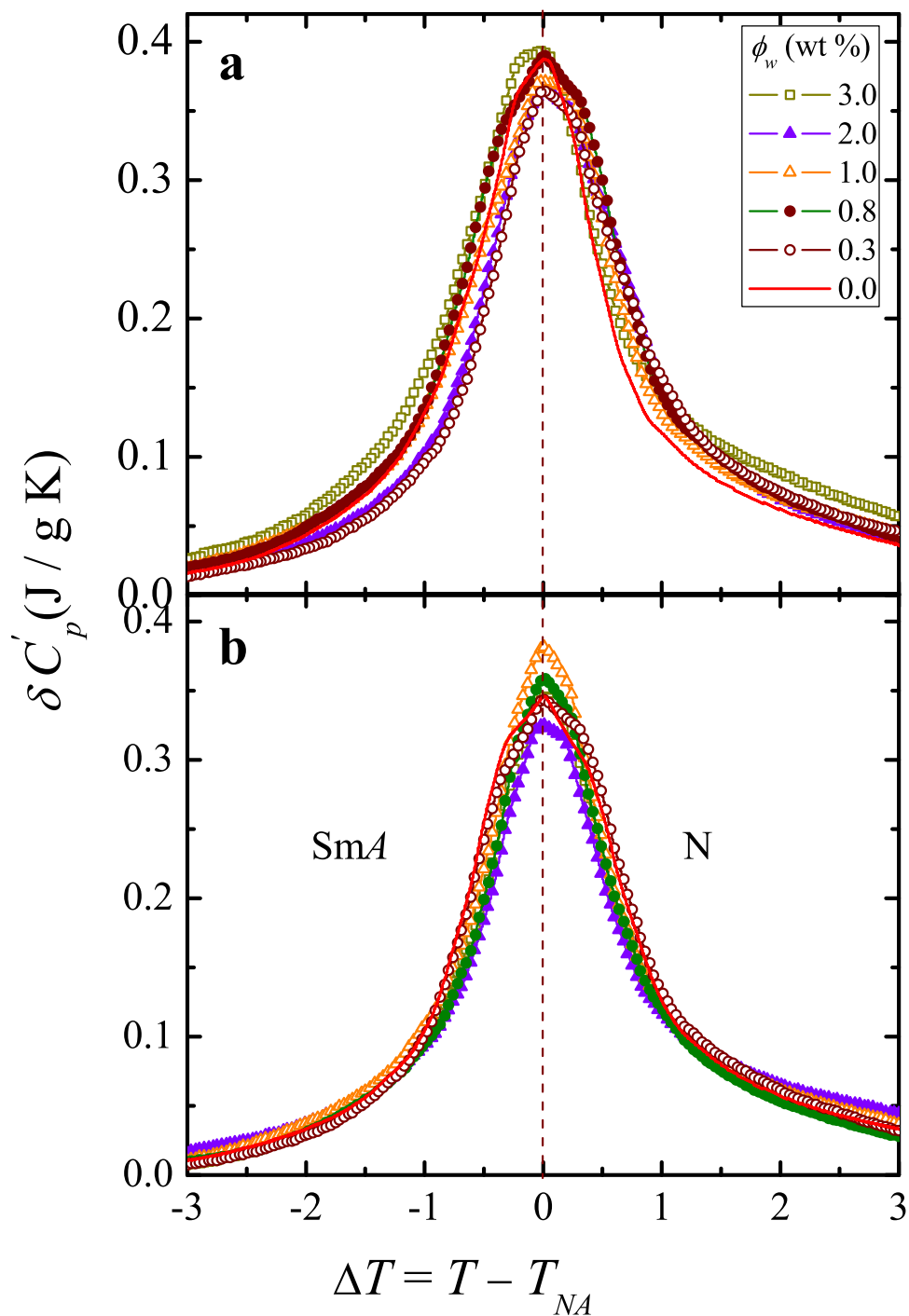


Figure 5.2. (a) Excess real specific heat $\delta C'_p$ associated with the N - SmA phase transition as function of temperature about T_{NA} on cooling. The definition of the symbols are given in the inset. (b) Excess real specific heat $\delta C'_p$ associated with the N - SmA phase transition as function of temperature about T_{NA} on heating.

C_p'' inflection point on the high-temperature side of the C_p'' peak [33]. Here, T_{IN} represents the lowest stable temperature of the isotropic phase. The N -SmA phase transition temperature T_{NA} is taken as C_p peak temperature. The T_{IN} and T_{NA} transition temperatures as the function of ϕ_w shown in Figure 5.7. The T_{IN} suppresses 2.67 K and T_{NA} suppresses 2.35 K as function of ϕ_w . Because of the uncertainty in the homogeneity of the 8CB/QD composite samples, the small noise appeared in the transition temperatures can be related to perfect mixing of 8CB/QD samples. The nematic range, ΔT_N is slightly increases on heating up to 0.65 wt% QDs then decreases by 0.5 K with increasing ϕ_w as shown in Figure 5.4 (a) and the ΔT_N decreases on cooling with increasing ϕ_w . The ΔT_{I+N} is constant up to 0.65 wt% and then increases with increasing ϕ_w on heating and cooling as shown in Figure 5.4 (b). The ΔT_{I+N} increases 1 K on cooling and 0.5 K on heating as a function of ϕ_w . For $\phi_w \leq 0.65$ wt%, I - N and N -SmA move together and no change in coexistence range, for $\phi_w \geq 0.65$ wt%, I - N transition temperatures decreases faster than N -SmA phase and coexistence range widens with increasing ϕ_w .

An integration was performed on ΔC_p over a wide temperature range of 290 to 330 K for all 8CB/QD samples to yield δH_T^* , while an integration of δC_p over ± 3 K about T_{NA} yields δH_{NA}^* . The I - N transition enthalpy is then determined as $\delta H_{IN}^* = H_T^* - H_{NA}^*$. The I - N imaginary enthalpy $\delta H_{IN}''$ is obtained by integrating the C_p'' peak. Figure 5.5(a) shows the δH_{IN}^* , and $\delta H_{IN}''$ on both heating and cooling as a function of ϕ_w . The I - N transition enthalpy of 8CB/QD composites on cooling decreases up to 0.3 wt %, slightly increases and then decreases with increasing ϕ_w . The I - N transition enthalpy of 8CB/QD composites on heating shows bulk like up to 0.65 wt%, slightly decreases with increasing ϕ_w . The heating and cooling enthalpies are not matching and there is a slight hysteresis observed. The imaginary part of enthalpy H_{IN}'' on heating and cooling is constant within the experimental uncertainties as the function of ϕ_w which indicates latent heat is constant as the function of ϕ_w as shown in Figure 5.5(a). The transition enthalpy of N -SmA phase transition δH_{NA}^* is also constant within the experimental uncertainties as the function of ϕ_w which means smectic fluctuations remains constant as shown in Figure 5.5(b).

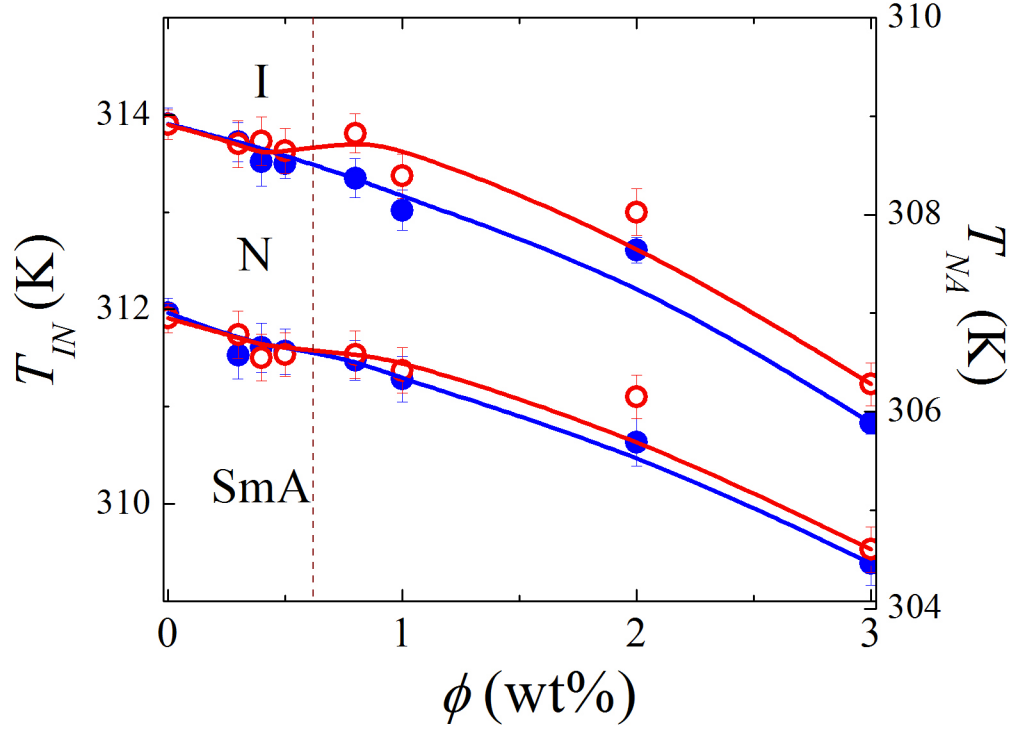


Figure 5.3. The I - N phase transition temperatures T_{IN} (left axis: heating (○) and cooling (●)) and N - SmA phase transition temperature T_{NA} (right axis: heating (○) and cooling (●)) as a function of ϕ_w . Lines are guides to the eye.

5.2.3 The I - SmA Phase Transition in 10CB

The I - SmA phase transition for pure 10CB occurred at $T_{IA}=324.33$ K, in good agreement with the literature value. The excess real specific heat $\Delta C'_p$ and the imaginary specific heat C''_p for pure 10CB and 10CB/QD samples on heating are shown in Figure 5.6 as a function of temperature about the lowest stable temperature of the isotropic phase $T_{IA} = T - T_{IA}$. The $\Delta C'_p$ peaks for I - SmA transition in 10CB/QD samples (higher QD content) are slightly broader than that in pure 10CB. The $\Delta C'_p$ and C''_p behavior are consistent on heating and cooling as well as being reproducible after multiple thermal cycles. The $\Delta C'_p$ wings above and below the I - SmA transition match each other and that in pure 10CB on heating and cooling. The I - SmA phase represents a strongly first-order transition are consis-

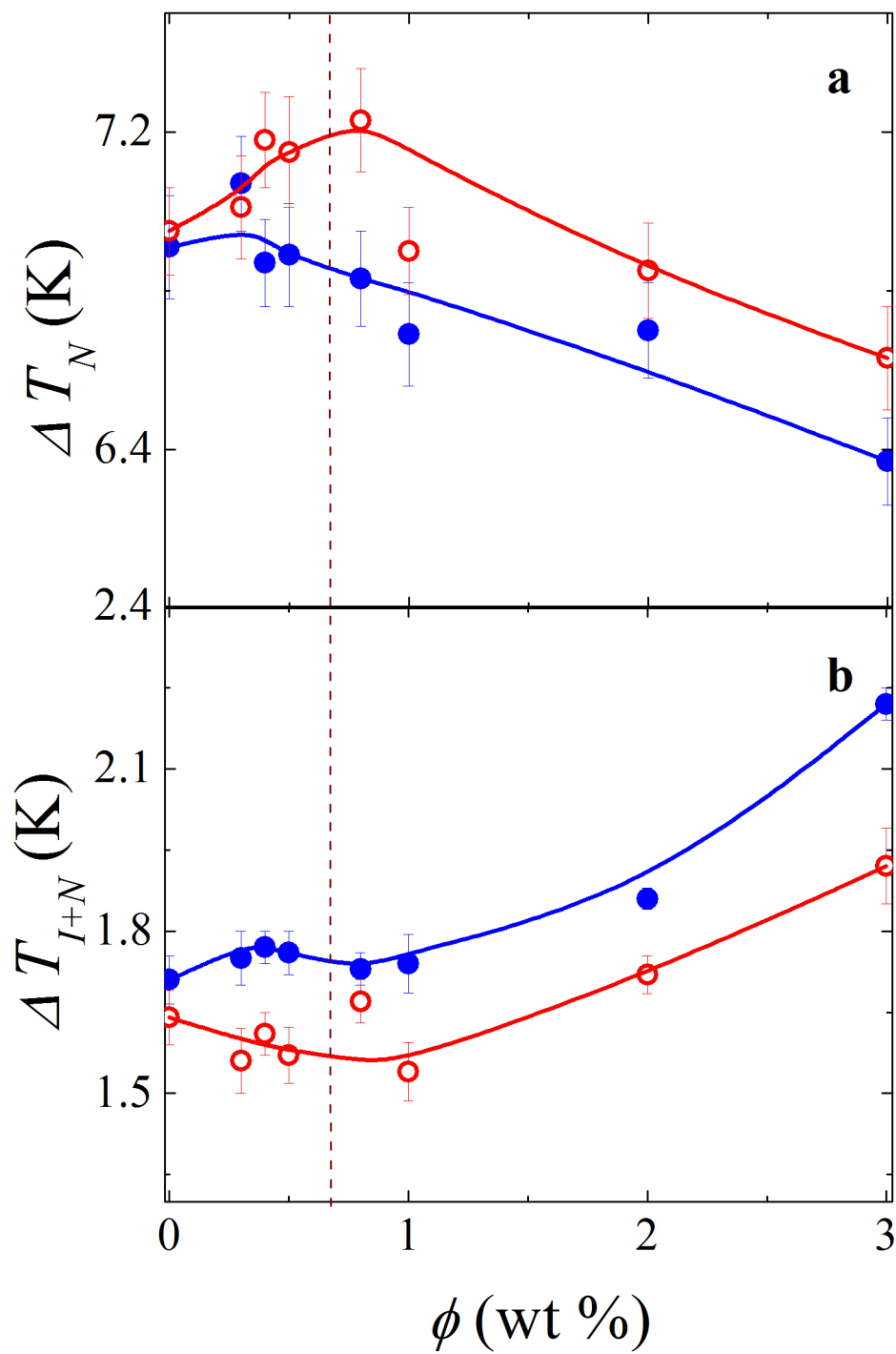


Figure 5.4. (a) The nematic range on heating (\circ) and cooling (\bullet) as a function of ϕ_w . (b) The $I+N$ coexistence region on heating (\circ) and cooling (\bullet) as a function of ϕ_w . Lines are guides to the eye.

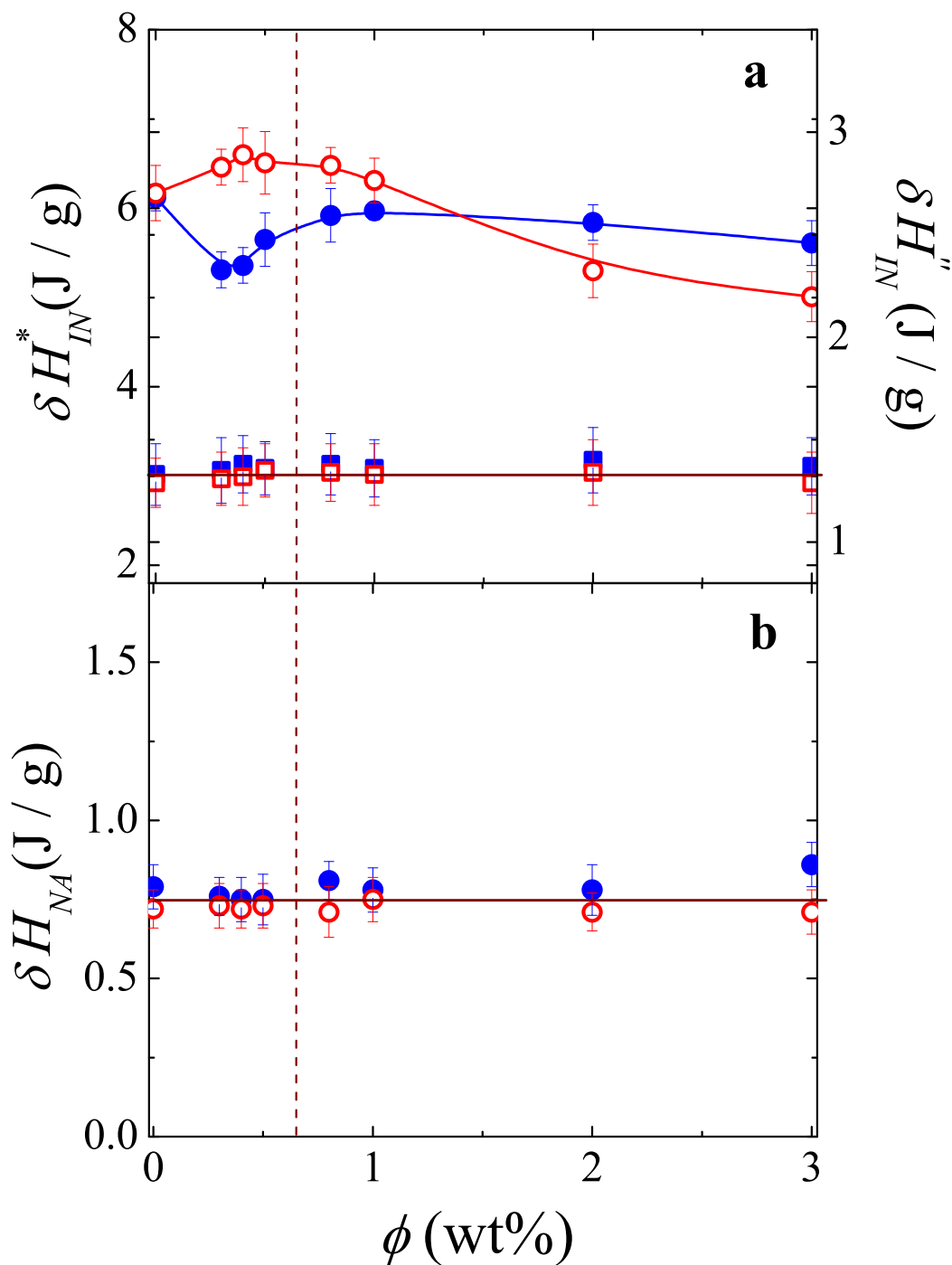


Figure 5.5. (a) The integrated ΔC_p I - N enthalpy δH_{IN}^* (left axis: heating (\circ) and cooling (\bullet)) and imaginary enthalpy $\delta H_{IN}''$ (right axis: heating (\square) and cooling (\blacksquare)) as the function of ϕ_w . (b) The integrated δC_p N - SmA enthalpy δH_{NA}^* on heating (\circ) and cooling (\bullet) as the function of ϕ_w . Lines are guides to the eye.

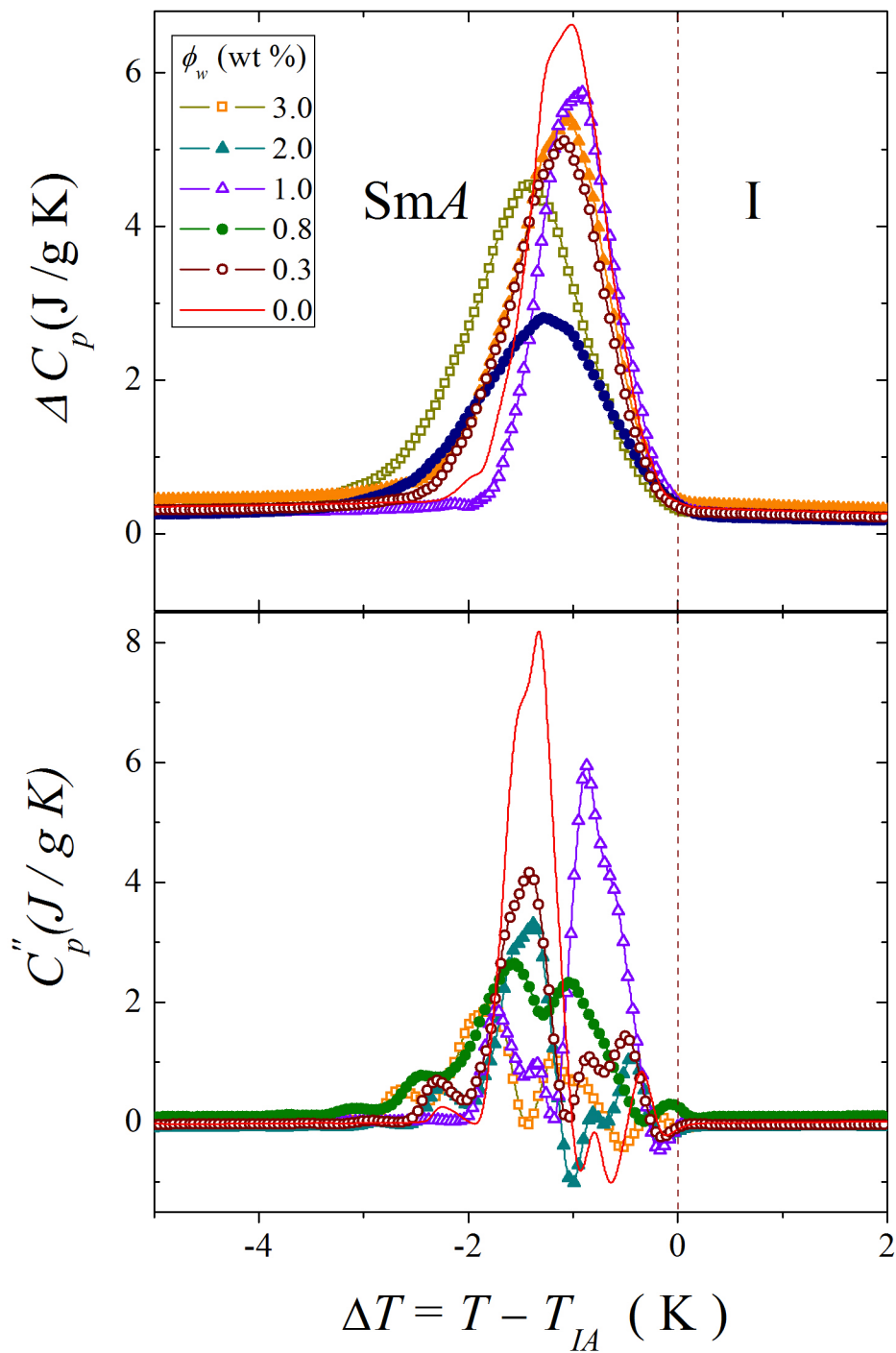


Figure 5.6. Excess real and imaginary specific heat $\Delta C_p'$ associated with the I -SmA phase transition as function of temperature about T_{IA} on heating. The definition of the symbols are given in the inset.

Table 5.1. Summary of the calorimetric results for pure and all 8CB/QD samples on cooling. Shown are quantum dots weight percent ϕ_w , the I - N transition temperature T_{IN} , the N -SmA transition temperature T_{NA} , the nematic range ΔT_N , the coexistence range range ΔT_{I+N} , the integrated enthalpy change δH_{IN}^* , the imaginary enthalpy $\delta H_{IN}''$, and the integrated enthalpy for N -SmA transition δH_{NA}^* . All temperatures are in Kelvin and enthalpies are in Joule per gram.

ϕ_w	T_{IN}	T_{NA}	ΔT_N	ΔT_{I+N}
0.0	313.91 ± 0.16	307.00 ± 0.15	6.91 ± 0.13	1.71 ± 0.04
0.3	313.72 ± 0.20	306.57 ± 0.24	7.01 ± 0.12	1.75 ± 0.05
0.4	313.52 ± 0.25	306.65 ± 0.25	6.87 ± 0.11	1.77 ± 0.03
0.5	313.50 ± 0.15	306.61 ± 0.23	6.89 ± 0.13	1.76 ± 0.04
0.8	313.35 ± 0.20	306.52 ± 0.20	6.83 ± 0.12	1.73 ± 0.03
1.0	313.02 ± 0.21	305.33 ± 0.23	6.69 ± 0.13	1.74 ± 0.05
2.0	312.61 ± 0.13	305.69 ± 0.24	6.70 ± 0.12	1.86 ± 0.02
3.0	310.83 ± 0.11	304.46 ± 0.22	6.37 ± 0.11	2.22 ± 0.03
ϕ_w	δH_{IN}^*	$\delta H_{IN}''$	δH_{NA}^*	
0.0	6.05 ± 0.15	1.33 ± 0.15	0.679 ± 0.07	
0.3	5.31 ± 0.20	1.35 ± 0.16	0.76 ± 0.06	
0.4	5.36 ± 0.20	1.38 ± 0.14	0.75 ± 0.07	
0.5	5.65 ± 0.30	1.36 ± 0.13	0.75 ± 0.08	
0.8	5.92 ± 0.30	1.38 ± 0.15	0.81 ± 0.06	
1.0	5.97 ± 0.10	1.36 ± 0.14	0.78 ± 0.07	
2.0	5.84 ± 0.20	1.40 ± 0.16	0.78 ± 0.08	
3.0	5.61 ± 0.25	1.37 ± 0.14	0.86 ± 0.07	

tent after multiple heating and cooling cycles and so appear to be in equilibrium. The I -SmA phase shows $\Delta C_p'$ peaks slightly becomes broader with with increasing ϕ_w . As ϕ_w increases, the I -SmA peak shifts to lower temperature and broadens in both $\Delta C_p'$ and C_p'' . Cooling scans are generally consistent with heating in that they are reproducible after multiple cycles.

The I -SmA phase transition temperature T_{IA} is defined as the temperature of C_p'' inflection point on the high-temperature side of the C_p'' peak [33]. Here, T_{IA} represents the lowest stable temperature of the isotropic phase. The I -SmA phase transition temperature T_{IA} is taken as C_p peak temperature. The T_{IA} transition temperatures as the function of ϕ_w shown in Figure 5.7. The T_{IA} suppresses 2.6 K as function of ϕ_w . The T_{IA} transition temperatures decreases up to 0.5 wt % and then increases as the function of ϕ_w . Because of the uncertainty in the homogeneity of the 10CB/QD composite samples, the small noise appeared in the

Table 5.2. Summary of the calorimetric results for pure and all 8CB/QD samples on heating. Shown are quantum dots weight percent ϕ_w , the I - N transition temperature T_{IN} , the N -SmA transition temperature T_{NA} , the nematic range ΔT_N , the coexistence range ΔT_{I+N} , the integrated enthalpy change δH_{IN}^* , the imaginary enthalpy $\delta H_{IN}''$, and the integrated enthalpy for N -SmA transition δH_{NA}^* . All temperatures are in Kelvin and enthalpies are in Joule per gram.

ϕ_w	T_{IN}	T_{NA}	ΔT_N	ΔT_{I+N}
0.0	313.90 ± 0.15	306.95 ± 0.13	6.95 ± 0.11	1.64 ± 0.05
0.3	313.70 ± 0.24	306.78 ± 0.24	7.01 ± 0.13	1.56 ± 0.06
0.4	313.73 ± 0.25	306.55 ± 0.24	7.18 ± 0.12	1.61 ± 0.04
0.5	313.63 ± 0.23	306.58 ± 0.22	7.15 ± 0.14	1.57 ± 0.05
0.8	313.81 ± 0.20	306.58 ± 0.24	7.23 ± 0.13	1.67 ± 0.04
1.0	313.37 ± 0.23	306.42 ± 0.23	6.90 ± 0.11	1.54 ± 0.05
2.0	313.00 ± 0.24	306.15 ± 0.22	6.85 ± 0.12	1.72 ± 0.04
3.0	311.23 ± 0.23	304.60 ± 0.23	6.63 ± 0.13	1.92 ± 0.07
ϕ_w	δH_{IN}^*	$\delta H_{IN}''$	δH_{NA}^*	
0.0	6.07 ± 0.31	1.29 ± 0.12	0.72 ± 0.06	
0.3	6.46 ± 0.20	1.31 ± 0.13	0.73 ± 0.07	
0.4	6.60 ± 0.30	1.32 ± 0.14	0.72 ± 0.06	
0.5	6.51 ± 0.35	1.35 ± 0.13	0.73 ± 0.07	
0.8	6.48 ± 0.20	1.34 ± 0.14	0.71 ± 0.08	
1.0	5.31 ± 0.25	1.33 ± 0.15	0.75 ± 0.07	
2.0	5.30 ± 0.30	1.34 ± 0.16	0.71 ± 0.06	
3.0	5.01 ± 0.28	1.29 ± 0.15	0.71 ± 0.07	

transition temperatures can be related to perfect mixing of 10CB/QD samples.

5.2.4 The Physical Model

Suspending colloidal particles in liquid crystals can be carried out with the aim of making new materials which exhibit new physical properties. In this section, we briefly review some of recent work done on colloidal self assemblies in liquid crystals and connect our work with recent studies. Using three-dimensional numerical modeling, the self assembly of triangular, square and pentagonal sub-micrometer sized platelets studied in thin layer of nematic liquid crystal [30]. The inter-particle potential depends in a complex way on the orientation of the particle and the particles form linear chains at higher concentration to minimize their free energy. Theory not yet developed to study such a small nano-size particles. The behavior

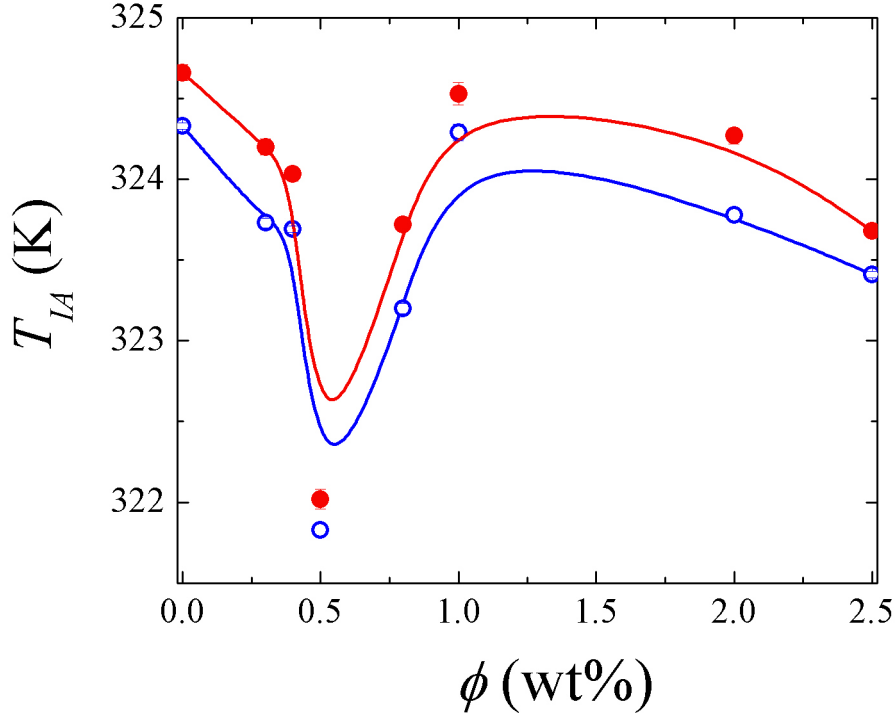


Figure 5.7. The I -SmA phase transition temperatures T_{IA} on heating (○) and on cooling (●) as a function of ϕ_w . Lines are guides to the eye.

of nano-particles depend sensitively on the nature of the LC, the anchoring conditions and the particle size. Exploring the re-orientations and interactions potential between nano-sized particle will be interesting in nano-scale photonics application. In this studies, we propose a physical model to explain results shown in Figure 5.8.

The key observations are I - N C_p peak changes with ϕ_w , N -SmA does not changes with ϕ_w , there is a difference in behavior $\phi_w \leq 0.65$ wt% and then $\phi_w \geq 0.65$ wt% with all transition temperatures decreasing with increasing ϕ_w . Since only ϕ_w changes, these effects must be come from QDs arrangements below and above $\phi_w = 0.65$ wt%. The arrangement of QDs is different in both N and SmA phases.

Considering the spherical symmetry of the QDs, for the dilute regime, the QDs likely exist separately much likely a dilute ideal gas. But as concentration increases, groups of QDs are more likely. An arrangement that minimizes free energy when dealing with spherical particles in uniaxial phase is a "pearl – necklace" chain of

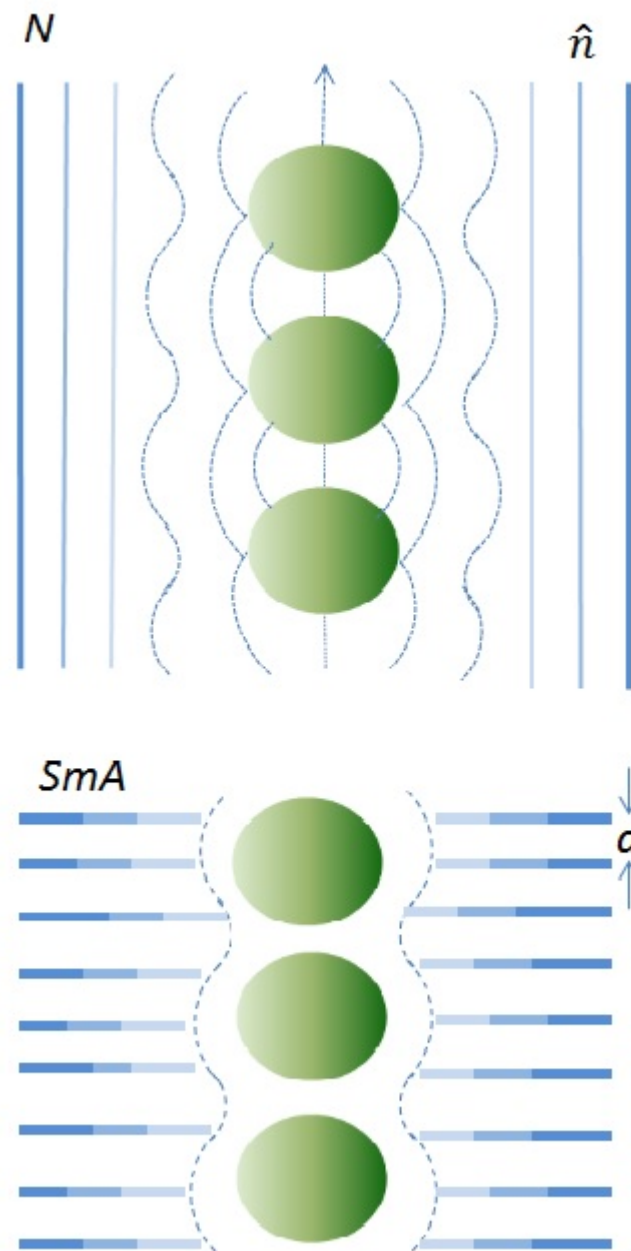


Figure 5.8. The QDs configuration in LC media at higher QD concentration in N phase (top panel) and the QDs configuration in LC media at higher QD concentration in SmA phase (bottom panel).

QDs. This arrangement more closely matched the symmetry of the nematic phase. This effect is essentially independent of surface anchoring of the \hat{n} , but it is most likely radial. However SmA is not coupled.

On cooling, the system move from disorder state to order state, QDs form highly anisotropic structures along nematic director and decreases nematic range for $\phi_w \geq 0.65$ wt%. In SmA phase, the size of QDs are much larger than the nematic layer and QDs do not pin the molecule. As result, the SmA phase remains bulk-like. On heating, the SmA- N and N - I phase transition temperatures are higher than cooling transition temperatures and the I - N phase transition temperatures decreases faster than N -SmA phase. This leads to the two phase coexistence range increases for $\phi_w \geq 0.65$ wt%. The QDs forms "*pearl-necklace*" chain configuration for $\phi_w \geq 0.65$ wt% due to minimize their free energy shown in top panel Figure 5.8. The QDs does not effect on SmA phase due to their size larger than the nematic layer shown in bottom panel Figure 5.8. This leads to the effective transition enthalpy for N -SmA phase remains bulk-like behavior. On cooling at low ϕ_w , the N nucleates in between QDs and hence coexistence range shift to minimum free energy state. At higher ϕ_w , QDs do not move as far due to they pin together as chains and as a result δH becomes stabilize. On heating at low ϕ_w , the N phase already at minimum free energy state with QDs stable positions and hence melting behaves bulk-like. At higher ϕ_w , QDs chains stabilize the N phase to para-nematic and hence the transition enthalpy reduce to I phase. As a results, the nematic phase impose self assembly on QDs to form one dimensional arrays leading to QDs induces net local disordering effect in LC media.

Bibliography

- [1] X. Tong and Y. Zhao, *J. Am. Chem. Soc.*, **129**, 6372 (2007).
- [2] S. W. Lee, C. Mao, C. E. Flynn, and A. M. Belcher, *Science*, **296**, 892 (2002).
- [3] C. Jiang, S. Xu, D. Yang, F. Zhang, W. Wang, and J. Biolumin, *Chemilumin*, **22**, 430 (2007).
- [4] J. Zhao, J. A. Bardecker, A. M. Munro, M. S. Liu, Y. Niu, I. K. Ding, J. Luo, B. Chen, A. K. Y. Jen, and D. S. Ginger, *Nano Lett.*, **6**, 463 (2006).
- [5] A. Balandin, K. L. Wang, N. Kouklin, and S. Bandyopadhyaya, *Appl. Phys. Lett.*, **76**, 137 (2000).
- [6] K. L. Wang and A. Balandin, *Optic of Nanostructure Material*, Wiley, New York (1999).
- [7] S. Fafard, Z. R. Wasilewski, C. N. Allen, D. Picard, P. G. Piva, and J. P. McCarey, *Super-lattices Microstruct.*, **25**, 87 (1999).
- [8] W. Chen, A. G. Joly, J. O. Malm, J. O. Bovin, and S. Wang, *Phys. Chem. B*, **107**, 6544 (2003).
- [9] M. Tamborra, M. Striccoli, R. Comparelli, M. Curri, A. Petrella, and A. Agostiano, *Nanotechnology*, **15**, S240 (2004).
- [10] I. Dierking, G. Scalia, and P. Morales, *J. App. Phys.*, **97**, 044309 (2005).
- [11] M. D. Lynch and D. L. Patrick, *Nano. Lett.*, **2**, 1197 (2002).

- [12] R. Basu and G. Iannacchione, *Appl. Phys. Lett.*, **93**, 183105 (2008).
- [13] L. Onsager, em *Ann. N. Y. Acad. Sci.*, **51**, 627 (1949).
- [14] P. G. de Gennes and J. Prost, *The Physics of Liquid Crystals*, (Oxford University Press, Clarendon, Oxford, England) (1993).
- [15] S. Chandrashekar, *Liquid Crystals*, (Cambridge University Press, England) (1992).
- [16] G. Iannacchione, J. Mang, S. Kumar, and D. Finotello, *Phys. Rev. Lett.*, **73**, 2708 (1994).
- [17] M. Olbrich, H. Brand, H. Finkelmann, and K. Kawasaki, *Euro. Phys. Lett.*, **31**, 281 (1995).
- [18] T. Bellini, A. Rappaport, N. Clark, and B. Thomas, *Phys. Rev. Lett.*, **77**, 2507 (1996).
- [19] A. Drozd, R. zoska, S. Rzoska, and J. Ziolo, *Phys. Rev. E*, **61**, 5249 (2000).
- [20] T. Bellini, N. Clark, and D. Link, *J. Phys. Condens. Matter*, **15**, S175 (2003).
- [21] M. K. Ramazanoglu, P. Clegg, R. J. Birgeneau, C. W. Garland, M. E. Neubert, and J. M. Kim, *Phys. Rev. E*, **69**, 061706 (2004).
- [22] J. Leys, G. Sinha, C. Glorieux, and J. Thoen, *Phys. Rev. E*, **71**, 051709 (2005).
- [23] P. Kedziora, *Acta Phys. Pol. A*, **107**, 907 (2005).
- [24] G. Chahine, A. V. Kityk, K. Knorr, R. Lefort, and M. Guendouz, *Phys. Rev. E*, **81**, 031703 (2010).
- [25] I. Lelidis and G. Durand, *J. Phys. II*, **6**, 1359 (1996).
- [26] P. Mukherjee, H. Pleiner, and H. R. Brand, *Euro. Phys. E*, **4**, 293 (2001).
- [27] P. Mukherjee, *J. Chem. Phys.*, **116**, 9531 (2002).
- [28] P. Mukherjee, H. Pleiner, and H. R. Brand, *Phys. Rev. E*, **65**, 051705 (2001).

- [29] B. Senyuk, J. S. Evans, P. J. Ackerman, T. Lee, P. Manna, L. Vigderman, E. R. Zubarev, J. van de Lagemaat, and I. I. Smalyukh, *Nano Lett.*, **12**, 955 (2012).
- [30] J. Dontabhaktuni, M. Ravnik, and S. Zumer, *Soft Matter*, **8**, 657 (2012).
- [31] J. Jeong and M. W. Kim, *Phys. Rev. Lett.*, **108**, 207802 (2012).
- [32] B. Zhou, G. S. Iannacchione, C. W. Garland, and T. Bellini, *Phys. Rev. E*, **55**, 2962 (1997).
- [33] L. Wu, B. Zhou, C. W. Garland, T. Bellini, and D. W. Schaefer, *Phys. Rev. E*, **51**, 2157 (1995).

Calorimetric Study of Nanocomposites of Multi-walled Carbon Nanotubes and Isotactic Polypropylene Polymer

6.1 Introduction

Since their discovery in 1991 [1], carbon nanotubes (CNTs) have emerged as a new class of nanosized particles for incorporation into various polymer systems, attracting considerable interest from both basic science research and industry. As a result of the exceptional intrinsic properties of the CNTs, novel materials can be envisaged which exhibit unprecedented property enhancements, moreover at CNTs loadings much lower than in conventional composite technology [2]. In the field of thermoplastic nanocomposites, reported property enhancements include improved mechanical performance [3, 4], high thermal and electrical conductivity [5, 6, 7], increased crystallization rate [8, 9, 10], and altered rheological behavior [11, 12]. However, a fundamental understanding of these nanocomposites is still lacking.

Because of its outstanding properties, low price, and wide applicability, isotactic polypropylene (iPP) is among the most well studied thermoplastics, with widespread application in various composite materials. Over the years, iPP has been reinforced with a wide range of fibers (e.g. carbon, glass, natural fibers)

essentially aiming at improving its mechanical performance. However, the emergence of carbon nanotubes as filler particles has paved the way for potential new applications, in fields which so far have required the use of expensive engineering polymers. For instance, a potentially highly important application is the use of nanocomposite films for the electromagnetic interference (EMI) shielding [13, 14]. The requirements to the material are manifold, however, as films need to be thin and transparent, yet mechanically stable and displaying a sufficiently high electrical conductivity. The use of CNTs as filler particles in iPP may provide a way to fulfill these requirements, as their incorporation simultaneously provides mechanical reinforcement as well as electrical conductivity. A prerequisite for the latter, however, is the achievement of an electrically conductive percolating network of nanofiller particles, at low enough loading so as to preserve the materials transparency [14].

The phase transition behavior of isotactic polypropylene from the mesomorphic phase to the monoclinic crystal reported form using DSC [15]. It has been long recognized that the addition of CNTs significantly affects the crystallization behavior and resulting crystalline morphology of the iPP matrix. However, high resolution complex calorimetry beyond traditional DSC has not been reported for nanocomposites. The carbon nanotubes were found to strongly nucleate iPP crystallization, resulting in a trans-crystalline morphology [16, 17, 18]. This highly oriented columnar morphology, extending over the entire fiber-matrix interface, is significantly different from the spherulitic crystal growth commonly encountered in neat iPP. It is, however, generally not associated with polymorphism, unless when crystallized from the sheared melt around a pulled fiber [19]. The origin of trans-crystallinity has been the subject of intensive research and is still a matter of debate. Its development is associated with the high density of heterogeneously nucleating sites on the fiber surface, restricting crystal growth to the direction perpendicular to the fiber, with the crystal *c*-axis aligned in the fiber long-axis [20]. However, several additional factors are believed to influence its formation, such as epitaxial crystal growth based on lattice matching, surface energy and topology of the fiber, flow-induced crystallization, or residual stresses resulting from a mismatch in the thermal expansion coefficients of fiber and matrix [16].

Trans-crystallinity has also been encountered in a number of other polymer

nanocomposite systems. For instance, nylon-6 crystals were reported to grow perpendicular to dispersed clay platelets [21], whereas carbon nanotubes were found to template the growth of polyethylene crystals in a direction perpendicular to the nanotubes long-axis [22, 23]. Crystallization from dilute solution was found to induce structures strongly resembling the shish-kebab morphology in polyethylene and nylon-6,6 [24]. For iPP/CNT nanocomposites, finally, several reports suggested the occurrence of trans-crystallinity, however without providing experimental evidence [25, 9, 26, 27, 28]. Moreover, contradictory findings subsist as to the possible occurrence of polymorphism in iPP nanocomposites containing carbon nanotubes [29, 26].

In the present study, we report on the complex calorimetry of crystallization and melting behavior of neat iPP and well dispersed iPP/CNT nanocomposite thin films as a function of CNT content and temperature scan rate. For the iPP/CNT samples, CNT content varied from 0.01 to 5 weight percent (wt %) and the baseline temperature scan rate varied from ± 0.5 to 4 K min^{-1} . In all measurements, the crystallization and melting calorimetric signatures were almost entirely non-reversible (imaginary) with only a very small feature discernible in the reversible (real) specific heat component, indicating their strong first-order character. The crystallization and melting temperatures, T_C and T_M , increase as a function of CNTs concentration. The enthalpy of crystallization and melting of the iPP/CNT samples increases strongly with increasing CNT content, saturating for CNT concentrations above 1 wt%. These results provide strong evidence that the CNT surface provides crystal nucleation sites for a different crystal phase than in the neat iPP, which becomes more dominant as the CNTs content increases. We also present the effect of temperature scan rates on the thermal evolution of neat iPP and iPP/CNT nanocomposites revealing a nonlinear driving of the transition temperatures and enthalpies. During subsequent melting, recrystallization phenomena may occur depending on the applied heating rate, the kinetics of which will be discussed in terms of polymer chain segment mobility.

6.2 Results and Discussions

6.2.1 Crystallization Behavior of iPP and iPP/CNT Nanocomposites

Figure 6.1 shows the total excess specific heat as a function of temperature for neat iPP and iPP/CNT samples with ϕ_w from 0.01 to 5 wt%. The crystallization temperature for neat iPP occurred at 404.6 K, in good agreement with the literature value [13]. As the CNTs content increases, the ΔC_p peak remains as sharp as in neat iPP, only changing amplitude slightly. Further, T_C shifts upward by +4.6 K for the 0.01 wt % sample and continues to increase with increasing ϕ_w reaching +7.5 K at 5 wt % of CNT. In addition to the large ΔC_p peak associated with crystallization, there appears a small ΔC_p feature for the neat iPP 9 K lower in temperature. This feature is likely the conversion to crystal of boundary regions between initially formed crystal domains. See inset of Figure 6.1. With the addition of CNTs, this small ΔC_p peak generally decreases in size and shifts closer to the main ΔC_p peak as ϕ_w increases, reaching 2.5 K below TC for the 2 wt % sample before disappearing in the 5 wt% sample. These results are consistent with the CNTs promoting the crystal phase and minimizing the delayed conversion of domain boundary regions

The upper panel of Figure 6.2 shows the upward shift in the crystallization temperature T_C and that of the small ΔC_p feature that reaches a plateau value, evidently suggesting saturation of the nucleating effect. An upward shift in the crystallization onset and peak temperatures is observed, even for CNT loadings as low as 0.01 wt %, suggesting a high degree of crystal nucleation on the surface of the CNTs. The overall crystallization process is enhanced as a result of the presence of CNTs, providing a large number of nucleation sites. This results in an increase in TC with respect to that of the homogeneously nucleated neat iPP. The crystallization behavior dependence on multiwall nanotube loading, as well as the plateau value of the crystallization onset, result from the increase in CNTs surface area as ϕ_w increases. The fact that the crystallization onsets level off at higher CNTs loadings and finally attain a plateau value is indicative of nucleation saturation. An incomplete CNT exfoliation at higher loadings provides a possible explanation, as poor CNTs dispersion at higher mass fractions implies that the outer surface

of the nanotubes becomes increasingly inaccessible for crystal nucleation. Incomplete exfoliation of CNT bundles may be due to Van der Waals interactions and nanotube clustering. Alternatively, from a certain loading onward, the crystallization rate may level off as a result of the fact that crystal growth becomes the rate-determining factor. Further increasing the loading does effectively increase the nuclei density, but under the resulting time and temperature conditions crystallization proceeds more slowly, resulting in a leveling off of the crystallization onset. The rate-determining factors can either be the high crystallization temperature, resulting from the nucleating action and diminishing the thermodynamic driving force for crystallization, or limitations in the diffusion of polymer chains toward the growing crystal front. The latter might result from reduced polymer mobility and from chain diffusion constraints in a geometrically confined space, as the average inter-particle distance is reduced at higher loadings. With respect to the above discussion on the crystallization of the iPP matrix, it is worth noting that the nucleating action of CNTs, increasing the crystallization temperatures by 8 K, is comparable to that of conventional nucleating agents. Indeed, shifts of up to 15 K have been reported after incorporation of sodium benzoate into iPP [30]. Moreover, saturation of the nucleating effects was also observed for such conventionally nucleated systems [30, 31] and was attributed to agglomeration of the nucleating particles due to over-dosage, limiting the number of effective nuclei. A summary of transition temperatures, enthalpies for crystallization and melting for all samples on heating and cooling are given in Table 6.1.

6.2.2 Melting Behavior of iPP and iPP/CNT Nanocomposites

Figure 6.3 shows the total excess specific heat as a function of $\Delta T = T - T_{M,2}$ for neat iPP and iPP/CNT samples with ϕ_w from 0.01 to 5 wt %. For clarity, the ΔC_p traces are shifted upward successively by 2 J/g K and shifted in temperature with respect to the final melting peak. The melting temperature occurred for neat iPP at 436.96 K, in good agreement with the literature value 436.1 K [30]. As shown in Figure 6.3, melting of neat iPP appears to proceed in a two-step process with a first order ΔC_p peak at a temperature $T_{M,1}$ appearing first followed by a large first order ΔC_p peak at $T_{M,2}$ on heating. The melting temperature $T_{M,2}$

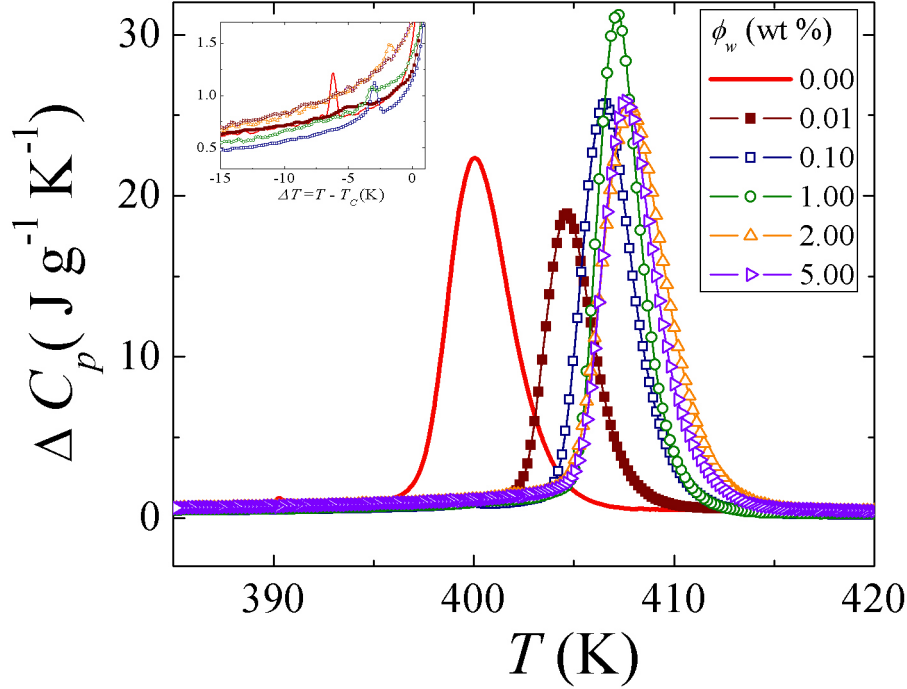


Figure 6.1. The total specific heat ΔC_p on cooling at -0.5 K/min through crystallization for neat iPP and iPP/CNT nanocomposites. See legend for wt % CNT. Inset shows an expanded view of the low temperature wings revealing a very small ΔC_p feature. See text for discussion.

shifts upward by 3.8 K from 0.01 to 0.1 wt % samples and remains same for higher loading of CNT content. See bottom panel of Figure 6.2 for the ϕ_w behavior of $T_{M,1}$ and $T_{M,2}$. Clearly, the presence of CNTs and the prior crystallization history have dramatic impact on the melting behavior of the polymer matrix. Whereas the neat polymer matrix unambiguously shows a double melting ΔC_p behavior, the shape of the melting ΔC_p progressively evolves toward single melting with increasing CNT concentration. Indeed, the lower melting peak $T_{M,1}$ progressively shifts to higher temperature upon increasing the CNTs loading, until it finally coincides with the higher melting peak $T_{M,2}$ at 5 wt % CNT loading.

Multiple melting features are generally assumed to result from polymorphism, from the successive melting of crystal populations with distinct degrees of perfection, or from the rapid succession of melting-crystallization-melting. The impact of CNTs on the polymorphic behavior of iPP has been extensively reported over

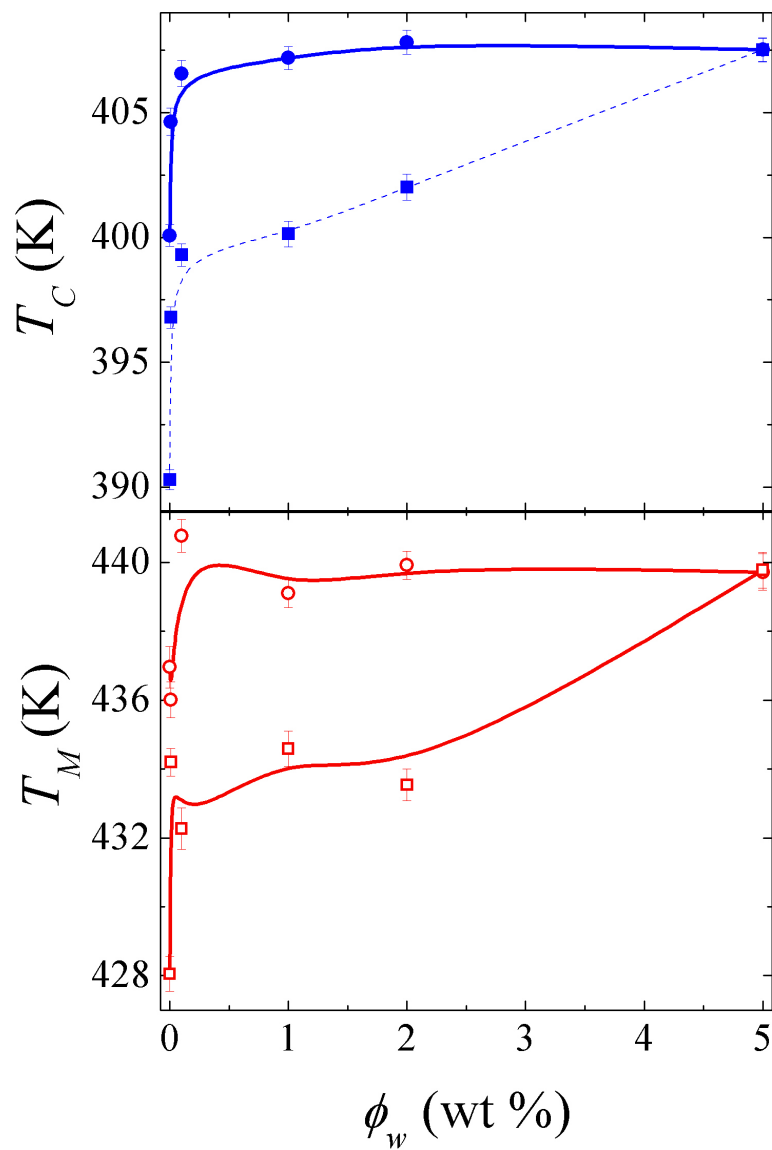


Figure 6.2. The crystallization and melting temperatures of the isotropic to mesomorphic α -monoclinic transition for neat iPP and iPP/CNT samples as a function of ϕ_w . Top panel shows the large crystallization ΔC_p position (●) and the small secondary feature (■) on cooling. Bottom panel shows the temperature of two melting features, $T_{M,1}$ (□) and $T_{M,2}$ (○) on heating. Lines are guides to the eye.

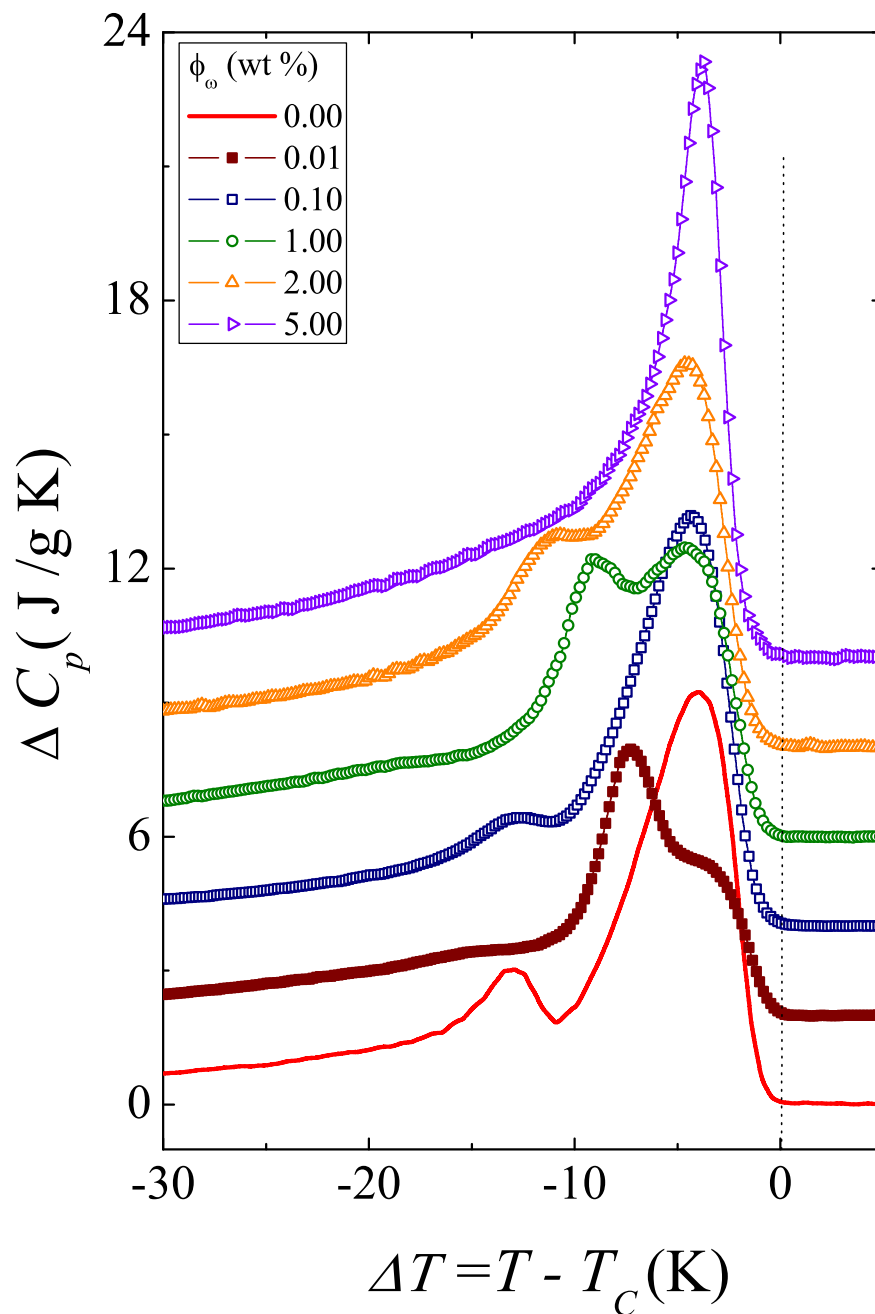


Figure 6.3. The total excess specific heat ΔC_p traces recorded during heating runs at +0.5 K/min through the melting region of the neat iPP and iPP/CNT nanocomposites containing loadings of CNTs listed in the legend. For clarity, the ΔC_p traces are shifted upward successively by 2 J/g K with respect to the neat iPP trace. See legend for sample wt% CNT.

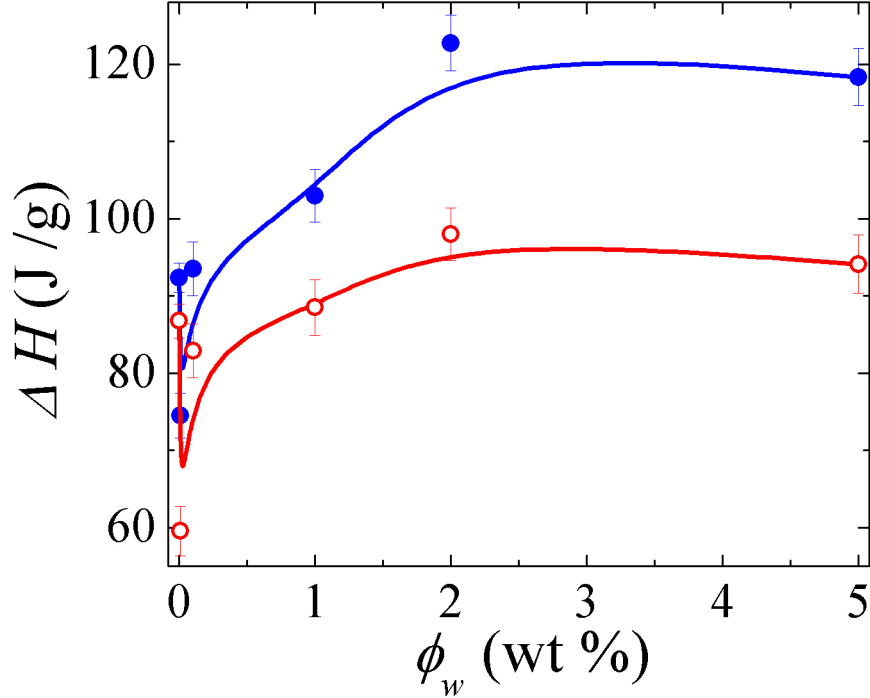


Figure 6.4. The total effective transition enthalpy of neat iPP and iPP/CNT nanocomposites on cooling (●) and heating (○) as a function of ϕ_w . Lines are guides to the eye.

the years. Some authors reported that CNTs can induce crystallization of iPP in the hexagonal polymorphic, instead of the more common monoclinic R-form [26]. Since both polymorphs display distinct melting temperatures, the observed changes in the shape of the melting transition in the presence of CNTs might potentially be the result of an altered balance between crystal forms co-existing in the sample [31]. This indicates that the CNTs surface not only nucleates the crystal phase but pins a particular crystal structures not common in neat iPP.

According to classical polymer crystallization theory, the melting temperature of a crystal T_M , is determined by its lamellar thickness [32, 33]. The latter, on the other hand, is inversely proportional to the super cooling below the equilibrium melting point T_M^0 . An equation relating the observed melting temperature to the crystallization temperature has been proposed, and the well-known linear Hoffman-Weeks method [33], by which the equilibrium melting temperature is determined as the intersection of the experimentally recorded T_M plotted against

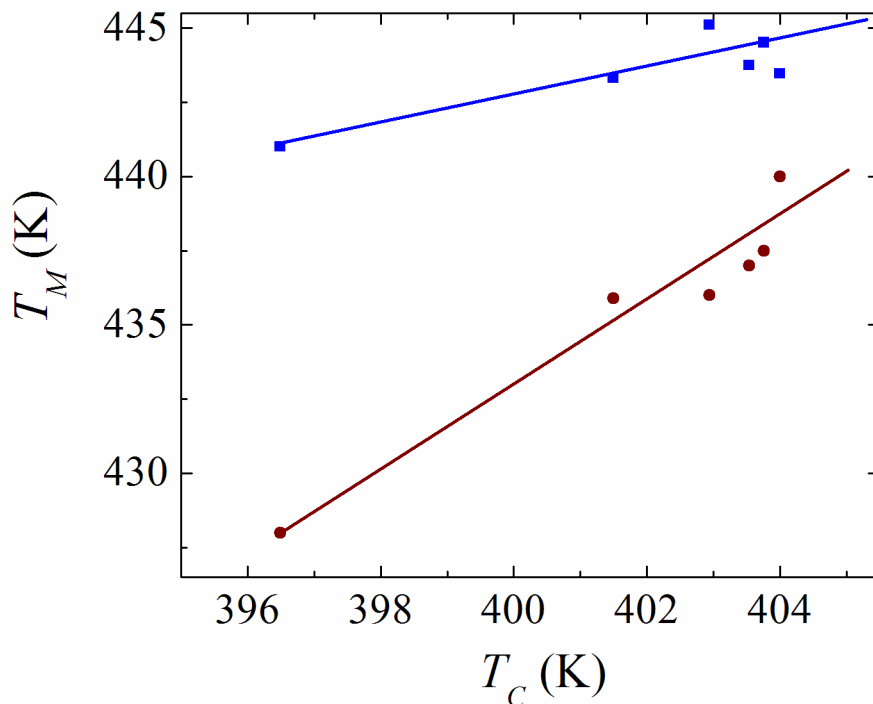


Figure 6.5. Melting temperatures $T_{M,1}$ (■) and $T_{M,2}$ (●) plotted against crystallization temperature for iPP filled with various loadings of CNTs. Crystallization and melting temperatures were obtained from nonisothermal MDSC experiments and straight lines from linear regression.

T_C (with a slope slightly below 0.5 in most cases) and the line $T_M = T_C$ (slope = 1). This diagram is typically constructed for isothermally crystallized samples, but the strong nucleation in the presence of CNTs allows a similar diagram to be constructed for nonisothermally crystallized samples. Here the lower melting peak temperature $T_{M,1}$ and higher melting peak temperature $T_{M,2}$ are plotted as a function of the corresponding crystallization peak temperature as shown Figure 6.5. The smaller ΔC_p peak at $T_{M,1}$ does very linearly with T_C with a slope of 0.51 and yields a $T_M^0 = 481.5$ K which is higher than the T_M^0 commonly reported for neat iPP [?]. The larger ΔC_p peak at $T_{M,2}$ marking the final melting point has a larger slope of 1.47 and a $T_M^0 = 329.9$ K. Clearly, on heating, the initial smaller ΔC_p peak behaves in a similar way as the melting in neat iPP and may represent regions far from CNT surface having a crystal structure similar to that in neat iPP. The final and larger ΔC_p peak behaves in a very different way with a T_M^0 for below that in

Table 6.1. Summary of the transition temperatures T_C and total effective transition enthalpies for iPP and composites based on the quasi-static MDSC results for both cooling and heating scans (superscripts c and h , respectively).

ϕ_{CNT}	$T_C^c(K)$	$T_C^h(K)$	$\Delta H^c(J/g)$	$\Delta H^h(J/g)$
0.00	400.08 ± 0.96	436.96 ± 0.88	92.33 ± 0.99	86.78 ± 1.33
0.01	404.64 ± 0.91	436.50 ± 0.92	74.47 ± 0.95	59.56 ± 0.98
0.10	406.57 ± 0.88	440.77 ± 0.86	93.53 ± 1.22	82.91 ± 1.41
1.00	407.19 ± 0.85	439.11 ± 0.91	102.97 ± 1.25	88.52 ± 1.42
2.00	407.82 ± 0.86	439.92 ± 0.96	122.74 ± 1.24	97.98 ± 1.44
5.00	407.52 ± 0.95	439.72 ± 0.85	118.36 ± 1.23	94.14 ± 1.35

neat iPP indicating a crystal structure influenced by the CNT nucleation sites.

MDSC allows for a more detailed study of possible crystallization and melting phenomena. The real part of the specific heat is very small compared to the imaginary part for both crystallization and melting, both transitions being strongly first-order. On melting, the total transition enthalpy decreases for $\phi_w = 0.01$ sample and then increases with increasing ϕ_w , saturating about 15 J/g above that for neat iPP at $\phi_w \geq 2$ wt % Figure 6.4. This indicates that the recrystallization phenomenon is progressively suppressed with increasing CNTs concentration. A summary of transition temperatures and enthalpies for all samples on heating and cooling are given in Table 6.1.

6.2.3 Effect of Scan Rates on neat iPP and 2 wt% iPP/CNT

Since recrystallization essentially concerns the least perfect crystals present in the polymer, and requires time to occur, it is sensitive to scan rate. The effect of increasing the cooling rate from -0.5 to -4 K/min on ΔC_p is shown in Figure 6.6. As the cooling rate increases for the neat iPP (top panel of Figure 6.6, the large ΔC_p peak shifts in temperature and eventually decreases in height and broadens in width for the fastest cooling rate of -4 K/min. As the heating rate increases from 0.5 to 4 K/min, see Figure 6.7, the ΔC_p traces do not shift in temperature but evolve in shape. The smaller ΔC_p peak at $T_{M,1}$ sharpens and increases in size while the larger ΔC_p peak at $T_{M,2}$ broadens and decreases in size.

The effect of increasing the cooling rate from -0.5 to -4 K/min on ΔC_p is shown

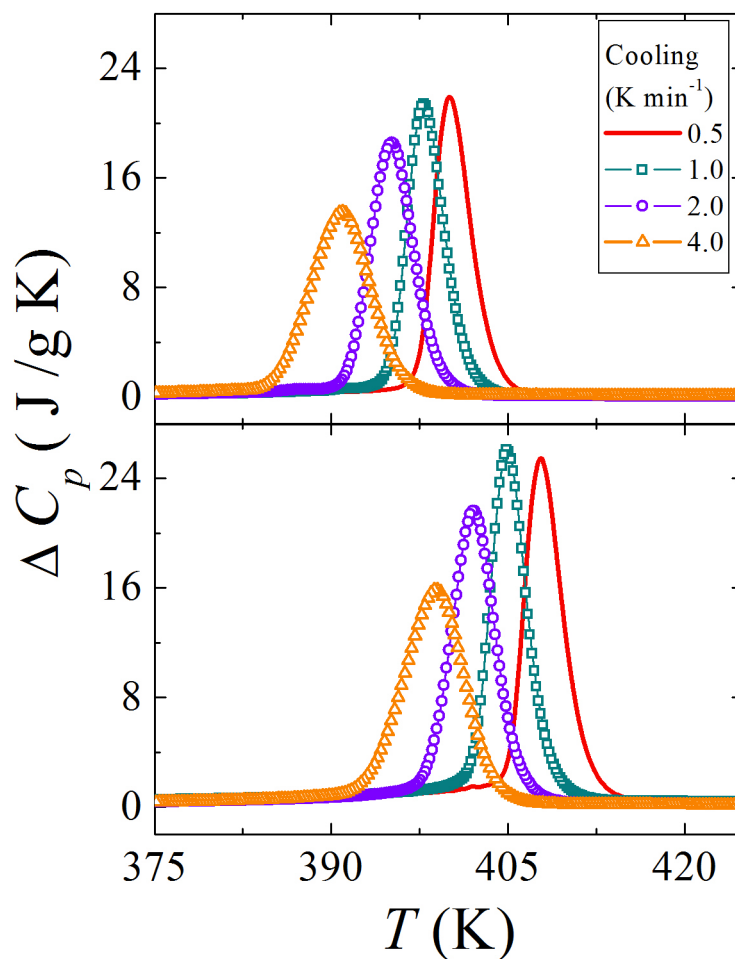


Figure 6.6. The total excess specific heat ΔC_p on cooling from the isotropic to mesomorphic to α -monoclinic transitions as a function of continuous scan rate (K/min) for neat iPP (top) and 2 wt% of CNTs (bottom). For clarity, every 15th data point has been plotted. Quasi-static modulation parameters were used; 0.5 K temperature modulation amplitude and 60 s heating period, while the cooling rate was varied from -0.5 to -4 K/min. See legend.

in Figure 6.6. As the cooling rate increases for the 2 wt % iPP/CNT (bottom panel of Figure 6.6), the large ΔC_p peak shifts in temperature and eventually decreases in height and broadens in width for the fastest cooling rate of - 4 K/min. As the heating rate increases from 0.5 to 4 K/min, see Figure 6.7(bottom panel), the ΔC_p traces shift to lower temperature and also evolve in shape. The smaller ΔC_p peak at $T_{M,1}$ sharpens and increases in size while the larger ΔC_p peak at $T_{M,2}$ broadens and decreases in size.

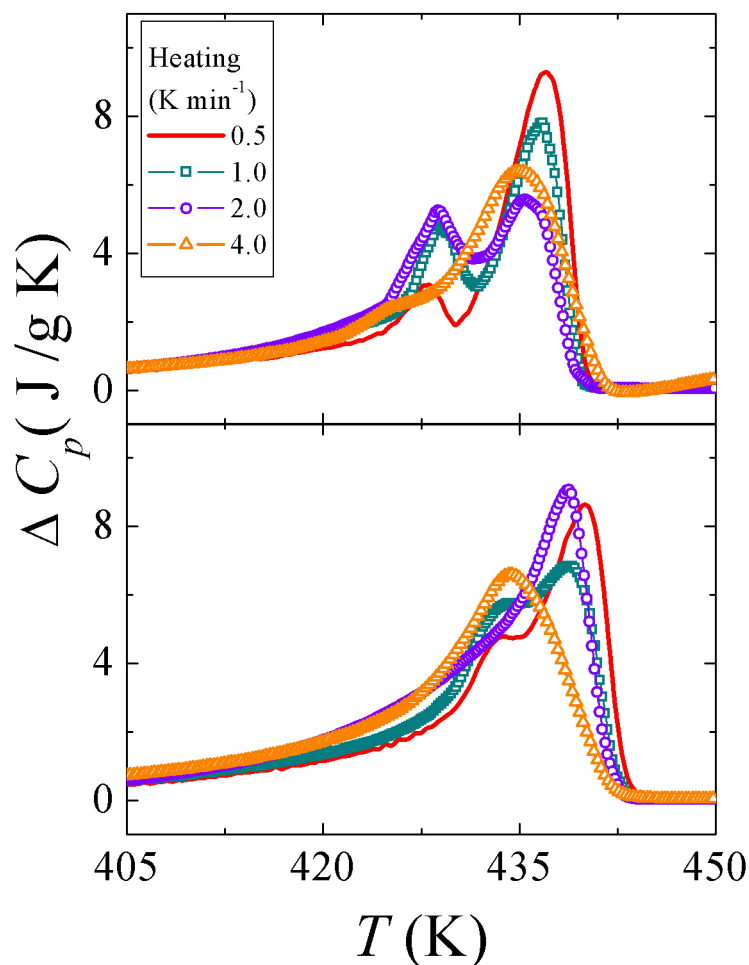


Figure 6.7. The total excess specific heat ΔC_p on heating from the mesomorphic- α monoclinic to isotropic transitions as a function of continuous scan rate (K/min) for neat iPP (top) and 2 wt% of CNTs (bottom). For clarity, every 15th data point has been plotted. Quasi-static modulation parameters were used; 0.5 K temperature modulation amplitude and 60 s heating period, while the cooling rate was varied from -0.5 to -4 K/min. See legend.

The crystallization temperature (T_C) and the melting temperatures (T_M) as a function of scan rates are shown in Figure 6.8. The T_C on cooling decreases approximately by 9 K for both neat iPP and 2 wt% iPP/CNT with increasing cooling rates from -0.5 to -4 K/min. The T_M upon heating decreases approximately by 2 K for both neat iPP and 2 wt% iPP/CNT with increasing heating rates from 0.5 to 4 K/min. The T_C and T_M show linear behavior for neat iPP and non-linear behavior for 2 wt% iPP/CNT. See in Figure 6.8.

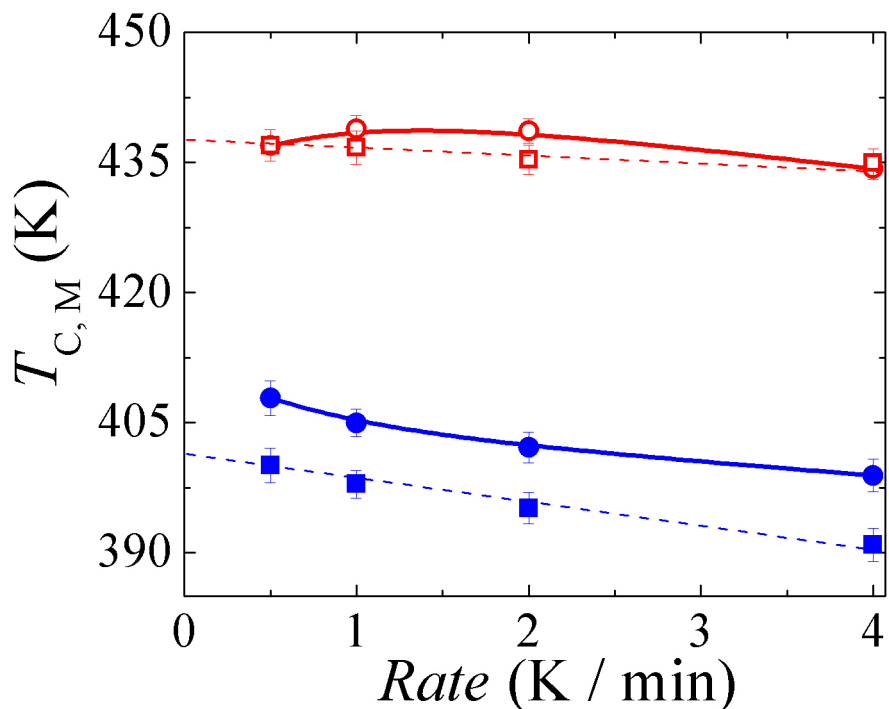


Figure 6.8. The crystallization and melting temperatures as a function for neat iPP (cooling (■), heating (□)) and for 2 wt% iPP/CNT sample (cooling (●), heating (○)). Lines are guides to the eye.

The effective transition enthalpy (ΔH) for both neat iPP and 2wt% iPP/CNT as a function of scan rates is shown in Figure 6.9. The ΔH increases by 8 J/g on heating and is approximately constant as the function of cooling rate for neat iPP, whereas the ΔH is approximately constant on heating and decreases by 20 J/g as a function of cooling rate for 2 wt% iPP/CNT. The effective transition enthalpy diverges between cooling and heating cycles with decreasing scan rates. The enthalpy dependence for neat iPP and 2 wt% iPP/CNT samples reversed between cooling and heating. See in Figure 6.9.

For the neat iPP sample, recrystallization during fast heating is largely suppressed, as opposed to the situation under slow heating. In the presence of CNTs, recrystallization no longer seems to occur, resulting in a lower temperature of melting shown in Figure 6.7. Unlike under slow heating conditions, this result suggests that the final degree of crystal perfection remains lower in the nanocomposite sample than in the neat material, an effect even more accentuated for the rapidly cooled

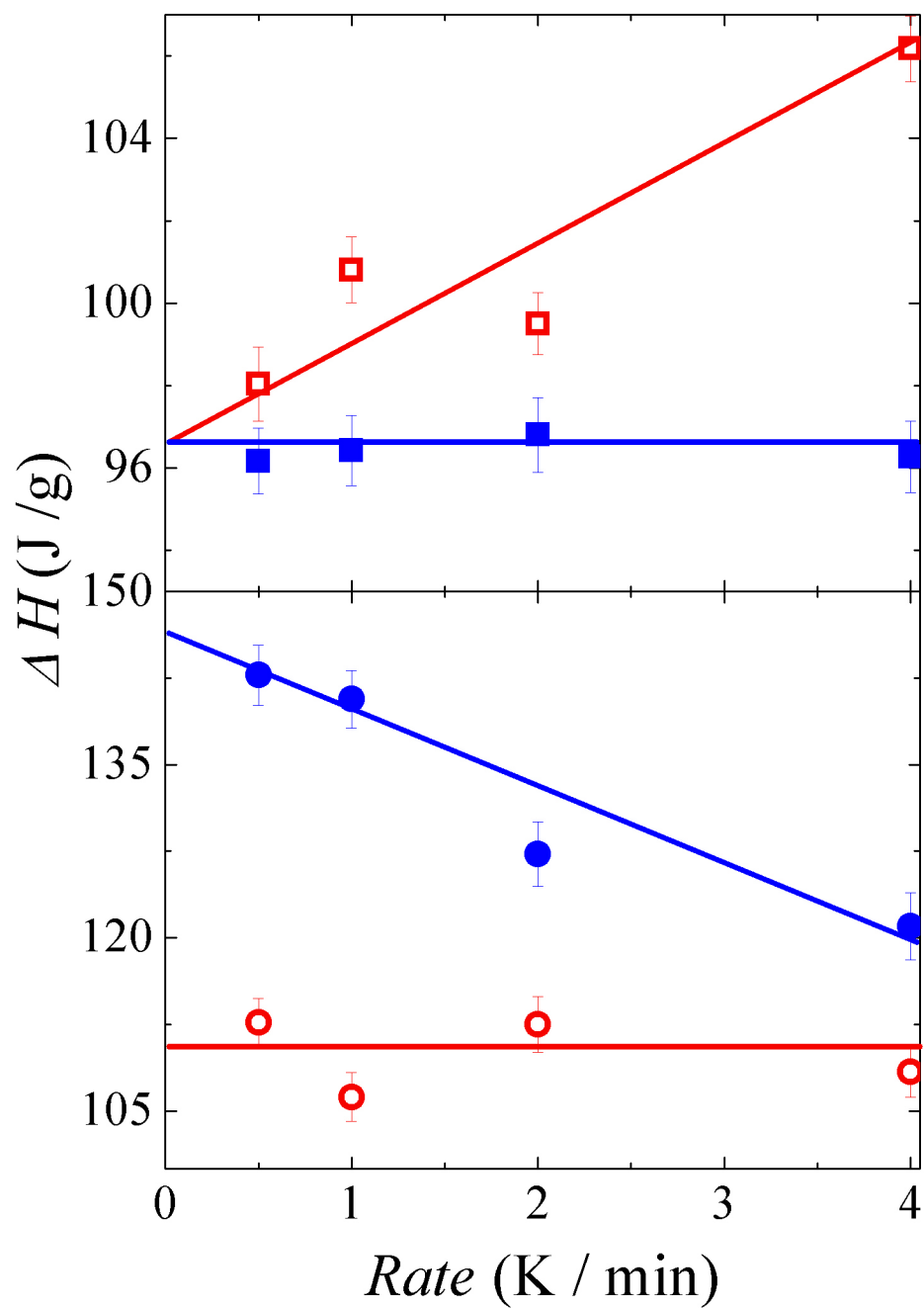


Figure 6.9. The total effective transition enthalpy as function of scan rate for neat iPP (top panel: cooling (■), heating (□)) and for the 2 wt% iPP/CNT sample (bottom panel: cooling (●), heating (○)). Lines are guides to the eye.

Table 6.2. Summary of the transition temperatures T_C , total effective transition enthalpies, peak heights (cooling only) for iPP and 2 wt% of CNT based on the quasi-static MDSC results for both cooling and heating rates (superscripts c and h , respectively). neat iPP (top) and 2 wt% of CNT bottom.

$Rate(K/min)$	$T_C^h(K)$	$T_C^c(K)$	$\Delta H^c(J/g)$	$\Delta H^h(J/g)$	$h_t^c(J/gK)$
0.5	400.08	436.967	96.16	98.03	21.91
1.0	397.89	436.70	96.42	100.81	21.41
2.0	395.13	435.32	96.80	99.50	18.56
4.0	390.90	434.94	96.27	106.20	13.55
0.5	407.82	436.96	142.76	112.66	25.48
1.0	404.97	438.89	140.67	106.20	26.07
2.0	402.12	438.66	127.27	112.50	21.64
4.0	398.90	434.30	121.00	108.35	15.89

samples. Prominent double melting behavior is observed in the neat iPP sample, showing that the degree of crystal perfection after fast cooling is lower than in the slowly cooled sample. The nanocomposite sample, however, exhibits single melting behavior for higher scan rates, despite the much lower crystal perfection as compared to low scan rate, with only a slight shoulder attesting for recrystallization shown in Figure 6.7. Hence, the observed differences in the melting temperatures of the nanocomposite and neat iPP under fast heating conditions, convincingly show that recrystallization in both is reduced. The suppression of recrystallization is stronger in the nanocomposite than in the pure iPP film. This becomes particularly noticeable under kinetically unfavorable fast heating conditions, pointing at a reduced mobility of the polymer chain segments in the presence of CNTs.

However, when sufficient time is given to allow for crystal melting, reorganization, and subsequent recrystallization of existing crystal lamellae, the degree of crystal perfection can attain a level comparable to that in neat iPP. Potentially important factors capable of kinetically suppressing the recrystallization phenomena under the conditions chosen are the occurrence of polymer-CNT interactions, increases in viscosity, and effects related to geometrical confinement. Even though van der Waals interactions between iPP and CNTs are rather weak, they may affect the polymer crystallization since it is known to be extremely sensitive to subtle changes in the chain segment mobility. Therefore, even the weakest interactions might cause changes in the recrystallization behavior, especially in view of the

tremendous interfacial area provided by the CNTs. Viscosity increases related to the formation of a percolating network of CNTs might equally affect the recrystallization behavior. Finally, geometrical confinement needs to be considered as the average distance between well dispersed CNTs becomes much smaller than the typical radius of gyration of the unperturbed polymer, hence also influencing its local segmental mobility and potentially hampering recrystallization phenomena. This was already noticed with respect to the nucleating action of the CNTs as well as in relation to their effect on the melting behavior of the matrix polymer. A key reason for their accentuated influence on the polymer in the considered nanocomposites is the much higher surface area they provide at equal mass fraction. Consequently, CNTs are also believed to more strongly affect the recrystallization behavior of iPP upon heating, as experimentally conformed at low heating rates shown in Figure 6.7. For higher heating rates, recrystallization is completely suppressed in the presence of CNTs, resulting in a lower melting temperature as compared to neat iPP.

In the CNT filled system, a slight shoulder at the low temperature end of the transition still accounts for some extent of recrystallization, but the crystalline perfection still does not reach that obtained in the neat material at the lowest rate. After the fastest cooling rates in this study, neat iPP shows clear double melting behavior for subsequent heating. Moreover, a slight shoulder at the low temperature end of the melting transition indicates that some of recrystallization even persists up to the highest heating rate. The recrystallization might be fully suppressed at even higher heating rates. For the first time, these observations therefore unambiguously evidence some degree of kinetic hindrance in CNT-filled iPP systems, as a result of alterations in the local mobility of the matrix polymer, induced by the surface of the CNTs. On the basis of the observation of an altered crystallization, melting, and recrystallization behavior, it is also anticipated that the presence of CNTs affects the local morphology of the polymer matrix, resulting in a very specific crystalline microstructure characteristic for the considered nanocomposite materials. A summary of transition temperatures, enthalpies on cooling and heating rates for neat and 2 wt% iPP/CNT are given in Table 6.2.

Bibliography

- [1] S. Iijima, *Nature*, **354**, 56 (1991).
- [2] E.T. Thostenson, Z.F. Ren, and T.W. Chou, *Compos. Sci. Technol.*, **61**, 1899 (2001).
- [3] J. N. Coleman, U. Khan, W.J. Blau, and Y.K. Gunko, *Carbon*, **44**, 1624 (2006).
- [4] J. N. Coleman, U. Khan, and Y.K. Gunko, *Adv. Matter.*, **18**, 689 (2006).
- [5] F.H. Gojny, M.H.G. Wichmann, B. Fiedler, I.A. Kinloch, W. Bauhofer, A.H. Windle, and K. Schulte, *Polymer*, **47**, 2036 (2006).
- [6] Z. Qunaies, C. Park, K.E. Wise, E.J. Siochi, and J.S. Harrison, *Compos. Sci. Technol.*, **63**, 1637 (2003).
- [7] R. Haggemueller, C. Guthy, J.R. Lukes, J.E. Fischer, and K.I. Winey, *Macromolecules*, **40**, 2417 (2007).
- [8] A.R. Bhattacharyya, T.V. Sreekumar, T. Liu, S. Kumar, L.M. Ericson, R.H. Hauge, and R.E. Smalley, *Polymer*, **44**, 2373 (2003).
- [9] E. Assouline, A. Lustiger, A.H. Barber, C.A. Cooper, E. Klein, E. Wachtel, and H.D. Wagner, *J. Polym. Sci. Part B: Polym. Phys.*, **41**, 520 (2003).
- [10] J. K.W. Sandler, S. Pegel, M. Cadek, F. H. Gojny, M.V. Es, J. Lohmar, W.J. Blau, K.Schulte, A.H. Windle, and M.S.P. Shaffer, *Polymer*, **45**, 2001 (2004).

- [11] P. Potschke, T.D. Fornes, and D.R. Paul, *Polymer*, **43**, 3247 (2002).
- [12] S.B. Kharchenko, J. F. Douglas, J. Obrzut, E. A. Grulke, and K.B. Migler, *Nat. Mater.*, **3**, 564 (2004).
- [13] H.M. Kim, K. Kim, C.Y. Lee, J. Joo, S.J. Cho, H.S. Yoon, D.A. Pejakovic, J.W. Yoo, and A. Epstein, *J. Appl. Phys. Lett.*, **84**, 589 (2004).
- [14] C. Park, Z. Ounaies, K.A. Watson, R.E. Crooks, J. Smith, S.E. Lowther, J.W. Connell, E.J. Siochi, J.S. Harrison, and T.L.S. Clair, *Chem. Phys. Lett.*, **364**, 303 (2002).
- [15] J. Cao and I. Sbarski, *Polymer*, **47**, 27 (2006).
- [16] H. Quan, Z. M. Li, M. B. Yang, and R. Huang, *Compos. Sci. Technol.*, **65**, 999 (2005).
- [17] J. Varga and Karger-Kocsis, *J. Polymer*, **36**, 4877 (1995).
- [18] C. Wang and C.R. Liu, *Polymer*, **40**, 289 (1999).
- [19] S. Bruckner, S. V. Meille, V. Petraccone, and B. Pirozzi, *Prog. Polym. Sci.*, **16**, 36(1991).
- [20] E. Assouline, E. Wachtel, S. Grigull, A. Lustiger, H.D. Wagner, and G. Marom, *Polymer*, **42**, 6231 (2001).
- [21] A. Dasari, Z. Z. Yu, and Y.W. Mai, *Macromolecules*, **40**, 123 (2007).
- [22] R. Haggemueller, J. Fischer, and K.I. Winey, *Macromolecules*, **39**, 2964 (2006).
- [23] M. Trujillo, M. Arnal, A.J. Muller, E. Laredo, S. Bredeau, D. Bonduel, and P. Dubois, *Macromolecules*, **40**, 6268 (2007).
- [24] C.Y. Li, L.Y. Li, W.W. Cai, S.L. Kodjie, and K.K. Tenneti, *Adv. Matter.*, **17**, 1198 (2005).
- [25] C.A. Avila-Orta, F. J. Medellin-Rodriguez, M.V. Davila-Rodriguez, Y.A. Aguirre-Figueroa, K. Yoon, and B.S. Hsiao, *J. Appl. Polym. Sci.*, **106**, 2640 (2007).

- [26] B.P. Grady, F. Pompeo, R.L. Shambaugh, and D.E. Resasco, *J. Phys. Chem. B*, **106**, 5852 (2002).
- [27] G. Georgiev, Y. Cabrer, L. Wielgus, S. Schoen, D. Ivy, and P. Cebe, *MRS Symposium Proceeding*, **1312**, 10.1250 (2011).
- [28] G. Georgiev, M.B. McIntyre, R. Judith, E.A. Gombos, and P. Cebe, *MRS Symposium Proceeding*, **1308**, 10.1252 (2011).
- [29] W. Leelapornpisit, M.T. Ton-That, F. Perrin-Sarazin, K.C. Cole, J. Denault, and B. Simard, *J. Polym. Sci. Part B: Polym. Phys.*, **43**, 2445 (2005).
- [30] G. S. Jang, W. J. Cho, and C. S. Ha, *J. Polym. Sci.*, **39**, 10011016 (2001).
- [31] J. Varga, *J. Macromol. Sci.*, **41**, 1121 (2002).
- [32] J.D. Homan, G.T. Davis, and N.B.E. Hannay, Jr., *Treatise on Solid State Chemistry*, **3**, 497 (1976).
- [33] J.D. Homan and J.J. Weeks, *J. Res. Natl. Bur. Stand.*, **66A**, 13 (1976).

Transport Properties of Melt-Shear Oriented iPP/CNT Thin Films

7.1 Introduction

Polymers are typically very good thermal and electrical insulators while carbon nanotubes (CNTs) have very high thermal and electrical conductivity as well as large anisotropy between properties measured parallel or perpendicular to the CNT long axis. This study are aimed at the interplay between nanoscale and macroscale phenomena in thin polymer/MWCNTs nanocomposite (PNC) films. Macroscale manipulation, like melt-shearing of PNCs, can induce nanoscopic order of the MWCNTs and polymer chains [1]. Here, it is investigated how the induced nanoscopic orientational order of MWCNTs and polymer chains affects one macroscopic property, namely the electrical and thermal conductivity of the films and its anisotropy [2, 3]. There are many factors that can affect the percolation of MWCNTs, like concentration, dispersion and size. The orientational order of MWCNTs is another factor which can influence the critical concentration when MWCNTs start forming networks. The concentration is varied and the induced electrical and thermal anisotropy in oriented nano-composite films under identical melt-shearing conditions is measured. Nanocomposites should allow for tunable material characteristics [4]. The conventional method to enhance electrical and thermal conductivity of polymers is to compound the polymer with conductive metallic powders. In this case with increasing CNT content the electrical and ther-

mal conductivity increases by an order of magnitude at the percolation threshold which depends on the dispersion state and geometry of the filler. In order to obtain a material with high conductivity, high loading of conductive filler is needed. The anisotropy of the carbon nanotubes can be used to adjust the macroscopic properties of the sample by orienting the nanotubes and polymer chains in the PNC film. The polymer isotactic polypropylene (iPP), has liquid crystalline properties being known to exhibit a smectic phase under shear stress [4]. It has also been shown, that MWCNTs accelerate the crystallization kinetics of iPP [5]. The iPP/CNT nanocomposites were prepared from a dispersion with CNTs at concentrations of 0 and 5 wt% by co-precipitation from a nonsolvent. Films of these composites were then made by compression molding [6, 7, 8]. Under shearing conditions in the liquid nanocomposite, in our experiments, they are expected to align in the direction of shearing with a certain degree of liquid crystalline order. It is expected to see CNT content not only change the magnitude of the electrical conductivity but also to induce anisotropy. In our previous work [9] on melt-sheared iPP/CNTs nano-composite films, anisotropy was suggested by x-ray scattering (2D-WAXS) patterns, polarized optical microscopy (POM), and two-dimensional microscopic transmission ellipsometry (2D-MTE) data. Anisotropy in melt-sheared samples indicates ordering of iPP/CNT nanostructures to thus produce oriented films.

The optical transport in polymer films and in carbon nanotubes differs significantly. Control of the internal order of both in nanocomposites can bring a tunable range of optical constants which can be used in their design for applications. It has been shown that MWCNTs align under shear stress in polymer melts [10].

Our results show that the electrical and thermal conductivity of the nanocomposites increases when MWCNTs are added, which is expected because of the generally lower volume resistivity of the CNTs. When nano-composites were melt-shear oriented the electrical and thermal conductivity was different in directions parallel and perpendicular to the direction of orientation, a property that can further be explored at different CNTs concentrations, orientation conditions and for other polymers. Control of the internal order of iPP and CNTs in nano-composites can bring a tunable range of electrical and thermal conductivity, which combined with other adjustable properties, like anisotropic thermal conductivity and optical properties, mechanical and chemical stability can be used for designing new

applications.

7.2 Results and Discussions

7.2.1 Electrical Transport Properties

In Fig. 7.1, the measured electrical conductivity of nonsheared σ_0 and sheared σ_s samples of iPP/CNT is shown for two different temperatures. The addition of CNTs increases the electrical conductivity by about four orders of magnitude for the non-sheared and sheared samples as compared to neat iPP. This agrees with the expectations because the pure iPP is an insulator and CNTs conduct electricity. For the nanocomposite, the resistivity for sheared samples is higher by over a factor of 2 than for nonsheared samples and is consistent with shear induced in-plane orientational order of the CNTs. Such planar orientational order of the CNTs would result in a larger average distance between the nanotubes perpendicular to the orientation axis (perpendicular to the film plane) than for random oriented CNTs. This would decrease the electrical conductivity for sheared samples in this experimental configuration. This is further supported by an absence of a shear induced difference in σ for neat iPP films, except a small difference for 300 K. This shows that orientation effects on the conductivity of PNCs is a novel property of the CNT distribution.

For all film samples, the electrical conductivity increases with increasing temperature from 273 to 230 K and is likely due to the thermally activated motion of the polymer chains, the CNTs, and the interaction between them (See Fig. 7.2). The resistivity drop of neat iPP is increasing with increasing temperature. This effect even more pronounced for iPP/CNT composite samples. The anisotropy in sheared and non-sheared sample is increasing for increasing temperature for the iPP/CNT samples, but it shows different trend for lower and higher CNT concentration for iPP/CNT samples (See Fig. 7.3). The effect of increased thermal motion and thermal expansion lead to better contact between the polymer chains and between the polymer chains and the nanotubes, measured as a decrease in resistivity in both neat iPP films and in their nanocomposites. The percolation threshold is not observed sudden drop and it pronounced slowly. It is due to the fact of pressing and shearing.

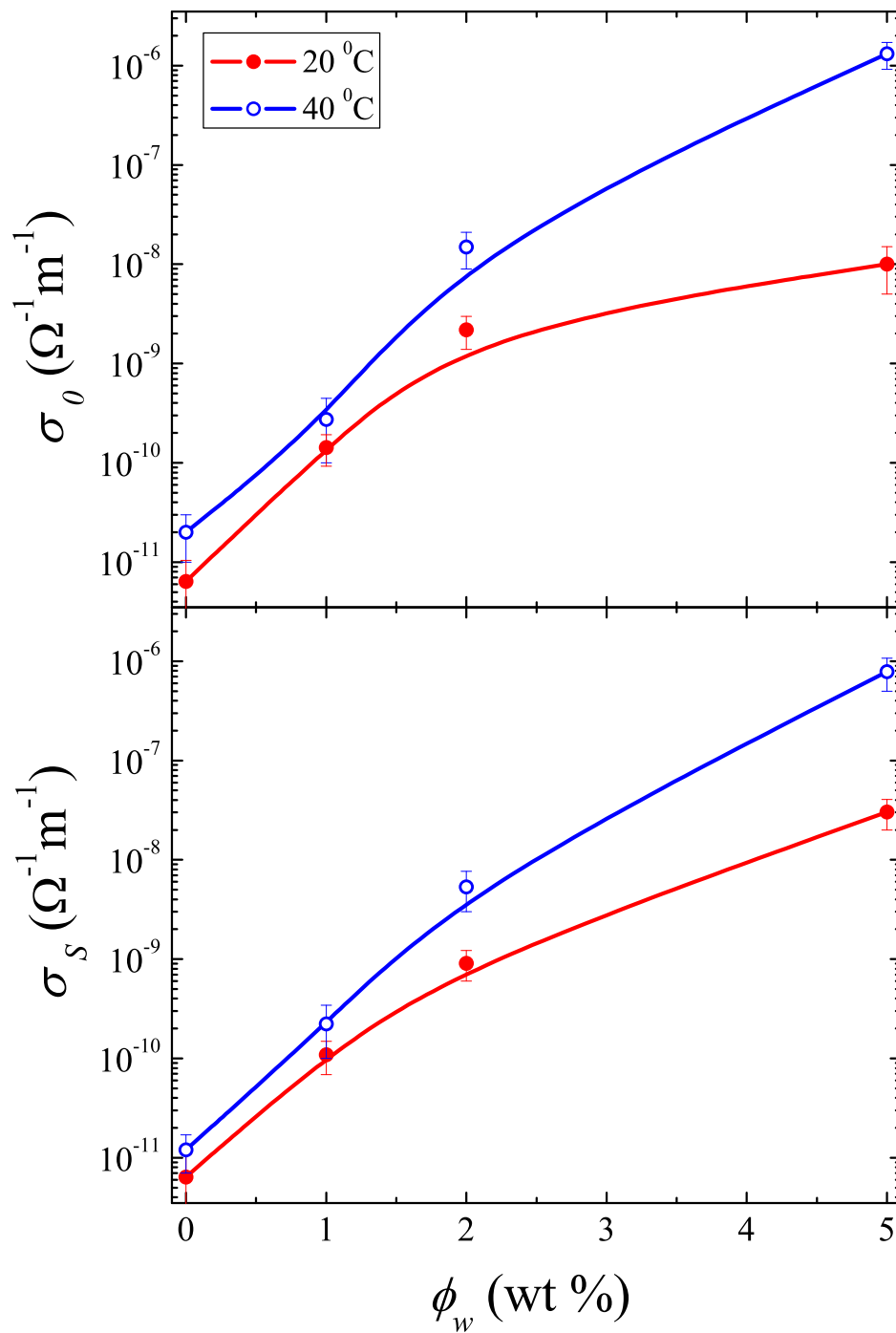


Figure 7.1. Electrical conductivity of non sheared (upper panel) and sheared (lower panel) IPP/CNTs nanocomposite for 40 °C and 20 °C as a function of CNT concentration.

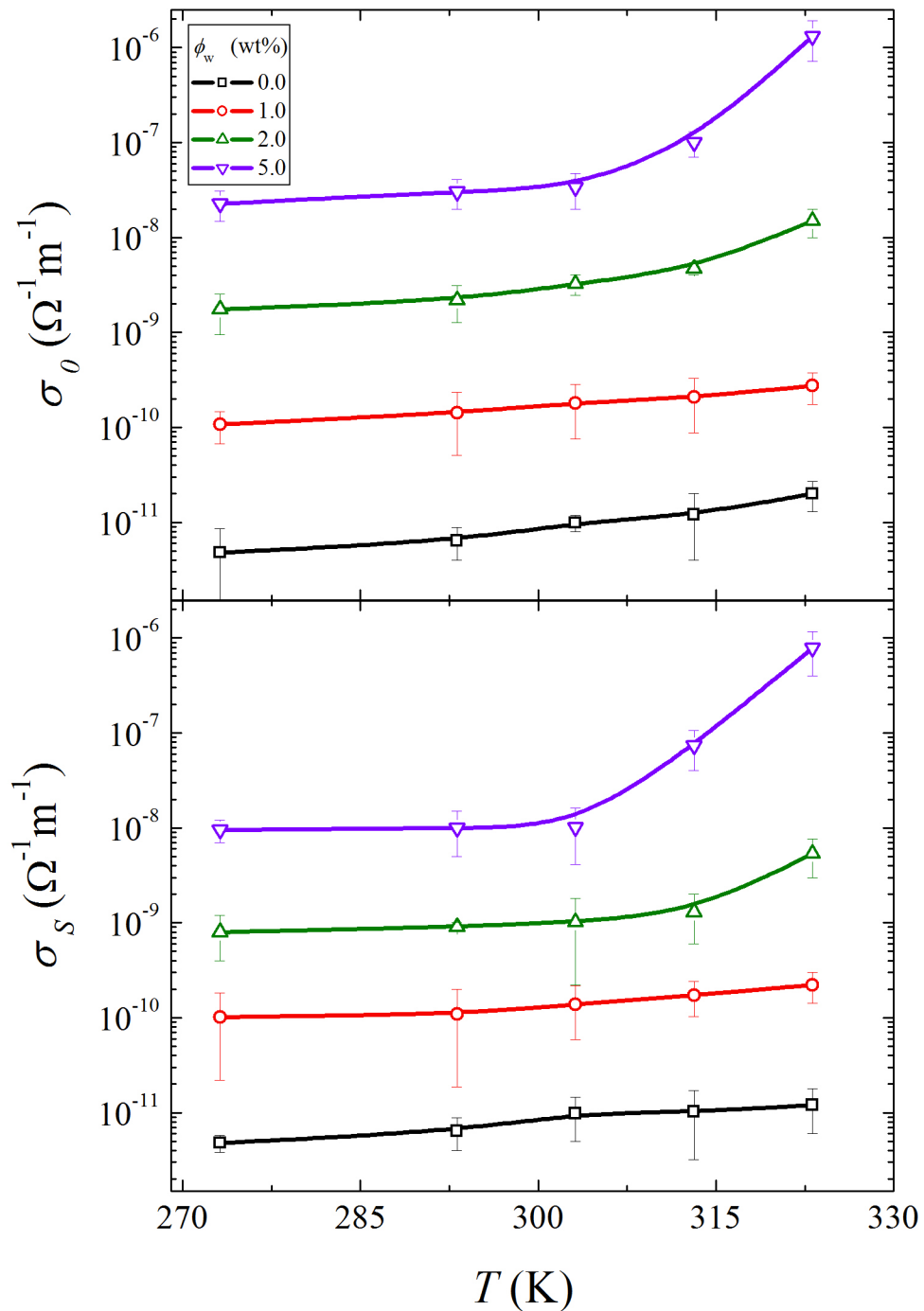


Figure 7.2. Electrical conductivity of non sheared (upper panel) and sheared (lower panel) IPP/CNTs nanocomposite as a function of CNT temperature.

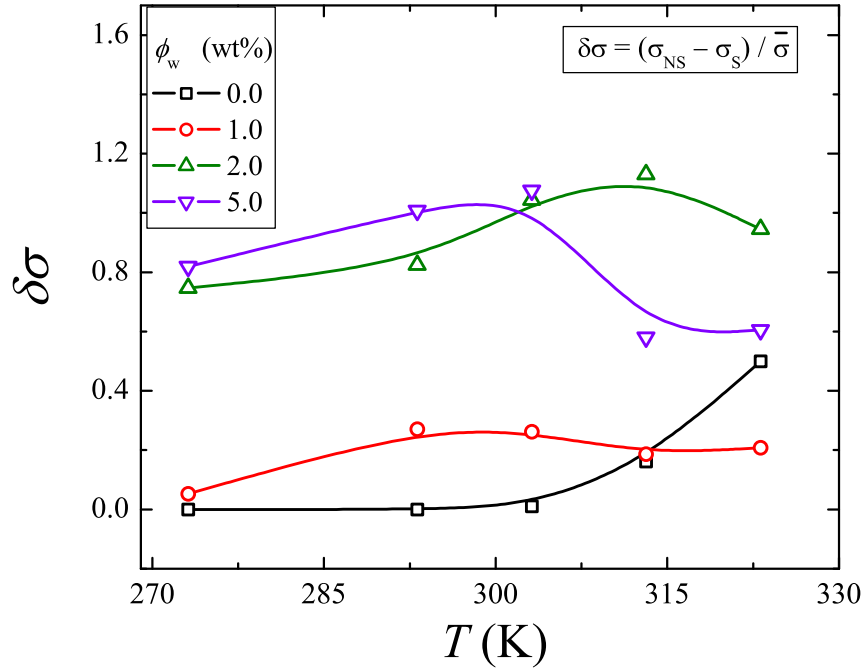


Figure 7.3. Anisotropy in electrical conductivity of non sheared and sheared IPP/CNTs nanocomposite as a function of CNT temperature.

It is possible that the dipole-dipole interactions in the polymer at higher temperature enhance its electrical conductivity. Our results also suggest that the interaction between polymer and CNTs are influenced more by kinetic factors at higher temperature. These interactions are reducing defects in the samples, increasing contact and therefore enhancing conductivity at higher temperature and in presence of CNTs.

Carbon nanotubes have large electrical conductivity, low resistivity, molecular scale and large anisotropy upon orientation due to their large aspect ratio. Polymers are electrical insulators and inducing internal order in polymer films does not significantly affect the electrical conductivity in sheared and non-sheared films. Combining the two shows that a new property in polymer nano-composites of anisotropy in electrical conductivity. Moreover it can be tuned in degree of anisotropy and in absolute magnitude by controlling several parameters of the nanocomposite films at different temperatures. The internal structure of the PNCs is determining whether the macroscopic electric transport properties will be those of the polymer, of the nanotubes, or will have an intermediate value. Also, the

degree of orientation in our samples induces a novel property of electric transport anisotropy, which we envision as useful for applications. The internal structure of our samples is determined by several constraints: 1) The thickness of the films restricts the degrees of freedom for the orientation of the CNTs to a preferential two dimensional one 2) The shearing procedure reduces additionally the dimensionality of ordering to closer to one dimensional. It induces order parameter of the CNTs and the iPP chains, which at low concentration leads to anisotropy of the electric transport through the films. If the order parameter was zero, we would not have observed the macroscopic anisotropy in electrical transport that we did 3) The percolation threshold depends on several parameters, such as concentration, order parameter, film thickness, length and thickness of CNTs, conductivity of the CNTs, and in future studies, the composition and structure of the polymer chains. The degree of orientation, the percentage of CNTs, the degree of dispersion, the percolation of CNTs, the film thickness and dimensions, all are controllable to achieve the desired anisotropy in electrical conductivity and the magnitude of the overall electrical conductivity of the nano-composites. This property can be combined with other properties of polymer-carbon nanotube nano-composites, like anisotropy and degree of electrical conductivity to achieve the ideal combination of these properties for desired applications. Conductivity increases with increasing temperature and increases with increased orientation of the CNTs. The conductivity increase can be due to the fact that at higher temperature defects are removed. In the nanocomposite this may also be due to the fact that thermal expansion coefficients for iPP than CNT are different and this process affects the CNTs percolation network. Further improvement of the methods of dispersion and alignment of the CNTs can enhance electrical anisotropy for PNC films.

7.2.2 Thermal Transport Properties

The measured thermal conductivity, κ , of nonsheared and sheared samples of iPP/CNT is shown Fig. 7.4, for two different temperatures. The addition of CNTs increases The thermal conductivity increases with increasing concentration. This matches with the expectations because the pure iPP is an insulator and CNTs highly thermal conductive material . For the nanocomposite, the conductivity for sheared samples is slightly lower by over a factor of 1.5 than for nonsheared

samples and is consistent with shear induced in-plane orientational order of the CNTs. Such planar orientational order of the CNTs would result in a larger average distance between the nanotubes perpendicular to the orientation axis than for random oriented CNTs. This would decrease the thermal conductivity for sheared samples. This is further supported by an absence of a shear induced difference in κ for neat iPP films, except a small difference for 300 K. This shows that orientation effects on the thermal conductivity of PNCs is a novel property of the CNT distribution.

In all samples, the thermal conductivity increases with increasing temperature from 233 to 230 K and is likely due to the thermal vibrations and expansions between the polymer chains, the CNTs, and the interaction between them (See Fig. 7.5). The thermal conductivity of neat iPP is remains same with increasing temperature. The anisotropy in sheared and non-sheared sample is increasing for increasing temperature for the iPP/CNT samples, but it shows negative slope anisotropy with increasing temperature (See Fig. 7.6). The effects of increased thermal vibrations and thermal expansion lead to better contact between the polymer chains and the nanotubes, measured as a increases in thermal conductivity in both pure iPP films and in their nanocomposites.

Our results also suggest that the interaction between polymer and CNTs are influenced more by thermal vibrations and expansions at higher temperature. These interactions are reducing defects in the samples, increasing contact and therefore enhancing thermal conductivity at higher temperature in presence of CNTs.

Carbon nanotubes have large thermal conductivity, molecular scale and strong anisotropy upon orientation due to their large aspect ratio. Polymers are thermal insulators and inducing internal order in polymer films does not significantly affect the thermal conductivity in sheared and non-sheared films. Combining the two shows that a new property in polymer nanocomposites of anisotropy in thermal conductivity. Moreover it can be tuned in degree of anisotropy and in absolute magnitude by controlling several parameters of the nanocomposite films at different temperatures. The internal structure of the PNCs is determining whether the macroscopic thermal transport properties will be those of the polymer, of the nanotubes. Also, the degree of orientation in our samples induces a novel property of thermal transport anisotropy, which we envision as useful for applications.

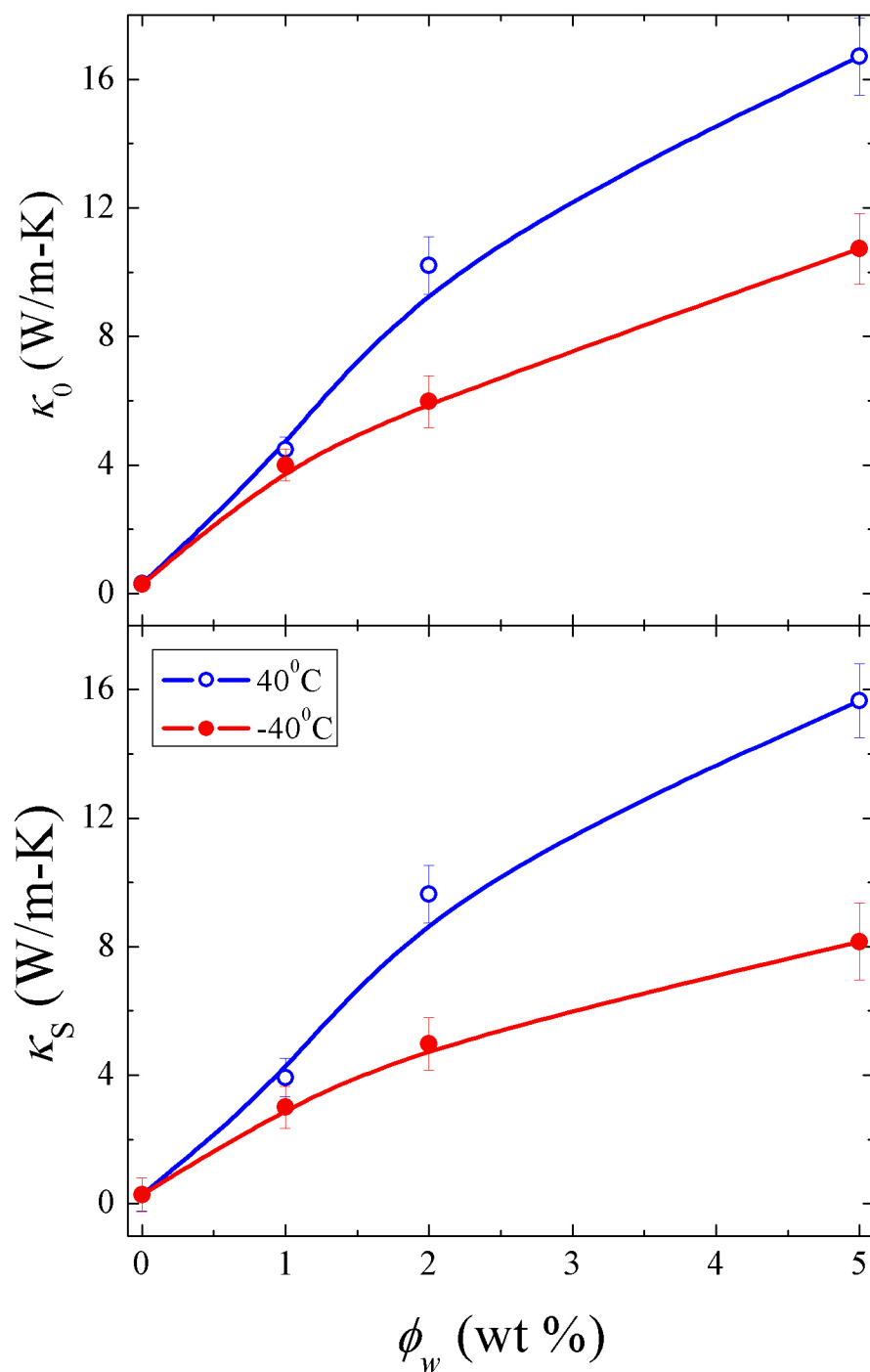


Figure 7.4. Thermal conductivity of non sheared (upper panel) and sheared (lower panel) IPP/CNTs nanocomposite for 40°C and 20°C as a function of CNT concentration.

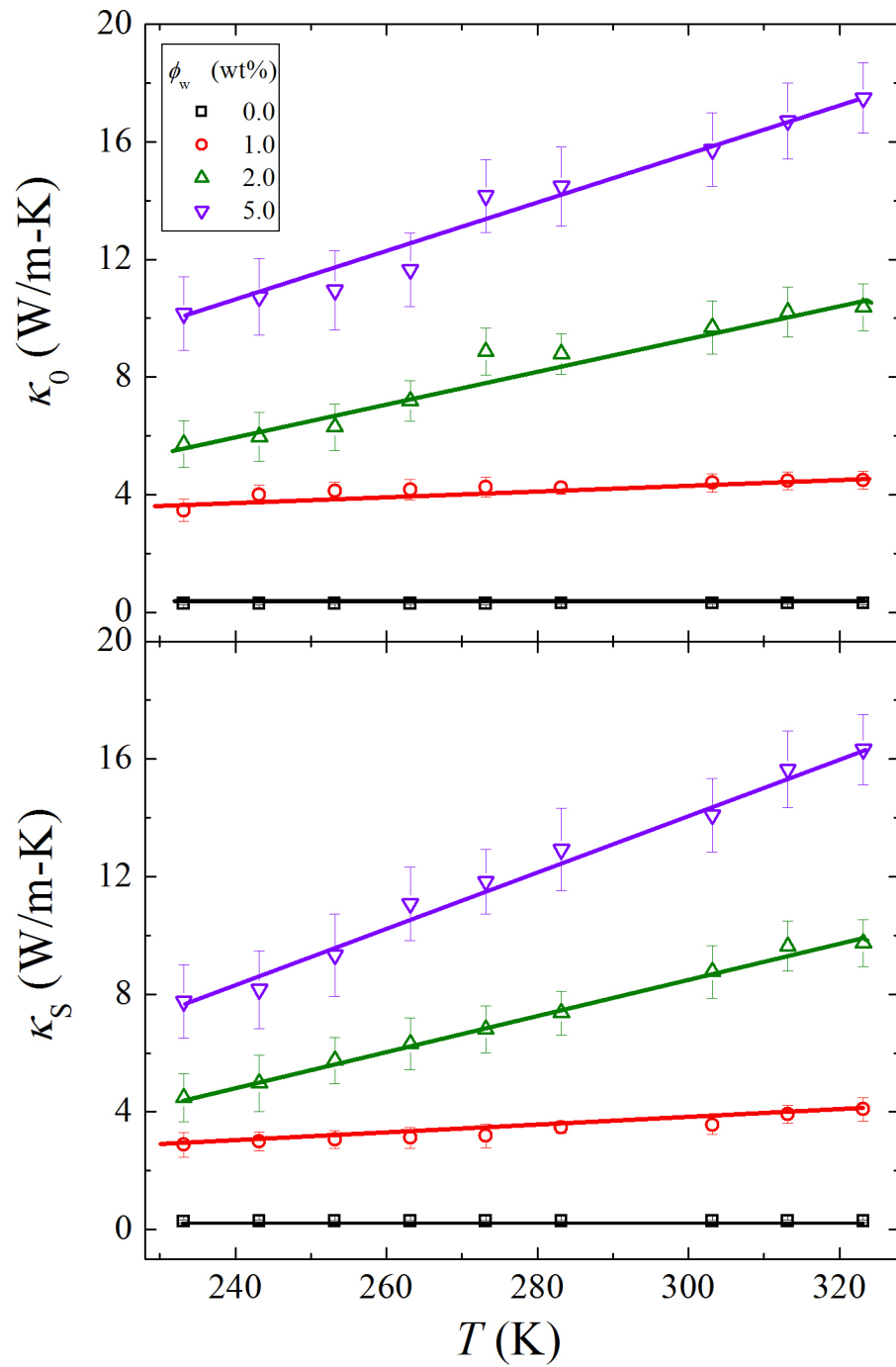


Figure 7.5. Thermal conductivity of non sheared (upper panel) and sheared (lower panel) IPP/CNTs nanocomposite as a function of CNT temperature.

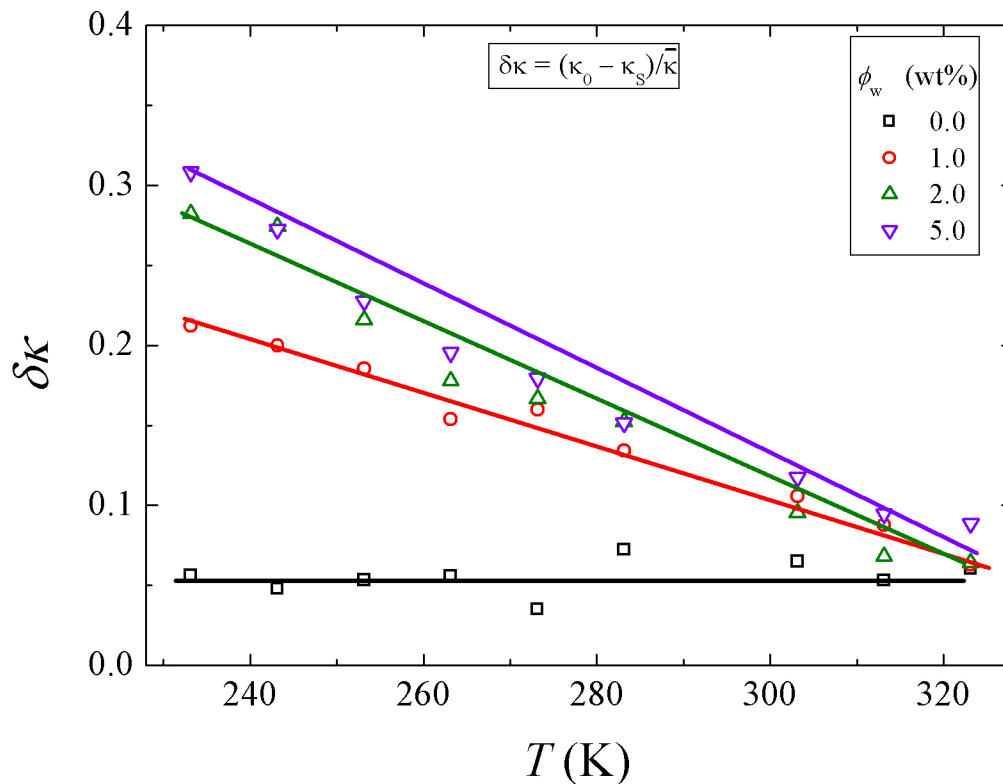


Figure 7.6. Anisotropy in thermal conductivity of non sheared and sheared IPP/CNTs nanocomposite as a function of CNT temperature.

The internal structure of our samples is determined by several constraints: 1) The thickness of the films restricts the degrees of freedom for the orientation of the CNTs to a preferential two dimensional one 2) The shearing procedure reduces additionally the dimensionality of ordering to closer to one dimensional. It induces order parameter of the CNTs and the iPP chains, which at low concentration leads to anisotropy of the thermal transport through the films. If the order parameter was zero, we would not have observed the macroscopic anisotropy in thermal transport that we did 3) The percolation threshold depends on several parameters, such as concentration, order parameter, film thickness, length and thickness of CNTs, conductivity of the CNTs, and in future studies, the composition and structure of the polymer chains. The degree of orientation, the percentage of CNTs, the degree of dispersion, the percolation of CNTs, the film thickness and dimensions, all are controllable to achieve the desired anisotropy in thermal conductivity and

the magnitude of the overall thermal conductivity of the nano-composites. This property can be combined with other properties of polymer-carbon nanotube nano-composites, like anisotropy and degree of thermal conductivity to achieve the ideal combination of these properties for desired applications. Conductivity increases with increasing temperature and increases with increased orientation of the CNTs. The thermal conductivity increase can be due to the fact that at higher temperature defects are removed. In the nanocomposite this may also be due to the fact that thermal expansion coefficients for iPP than CNT are different and this process affects the CNTs percolation network. Further improvement of the methods of dispersion and alignment of the CNTs can enhance thermal anisotropy for PNC films.

7.2.3 Optical Transport Properties

Our results on the unsheared film samples show that the CNTs lower slightly the index of refraction for the entire range of wavelengths studied (Fig. 7.7), which is expected due to the lower index of refraction of pure carbon nanotubes and a random distribution/alignment of the CNTs [11]. The extinction coefficient k for the pure iPP film is zero over the entire range of wavelengths studied. For 1 wt% CNTs sample, however, k is roughly constant from 1000 to 600 nm but decreases sharply below 600 nm and approaches zero near 300 nm. The increase of the extinction coefficient is a controllable property of the polymer films by the nanofiller and is tunable with careful calculation of the content of the nanocomposites.

The anisotropy of the refractive index n parallel to the shearing direction (n_{\parallel}) and perpendicular (n_{\perp}) for the iPP and 1 wt% CNT nanocomposite sample is shown in Fig. 7.8. Over the entire range of wavelengths studied (350 to 1000 nm), n_{\perp} is larger than n_{\parallel} , both being larger than n measured for the unsheared 1 wt% CNTs sample (comparing upper panels of Fig. 7.7 and Fig. 7.8). This is consistent with the view that the shearing has aligned the polymer and CNTs, which would change the polarizability along this direction. The fractional anisotropy, for the 1 wt% CNTs nanocomposite sheared film sample is weakly wavelength dependent, decreasing from 0.0063 at 350 nm to just under 0.005 at 1000 nm.

According to our measurements, the CNTs decrease the refractive index in iPP/CNT nanocomposites in unsheared films, at small concentration of 1 wt%

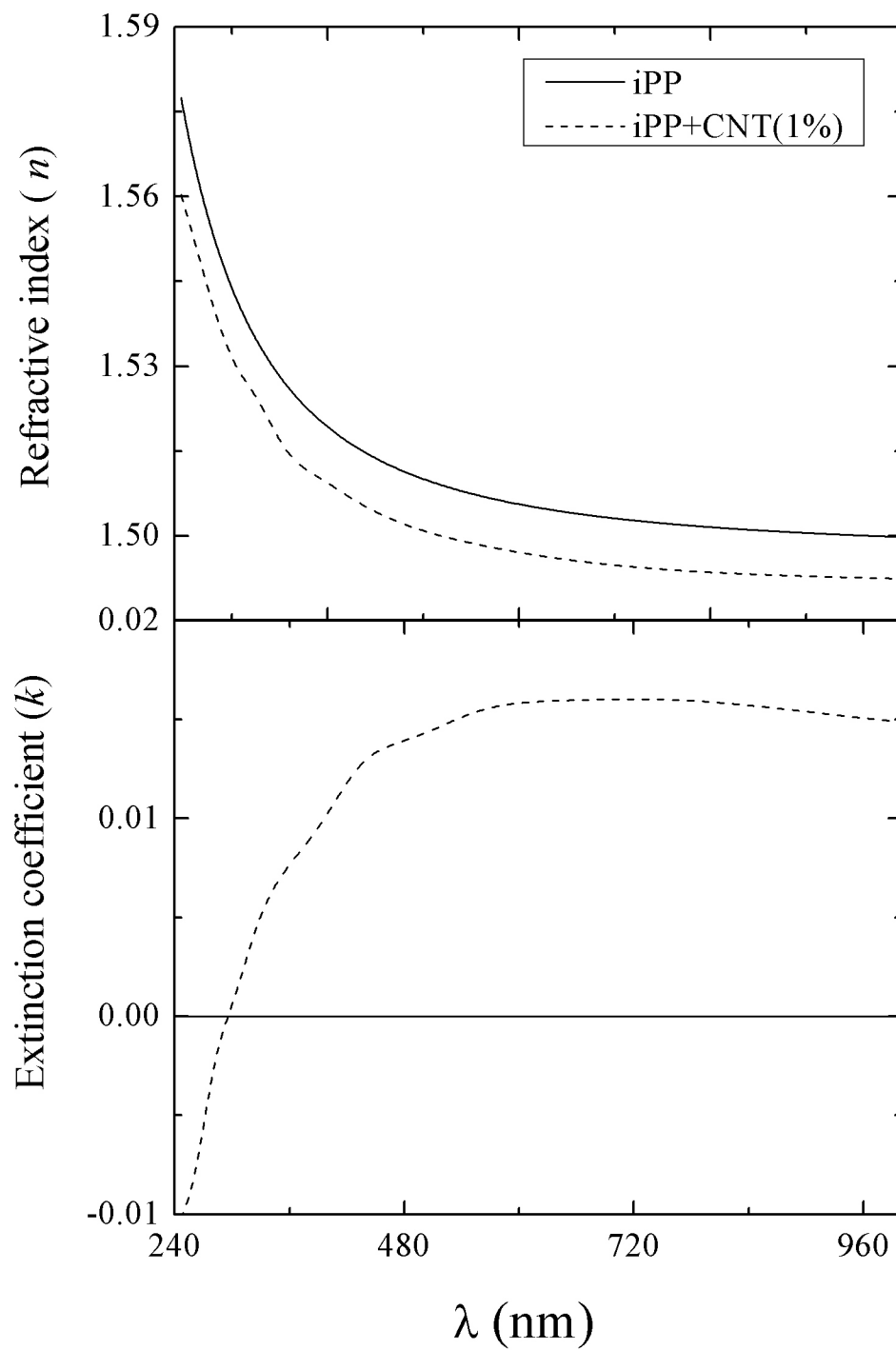


Figure 7.7. Index of refraction (upper panel) and extinction coefficient (lower panel) for pure iPP and 1 wt% CNTs, IPP/CNTs nanocomposite as a function of wavelength.

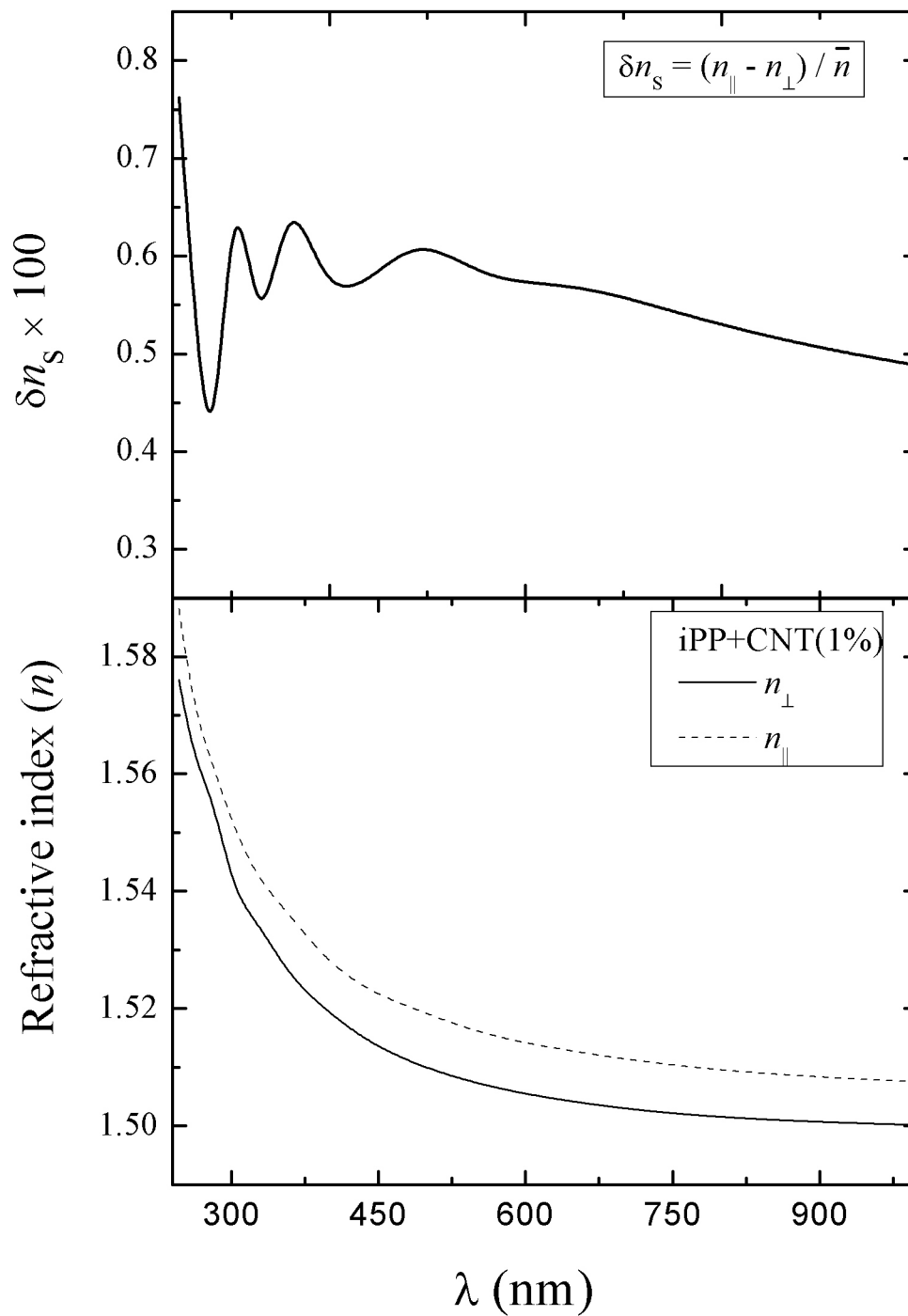


Figure 7.8. The refractive index n for iPP nanocomposite with 1 wt% CNT in directions parallel (n_{\parallel}) and perpendicular (n_{\perp}) to the shear direction (top panel) and the percent anisotropy of n (δ, n_s) as a function of wavelength λ (bottom panel).

of CNTs, as expected by their generally lower index of refraction than iPP [11]. These results are consistent if the CNTs can be reasonably considered randomly distributed and aligned, thus the respective n of the iPP and CNTs simply superimpose for the nanocomposite. More interestingly, we observe a difference in n parallel and perpendicular to the shearing direction in addition to a shift in the average n compared to the unsheared iPP/CNTs nanocomposite at 1 wt% of CNTs. It is possible that the shear aligning may have altered the percolation threshold for this sample to yield an increase in. These effects of baseline shifts and anisotropy due to shear alignment will be explored further at higher concentrations of CNTs and varying shearing conditions for applications that require anisotropy of the optical properties. The usefulness of this approach of creating carbon nanotube nanocomposites with different concentrations is also for applications where tuning of the extinction coefficient in the polymer nanocomposite films is necessary. CNTs are an important agent for modulating the optical transport properties of oriented and un-oriented polymer films.

Bibliography

- [1] G. Georgiev, M. B. McIntyre, R. Judith, E. A. Gombos, P. Cebe, *MRS Symposium Proceeding*, **1308**, 10.1557/157 (2011).
- [2] P. Kalakonda, E. A. Gombos, G. S. Hoonjan, G.Y. Georgiev, G. S. Iannacchione and P. Cebe, *MRS Symposium Proceeding*, **1410**, 10.1557/817 (2012).
- [3] P. Kalakonda, S. Sarkar, E. A. Gombos, G.Y. Georgiev, G.S. Iannacchione and P. Cebe, *MRS Symposium Proceeding*, **1403**, 10.1557/371 (2012).
- [4] F. Gojny, M. Wichmann, B. Fiedler, I. Kinloch, W. Bauhofer, A. Windle, K. Schulte, *Polymer*, **47(6)**, 2036 (2006)
- [5] G. Georgiev, Y. Cabrera, L. Wielgus, Z. Iftikhar, M. Mattera, P. Gati, A. Potter, P. Cebe, *MRS Symposium Proceeding*, **1150**, 10.1150/185 (2009).
- [6] W. Song, I.A. Kinloch, A.H. Windle, *Science*, **302**, 1363 (2003).
- [7] A. Dawid, W. Gwizdaa, *J. of Non-Cryst. Sol.*, **355**, 1302 (2009).
- [8] W. Gwizdaa, K. Grny, Z. Gburski, *J. of Mol. Struct.*, **887**, 148 (2008).
- [9] G. Georgiev, E. A. Gombos, M. McIntyre, M. Mattera, P. Gati, Y. Cabrera, P. Cebe, *MRS Symposium Proceeding*, **1228**, 10.1557 (2010).
- [10] E. K. Hobbie, H. Wang, H. Kim, S. Lin-Gibson and E. A. Grulke, *Phys. of Fluids*, **15(5)**, 1196 (2003).
- [11] L. Hu, D. S. Hecht and G. Gruner, *Chem. Rev.*, **110**, 5790 (2010).

Concluding Remarks

This work reveals the dramatic effects of nanomaterials on the liquid crystalline polymer crystallization and melting phase transitions. It also shows the effect of nanomaterials like carbon nanotubes and quantum dots (CdS) nano-particles on the phase transitions of 90O4, 8CB and 10CB. It also shows the anisotropy of transport properties of polymer melt shear nanocomposites over a wide range of temperatures.

In the LC 90O4 system, the effect of scan rates causes the change in the dynamic of liquid crystal. The specific heat, dielectric constant, and molecular modeling suggest that the combination of bent/twisted core structure, core flexibility, and orientation of the effective dipole moment lead to the onset of a monotropic Sm*B* phase that converts very slowly from a Sm*C* phase, an *N*-Sm*A* transition similar to a very different LC structure, and the appearance of an intermediate smectic-like phase between melting and the Sm*A* phases.

In 90O4/CNT composite system, the introduction of CNT on 90O4 causes the change in the phase behavior. All mesophases have transition temperatures 1 K higher and a crystallization temperature 4 K higher than that of the pure 90O4. The crystal phase super heats until a strongly first-order specific heat feature is observed, indicating melting 0.5 K higher than in the pure 90O4. The enthalpy change associated with *I*-*N* and *N*-Sm*A* phase transitions are only slightly changed with increasing ϕ_w , but are generally lower than pure 90O4. The total transition enthalpy associated with the all transitions is independent on the CNT concentration and thermal treatment. The bulk or pure-like behavior of the phase

transitions is supported by the bulk-like 9004 ECE behavior of the SmA-SmC for the 0.05 wt% sample. The results are arising from the LC-CNT surface interactions breaking orientational symmetry uniformly over a distance along the CNT greater than the nematic correlation length but allowing the LC to slide essentially freely on the CNT surface to accommodate various translational symmetries, leading to a net ordering effect for all transitions. These results suggest that the interactions between molecular structure, dipole moment of liquid crystal and graphene-like surface can allow a random dispersion of CNT to promote both orientational and positional order depending on the length scale of the local order and the degree of surface freedom.

In 8CB/QD composite system, the addition of QD on 8CB causes the change in the phase behavior. The I - N phase transition temperature 2.67 K suppresses and a N-SmA phase transition temperature 2.35 K suppresses than that of the pure 8CB. The enthalpy change associated with I - N phase transitions shows slightly different on heating and cooling and it also shows crossover behavior at lower and higher QDs content. The enthalpy change associated with N -SmA phase transitions is independent on QD concentration and thermal treatment. The order of the transition remains the same being the I - N weakly first-order and the N -SmA second-order. The behavior of QDs depends sensitively on the nature of the LC, anchoring conditions and QDs size. The results clearly demonstrates that the nematic phase impose self assembly on QDs to form one dimensional arrays leading to QDs induces net local disordering effect in LC media.

In iPP/CNT composite system, the addition of CNT on iPP causes the dramatic change on melting and crystallization behavior. The CNTs act as a strong nucleating agent for crystal growth and it displayed nucleating effect comparable to that of traditional nucleating agents. An increase in the melting temperature after non-isothermal crystallization pointed at a higher degree of crystalline perfection in the presence of CNTs. The complex multiple melting behavior was interpreted in terms of recrystallization phenomena occurring during heating. The scan rate effects causes dramatic change on melting and crystallization behavior of iPP/CNT system. The combination of these two important materials has many practical applications that require a deeper understanding of the thermo-physical properties and their connection to the microscopic order.

Finally, iPP/CNT system, the internal structure of anisotropic nanocomposites determines the anisotropy of their macroscopic properties. Nanoscale oriented carbon nanotubes (CNTs) in a polymer matrix allow for anisotropy of thermal and electrical transport and their control by varying concentration, alignment methods and temperature. A better understanding of the transport of energy through such unique systems will improve the applications of these materials. The macroscopic thermal and electrical transport of iPP/CNT thin films show the dramatic change as function of shearing, temperature and CNT concentration. The percolation threshold is clearly pronounced in both electrical and thermal conductivities due to shearing and pressing treatment of the samples. This will further our abilities to nano-engineer material for many important applications.

8.1 Future Directions

Continued research efforts are needed to further understand the behavior of the system we have studied.

1. In 9OO4 system, detailed dielectric measurements exploring the anisotropy as a function of frequency through the various transitions would be very interesting as well as x-ray scattering to determine the smectic-*A* layer spacing behavior. Higher resolution calorimetry would confirm the expected critical behavior of the continuous transitions.
2. In 9OO4/CNT composite system, experimental efforts for studying the sample homogeneity in the liquid crystal and nanomaterials composite system would be interesting and are needed to understand the behavior of the liquid crystal nanocomposite systems.
3. In 8CB/QD composite system, continued experimental efforts probing the the homogeneity of the sample, frequency-dependent dynamics, smectic structures via x-ray scattering and elastic behavior via light-scattering of the homogeneous sample as a function of QDs concentration and temperature would be particularly important and interesting.
4. In iPP/CNT composite system (shear and non-sheared samples), continued experimental efforts probing the the homogeneity of the sample, temperature

dependence of optical properties and dielectric properties of the homogeneous sample as a function of CNT concentration and temperature would be particularly important and interesting.

So far, I have studied the behavior of thermotropic liquid crystals and iPP polymer only. I would like to study the behavior of various lyotropic liquid crystal materials and various polymers with nanoparticles.

Appendix

A.1 Publications

1. **P. Kalakonda**, E. A. Gombos, G.S. Iannacchione, G. Y. Georgiev and P. Cebe, “Calorimetric Study of Nanocomposites of Multiwalled Carbon Nanotubes and Isotactic Polypropylene Polymer” *J. Appl. Polym. Sci.*, **10**, 39204 (2013).
2. **P. Kalakonda**, R. Basu, C. Rosenblatt, G.S. Iannacchione, “Studies of Nanocomposites of Carbon Nanotubes and a Negative Dielectric Anisotropy Liquid Crystals” *Phys. Rev E*, (2013) submitted.
3. **P. Kalakonda**, E. A. Gombos, G.S. Iannacchione, G. Y. Georgiev and P. Cebe, “Thermal Transport Properties of Melt-Shear Oriented iPP/Carbon Nanotube Thin Films”, *Mater. Res. Soc. Symp. Proc.*, **1410**,10.1557/350 (2012).
4. **P. Kalakonda**, E. A. Gombos, G.S. Iannacchione, G. Y. Georgiev and P. Cebe, “Electrical Conductivity of Anisotropic iPP Carbon Nanotube Thin Films”, *Mater. Res. Soc. Symp. Proc.*, **1410**, 10.1557/817 (2012).
5. **P. Kalakonda**, E. A. Gombos, G.S. Iannacchione, G. Y. Georgiev and P. Cebe, “iPP/CNTs Multifunctional Polymer Nano composite”, *Mater. Res. Soc. Symp. Proc.*, **1410**, 10.1557/371 (2012).

6. S. Sarkar, **P. Kalakonda**, E. A. Gombos, G.S. Iannacchione, G. Y. Georgiev and P. Cebe, “Optical transport Properties of Oriented Isotactic Polypropylene and Carbon Nanotubes II”, *Mater. Res. Soc. Symp. Proc.*, **1410**, 10.1557/827 (2012).
7. **P. Kalakonda**, E. A. Gombos, G.S. Iannacchione, G. Y. Georgiev and P. Cebe, “Structure- Electrical Transport property relationship of Anisotropy IPP/CNT films”, *Mater. Res. Soc. Symp. Proc.*, **1499**, 10.1557/445 (2013).